Università degli Studi di Catania
Scuola Superiore di Catania

International PhD
in
Nuclear and Particle Astrophysics
XXVI cycle

Development of reconstruction algorithms for large volume neutrino telescopes and their application to the KM3NeT detector

Agata Trovato

Coordinator of PhD
Prof. Stefano Romano

Tutor
Prof. A. Insolia
Dott.ssa R. Coniglione
Dott.ssa P. Sapienza

a.a. 2010/2013

CONTENTS

INTRODUCTION

After almost 50 years since the first proposal of exploiting deep-sea waters to detect cosmic high-energy neutrinos we are now at the verge of opening a new observational window on our Universe. In the last months the IceCube neutrino telescope in the Antarctica has presented mounting evidence of a flux of neutrinos in the 10 TeV - 1 PeV range that exceeds the known flux of atmospheric neutrinos by a statistically significant factor. Even if this signal, which includes upward- and downward-going neutrinos of all species, sums up to a handful (twenty-eight) of neutrinos it marks a major turning point in astroparticle physics. The origin of this signal is however not yet clear, due to the scarceness of the detected neutrinos and mostly to the limited angular resolution of the IceCube detector. A confirmation, possibly accompanied by the identification of the sources is therefore necessary.

KM3NeT will be the next generation neutrino telescope, to be installed in the depths of the Mediterranean Sea. With about five cubic kilometers of sea water instrumented with thousand of optical sensors it will be the most sensitive high energy neutrino telescope, with a sensitivity exceeding that of IceCube by a substantial factor. In addition, thanks to it location in the Northern hemisphere, KM3NeT will be able to observe a large fraction of the sky including some of the most interesting regions like the centre of our Galaxy.

Neutrinos are an optimal probe to observe high energy astrophysical phenomena, since they interact only weakly with matter and are not subject to the influence of magnetic fields. They can therefore travel long distances without being deflected or absorbed and can provide unique information on the most violent and highest energy processes in our Galaxy and far beyond. Their measurement will allow for new insights into the acceleration mechanisms, shedding light on the mechanisms that are at the origin of the highest energies cosmic rays. Our present knowledge of the high energy Universe is based on the observation through electromagnetic radiation (gamma-rays) and charged particles (cosmic rays). The observations of cosmic rays with energies up to 3×10^{20} eV proves the existence of astrophysical objects able to accelerate hadrons up to extreme energies. In these sources, acceleration of protons, little affected by synchrotron energy losses, can be efficient up to $10^{19\div20}$ eV. Proton acceleration, followed by electromagnetic or nuclear interactions, can lead to fluxes of very high energy neutrinos and photons. Photons up to ~ 10 TeV have been recently observed from Galactic Supernova Remnants and closest Active Galactic Nuclei. Nevertheless, the gamma-ray astronomy potential at energies above 100 TeV is limited due to the interaction with the cosmic microwave background radiation (CMBR). This restricts the observation horizon to our Galaxy and some closest extragalactic objects, precluding the observation of the most distant sources. The use of hadrons as probes to explore remote Universe is also limited: neutrons have a mean life too short ($\tau_0 \approx 900$ s), heavy nuclei suffer fragmentation processes in their interaction with interstellar medium and protons are deflected by the Galactic magnetic field ($\sim 3\ \mu$G), precluding the identification of their sources. Extremely high energy protons (10^{21} eV), which are less sensitive to magnetic fields, are absorbed by the interaction with CMBR within few hundreds Mpc.

Candidate neutrino sources in the cosmos are numerous, such as supernova remnants (SNR), Pulsar Wind Nebulae (PWN) and microquasars in the Galaxy, while possible extragalactic sources include Active Galactic Nuclei (AGN) and Gamma-Ray Bursts (GRB). The estimate of extragalactic neutrino fluxes either from AGNs and GRBs has large uncertainties due to model assumptions and to the intergalactic absorption of VHE γ-rays that strongly modifies the spectra measured at Earth. On the other hand, in the hypothesis of hadronic gamma emission, models for galactic neutrino sources are constrained by TeV γ-ray observations that allow to obtain realistic expectations on the detection perspectives.

Neutrino telescopes detect neutrinos indirectly through charged leptons produced in weak charged current (CC) interactions. In transparent media, tracks of relativistic particles can be reconstructed by detecting the light produced via Cherenkov effect, with a three-dimensional array of optical sensors. The "golden channel" for such a neutrino detector is the ν_μ CC interaction since the muon range in water is, at $E_\mu \sim$ TeV, of the order of kilometres and the muon track is almost co-linear to the ν_μ permitting to point back to the neutrino cosmic source. High energy neutrino astronomy requires detector volumes of the km^3 scale hosted in deep water or in deep Antarctic ice, where several thousands of metres of water (or ice) reduce the flux of atmospheric muons by several orders of magnitude. Since neutrinos are the only particles that can pass through the whole Earth, neutrino telescopes look mainly at the up-going neutrinos coming from the opposite hemisphere.

The KM3NeT neutrino telescope will consist of a 3D-array of Digital Optical Modules (DOMs) made of pressure resistant glass spheres with optical sensors and electronics inside, each containing 31 photomultiplier tubes (PMTs) with a diameter of 3 inch. The DOMs are arranged in vertical string-like structures, approximately 1 km in height, called Detection Units (DUs).

In this thesis a complete simulation of the incident muon neutrinos has been performed using a software originally developed by the ANTARES Collaboration for detectors using large area PMTs and adapted here to exploit the KM3NeT DOM peculiarities. In particular, an algorithm to reconstruct the muon track from the set of photons hits on the PMTs has been developed. After an initial hit selection requiring space-time coincidences between hits, the reconstruction proceeds through four successive fitting procedures each one allowing to obtain a better track reconstruction. As output, the code gives the reconstructed track and a track fit quality parameter that is used to reject badly reconstructed events. The achieved KM3NeT angular resolution, that is the angle between the true neutrino direction and the reconstructed track, is about 0.2° at 10 TeV.

The reconstructed events are analysed through a statistical technique to identify a weak neutrino signal from a cosmic source amongst the large background of atmospheric muons and neutrinos, both produced by the interaction of primary cosmic rays with the atmosphere. The analysis of the two specific sources, the SNR RX 1713.7-3946 and the PWN Vela X is presented. These sources are among the most interesting and intense γ-ray emitters that have a large visibility for a detector located in the Mediterranean Sea. In particular, the RX J1713.7-3646 has been chosen as a reference to evaluate the performance of the KM3NeT neutrino telescope.

Recently it has been also proposed to exploit underwater Cherenkov neutrino telescopes to investigate the neutrino mass hierarchy by studying atmospheric neutrino oscillations at low energies. To perform such studies an as much as possible accurate determination of the neutrino energy and of the zenith angle are crucial. This requires a much denser array of photosensors with adequate containment conditions. The KM3NeT collaboration is undertaking a feasibility study, called ORCA, to evaluate the potential of such a measurement with a dedicated detector. The energies of interest are, in this case, of the order of 10 GeV, thus a different version of the reconstruction code has been developed with an additional estimate of the interaction vertex and of the muon energy.

The thesis is organized as follows:

- Chapter 1 presents a summary of the present knowledge of cosmic ray physics and the gamma-ray astronomy as an introduction to the neutrino astronomy. An overview of candidate galactic and extra-galactic neutrino sources as well as their estimated neutrino fluxes is presented.

- Chapter 2 gives a description of the under-water(-ice) Cherenkov technique for the detection of high energy astrophysical neutrinos. Recent results of the operating neutrino telescopes Antares and IceCube are discussed.

- Chapter 3 is dedicated to the description of the key elements of the KM3NeT detector.

- In Chapter 4 the simulation codes used in this work to perform a complete simulation of the incident muon neutrinos, including their interaction in the medium and the propagation of the resulting secondary particles, the light generation and propagation in water and the detector response are described in detail.

- Chapter 5 is dedicated to a detailed description of the muon track reconstruction code.

- In Chapter 6 the main statistical methods applied to the search of cosmic neutrino sources are explained and the results obtained for the SNR RX 1713.7-3946 and the PWN Vela X are reported.

- Chapter 7 presents the status of the feasibility study for the low energy ORCA detector.

CHAPTER 1

HIGH-ENERGY NEUTRINO ASTRONOMY

In the last decades, thanks to a multi-messenger approach, our knowledge of the high-energy Universe has been widely extended. Nevertheless many open questions remain. The observation of γ-rays has been complemented with the detection of cosmic rays, particles accelerated to the highest energies in the sources, and the search for neutrinos produced by the interaction of cosmic rays with gas or matter around the source. Being uncharged and weakly interacting, neutrinos are very promising probes for high-energy astrophysics. In fact, they are not deflected by interstellar magnetic fields nor absorbed in dense matter. Therefore they can provide information from astrophysical environment obscure to high-energy γ-rays and charged particles. Since neutrinos can only be produced in hadronic processes, the detection of even a faint flux of high energy astrophysical neutrinos will also reveal the nature of the most energetic processes in the most powerful astrophysical systems.

This Chapter presents a summary of the current experimental and theoretical status of the research in the field of high-energy astroparticle physic with a focus on Neutrino Astronomy. Since astrophysical neutrinos, together with γ-rays, are expected to be the result of cosmic ray interaction in the astrophysical source, the discussion on the estimated neutrino fluxes from different source classes is introduced by presenting the most relevant aspects of cosmic rays and γ-rays astronomy.

1.1 Cosmic rays

The atmosphere of the Earth is steadily bombarded by an isotropic flux of charged particles, mostly protons and heavy nuclei, called cosmic rays [1–3], that interact in the atmosphere revealing their existence on the ground by indirect effects such as ionisation and formation of showers of secondary charged particles. The discovery of cosmic rays (CRs) is attributed to Victor Hess who, in 1912, flying in a balloon to an altitude of 5 km discovered that the ionisation of the air strongly increases with altitude [4]. The only explanation of his measurement, he believed, was that "a radiation of very high penetrating power enters the atmosphere from above". Despite a century of studies CRs are still a puzzling subject for physicists. Up to date measurement show that the CR flux extends over 10 orders of magnitude in energy, from hundreds of MeV up to at least several 10^{20} eV. One of the open questions is whether the spectrum continues to even higher energies and we just have not been able to detect it because of limited statistics or due to the presence of a hard cut-off for physical reasons. Over the observed energy range the differential all-particle flux, shown in fig. 1.1, drops by 32 orders of magnitude down to few particles per 100 km^2 per century, thus requiring different detection techniques for each energy range. At energies below $\sim 10^{14}$ eV a direct measurement is possible through atmospheric balloons or satellites permitting an accurate study of the cosmic ray composition. At higher energies the CRs detection requires detectors with areas that must be exposed for periods of time too long to be placed on board of a satellite. The measurement is possible only in big infrastructures located on the ground. Such detectors, called air shower arrays, can cover areas of many km^2 and detect the remnants of the atmospheric cascades of particles initiated by the incident primary particle. Another technique used in this energy range is represented by the detection of the fluorescence light produced by the passage of charged particles through the atmosphere and subsequent nitrogen excitation and disexcitation. None of the two techniques is particularly effective in identifying the nature of the primary. The first detectors used only one of the two techniques. For instance, High Resolution Fly's Eye (HiRes [6]) was a fluorescence observatory while Yakutsk EAS Array (Yakutsk [7]) and AGASA [8] were air shower arrays. The results obtained with this experiments was not completely consistent. More recent experiments, such as The Pierre Auger Observatory (Auger [9]) in the southern hemisphere and Telescope Array (TA [10]) in

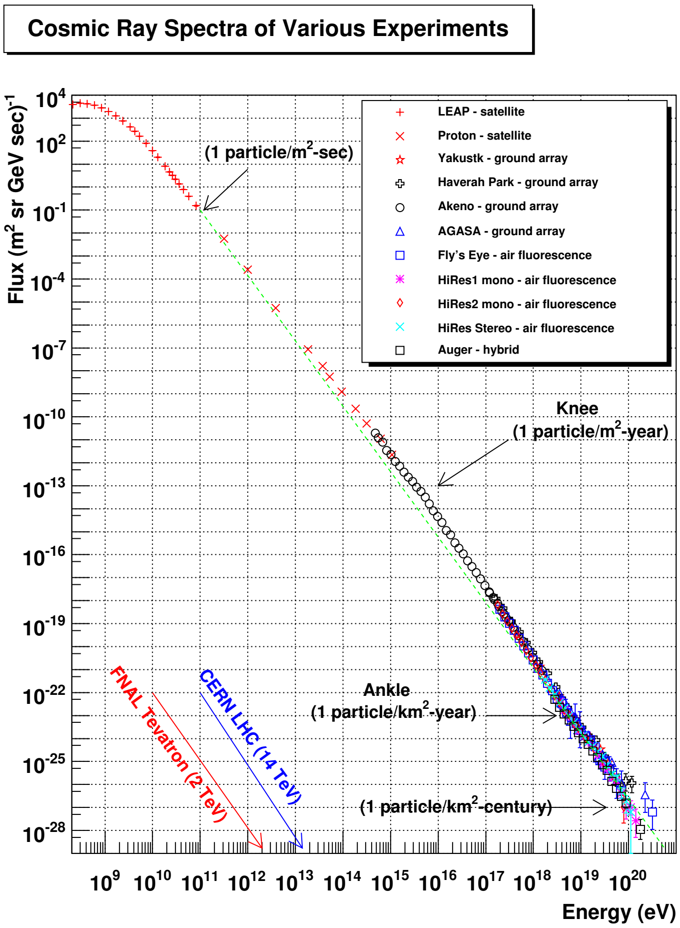

Figure 1.1: The all-particle cosmic ray spectrum and experiments relevant for its detection. Taken from [5].

the northern hemisphere, use both the techniques.

The spectrum in fig. 1.1 incorporates the results of many different experiments. At energies less than ∼ 1 GeV it can explained by the solar activity, in fact at such energies the solar wind shields charged particles coming from outside the solar system. Above a few GeV the CR energy spectrum follows a power law $E^{-2.7}$ up to $E \simeq 4 \times 10^{15}$ eV. At this energy the CR spectrum steepens to a power law E^{-3}, with a break usually referred as the *knee*. This break may sign the limitation of the confinement in the galaxy [11, 12] and is accompanied by a gradual change of composition from light to heavy nuclei [13], with consecutive cut-off in the flux of the individual mass components starting with protons at a few 10^{15} eV up to iron at around 10^{17} eV as confirmed by the experimental results [14]. In fig. 1.2 measurements of the CR composition are reported as a function of X_{max} that is the slant depth at which the particle cascade reaches its maximum in terms of the number of particles, being this variable sensitive to the CR primary mass. To interpret the data, air shower simulation considering heavy and light primaries are included. It's evident that the composition becomes heavier above the knee. This is expected in any scenario which is dominated by propagation in magnetic fields, both during the acceleration and the propagation from the source to the observer, and energy losses can be neglected, such that the particle transport only depends on rigidity, the ratio of energy to charge E/Z. This is usually true for baryonic galactic cosmic rays because their interaction probability during the lifetime of the galaxy is less then unity.

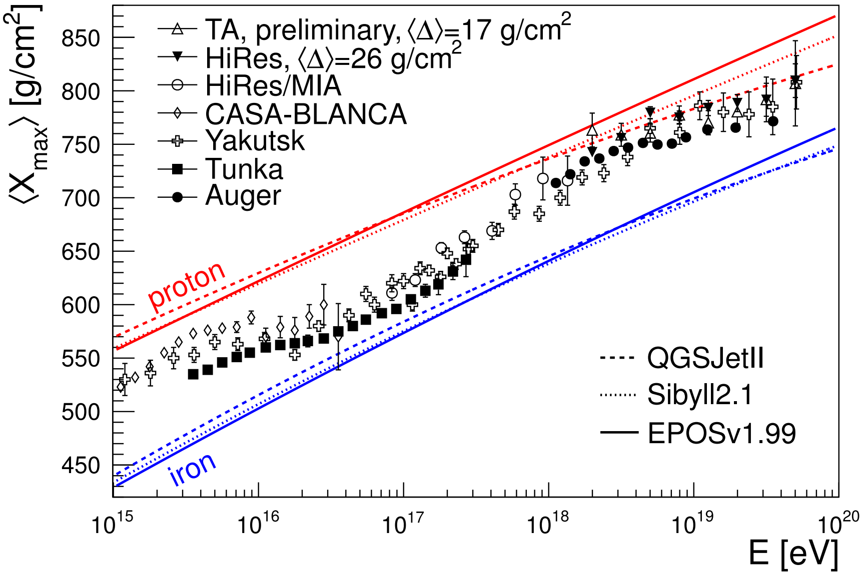

Figure 1.2: Measurements of $\langle X_{max} \rangle$ with different detectors compared to air shower simulations using various hadronic interaction models. See [14] for details.

At $E \simeq 5 \times 10^{18}$ eV the cosmic ray spectrum flattens again to a power law $E^{-2.7}$ with a break called *ankle*, interpreted as a crossover of the fading galactic component and the rising of a harder extragalactic component. Cosmic rays above 10^{18} eV are usually called ultra high energy cosmic rays (UHECR). In the energy region of the ankle, air shower measurements indicate a decrease of the average mass of cosmic rays, as can be seen in fig. 1.2, but at highest energies, above $10^{18.5-19}$ eV, the experimental uncertainties are still too large to draw firm conclusions from the data: the measurements from Auger [15] may be interpreted as a transition to a heavier composition while results from HiRes [16], TA [17] and Yakutsk [18] indicate a systematically lighter composition at these energies. The knowledge of the UHECR mass composition is an extremely relevant piece of information for the possibility of doing proton astronomy, because only UHE protons could be good astrophysical probes. In fact, the galactic magnetic field $B_G \simeq 3\,\mu$G cause particles with charge Z and energy E to describe helical trajectories with a Larmor radius $R_L = E/(ZeB_G)$ that for a proton with E $\simeq 10^{18}$eV is of the same order of the thickness of the Galactic disc halo ($\simeq$ 300 pc), and for $E \simeq 5 \times 10^{18}$eV is of the order of the Galactic disk radius ($\simeq$ 15 kpc). Therefore, protons with $E > 10^{18.5-19}$ eV go approximately along a straight line while this is not true for heavier nuclei, since R_L depends on Z.

On the other hand, additional constraints about the charge of cosmic rays may be acquired from the anisotropy (or lack thereof) of the arrival directions of cosmic rays. Data from HiRes and TA show no correlation with extragalactic objects at this energy [19, 20]. In 2007 the Pierre Auger Collaboration has reported directional correlations of the most energetic particles ($E > 5.5 \times 10^{19}$ eV) with the positions of nearby Active Galactic Nuclei [21, 22] but, enlarging the data set, the anisotropy in the arrival directions resulted less evident [23].

Another open question about the highest energy component of the CRs spectrum concerns the Greisen-Zatsepin-Kuzmin (GZK) cutoff [24, 25], which imposes a theoretical upper limit on the energy of cosmic rays from distant sources. Above a threshold of few 10^{19} eV, protons interact with the 2.7 K Cosmic Microwave Background radiation (CMB) and lose energy through the resonant pion production

$$\begin{aligned} p + \gamma &\rightarrow \Delta^+ \rightarrow \pi^0 + p \\ p + \gamma &\rightarrow \Delta^+ \rightarrow \pi^+ + n \end{aligned} \tag{1.1}$$

The threshold energy for the $p\gamma$ interaction is $E_p \simeq 6 \times 10^{19}$ eV with a cross section $\sigma_{p\gamma} \simeq 100\,\mu$barn so, considering that the average CMB radiation density is $n_\gamma \simeq 400$ cm^{-3}, the absorption length of ultra high energy protons in the Universe is roughly

$$L_{p,\gamma_{CMBR}} \simeq (n_\gamma \cdot \sigma_{p\gamma})^{-1} < 50 \text{ Mpc} \tag{1.2}$$

well shorter than the distance between cosmological sources and the Earth. A strong suppression of the CR flux is therefore expected above the GZK threshold. In the 90s the Akeno Giant Air Shower Array (AGASA) observed an UHECR spectrum continuing as a power law around 10^{20} eV [26] contradicting the GZK cutoff. More recent measurements made by the HiRes [27, 28], Auger [29] and TA [30] experiments are consistent with the presence of a GZK effect. It is likely that the seeming absence of the GZK suppression in the AGASA spectrum was due to energy calibration problems [31, 32]. In fig. 1.3 the all particle energy spectrum for E > 10^{14} eV observed by different experiment is multiplied by $E^{2.6}$ to highlight all the feature described above.

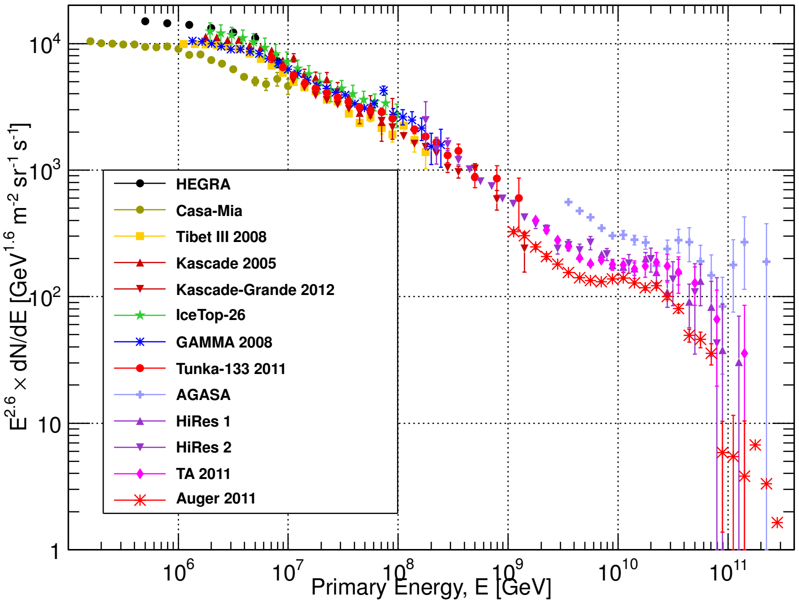

Figure 1.3: All particle cosmic ray spectrum from air shower experiments taken from [33].

In conclusion, even in the hypothesis of composition dominated by protons, the proton bending due to cosmic magnetic field and the GZK effect, shrinks the energy and distance region accessible to UHE proton astronomy between $\simeq 10^{19}$ eV and $\simeq 10^{20.5}$ eV to a few hundreds Mpc in distance.

The mechanism most likely responsible for accelerating particles up to observed CR energies is known as "shock acceleration" or "first order Fermi acceleration" and is described in detail in the appendix A. This process occurs when two plasmas collide, forming a shock at the boundary. In this model, particles are magnetically confined to the source and they are elastically scattered by magnetic irregularities that are frozen into the plasma. The continuos scattering on both sides of the shock front result in an energy gain.

The differential energy spectrum predicted by the Fermi mechanism is an E^{-2} power law. The observed CR differential energy spectrum is steeper than the typical spectra predicted by the shock acceleration mechanism. Models of CR propagation explain the changing of the spectral index with the CR propagation in the irregular component of the Galactic magnetic field and the nuclear interactions with the gas present in the interstellar medium [34].

Although theories for particle acceleration in the astrophysical plasma have empirical foundation, the models would benefit greatly from neutrino astronomy, which provides crucial information about the accelerated proton spectra at the sources, unaffected by propagation effects.

Fermi acceleration ceases to operate when the energy-loss time scale becomes shorter than the acceleration time scale, when the scattering length becomes larger than the shock radius, when the sideways diffusion time scale becomes shorter than the acceleration time scale, or simply after the shock decays. Neglecting the energy loss and diffusion processes, the maximum energy that a particle can reach is a function of the confinement time within the shock. Since confinement is a function of the object dimensions and strength of the magnetic fields, Hillas [35] provided a useful rule to estimate the maximum energy that a charged particle can reach in a shock:

$$E_{\rm max} \approx eZRBv \simeq 10^{18} v \left(\frac{B}{\mu{\rm G}}\right)\left(\frac{R}{\rm kpc}\right) {\rm eV}, \tag{1.3}$$

where Z is the particle charge, v is the shock wave velocity in units of c, B and R are the source magnetic field and the source linear extension, respectively. Note that for relativistic shock, $v \approx 1$, the Hillas criterion is equivalent to the intuitive condition that the gyroradius has to be smaller than the size of the shock.

The modifications resulting form taking into account energy loss processes have recently been discussed in ref. [36]. For example, for diffuse shock acceleration synchrotron radiation by the accelerated nuclei is the dominant energy loss mechanism and yields the additional constraint

$$E_{\rm max} \approx 3 \times 10^{16} \frac{A^4}{Z^4} \left(\frac{B}{\rm G}\right)^{-2} \left(\frac{R}{\rm kpc}\right)^{-1} {\rm eV}\,. \tag{1.4}$$

Several astrophysical environments are identified as possible candidate where the Fermi acceleration mechanism can take place. The proposed acceleration sites are often presented graphically in terms of the Hillas plot where the accelerator size R and the magnetic field B are plotted, as in fig. 1.4. Particular values for the maximal energy correspond to diagonal lines in this diagram, blue for protons and red for iron. Only sources for which the product BR is above the displayed lines can accelerated proton (or iron) up to the corresponding energy. For a shock velocity v ∼1, neutron stars, Active Galactic Nuclei (AGN), Radio Galaxies or Galactic clusters can accelerate protons to $E \sim 10^{20}$ eV. For typical non-relativistic shocks with $v \sim 1/300$, as they are realised, for example, in supernova remnants (SNR), no astrophysical objects of sufficient size and magnetic field to produce 10^{20} eV protons are known, but SNR can accelerate protons with E$\geq$ 10^{12} eV. A more detailed description of the accelerating sources will be given in the sections 1.3 and 1.4.

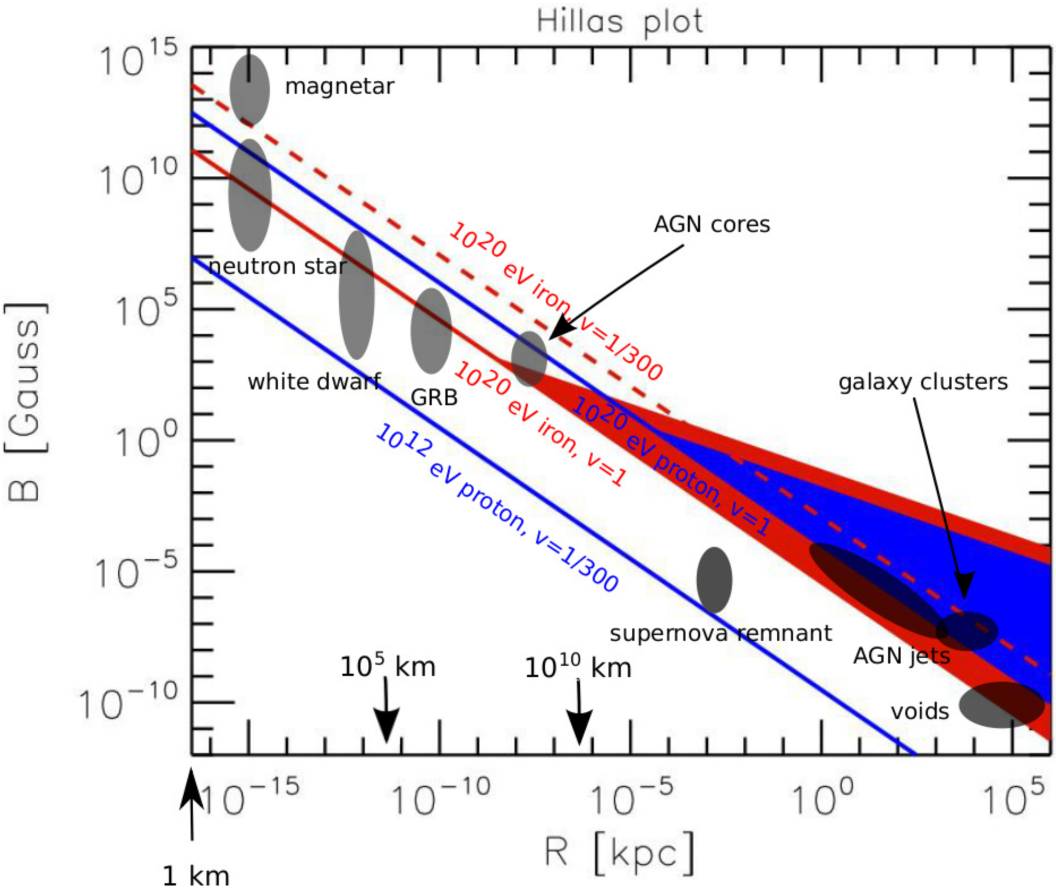

Figure 1.4: The “Hillas plot” taken from [37]. The blue and red shaded wedges signify the parameter ranges satisfying both the Hillas condition (eq. 1.3) and the synchrotron condition (eq. 1.4) for a 10^{20} eV proton and iron, respectively in the shock rest frame.

1.2 TeV γ-rays and neutrinos from hadronic processes

Some of the possible ultra-high energy cosmic rays sources are associated with relatively dense concentration of matter or a photon field that make them likely point sources of photons and neutrinos. Such a configuration, in which accelerated particles interact with material near their source, is usually called “astrophysical beam dump”. While primary cosmic ray nuclei do not travel in straight lines, secondary photons and neutrinos point back to their sources permitting to identify them as cosmic accelerators.

Accelerated protons interact in the surroundings of the CRs emitter with photons predominantly via the Δ^+ resonance producing pions in the final state (see eq. 1.1).

Protons will interact also with ambient matter (protons, neutrons and nuclei), giving rise to the production of charged and neutral mesons. Neutral pions decay in photons (observed at Earth as γ-rays):

$$\pi^o \rightarrow \gamma\gamma \tag{1.5}$$

while charged pions decay in neutrinos:

$$\begin{aligned} \pi^+ &\rightarrow \mu^+ + \nu_\mu \\ &\quad \hookrightarrow e^+ + \overline{\nu}_\mu + \nu_e \\[1em] \pi^- &\rightarrow \mu^- + \overline{\nu}_\mu \\ &\quad \hookrightarrow e^- + \nu_\mu + \overline{\nu}_e \end{aligned} \tag{1.6}$$

Roughly speaking the threshold of the $p\gamma$ reaction is $E_p \simeq 300$ MeV in the center-of-mass reference frame and the pion carries about 20% of the proton energy. This energy is statistically equally divided among the final decay chain products so each neutrinos carries $\sim 5\%$ of the interacting proton energy. Therefore, in the framework of the hadronic model and in the case of *transparent sources*, the energy escaping from the source is distributed between CRs, γ-rays and neutrinos. A transparent source is defined as a source of a much larger size that the proton mean free path, but smaller than the meson decay length. For these sources, protons have large probability of interacting once, and most secondary mesons can decay.

In the $\pi^\pm$ decay chain the three neutrino species are produced with a ratio $\nu_e : \nu_\mu : \nu_\tau = 1 : 2 : 0$, but due to neutrino flavour oscillations during the source to Earth journey, equipartition between the three leptonic flavors ($\nu_e : \nu_\mu : \nu_\tau = 1 : 1 : 1$) is expected at the Earth.

Because the mechanisms that produce cosmic rays can also produce neutrinos and high-energy photons (from eqs. 1.5 and 1.6), candidates for neutrino sources are in general also γ-ray sources. In the hadronic model there is a strong relationship between the spectral index of the CR energy spectrum $E^{-\alpha_{CR}}$, and the one of γ-rays and neutrinos. It is expected [38–40] that near the sources, the spectral index of secondary γ and ν should be almost identical to that of parent primary CRs: $\alpha_{CR} \sim \alpha_\nu \sim \alpha_\gamma$. Hence γ-ray measurements give crucial information about primary CRs, and, if their origin is hadronic, they constrain the expected neutrino flux.

1.2.1 High energy γ-ray astronomy

Photons are the most used “probes” in astronomical observations. Being electrically neutral and not deflected by Galactic and extra-Galactic magnetic fields, they permit to trace their origin and study their sources.

Detectors for photons in the MeV-GeV energy range are usually placed on satellites. The most up to date sky maps in this energy range has been produced by the Large Area Telescope (LAT) [41] that is the principal scientific instrument on board of the The Fermi Gamma-Ray Space Telescope (Fermi) spacecraft. The Fermi-LAT has been surveying the sky since August 2008 enlarging the previous catalog of the Energetic Gamma-Ray Experiment Telescope (EGRET), which operated on board the Compton-GammaRay Observatory from April 1991 to May 2000 revealing 271 point sources. The last catalog of Fermi-LAT sources, called 2FGL [42], records 1873 sources which emit high-energy gamma rays between 100 MeV and 100 GeV, and the collaboration is preparing a new catalog that will contain more than 2500 γ-ray sources [43]. Figure 1.5 illustrates where the different classes of sources in the 2FGL catalog are located in the sky, with a blow-up of the galactic plane where many of the sources are concentrated.

Since gamma ray fluxes at energies greater than 100 GeV become very weak, ground-based detectors are needed. There are two main classes of ground based high energy gamma-ray detectors: the Extensive Air Shower arrays (EAS) and the Imaging Air Cherenkov Telescopes (IACT).

The EAS detectors are made by a large array of detectors sensitive to charged sec-

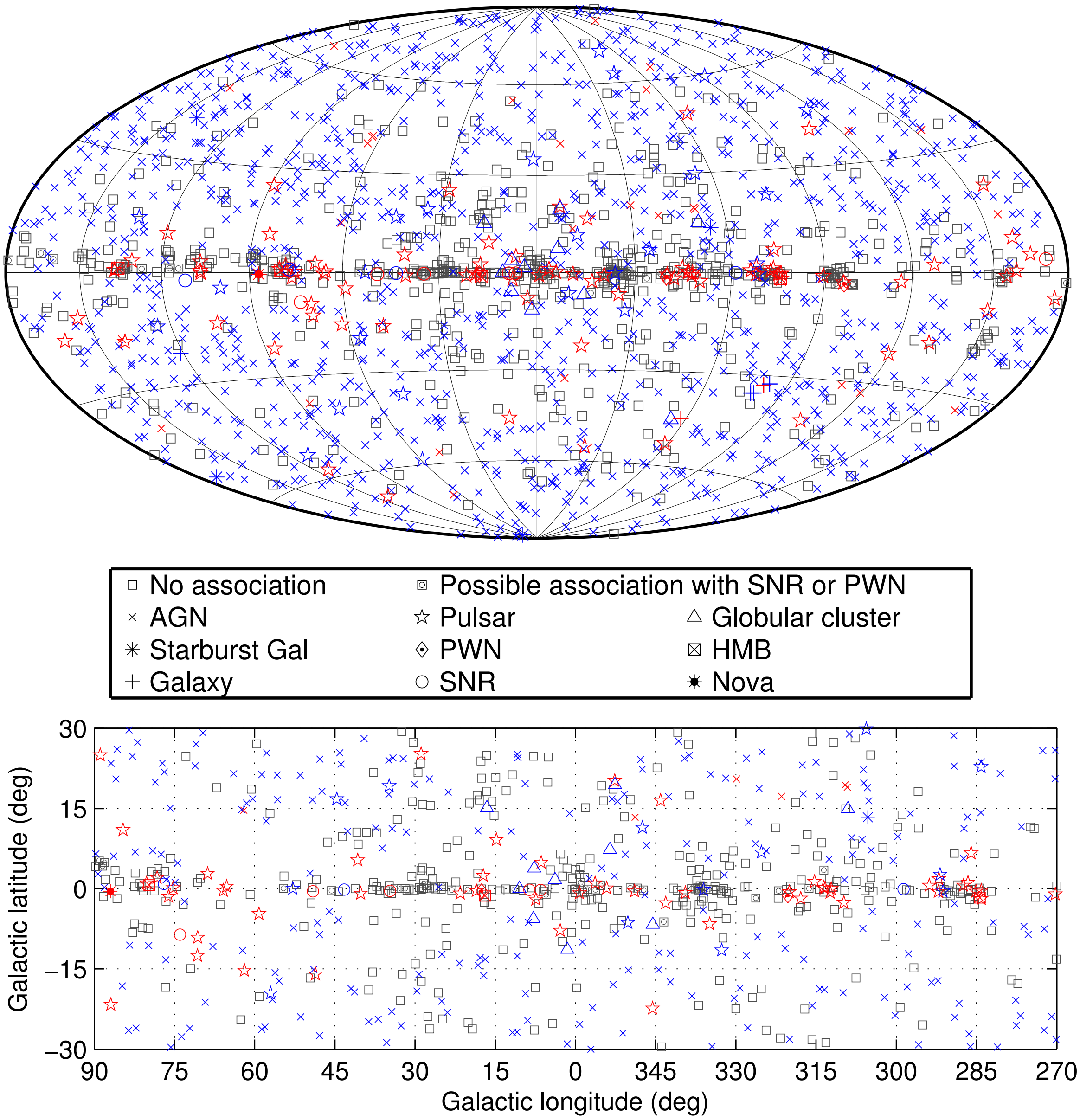

Figure 1.5: Full sky map (top) from the Fermi second catalog and blow-up of the inner Galactic region (bottom) showing sources by source class. Identified sources are shown with a red symbol, associated sources in blue (see [42]).

ondary particles generated by the atmospheric showers. They have high duty cycle and a large field of view, but a low sensitivity and a rather large energy threshold (at best in the 0.5 TeV - 1 TeV range). After the operation of MILAGRO [44], a water Cherenkov radiation telescope situated in New Mexico that stopped taking data in April 2008 after seven years of operation, and ARGO-YJB [45] a full coverage extensive air shower detector with Resistive Plate Counters placed in Tibet and in stable data taking from November 2007 to January 2013, new experiments are planned like the High Altitude Water Cherenkov Experiment (HAWK [46]) currently under construction in Mexico or the Large High Altitude Air Shower Observatory (LHAASO [47]) to be built in China.

IACT telescopes detect the faint and brief Cherenkov signal of relativistic electrons produced during the development of the electromagnetic cascades in the atmosphere with large optical reflectors equipped with fast optical receivers. Thanks to the very large collection area, the IACT technique provides large gamma-ray photon statistics even from relatively modest TeV gamma-ray emitters. In combination with good energy and angular resolutions, the gamma-ray photon statistics appears to be adequate for deep morphological, spectroscopic and temporal studies. On the other hand, the potential of IACT arrays is rather limited for the search of very extended structures or “hunting” of solitary events because of the modest duty cycle and field of view. The potential of the IACT arrays has been convincingly demonstrated by the H.E.S.S. [48], MAGIC [49] and VERITAS [50] collaborations, that in the recent years have greatly contributed to the survey of the TeV gamma-ray sky and the discovery of more than 100 TeV sources.

The TeV gamma-ray sky map is shown in figure 1.6 highlighting the visibility of HESS in pink and the one of VERITAS and MAGIC in pale blue.

Origin of high energy γ-rays

It is still not clear if the observed gamma rays are produced through astrophysical beam dump in an hadronic source scenario as discussed in the section 1.2 or by photon radiation off charged particles, in general electrons (leptonic source scenario).

In the last case the basic interpretation for the production of high-energy photons is the so-called self-synchrotron Compton (SSC) mechanism. Synchrotron emission from ultra-relativistic electrons accelerated in a magnetic field generates photons with an energy spectrum that can extend up to the X-ray range depending on the energy density

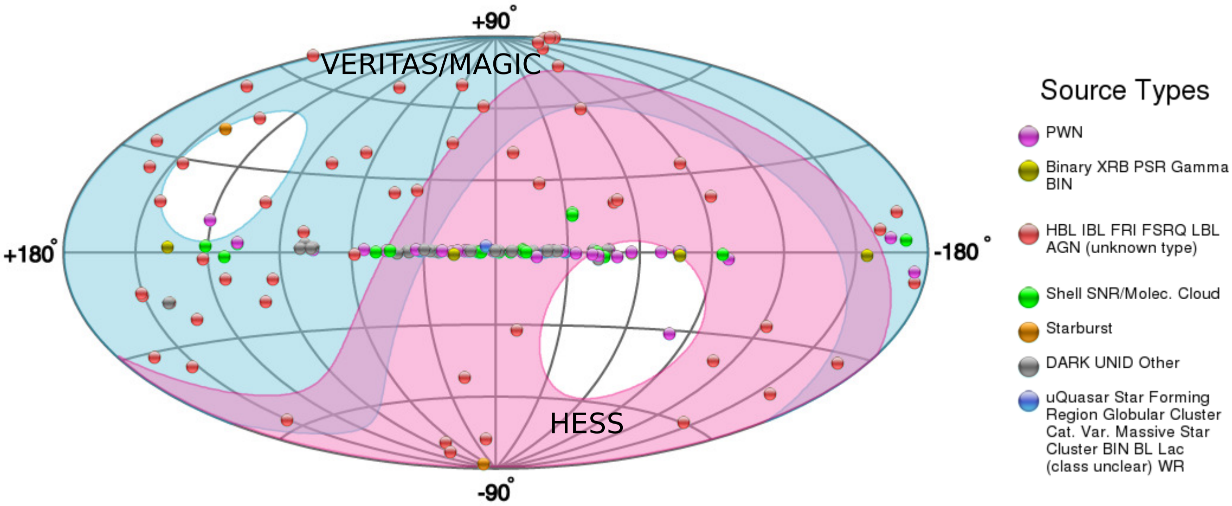

Figure 1.6: TeV gammara-ray sky map from TeVCat [51], an online, interactive catalog for very high energy (VHE; E > 50 GeV) gamma-ray astronomy.

of the magnetic field. Such photons in turn interact via Inverse Compton (IC) scattering with their own parent electron population. The IC scattering is very effective for increasing the photon energy, and is important in regions of high soft-photon energy density and energetic electron number density.

The SSC mechanism produces in the gamma-ray differential energy spectrum two characteristic synchrotron and inverse Compton peaks that are clearly visible on top of a general E^{-2} dependence. This behaviour has been verified with high accuracy on the Crab Nebula (see fig. 1.7), a steady VHE gamma emitter in the Milky Way which is often used to calibrate VHE gamma instruments.

The observation of the low energy gamma ray emission from the high energy gamma ray sources is, therefore, essential to identify the production scenario. However, because of unknown parameters, different models can explain the observed data both within hadronic and leptonic scenario (see e.g. section 1.3.1). Therefore only the neutrino detection can provide the smoking gun to reveal the origin of the cosmic radiation.

Limits of the gamma ray astronomy

At high energy the Universe is no longer transparent to gamma rays. In fact, they interact with the interstellar medium and also with the cosmic radiation through the pair-production reaction, which has an energy threshold E given by:

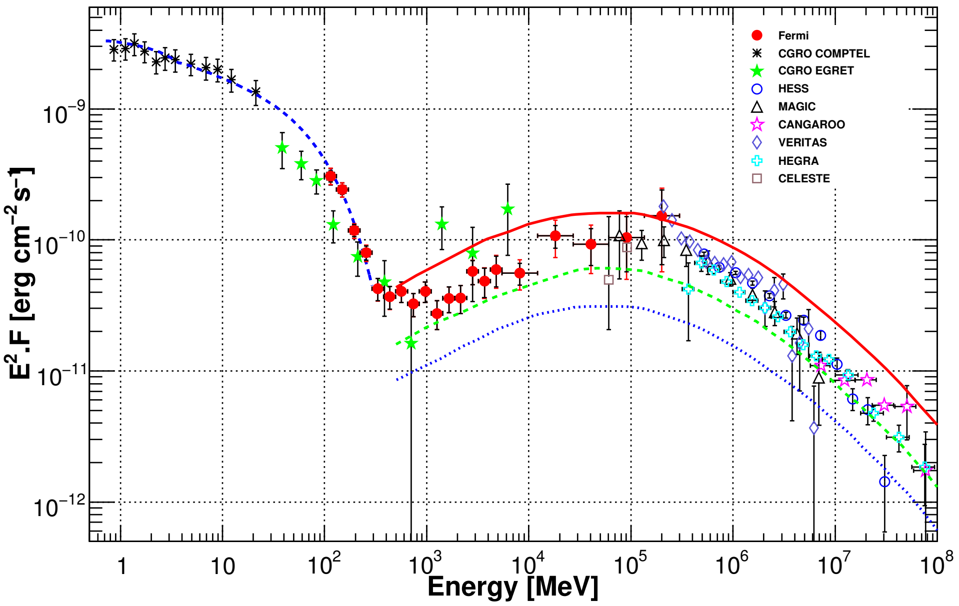

Figure 1.7: The spectral energy distribution of the Crab Nebula from soft to very high energy γ-rays. The fit of the synchrotron component is overlaid with a blue dashed line and the other three lines represents the predicted inverse Compton spectra for three different values of the mean magnetic field. See [52] and reference therein.

$$4E\varepsilon \sim (2m_e)^2, \tag{1.7}$$

where E and ε are the high energy gamma and the background photon energies respectively.

The absorption length of the photons as a function of the energy is shown in fig. 1.8. According to eq. 1.7, TeV photons interact with the infrared radiation limiting their horizon to few tens Mpc, PeV photons are absorbed within 100 kpc by their interaction with the Cosmic Microwave Background Radiation (CMBR) and EeV photon interact the radio waves.

Therefore, the observation of gamma-rays with energies $E \geq 100$ TeV is strongly hindered by their interaction with the interstellar photon background. In this case neutrino astronomy is the only solution.

1.2.2 Astrophysical neutrinos

Neutrinos are expected to be produced by interactions of accelerated protons (or nuclei) with photon or matter fields in or near the accelerating astrophysical objects,

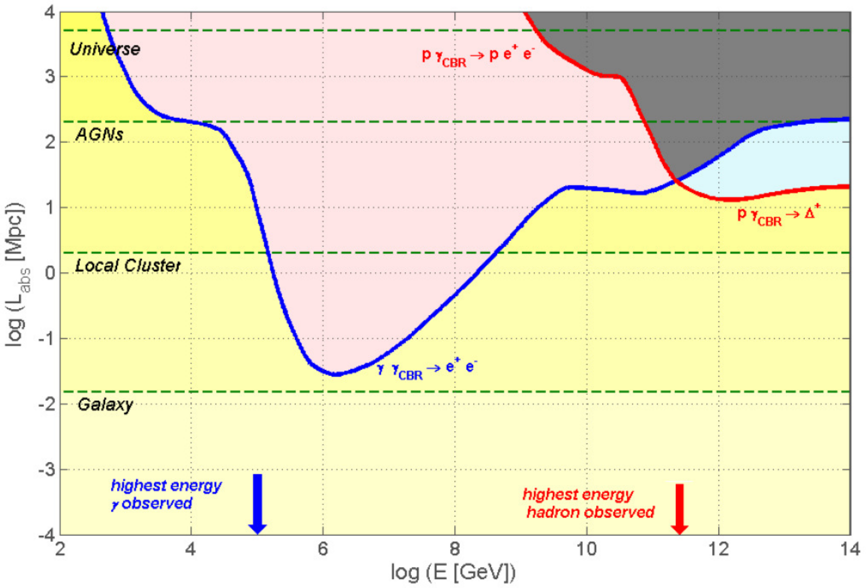

Figure 1.8: Absorption length of the photons in the interstellar medium as a function of the energy (blue line). For comparison, the plot includes the absorption of the proton in CMBR (red line). The regions above the lines are not accessible to proton and gamma astronomy [53].

as discussed in sec. 1.2. An overview of the measured or expected neutrino spectrum at the Earth is shown in fig. 1.9. From the lowest energies of $E \sim$ meV to the highest energies of $E \sim$ EeV, the expected intensity of the signal decreases by more then 40 orders of magnitude, making it necessary to introduce new methods of neutrino detection and analysis in order to increase the sensitivity to the neutrino fluxes especially at the highest energies.

The figure is a mixture of observations and theoretical predictions. At low energy, the neutrino sky is dominated by the yet unobserved Cosmic Neutrino Background (CνB), an isotropic neutrino flux having decoupled in the early Universe already 1 s after the Big Bang and corresponding to the cosmological relic black-body spectrum at a temperature of $\simeq$ 1.9 K. Detection of these neutrinos is an extremely challenging experimental problem which can hardly be solved with the present technologies.

Neutrinos with E $\sim$ MeV energy are produced by the Sun and by supernova explosions. The detection of neutrinos from the Sun and the supernova SN1987A in the Large Magellanic Clouds in 1987 represents the first successes of the extraterrestrial neutrino detection. The sun emits neutrinos in different fusion processes. In the figure, neutrinos from pp interactions and the ^{8}B spectrum are shown.

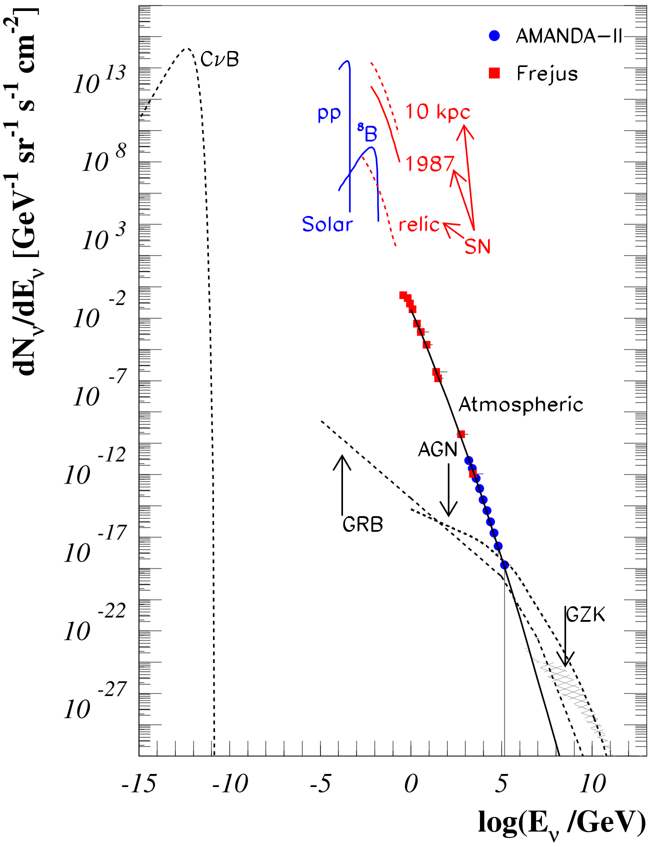

Figure 1.9: The astrophysical neutrino spectrum including different source predictions [54]. The fluxes based on mere predictions are shown as dashed lines while the solid lines represent those fluxes already measured. Point source fluxes have been scaled by $1/4\pi$ in order to be comparable to diffuse spectra.

At $E_\nu > 0.1$ GeV, neutrinos produced by cosmic ray interaction in the atmosphere appear in the spectrum (see sec. 1.5). Atmospheric neutrinos are measured up to energies of 100 TeV and represent the dominant background for extraterrestrial searches. Expected neutrino fluxes from extragalactic sources, such as GRB and AGN, are also indicated and will be discussed in detail in the section 1.4.

The highest energy neutrinos are those expected from the absorption of protons by the GZK effect. As discussed in section 1.1, the interaction of the cosmic rays with the microwave photons of the CMBs limits their mean free path to less than 100 Mpc producing a Δ-resonance that decay in pions and then in neutrinos. An observation of such cosmogenic neutrinos is considered as a “smoking gun” that would complement the observation of the flux suppression seen in the cosmic ray energy spectrum. In fact, neutrino are expected only if the origin of the flux suppression is due to the GZK effect and if the flux of primaries is composed mostly by protons.

Recently the IceCube collaboration has reported evidence of a flux of cosmic high energy neutrinos exceeding the expected flux of atmospheric neutrinos by a statistically significant factor, de facto opening a new era of neutrino astronomy.

1.3 Candidate high energy galactic neutrino sources

The operation of gamma-ray telescopes, described in section 1.2.1, revealed a large number of TeV sources located in the Milky Way and mainly associated with SNR and X-ray binaries and with their subclasses, Pulsar Wind Nebulae (PWD) and micro-quasars. Due to the approximate isospin symmetry of known pion production, if the γ-ray production scenario is hadronic, a corresponding neutrino flux is expected and can be estimated.

1.3.1 Supernova Remnant

The stellar evolution can end with a phase called *Supernova*, in which the whole star explodes and its envelope is ejected at supersonic velocity producing shock waves that move outwards from the central star and giving rise to *Supernova Remnants* (SNR). Shortly after the supernova explosion, in the “free expansion” phase, while the material swept up by the shock is much less than the mass of the stellar ejecta, the expansion of the stellar ejecta proceeds at essentially a constant velocity equal to the initial shock wave speed, typically of the order of 10000 km/s. As the remnant sweeps up ambient mass equal to the mass of the stellar ejecta, the wave will begin to slow and the remnant enters a phase known as adiabatic expansion, or the Sedov-Taylor or blast wave phase. The internal energy of the shock continues to be very large compared to radiation losses from thermal and synchrotron radiation, so the total energy remains nearly constant. According to the conventional theory of shock acceleration, in this phase the highest energy CR are produced. As the shock wave cools, it will become more efficient at radiating energy because once the temperature drops below 20000 K or so, some electrons will be able to recombine with carbon and oxygen ions, enabling ultraviolet line emission which is a much more efficient radiation mechanism than the thermal X-rays and synchrotron radiation. In this new phase, called “radiative phase”, the remnant cools and disperses into the surrounding medium over the course of the next 10000 years (see [55] for a review on SNR and their CR acceleration).

According to the CR standard paradigm, SNRs are the main accelerators of galactic cosmic rays with energies up to the knee region. Following an old argument by Baade and Zwicky [56], given a CR density $\rho_{\mathrm{CR}} \approx 1\,\mathrm{eV/cm^3}$ and a CR galactic confinement time of about $\tau_{\mathrm{esc}} \approx 10^7$ yr in a galactic volume $V_{\mathrm{gal}} \approx 10^{67}\,\mathrm{cm}^3$, the CR luminosity is

$$\mathcal{L}_{\mathrm{CR}} = \rho_{\mathrm{CR}} V_{\mathrm{gal}} / \tau_{\mathrm{esc}} \approx 10^{41}\,\mathrm{erg/s}.$$

With one supernova releasing 10^{51} erg every 30 yr (10^9 s), $\mathcal{L}_{\mathrm{CR}}$ can be sustained provided a plausible conversion efficiency of about 10% of the SNR energy into CR kinetic energy.

However, this postulate has not been unambiguously established through multi-wavelength studies, because of the difficulty in disentangling the electronic component from the π^0-decay component signing hadronic acceleration. In fact, detailed modelling of the evolution of SNRs in their environments is required but this is a challenging task since many of the relevant quantities are unknown. The observation of HE neutrinos would provide an incontrovertible proof of hadronic acceleration.

Recently Fermi-LAT reported an indication of the pion-decay signature from the SNRs W 44 and IC 443 [57]. A characteristic spectral feature of the neutral pion decay, referred as “pion-decay bump” was detected. When the π^0 decay into two gamma rays, each have an energy of 67.5 MeV in the rest-frame of the pion. The spectrum dN/dE in the lab-frame is thus symmetric about 67.5 MeV in a log-log representation. Transforming to the usual $\mathrm{E}^2\mathrm{dN/dE}$ representation generates the observed bump around 200 MeV (see fig. 1.10). The data could be explained by bremsstrahlung models only adding an additional ad hoc abrupt break in the electron spectrum, so these measurements provide strong evidence for the acceleration of protons in the remnants, but being model dependent they are not a conclusive proof.

Another indirect support to the hadronic scenario for the gamma ray emission, comes from the observation of thin X-ray synchrotron filaments surrounding some SNRs [58] [59] [60] and of the rapid variability time scale of the synchrotron X-rays [61] [62]. Moreover, the presence of a massive molecular cloud close to a SNR can provide a dense target for CR hadronic interactions and thus enhance the expected gamma-ray emission [63]. This observation may explain why the position of many sources of TeV γ-rays do

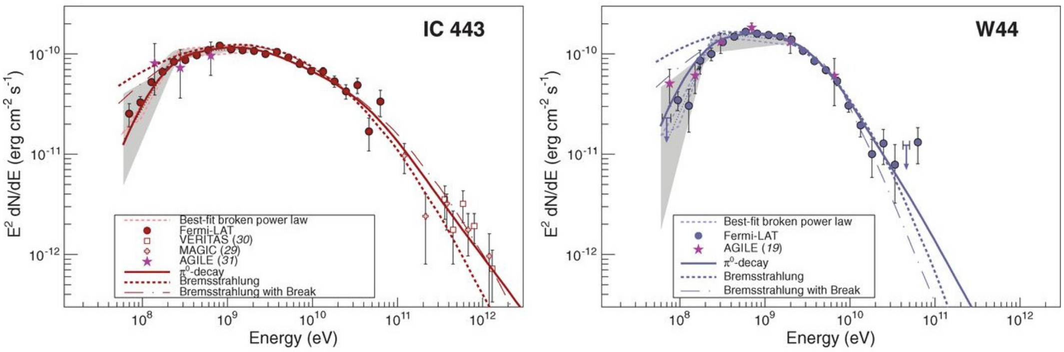

Figure 1.10: Gamma-ray spectra of IC 443 and W44 as measured with the Fermi LAT [57]. Color-shaded areas bound by dashed lines denote the best-fit broadband smooth broken power law (60 MeV to 2 GeV); gray-shaded bands show systematic errors below 2 GeV due mainly to imperfect modelling of the galactic diffuse emission. Data points from AGILE, MAGIC and VERITAS are shown. Best-fits of the pion-decay gamma-ray spectra (solid lines), of the bremsstrahlung spectra (dashed lines) and of the bremsstrahlung spectra when including an ad hoc low-energy break (dash-dotted lines) are also indicated.

not exactly coincide with the location of the SNR where the cosmic rays are accelerated but can be associated with close molecular clouds where the protons interact producing γ-rays and neutrinos.

Among the most interesting and intense SNR are the RXJ 1713.7-3946 and RX J0852.0-4622, also known as Vela Junior. The former will be discussed in detail in sec. 6.3, since, being one of the most promising neutrino sources, it has been chosen as a reference to evaluate the performance of the KM3NeT neutrino telescope. The latter has a radius of about 1° and its VHE γ-ray energy spectrum measured by H.E.S.S. [64] [65] extends up to 20 TeV. This spectrum, shown in fig. 1.11 can be fitted by a power-law function but, for the lack of statistics, there is no indication about a high energy cut-off.

1.3.2 Pulsar Wind Nebulae

Pulsars, rapidly rotating neutron stars left over after supernova explosions, are source of high energy gamma-rays. Their rotational energy is converted into the kinetic energy of the pulsar wind, a plasma of relativistic electrons and positrons that terminates in a shock when it encounters the ambient medium. The termination shock is the place where additional particle acceleration can take place. A comprehensive review on observational and phenomenological studies on evolution and structure of Pulsar Wind

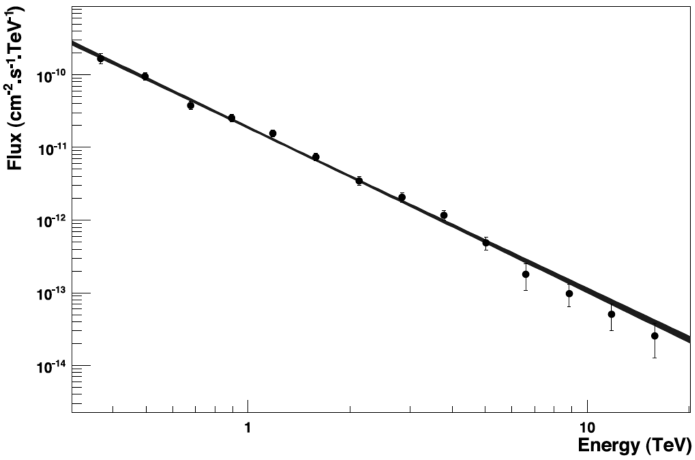

Figure 1.11: Differential energy spectrum of RX J0852.0-4622 from [64]. The shaded area gives the 1σ confidence region for the spectral shape under the assumption of a power law. The spectrum ranges from 300 GeV to 20 TeV.

Nebulae (PWNe) can be found in [66].

Presently PWNe constitute the largest galactic TeV source population. The similar morphologies of PWNe in X-ray and gamma-ray bands support the widely accepted view that both emission components are due to radiation of the same population of multi-TeV electrons via synchrotron and inverse Compton channels respectively.

1.3.3 X-ray binaries and microquasar

X-ray binaries are binary systems consisting of compact object, such as a neutron star or a black hole, called "accretor" and a companion star, the "donor", that feed the accretor with mass through an accretion disc. The compact object in turn emits the energy gained in form of X-rays. A special case of an X-ray binary is the so-called microquasar, in which the compact object exhibits relativistic radio jets. Such a phenomenon is believed to be caused by instabilities in the accretion disk of the system. A burst is caused every time a particularly large amount of matter is accreted from the accompanying star. The development of the burst can be traced by observation of the electromagnetic emission. Enhanced X-ray emission is seen close to the accretion disk, and radio to optical emission can be observed along the jet [67, 68]. The observed radiation from microquasar jets is consistent with non-thermal synchrotron radiation emitted by a population of relativistic shock-accelerated electrons. A periodic emission of TeV photons was observed from three systems in the Milky Way, LS 5039 and PSR B1259-63 were detected by the H.E.S.S. experiment [69, 70], while LS I 61+303 was seen by MAGIC [71], clearly demonstrating that microquasars are sites of effective acceleration of charged particles uo to multi-TeV energies. As for other sources, the key question is whether the γ-rays are of hadronic or leptonic origin and the answer is not straightforward. The possibility that protons, accelerated at energies >100 TeV by internal shocks within microquasars jets, could produce TeV neutrinos fluxes through photomeson interaction on ambient X-ray radiation was first proposed by Levinson and Waxman [72]. In this scenario, Distefano *et al.* [73], calculated that the expected neutrino fluxes range in the interval $\Phi(E) = 10^{-12} - 10^{-10}\mathrm{cm}^{-2}\,\mathrm{s}^{-1}\,\mathrm{TeV}^{-1}$ depending on source parameters. Other authors [74–77] suggest that both TeV gamma rays and neutrinos could also be produced by the interaction of Fermi-accelerated protons in the jet with cold protons of the donor stellar wind estimating the expected neutrino flux for specific microquasar, such as LS 5039 and LS I +61 303. Upper limits on the E^{-2} muon neutrino flux emitted by various microquasar have been recently placed by the Ice Cube [78] and the ANTARES collaborations [79]. The order of magnitude of these limits is $10^{-12} - 10^{-11}\mathrm{cm}^{-2}\,\mathrm{s}^{-1}\,\mathrm{TeV}^{-1}$.

1.3.4 Fermi Bubbles

The Fermi bubbles are two large structures extending up to 50 degrees above and below the Galactic centre with a width of 40 degrees in Galactic longitude, whose γ-ray emission has been revealed by a dedicated analysis of sky maps constructed out of 20 month of Fermi-LAT data [80]. The gamma-ray spectrum, measured from about 1 GeV to about 0.1 TeV, is compatible with a power-law spectrum described by $E^2\, d\Phi_\gamma/dE \approx 3{-}6 \times 10^{-7}\,\mathrm{GeV}\,\mathrm{cm}^{-2}\,\mathrm{s}^{-1}\,\mathrm{sr}^{-1}$, as it can be seen in fig. 1.12. No spatial variation in the spectrum shape or gamma-ray intensity inside the two bubbles has been observed. A preliminary analysis performed by the Fermi collaboration with larger statistics (50 months of Fermi LAT data) confirms an E^{-2} spectrum with an intensity of about $3{-}5 \times 10^{-7}\,\mathrm{GeV}\,\mathrm{cm}^{-2}\,\mathrm{s}^{-1}\,\mathrm{sr}^{-1}$ [81].

The edges of the bubbles seem to be correlated with ROSAT X-ray maps at 1.5−2 keV, while the inner parts are correlated with the hard-spectrum microwave excess, known as Galactic "haze", measured by WMAP and Planck [82–84]. Recently, also

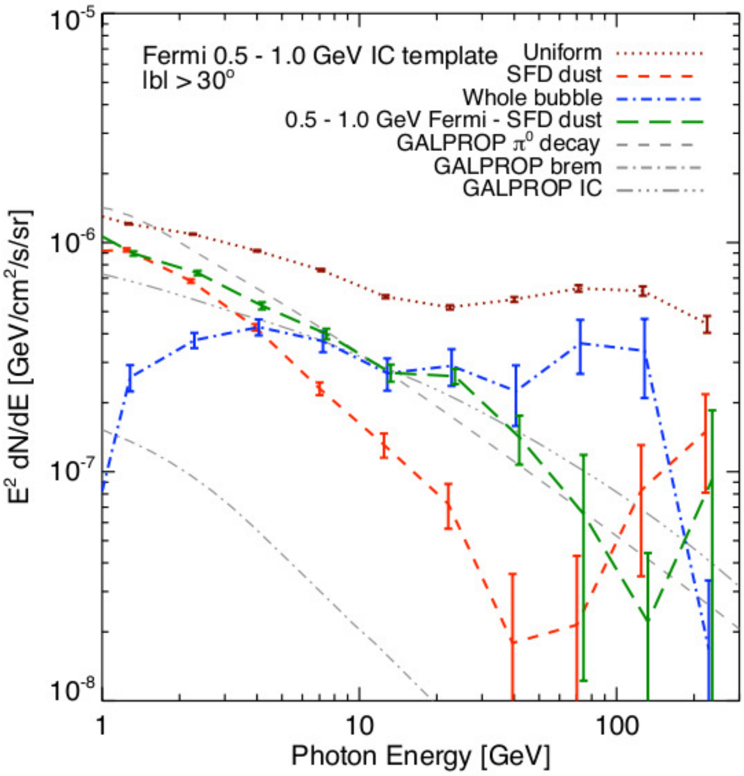

Figure 1.12: Fermi bubbles spectrum as reported in [80]. The spectrum correlated with the Fermi bubble template (blue dot-dashed line) is harder (consistent with flat in $E^2 dN/dE$) than the spectra correlated with the other templates, and the models for the various emission mechanism generated from `GALPROP`, indicating that the Fermi bubbles constitute a distinct gamma-ray component with a hard spectrum. The fitting is done for $|b| > 30°$. See [80] for details.

a linearly-polarized radio lobes emission in the Fermi bubble region emanating from the Galactic center has been measured [85]. The origin of the emission of high energy gamma rays and of the associated counterparts is still not clearly understood and many explanations, invoking both the hadronic [86–88] and leptonic mechanisms [80, 87, 89, 90] , have been suggested but none of them has been able to explain all the gamma and the counterparts features.

In a hadronic scenario, Fermi bubbles are promising sources candidate of high-energy neutrinos. Present upper limits on the neutrino flux from the Fermi bubbles, provided by the ANTARES collaboration, are within a factor of three of a prediction from the purely hadronic model [91], but the next generation KM3NeT neutrino telescope will provide more than an order of magnitude improvement in sensitivity [92].

1.4 Candidate high energy extra-galactic neutrino sources

Extra-galactic sources are believed to be responsible of the CR spectrum above the ankle. The observed TeV γ-ray spectrum from extragalactic sources is steepened due to absorption by the Extragalactic Background Light (EBL) [93], making uncertain and highly model-dependent the neutrino flux estimate for these sources.

Waxman and Bahcall (W&B) [94] have presented an interesting benchmark for the neutrino flux expected from extragalactic cosmic ray accelerators, whatever they may be. Assuming that the proton spectrum at the source follows an E^{-2} power law and considering an energy density injection rate of 10^{44} Mpc^{-2} yr^{-1}, they estimated an upper bound of $\mathrm{E}_\nu^2\Phi_\nu < 2 \times 10^{-8}$ GeV cm^{-2} s^{-1} sr^{-1} to the intensity of high-energy neutrinos produced by photo-meson (or p-p) interactions in sources of size not much larger than the proton photo-meson (or p-p) mean free path.

The upper bound proposed by Waxmann and Bachall has been extended even further by Mannheim, Protheroe and Rachen (MPR) [95] that do not assume a fixed E^{-2} cosmic ray spectrum at the source and take into account “optically thick” sources in which protons are absorbed within the source. It is conceivable that neutrons, which were produced in previous hadronic interactions in the source such as $p + \gamma \to \pi^+ + n$, are, unlike protons, not confined by magnetic field and can thus escape the cosmic accelerators without energy losses. These neutrons would then decay to produce protons which would consequently be measured in the cosmic ray flux. The authors arrive at a higher flux limit:

$$E_\nu^2\Phi_\nu < 2 \times 10^{-6}\ \mathrm{GeV\ cm^{-2}s^{-1}sr^{-1}}. \tag{1.8}$$

This limit was already excluded in a wide energy range by different experiment, as shown in fig. 1.13.

In [95] a limit for sources transparent to neutrons is also calculated and it decreases from the value of eq. 1.8 at $\mathrm{E} \sim 10^4$ GeV to the Waxmann and Bachall limit at $\mathrm{E} \sim 10^9$ GeV. Above this energy, the limit increases again due to poor observational information.

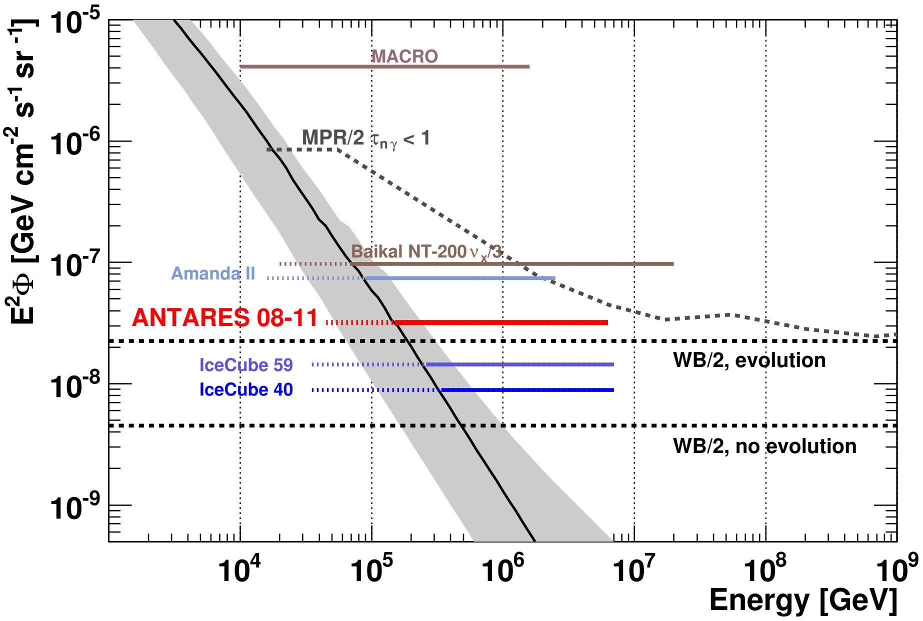

Figure 1.13: Experimental upper limits on an astrophysical ν_μ flux with an E^{-2} spectrum from different experiments. The MACRO [96] limit refers to $\nu_\mu + \overline{\nu}_\mu$ while the Baikal [97] limit refers to neutrinos and antineutrinos of all flavours and is divided by 3. Icecube and AMANDA limits are taken from [98], while the reference for the ANTARES limit is [99]. For reference, the W&B [94] and the MPR [95] upper bounds for transparent sources are also shown. They are divided by two, to take into account neutrino oscillations. The grey band represents the expected variation of the atmospheric ν_μ flux.

1.4.1 Active Galactic Nuclei

Active Galactic Nuclei (AGN), the most luminous persistent object observed in the sky, are galaxies with a very bright core of emission embedded in their centre. The standard scenario for AGNs assumes the presence of a very massive central black hole (10^6 - 10^9 $M_\odot$) swallowing huge quantities of surrounding matter from an accretion disk and two relativistic jets where particles can be accelerated to ultra-high energies via Fermi acceleration in a series of consecutive shock fronts, leading to a very concentrated energy output from a relatively small volume. According to some models [100], the energy rate generated by the brightest AGNs can be greater then 10^{47} erg/sec. Early models [101–103], postulating the hadronic acceleration in the AGN cores, predicted a production of secondary neutrinos well above the W&B upper limit, and the prediction from some of these models has been experimentally disproved by AMANDA [104]. More recent models [105] predict fluxes close to the W&B bound. For instance, a prediction has recently been carried out for the Centaurus A Galaxy, which is only 3Mpc away. In

[106] the estimate neutrino flux from hadronic process is $E^2 d\Phi_\nu/dE \leq 5 \times 10^{-13}$ TeV^{-1} cm^{-2} s^{-1}.

Depending on the observation angle, the AGN model can be responsible for a whole group of astronomical objects with seemingly different properties, ranging from blazars, if the jet is directly pointed towards the observer, to radio galaxies, including quasar, Seyfert galaxies, BL Lacs [107]. In particular, blazars present the best chance of detecting AGNs as individual point sources of neutrinos because of a significant flux enhancement in the jet through Doppler broadening. Blazars exhibit non-thermal continuum emission from radio to VHE frequencies and are highly variable, with fluxes varying by factors of around 10 over timescales from less than 1 hour to months. Several blazars have been recently observed in terms of TeV emission and they are indeed the most numerous extra-galactic object observed in these wavelengths. However, as previously discussed, VHE gamma energy spectra observed at the Earth are distorted by the interaction with the EBL that produces both a reduction of the VHE gamma flux and a softening of their energy spectra that become more and more relevant with increasing distances. Moreover, the question about the origin of the VHE gamma emission observed in blazars, namely leptonic or hadronic is still open. A deeper discussion of the various models and of neutrino fluxes can be found in [54].

1.4.2 Gamma Ray Burst

Gamma-Ray Bursts (GRB) are among the most mysterious and violent phenomena ever observed in the Universe. GRBs are transient sources with emission in hard-X-ray and soft-gamma photons lasting from millisecond to several hundreds of seconds and a late afterglow in IR, radio and optical band. In this short time interval each GRB releases a huge total energy ($\geq 10^{51}$ erg/s).

Historically, gamma-ray bursts were discovered as extremely intense gamma-ray flashes in 1967 by the Vela satellites [108], launched by the U.S. to monitor the sky for nuclear explosions that might violate the Nuclear Test Ban Treaty. Systematic studies of the GRBs were then conducted by the BATSE experiment which operated between the 1991 and the 2000 detecting nearly 3000 GRBs [109]. The spatial distribution of GRBs in galactic coordinates as observed by the BATSE reveals an isotropic distribution with no visible clustering in the galactic plane or anywhere else. This indicates an extragalactic origin of the events. The final proof of a cosmological distance of GRBs was possible in 1997 by the first afterglow observation by the BEPPOSAX satellite, see e.g. [110]. In fact, from the afterglow observation, the redshift at which the GRB occurred can be determined so the GRB can be localised. Moreover, the detection of the supernova SN 1998bw in coincidence with GRB 980425 [111] and SN 2003dh in coincidence with GRB 030329 [112] lead to the conclusion that there is a connection between the GRBs and supernovae.

However, in spite of a large numbers of GBRs observed since their discovery and of the fact that their emission features have been studied in details, the nature of these objects remains mysterious to a large extent. The bulk of the emission features indicate a non-thermal process, driven by a catastrophic event involving charged particle acceleration and the conversion of huge quantities of matter into energy. Accordingly to the duration of their γemission, GRBs are labelled as "long" GRB (t$\geq$ 2 s) or "short" GRB (t$\leq$ 2 s). These two classes of observations seem to be associated to different progenitors: the core collapse of a massive star appears as a convincing explanation for long GRB, while compact merger of neutron star-neutron star or black hole-neutron star is the proposed scenario for short burst.

The most widely accepted model that describes the actual emission of radiation of the GRB is the fireball model in combination with the internal-external shock model, described in detail in [113] In the fireball model, an inner compact source produces a variable relativistic wind. During expansion, the opaque fireball cannot radiate and any particles present, leptons and baryons alike, will be shock-accelerated, thus converting radiation into bulk kinetic energy. When radiation is eventually emitted, the fireball expands at constant velocity, which is determined by the amount of baryonic matter present because it increases the optical depth due to Thompson scattering. The flow of the relativistic ejecta is not steady but, similar to the emission of jets in AGNs, composed of multiple shocks expanding with a range of velocities. Relativistic internal shocks arise in this irregular flow when faster shells overtake slower ones. As the fireball expands further, it drives the relativistic forward shock into the ambient medium, heating new gas and producing relativistic electrons which give rise to the delayed afterglow radiation. The non-thermal features that dominate the γ-ray spectrum are therefore due to charged-particle interaction with the shock waves created as a consequence of the fireball expansion.

GRBs are expected to emit neutrinos during several stages of their evolution. Quite a large fraction of the whole energy released is expected to be carried out by neutrinos (at 1-10MeV energy) and gravitational waves in first stages following the collapse. A "precursor" TeV neutrino flux, without gamma counterpart, due large optical depth of the medium, is expected about 100 s before the gamma flash, that is seen only when the jet outcomes the external progenitor shells. Then, hadron acceleration in both internal shocks (jet) and external shocks (afterglow) would lead to high energy neutrino production due to p-p or p-γ interaction.

The possibility of detecting neutrinos from a single burst strongly depends on burst features, such as its fluence, redshift and Γ Lorentz factor, but in general the GRB neutrino detection seems very promising because it is almost background free thanks to the triggers by satellite alerts, that allow to tune the search for neutrino signals from the burst direction in a time window around the γ burst. However, until now the expected neutrino flux have never been detected and a recent GRB analysis presented by the IceCube Collaboration [114] sets an upper limit on the flux of energetic neutrinos associated with gamma-ray bursts that is at least a factor 3.7 below the predictions. This implies that either the proton density in gamma ray burst fireballs is substantially below the level required to explain the highest energy cosmic rays or the physics in gamma ray burst shocks is significantly different from that included in current models.

1.4.3 Cosmogenic neutrinos

As discussed in section 1.1, the interaction of protons having E $> 10^{19}$ eV with the CMB through the Δ-resonance produces a cut-off in the cosmic ray energy spectrum called GZK cut-off. A natural consequence will be the existence of a diffuse flux of ultra-high energy cosmogenic (or GZK, or BZ) neutrinos coming from the decay of the Δ-resonance via the channel of charged pion production. The diffuse flux of GZK neutrinos is considered, to some extent, a "guaranteed" neutrino flux with an energy spectrum that can range from approximately $E_\nu \sim 10^{16}$ eV up to $E_\nu \sim 10^{21}$ eV. The shape and the strength of the neutrino flux depend on several factors such as the primary UHECR flux spectral index and composition. This lead to predictions from different models that show remarkable variations on GZK neutrino fluxes [115–117]. In particular, the composition of UHECR is a central issue since, while protons are very efficient neutrino generators via p-γ interactions, heavier nuclei lose energy via photon-disintegration, so if heavy nuclei dominate the CR spectrum at the highest energies, the neutrino flux can be drastically reduced [118].

1.5 Atmospheric neutrinos

Hadronic interactions between cosmic rays and particles in the Earths atmosphere produce large numbers of mesons, primarily pions and kaons. Neutrinos are produced in the decays of charged pions or kaons, as well as in the subsequent decay of the muons.

Neutrinos directly from muon decay are important up to a few GeV. Pions and kaons that decay in-flight are the primary source of atmospheric muon neutrinos from a few GeV up to about 100 TeV. With rest-frame lifetimes on the order of 10^{-8} s, these mesons often lose some of their energy in collisions prior to decaying, leading to lower energy neutrinos among the decay products. Hence, the spectral slope of this "conventional" atmospheric neutrino flux [119–121] asymptotically becomes one power steeper than that of the primary cosmic ray spectrum, assuming a $E^{-3.7}$ spectrum. Being γ_p the spectral index of the cosmic ray spectrum, the conventional atmospheric neutrino flux can be expressed as:

$$\frac{d\Phi_\nu}{dE_\nu d\Omega}(E_\nu,\theta) = A_\nu E_\nu^{-\gamma_p}\left(\frac{1}{1+\dfrac{aE_\nu}{\epsilon_\pi}\cos\theta} + \frac{B}{1+\dfrac{bE_\nu}{\epsilon_k}\cos\theta}\right)\mathrm{cm}^{-2}\mathrm{s}^{-1}\mathrm{sr}^{-1}\mathrm{GeV}^{-1}. \quad (1.9)$$

Here, the scale factor A_ν, the balance factor B (which depends on the ratio of muons produced by kaons and pions) and the a, b coefficients are parameters which can be derived from Monte Carlo computation, numerical approximations or from experimental data. The quantity ϵ_i (the characteristic decay constant) corresponds to the energy at which the hadron interaction and decay lengths are equal. For pions and kaons, ϵ_π = 115 GeV and ϵ_k = 850 GeV respectively.

Theoretical uncertainties in predictions for the conventional flux are dominated by uncertainties in the normalization and spectral distribution of the cosmic ray flux. Additional uncertainties include the ratio of pions to kaons produced by cosmic ray interactions, which affects the zenith angle distribution, particularly near the horizon.

The atmospheric neutrinos spectra calculated by different groups (Bartol [119, 120], Honda [121] and Fluka [122]) are shown in fig. 1.14.

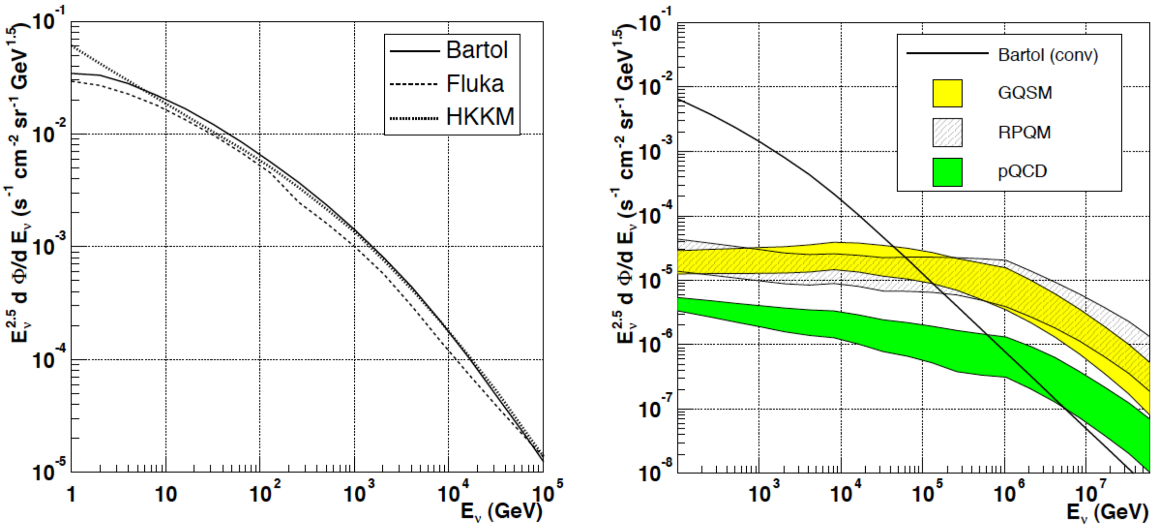

Figure 1.14: Models of atmospheric neutrino fluxes. Left: three models for the conventional atmospheric neutrino flux. Right: The Bartol model and three models for prompt neutrino fluxes taken from [123]. The results have been integrated over all directions.

At sufficiently high energies, another production mechanism is possible. The "prompt" atmospheric neutrino flux [124, 125] is made up of neutrinos produced in the decays of charmed mesons and baryons. These particles decay almost immediately, having rest-frame lifetimes on the order of 10^{-12} s, before losing energy in collisions. Hence, the spectrum for the prompt flux more closely follows the cosmic ray spectrum and is about one power harder than the conventional flux at high energy.

Even if the prompt flux has not yet been measured, it is expected to be important above about 100 TeV. Just like the conventional flux, the uncertainties in the normalization and spectral distribution of the cosmic ray flux impact the predictions for the prompt flux. Additional sources of uncertainty for the prompt flux include charm production cross sections and fragmentation functions, which have not been measured at these energies in accelerator experiments.

In particular, in [123] the effect of different models of charmed particle production is studied. For each model, the ingredients of the calculation (e.g. the parameterisation used to represent the flux of primary cosmic rays) are varied, yielding a range of fluxes. In fig. 1.14 the range of allowed prompt neutrino fluxes is shown for each of the charm production models. This illustrates that, in contrast to the models for the conventional neutrino flux, the uncertainty on the prompt neutrino flux is very large.

Although high energy cosmic rays arrive almost isotropically, the zenith angle dependence of high energy atmospheric neutrino production is complicated by the direction of the shower through the atmosphere. The energy spectrum of nearly horizontal conventional atmospheric neutrinos is flatter than that of almost vertical neutrinos because pions and kaons in inclined showers spend more time in the tenuous atmosphere where they are more likely to decay before losing energy in collisions. Additionally, attenuation of the neutrino flux by the Earth is a function of energy and zenith angle. Above about 10 TeV, attenuation of the neutrino flux in the Earth is important, and affects the zenith and energy dependence of the flux at the detector.

Recent measurement of the conventional muon neutrino and antineutrino fluxes reported by the Antares [126] and IceCube [127, 128] neutrino telescopes are summarised in fig. 1.15. All these analyses cannot establish the presence of a prompt contribution to the neutrino flux, but some extreme contribution from prompt neutrino models have already been ruled out [129].

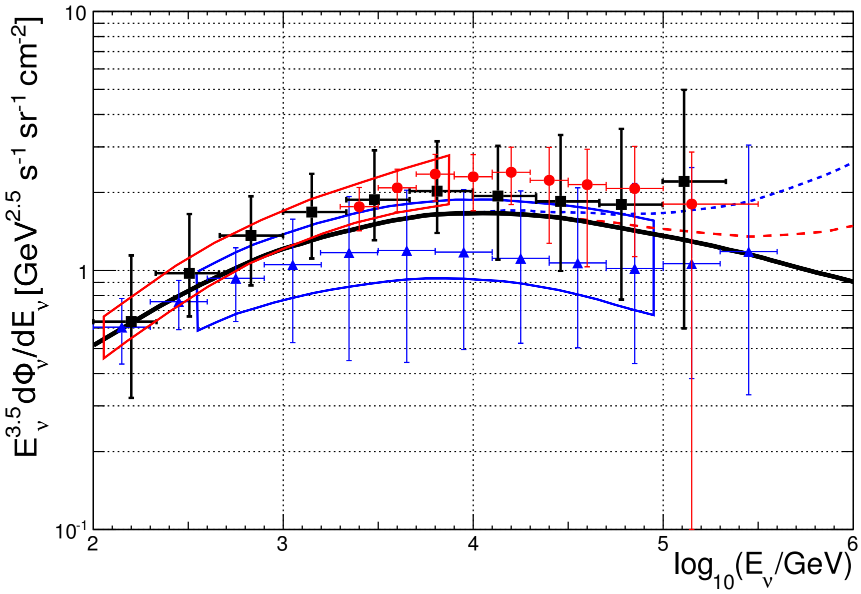

Figure 1.15: Comparison between the atmospheric neutrino energy spectrum $E_\nu^{3.5} d\Phi_\nu/dE_\nu$ measured by different experiments and the theoretical expectations. The full line represents the ν_μ flux from [120]. The red and blue dashed lines include two prompt neutrino production models from [125] and [124], respectively. All theoretical expectations are zenith-averaged from 90° to 180°. The black full squares refers to the Antares [126] measurement in the zenith angle region $\theta > 90°$. The result of the AMANDA-II unfolding [127] averaged in the region 100° to 180° is shown with red circles and that of IceCube40 [128] zenith-averaged from 97° to 180° is shown with blue triangles. The red region corresponds to the ν_μ measurement from [130], and the blue one the IC40 update from [129].

CHAPTER 2

CHERENKOV NEUTRINO TELESCOPES

The neutrino is a lepton with a very small mass and no charge, which makes it a very elusive particle, as it only interacts through the weak force and gravitation (the latter is negligible in most cases). This fact is the reason for its usefulness for astroparticle physics. Unfortunately this also prevents direct detection and makes indirect detection difficult, as the extremely small cross sections require extremely large target masses.

A cost effective way to obtain a huge target mass is to use a large volume of sea-water as detection medium, as proposed by Markov and Zheleznykh in 1960 [131]. The sea-water acts in this case simultaneously as the target, the shield and the active detection volume. The proposal foresaw the instrumentation of a large volume of water (as well as ice) with several optical sensors in order to detect the Čerenkov light emitted by the charged particles produced in the CC interaction of neutrinos with rock and water in proximity of the telescope.

After the pioneering work carried out by the DUMAND collaboration offshore Hawaii Island[132], Baikal was the first collaboration which installed a small scale underwater neutrino telescope in the Siberian Lake Baikal (Russia) [133]. On the other hemisphere, the AMANDA detector, constructed at the Amundsen-Scott South Pole Station was completed in 2001 [134]. AMANDA was a first-generation instrument that served as test bench for technologies and as prototype for the km^3-size detector IceCube, which is taking data in its final configuration since December 2010. In the Northern Hemisphere the biggest operating detector is now Antares that has a total instrumented volume of about 0.025 km^3. The construction of KM3NeT, a cubic kilometres detector in the

Mediterranean Sea, has just started. This project will be treated in the next Chapter.

In this Chapter the basics of neutrino telescopes are presented. The detection principle is explained in more detail discussing the signatures of neutrinos in the detector. Basic reconstruction principles and the treatment of the background is explained. The most relevant results of the main operating telescope, Antares and Icecube, will be then presented.

2.1 High-energy neutrino detection

The proposed technique consists in detecting optical signals emitted by secondary particles generated in neutrino interactions (see section 2.1.1). Muons produced in charge current neutrino interactions represent the "golden channel" for high-energy neutrino telescopes since they are highly penetrating particles, massive enough ($m_\mu \sim 200$ m_e) not to loose all the energy via radiative processes (their range in water or rock is several kilometres at $E_\mu \geq$ 1TeV, see section 2.1.2). When muons propagate with a velocity grater than the speed of light in the medium, they emit Čerenkov radiation (section 2.1.3). The instrumentation of large volumes of water (or ice) with an array of optical sensors will therefore allow for muon tracking with god angular accuracy.

However, also electron and τ neutrinos can be detected, although with a lower angular accuracy, through the detection of the electromagnetic cascade. Also neutral charged current interactions of high energy neutrinos occurring inside the telescope volume can be detected through the measurement of the hadronic cascade.

Theoretical expectations of neutrino fluxes indicate that a detection area of the order of 1 km^2 is necessary for astrophysical neutrino telescopes. This implies that, even with several thousands of optical sensors, the detector will have a very low density of optical sensors per unit of volume. Such detectors should be as much isotropic as possible to be sensitive to event coming from different direction and should have a volume large enough to efficiently track crossing and internal muons. The typical scale of Čerenkov neutrino telescopes is of the order of 1 km^3.

These detectors have to be shielded from the intense flux of atmospheric muons (see section 2.1.6), originated in the interactions of cosmic rays with the atmosphere. At the Earth surface their flux is about 10^{11} times larger than the one of atmospheric neutrinos neutrino events [135]. A solution is to deploy the neutrino telescope deep underwater(-ice). Fig.3.10 shows the intensity of the vertical atmospheric muon flux as a function of depth. Even at large depths ($\sim$ 3000 m), the flux of muons that reaches the detector is about 6 orders of magnitude more intense than the atmospheric neutrino-induced muon flux [135] (see fig. 2.15). This is the reason why *down-going* muon cannot be used in the search for astrophysical sources, being the signal almost completely washed out by the background. On the contrary, upward-oriented muon events are considered good neutrino candidates, since they cannot be atmospheric muons. Even at the highest

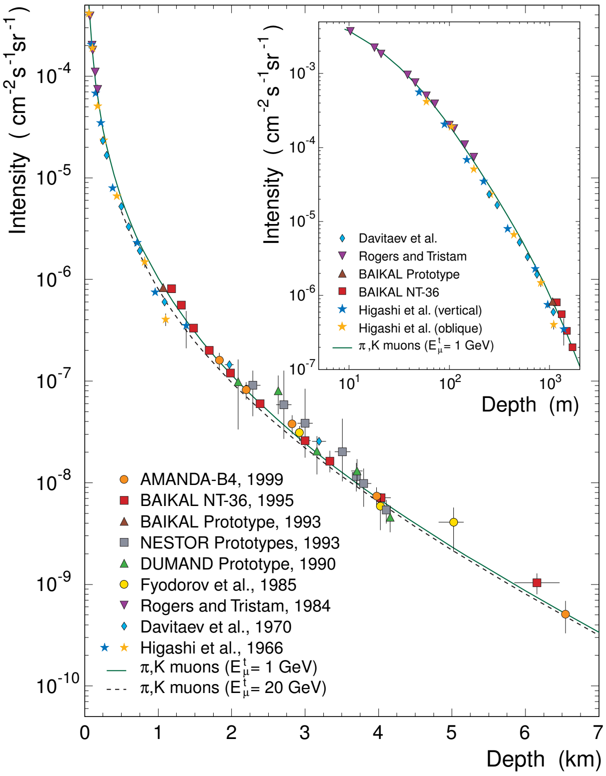

Figure 2.1: Muon intensity versus depth in water (see [135]).

energies, in fact, muons are absorbed within a path of about 50 km of water, so they cannot traverse the entire Earth diameter (~ 13000 km). However also a *downward-looking* neutrino telescope suffers the background due to atmospheric muons that are mis-reconstructed as up-going and may contaminate the *up-going* astrophysical neutrino event ensemble. A water layer of about 3000 m is therefore required in order to strongly reduce the number of mis-reconstructed down-going events.

An unavoidable background in astrophysical neutrino searches is due to neutrinos produced by the interaction of cosmic ray with the atmosphere. However, the energy spectrum of atmospheric neutrinos is softer than the expected spectrum of cosmic neutrinos (see section 1.5). This is a key for a possible discrimination. A search bin around the source position can be also used (see section 6.2). A simplified illustration of the origin of muons constituting the background is sketched in Fig.2.2.

A completely different source of background is the optical background due to bioluminescence and to radioactive salts present in sea-water, that gives spurious signals on the optical sensor. The reduction of the background is obtained in this case by requiring

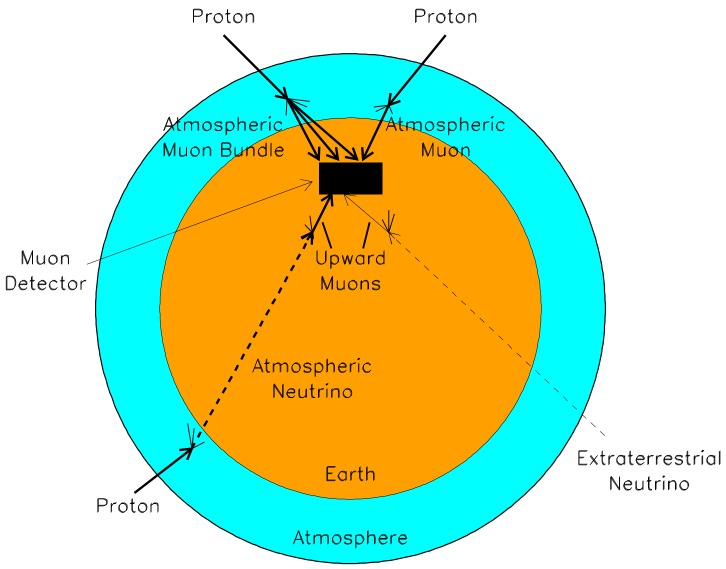

Figure 2.2: Simplified illustration of the origin of atmospheric muons and neutrinos. They are the dominant background for astrophysical neutrino detection.

space-time correlation between hits in nearby photomultipliers.

2.1.1 High-energy neutrino interactions

Neutrinos can interact with target nucleons through deep inelastic scattering. The different event classes produced by the different neutrino flavours are shown in fig. 2.3. The type of the interaction, charged current or neutral current, and the neutrinos flavour greatly affect the signature of the neutrino event in the detector. An example of the light deposit of a typical shower-like event and a track-like event is shown in fig. 2.4.

Neutral current interactions are similar for all flavours. In this case the neutrino will react with a nucleon, resulting in a lower energy scattered neutrino and a hadronic shower in the final state:

$$\nu_l(\bar{\nu}_l) + N \rightarrow \nu_l(\bar{\nu}_l) + X \qquad l = e, \mu, \tau. \tag{2.1}$$

Charged current interactions produce a relativistic charged lepton and a hadronic shower:

$$\nu_l(\bar{\nu}_l) + N \rightarrow l(\bar{l}) + X \qquad l = e, \mu, \tau. \tag{2.2}$$

The emerging lepton inherits the flavour of the incident neutrino. Electron-neutrinos will therefore produce electrons and thereby an electromagnetic shower overlapping with

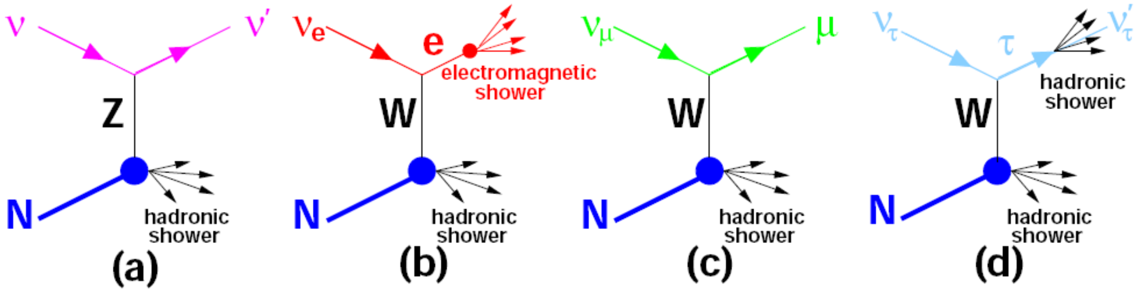

Figure 2.3: Depiction of neutrino interactions relevant for neutrino telescopes. (a) Neutral current reaction resulting in a scattered neutrino and a hadronic shower; (b) Charged current reaction of an electron-neutrino resulting in an electromagnetic and a hadronic shower; (c) Charged current reaction of a muon neutrino resulting in a muon and a hadronic shower; (d) Charged current reaction of a tau-neutrino resulting in a double bang event (see text).

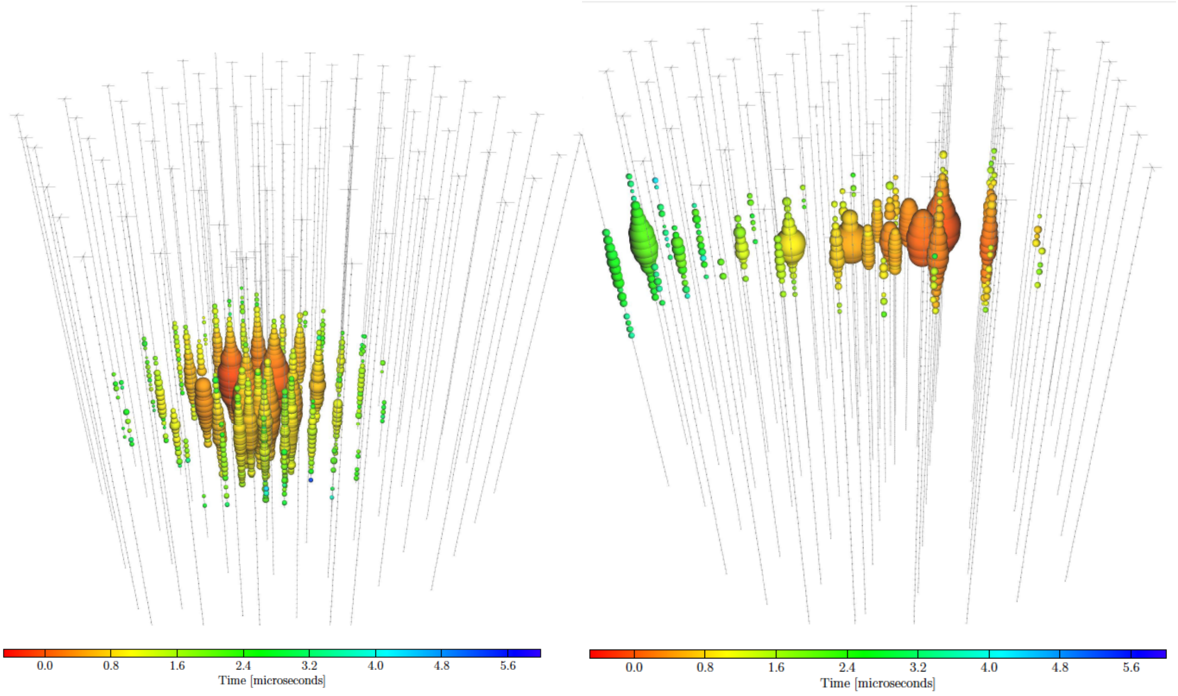

Figure 2.4: Example of a shower-like and a track-like event. The colour scale refers to the time evolution of the light deposit. Taken from [136].

the hadronic shower. Tau neutrinos will produce a τ-lepton which will travel a certain distance and then decay, producing, among other possibilities, another hadronic shower (depending on the type of decay). This type of event with two separated hadronic showers is often called a “double-bang” event. The path lengths of the three lepton and of the hadronic and electromagnetic cascade are shown in fig. 2.5. The long muon range

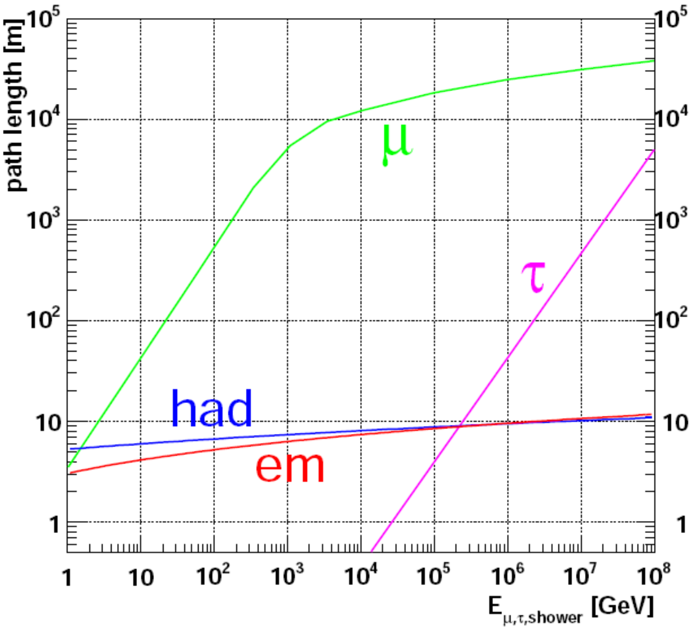

Figure 2.5: Path lengths of muons, taus and electromagnetic (*em*) and hadronic (*had*) showers in water. Taken from [137].

(at $E_\mu > 1$ TeV allows to detect muons produced far outside the instrumented detector volume and provides a long lever arm for direction reconstruction. For this reason, the muon tracks are the golden event signature for neutrino astronomy and the only one considered in this thesis.

Fig. 2.6 summarises the existing measurements of CC neutrino and antineutrino cross sections accumulated over many decades using a variety of neutrino targets and detector technologies [138]. The contributing processes are the quasi-elastic scattering

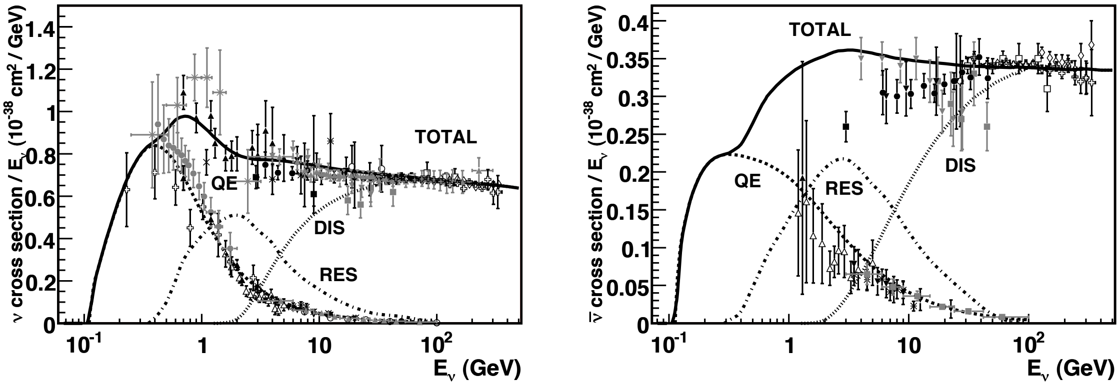

Figure 2.6: Total neutrino (left) and antineutrino (right) per nucleon CC cross sections divided by neutrino energy and plotted as a function of energy [138].

(QE), the resonance production (RES) and the deep inelastic scattering (DIS), that is dominant above about 100 GeV. The kinematics of this interaction is such that there is a small angle between the neutrino and the produced muon directions, that is shown in fig. 2.7 as a function of the neutrino energy. As only the muons direction can be reconstructed, this imposes a limit on the achievable angular resolution. Since the kinematic angle in fig. 2.7 decreases with energy, the angular resolution of a neutrino telescope is dominated by the reconstruction above energies of typically a few TeV and by the kinematics of the neutrino interaction below. Muons produced by neutrinos with $E_\nu > 10$ TeV can be considered almost collinear with their parent neutrino.

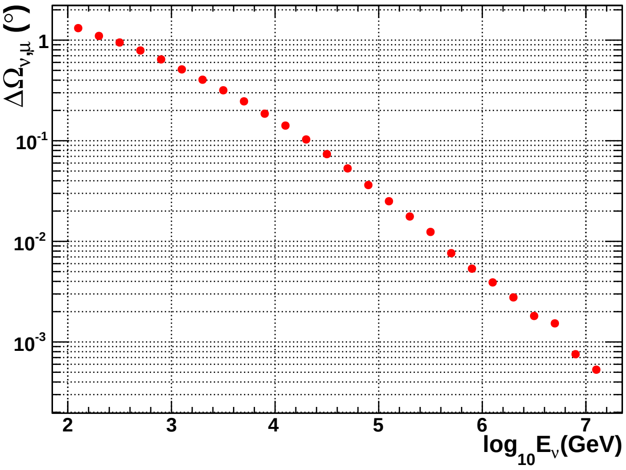

Figure 2.7: Median of the angle between the neutrino and the produced muon directions for each neutrino energy bin.

The cross section shown in fig. 2.6 is measured up to a few hundred GeV. For higher energies the cross section for deep-inelastic neutrino-nucleon scattering has been calculated by Gandhi et al. [139] and is shown in fig. 2.8. Below about 5-10 TeV the cross section increases linearly with the neutrino energy. For higher energies $\sigma \propto E^{0.4}$.

Another important parameter that characterises the interaction is the inelasticity y that gives the fraction of the initial neutrino energy taken by the hadronic shower (Fig. 2.9). The behaviour of neutrino and antineutrino differs below 10^6 GeV. Around 10 GeV the percentage of energy transferred to the shower is about 50% in case of νN interaction and 35% for $\bar{\nu}$N. Above 10^6 GeV y is about 0.2 for both neutrinos and antineutrinos. As a consequence of the increase of the νN and $\bar{\nu}$N cross section with increasing E_ν, the

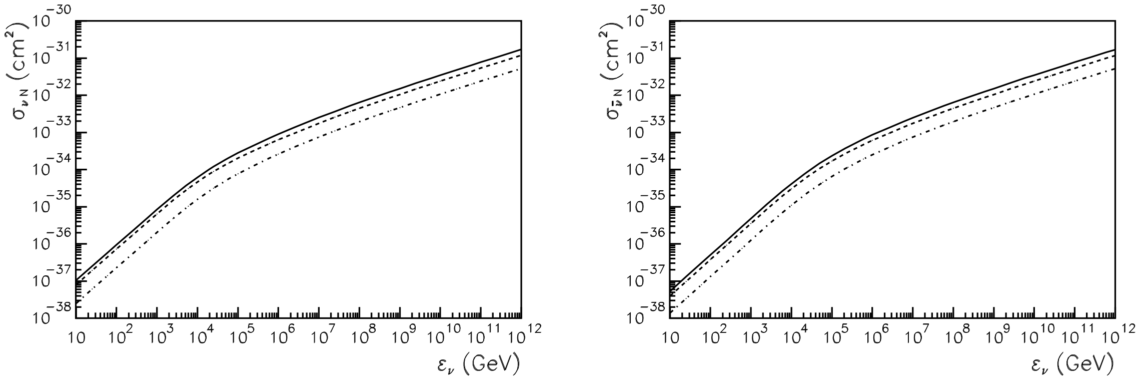

Figure 2.8: Coss section for νN (left) and $\bar{\nu}$N (right) interaction at high energies.The CC (dashed lines), NC (point-dashed lines) and total (solid line) cross section are indicated [139].

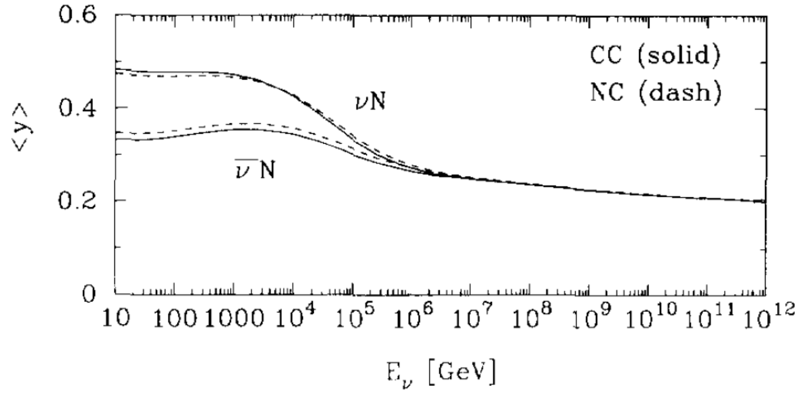

Figure 2.9: Energy dependence of the inelasticity parameter y for charged-current (solid lines) and neutral-current (dashed lines) interactions as a function of the incident neutrino energy [139].

neutrino interaction length defined as

$$L_{int}(E_\nu) = (\sigma_{\nu N}(E_\nu) < \rho >)^{-1} \ . \tag{2.3}$$

where $< \rho >$ is the crossed medium density, decreases with E_ν, as shown in fig. 2.10. Starting at about 40 TeV the interaction length gets shorter than the diameter of the Earth, so that at higher energies a significant part of the incident neutrinos is absorbed in the Earth.

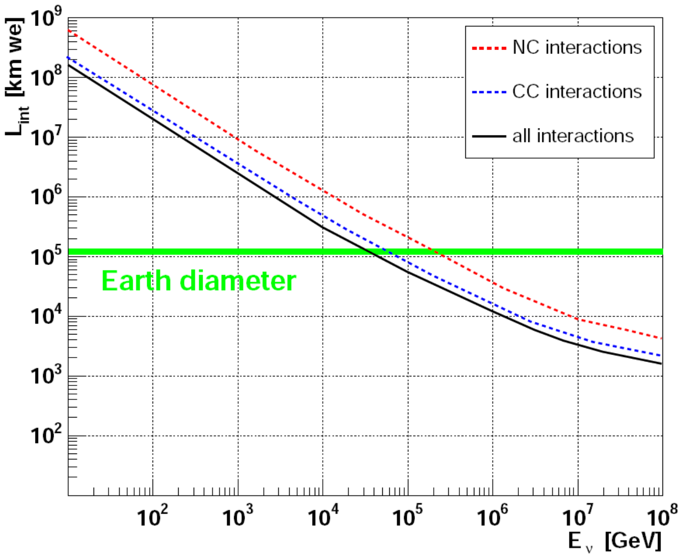

Figure 2.10: Interaction lengths as a function of the neutrino energy for different types of neutrino-nucleon interactions, given in km water equivalent [139].

2.1.2 Muon propagation

When a high energy muon propagates in a transparent medium (like water or ice), it loses a small amount of energy through the emission of Čherenkov radiation, which is the physics process of interest for high-energy ν detectors. The majority of the muon energy loss is due to other mechanisms (see fig. 2.11):

1. *ionization of matter*, which is the dominant process at low energies (below 1 TeV);
2. e^+e^- *pair production*, which is the dominant energy loss process at energies greater than 1 TeV;
3. *bremsstrahlung*;
4. *photo-nuclear interactions.*

The total energy loss for muons with energy above about 1 TeV can be expressed as:

$$\frac{dE}{dx} = -\alpha(E) - \beta(E)E \tag{2.4}$$

At high energies as a first approximation, the ionisation term α and the radiative losses term β can be considered as energy independent. With equation 2.4 it is possible

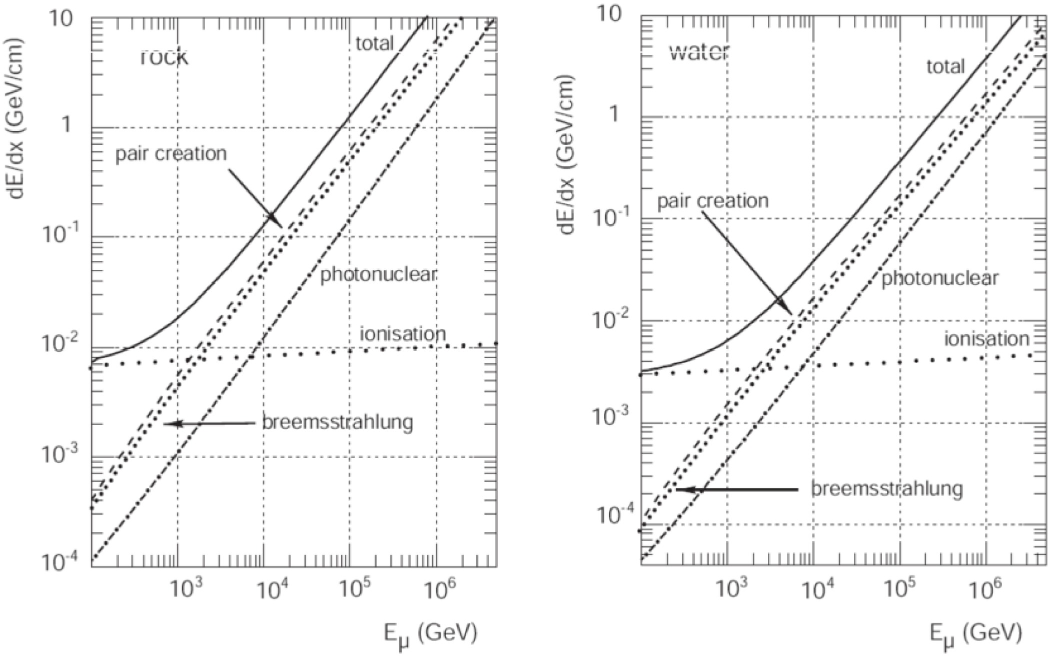

Figure 2.11: Partial and total muon energy losses in water (left) and rock (right) as a function of the muon energy [140].

compute the muon range R:

$$R = \frac{1}{\beta} ln\left(1 + \frac{E_\mu \beta}{\alpha}\right) \tag{2.5}$$

2.1.3 Cherenkov radiation

When a charged particle with velocity v traverses a dispersive medium of refractive index n, excited atoms in the vicinity of particle become polarized. If v is larger than the speed of light in the medium c/n, a part of the excitation energy reappears as coherent radiation emitted at a characteristic angle θ_C with respect to the direction of the motion (see fig. 2.12). The angle θ_C is linked to n and v by the relation

$$cos\theta_C = \frac{1}{\beta n} \tag{2.6}$$

with $\beta = v/c$. The number of Cherenkov photons N emitted by a charged particle of charge ze per unit wavelength interval $d\lambda$ and unit distance travelled dx, is given by:

$$\frac{d^2N}{dxd\lambda} = \frac{2\pi\alpha z^2}{\lambda^2}\left(1 - \frac{1}{\beta^2 n^2(\lambda)}\right) \tag{2.7}$$

where λ is the wavelength of the photon and α is the fine structure constant. In the wavelength range from 300 nm to 600 nm, where water is transparent, this results in

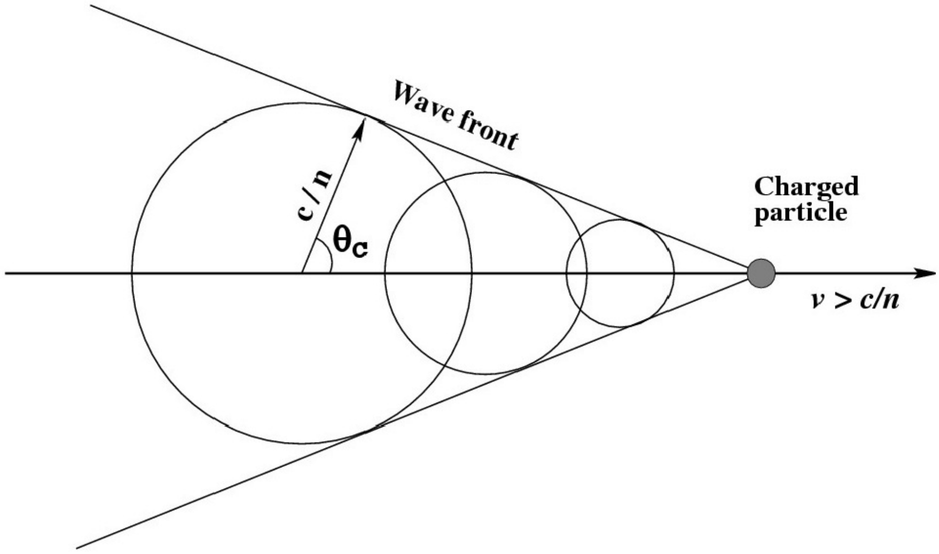

Figure 2.12: Overlapping of the wavefronts emitted in the depolarisation of the molecules in a medium crossed by a particle with speed $v > c/n$.

about 3.4×10^4 emitted photons per meter of particle track. In this relevant wavelength region, the refractive index of water is $n \sim 1.35$, thus for a highly relativistic particle with $\beta \sim 1$ this leads to Cherenkov angle of $\theta_C \simeq 42°$

2.1.4 Light transmission properties

The attenuation of the Cherenkov light in water sets an upper limit to the distance between the optical sensors of the telescope. In order to properly describe the transparency of sea water as a function of wavelength, it is necessary to measure the parameters describing absorption and scattering, such as the absorption length $\lambda_{abs}(\lambda)$ and the scattering length $\lambda_s(\lambda)$ Each of these lengths represents the path after which a beam of initial intensity I_0 and wavelength λ is reduced in intensity by a factor of $1/e$ through absorption or scattering according to

$$I_{abs,s}(x) = I_0 exp\left(-\frac{x}{\lambda_{abs,s}}\right) \tag{2.8}$$

where x is the optical path traversed by the beam. The attenuation length is defined as $1/\lambda_{att}(\lambda) = 1/\lambda_{abs}(\lambda)+1/\lambda_s(\lambda)$. In the literature, also the coefficients of absorption, $a = 1/\lambda_{abs}(\lambda)$, and scattering, $b = 1/\lambda_s(\lambda)$, are used to characterise the light transmission through matter. The sum of scattering and absorption coefficients is called "attenuation

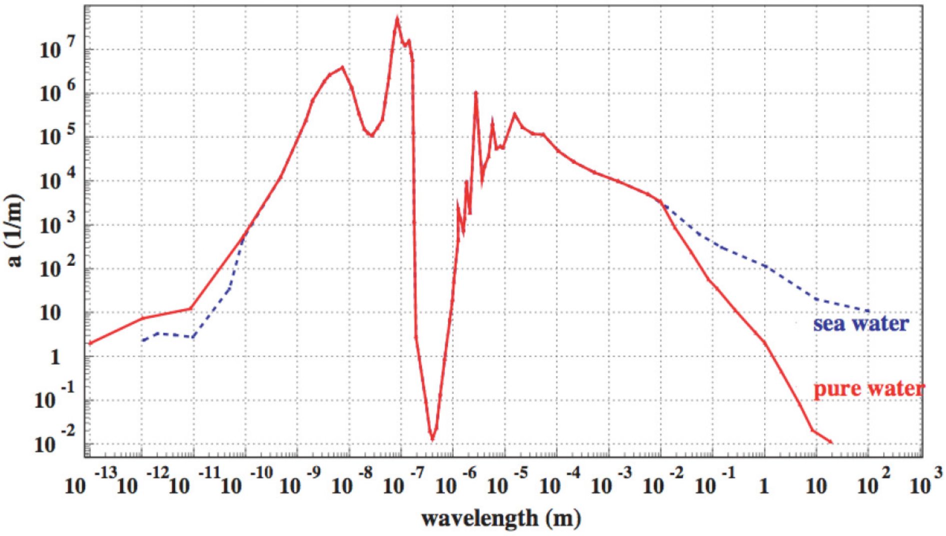

Figure 2.13: Light absorption coefficient a as a function of wavelength for pure water (solid line) and sea water (dashed line). [142].

coefficient" c.

As shown in fig. 2.13, water is transparent only to a narrow range of wavelengths (350 nm $\leq \lambda \leq$ 550 nm). In particular, λ_{abs} is about 100 m for deep polar ice [141], and it is about 70 m for clear ocean waters [142]. From these values one can get a first rough estimate of the number of optical sensors that are needed to instrument a km^3 of water, that turns out to be about 5000.

2.1.5 Environmental optical background

The muon track is reconstructed using the time and spatial position informations of the photon hits (see Chapter 5). Despite the fact that the deep-sea environment where the neutrino telescope has to be located is completely shielded from sunlight, still a light background exists. This is due to two sources: Cherenkov light produced in the propagation of charged particles originating in the decay of radioactive elements in sea water and luminescence induced by biological organisms, the so called bioluminescence. This optical background gives spurious signal on the optical sensors making the muon track reconstruction more complex .

Radioactivity

Several radioactive elements can be found in sea water, the most abundant is ^{40}K, that has two main decay channels:

$$^{40}K \longrightarrow^{40} Ca + e^- + \bar{\nu}_e \; B.R. = 89.3\% \tag{2.9}$$

$$^{40}K + e^- \longrightarrow^{40} Ar + \nu_e + \gamma \; B.R. = 10.7\% \tag{2.10}$$

The electrons produced in the first process often have sufficiently high energy to induce the Cherenkov effect, while in the electron capture process, the photon in final state is produced with an energy of 1.46 MeV, which can easily lead to the production of electrons with energies over the threshold for Cherenkov light emission. Light pulses due to ^{40}K decays are uncorrelated. However radioactive decays may produce many photons within 1 ns, giving raise to narrow coincidences on neighbouring PMTs.

Bioluminescence

There are two contributions to bioluminescent light, one varying on time scales of hours to days (presumably from bacteria) and one coming in "bursts" with durations of the order of seconds (assigned to larger size organisms). The photomultiplier count rate from the steady component can be of similar size as that from ^{40}K and is typically homogeneous over the full detector. Instead a burst can cause rates that are larger than the steady background by orders of magnitude, but affect only a local group of optical modules. Both components thus differ significantly in their impact on data taking, filtering and analysis. The most direct assessment of bioluminescence and its impact on the neutrino telescope is by measuring the intensities of deep-sea background light over long-term periods. To investigate the occurrence of bioluminescent organisms, water samples have been retrieved from different depths at a location near the Capo Passero site (one of the installation site of the KM3NeT neutrino telescope; see section 3.4). Subsequently, the density of luminescent bacteria cultivatable at atmospheric pressure has been determined. The results in the left plot of fig. 2.14 indicate that such bacteria are essentially absent at depths beyond 2500 m [143].

Recently an 8 floors tower equipped with a total of 32 photomultipliers has been installed at the Capo Passero Site at a depth of about 3500 m. In the right panel of fig. 2.14 the average rate in kHz recorded by one of the optical modules for each floor is plotted for a period of few months. The rates have values of about 50-60 kHz, corresponding to the expected contribution due to the ^{40}K decays in water. The peaks above this baseline are due to the bioluminescence activity which seems very modest during the monitored period.

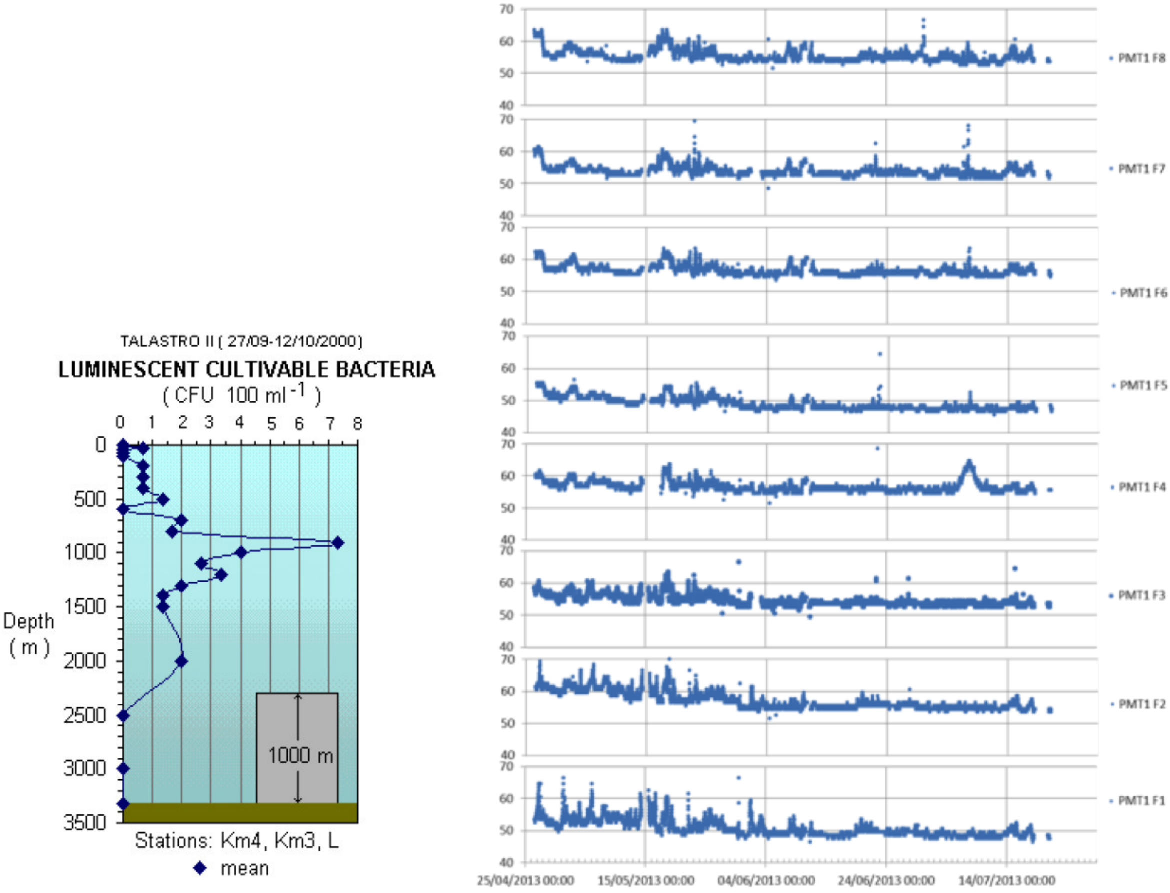

Figure 2.14: Left: concentration of luminescent bacteria cultivatable at atmospheric pressure, as a function of depth. The data have been obtained from water samples taken at the Capo Passero site. Right: average single counting rates in kHz measured in by the photomultipliers at the Capo Passero site from April to July 2013.

2.1.6 Physical background

In the previous chapter, an overview of the general neutrino sources was presented. These neutrino sources can produce a detectable neutrino-induced muon flux. However, only a fraction of the total muon flux that arrives to the detector is produced by astrophysical sources, the rest is background that must be rejected.

As mentioned, there are two sources of background. The origin of both is the interaction of cosmic rays in the atmosphere. When a cosmic proton interacts with an atmospheric nucleus it gives rise to a hadron cascade composed, among others, of π^+ and π^- that can decay giving μ and ν. Therefore, on one hand, there are muons produced in atmospheric cascades by primary cosmic rays, on the other, there are also atmospheric neutrinos (see section 1.5) from the same origin, that can produce muons through the same mechanism described for astrophysical neutrinos.

Figure 2.15 shows the muon flux induced by atmospheric neutrinos [144] and the direct atmospheric muon flux [145] as a function of the zenith angle calculated for 2400 m depth. For downward events the atmospheric muon flux exceeds that of muons induced by atmospheric neutrinos by six orders of magnitude, although it is completely suppressed for the up-going direction. Atmospheric muons, in fact, can cross the atmosphere and reach the Earth or the sea where they are absorbed after several kilometers. As a consequence, the expected background is solely constituted of *down-going* muons and, therefore, they can be in principle rejected if we restrict the search for signal exclusively to *up-going* reconstructed events since *up-going* muons can only be produced by interaction of *up-going* neutrinos.

As already pointed out, misreconstructed down-going events can mimic up-going neutrino-induced muon and they are extremely dangerous for a detector searching for a few tens of events per year. For this reason it is important to reduce the atmospheric muon flux installing the detector at large depths and improve the reconstruction technique.

There are also up-going muons produced by atmospheric neutrinos that have partially or fully crossed the Earth. Atmospheric neutrinos are an irreducible background component, since they cannot be distinguished from astrophysical neutrinos. At high energies ($E_\nu \gtrsim 10$ TeV), however, we expect that the cosmic neutrino diffuse flux (due to the combination of several unresolvable neutrino sources) may dominate over the atmospheric neutrino background, since the latter is lower due to its softer energy spectral index ($\gamma \sim 3.7$) compared to the one of cosmic neutrino spectrum ($\gamma \sim 2$).

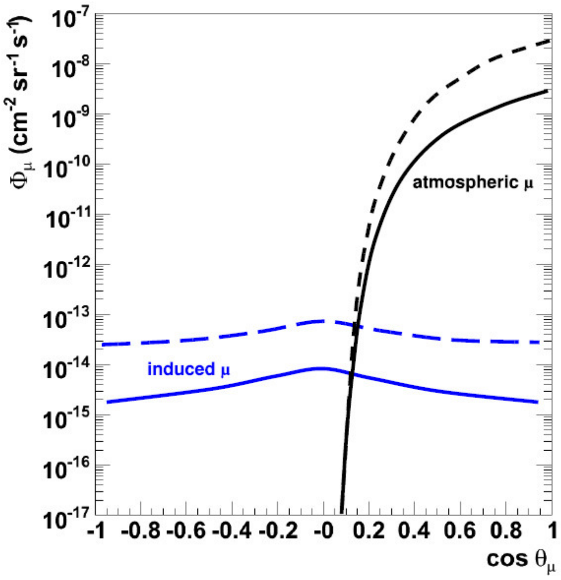

Figure 2.15: Different contributions to muon background as a function of the zenith angle calculated for 2400 m depth: atmospheric muons (from [145]) and atmospheric neutrino induced muons (from [144]). The solid lines stand for $E_\mu > 1$ TeV and the dashed lines for $E_\mu > 100$ GeV.

2.2 Main existing Cherenkov Neutrino Telescopes

2.2.1 ANTARES

The ANTARES detector [146], located 40 km off the French town of Toulon at a depth of 2475 m, is the first operational Neutrino Telescope in the Mediterranean Sea. It was completed in May 2008 with a total of 885 Optical Modules (OMs) looking 45° downward and distributed along 12 vertical detection lines. Figure 2.16 shows a schematic view of the detector. An OM consists of a 10-inch photomultiplier housed in a glass sphere together with its base, a special gel for optical coupling and a μ-metal cage for magnetic shielding. The OMs are grouped in 25 triplets (or storeys) on each line, except for one of the lines which contains only 20 optical storeys because acoustic devices are installed. Each line has a length of 450 m and is kept taut by a buoy located at its top. The lower 100 m are not instrumented. The distance between triplets is 14.5 m and the separation between the lines ranges from 60 to 75 m, reaching an instrumented volume of about 0.025 cubic kilometers. The lines are connected to a central junction box, which in turn is connected to shore via an electro-optical cable.

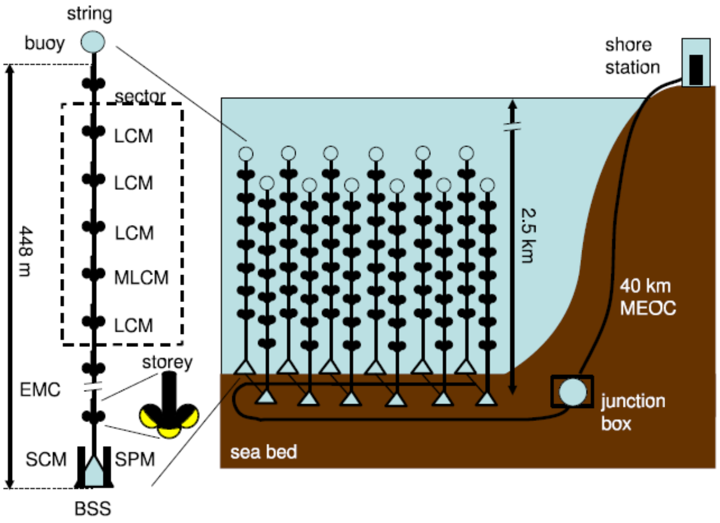

Figure 2.16: A schematic view of the ANTARES detector layout. The main elements of the ANTARES detector are outlined in the figure.

Some of the results obtained with the Antares detector have been mentioned in Chapter 1. A result that will be discussed again later is the sensitivity to point-like sources that is shown in fig. 2.17 as a function of the source declination. The Antares sensitivity calculated for 1339 observation day (equivalent to 3.7 years) is $E^2\Phi_{90} \sim 1.5$ - 3 $\times 10^{-8}$ GeV cm^{-2} s^{-1}.

2.2.2 ICECUBE

IceCube is the first built km^3 neutrino Cherenkov detector [148]. It comprises 5160 photomultipliers installed at depths between 1450 and 2450 meters in the Antarctic ice. The PMTs are arranged in 80 vertical strings each containing 60 PMTs (+6 strings for Deep Core), installed via hot water drills. A drawing of the IceCube array is shown in fig. 2.18.

A recent IceCube search for neutrinos of EeV (10^6 TeV) energy found two events at energies of 1 PeV (10^3 TeV), above what is generally expected from atmospheric backgrounds [150]. A follow-up analysis with improved sensitivity and extended energy coverage down to approximately 30 TeV have observed twenty-six additional events above the expected background of $10.6^{+5.0}_{-3.6}$ events from atmospheric muons and neutrinos. [136]. Combined, both searches reject a purely atmospheric origin for the twenty-eight events at the 4σ level. For this analysis, in order to select contained events, all

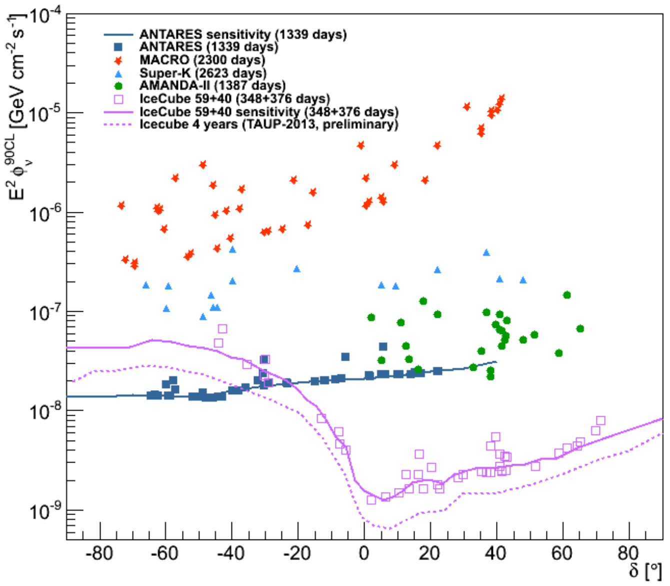

Figure 2.17: Upper limits (points) and sensitivity flux (lines) to sources with an E^{-2} flux for various experiment, in particular Antares and IceCube detector [147].

the events producing light in an area surrounding the detector corresponding to a veto region (see right panel of fig. 2.18) were discarded. The distribution of the observed deposited charge on the detector for the 28 events is shown in fig. 2.19.

Of these 28 events, seven events are clearly identifiable muon tracks, whereas the remaining twenty-one show spherical photon distributions consistent with the pattern of Cherenkov photons from particle cascades induced by neutrino interactions other than ν_μ charged-current. Four of the low energy track-like events started near the detector boundary and are downgoing, consistent with the properties of the expected 6.0 ± 3.4 background atmospheric muons, as measured from a control sample of penetrating muons in data.

A search of neutrino sources through a clustering has been performed but no statistical significance neither in spatial nor in time clustering of these events has been found.

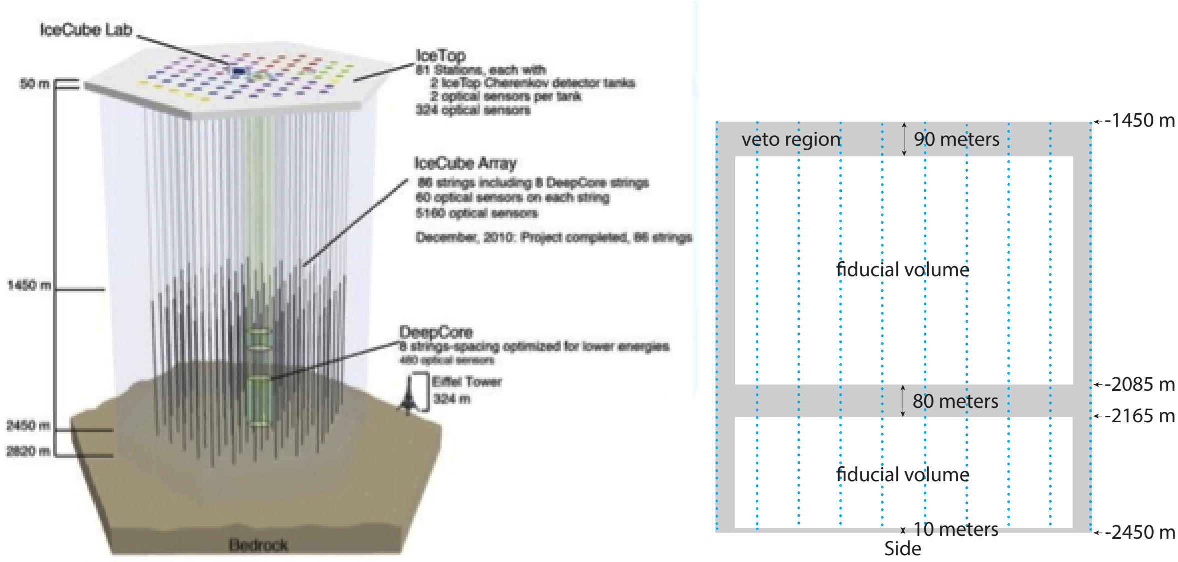

Figure 2.18: Left: sketch of the IceCube detector. Left: schematic view of a cross-section of the detector. The shaded area surrounding the detector refer to a veto region, while the shaded region in the middle contains ice of high dust concentration [149].

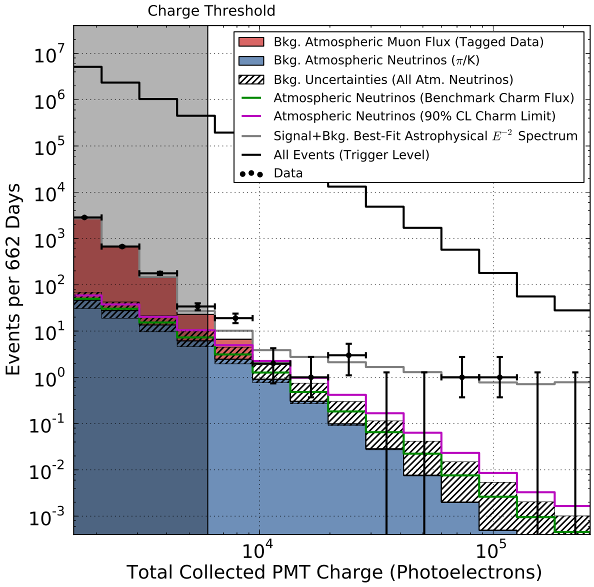

Figure 2.19: Distribution of deposited PMT charges (Q_{tot}). Muons at higher total charges are less likely to pass the veto layer undetected, causing the muon background (red, estimated from data) to fall faster than the overall trigger rate (uppermost line). The discussed 28 events are in the unshaded region, at $Q_{tot} > 6000$. The best-fit E^{-2} astrophysical spectrum (gray line) and atmospheric neutrino flux (blue) have been determined using Monte Carlo simulations, with the hatched region showing current experimental uncertainties on the atmospheric neutrino background. See [136] for details.

CHAPTER 3

THE KM3NET PROJECT

KM3NeT [151] is the next generation multi-km^3 neutrino telescope to be installed in the Mediterranean Sea, a convenient location to look for high-energy neutrino sources in the inner part of the Galaxy. In the early 2013 the collaboration has started to engineer and implement the KM3NeT technology in KM3NeT-phase1. The design, construction and operation of KM3NeT is pursued by a collaboration formed around the institutes involved in the ANTARES (see section 2.2.1), NESTOR [152] and NEMO [153] pilot projects. Three sites (40 km offshore Toulon, France at a depth of 2500 m; 80 km offshore Capo Passero, Italy at a depth of 3500 m; 20 km offshore Pylos, Greece at depths of 2500-5000 m) are candidate for hosting part of the telescope.

The detector will consist of a three-dimensional array of large diameter pressure-resistant spheres, the so-called DOMs (Digital Optical Modules), each equipped with 31 photomultipliers with 3-inch photocatode diameter. The DOMs will be arranged in detection units, vertical strings anchored on the sea floor, each equipped with up to 20 DOMs. In each detection unit, the data and power flow proceed vertically and is connected via the anchor to a deep-sea cable network. This network typically contains some junction boxes and electro-optical cables through which the OM data are transferred to shore. It also provides power and slow-control communication to the detector. A shore station hosts both the power feeding system and the computing farm required for collecting the data, applying online filter algorithms and transmitting the data to mass storage devices. A description of the detector can be found in [154]. Here, for the purposes of this work, only a description of the key elements of the detector, the DU and the DOM, is given. The optimisation of the detector footprint is one of the aims of this work and will be discussed in detail in the following Chapters.

3.1 Optical Modules and photomultipliers

The active part of a neutrino telescope is the optical module. The solution chosen for KM3NeT is based on a multi-PMT optical modules, built by means of a large number of small-size PMTs housed in a pressure-resistant glass sphere [154, 155]. This choice offers some advantages compared to more traditional designs based on large-area PMTs, such as:

- The total photocathode area in a single sphere is maximised.
- Small photomultipliers are less sensitive to the Earths magnetic field and therefore do not require mu-metal shielding.
- The segmentation of the detection area in the OM will aid in distinguishing single-photon from multi-photon hits. With the multi-PMT OM two-photon hits can be unambiguously recognized if the two photons hit separate tubes, which occurs in 85% of cases for photons arriving from the same direction. This feature helps for rejection of the environmental optical background.
- These photomultipliers have a small integrated anode charge and are therefore less subject to ageing.

The Digital Optical Module (DOM) of KM3NeT is made of 31 3-inch PMTs housed in a sphere of 17-inch diameter (see fig. 3.1). The PMTs are arranged in 5 rings of tubes with zenith angles of 50°, 65°, 115°, 130° and 147°, respectively. In each ring the 6 PMTs are spaced at 60° in azimuth and successive rings are staggered by 30°. The last PMT has a zenith angle of 180°.

The PMTs have a standard bialkali photo-cathode with a maximal quantum efficiency of about 30%. Their FWHM of transition time spread is less than 5 ns allowing for a good timing. Each PMT is surrounded by an expansion cone that is designed to enlarge its sensitive photocathode area collecting photons that would otherwise miss the photocathode (see fig. 3.2). Results for various angles of incidence of the light on the PMT indicate an increase in collection efficiency by 30% on average for angles of incidence from -50° to +45°, with a maximum of 35% for perpendicular incidence [156].

Electronics digitize and send the data to shore is located inside the sphere. An active base, is attached to each PMT allowing to control from the shore the HV and threshold

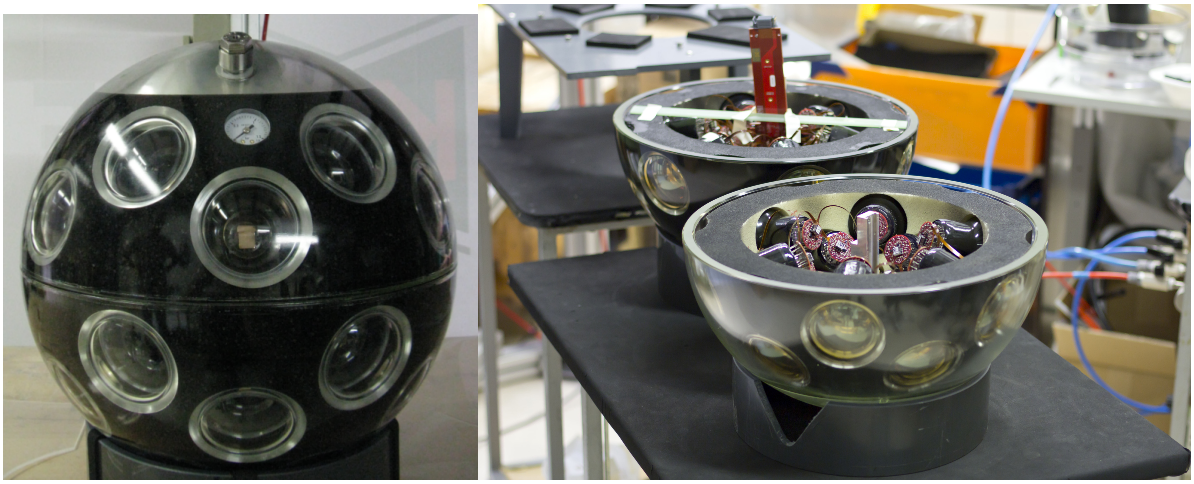

Figure 3.1: The Digital Optical Module (DOM) of KM3NeT. In the right picture the assembly of a prototype is shown.

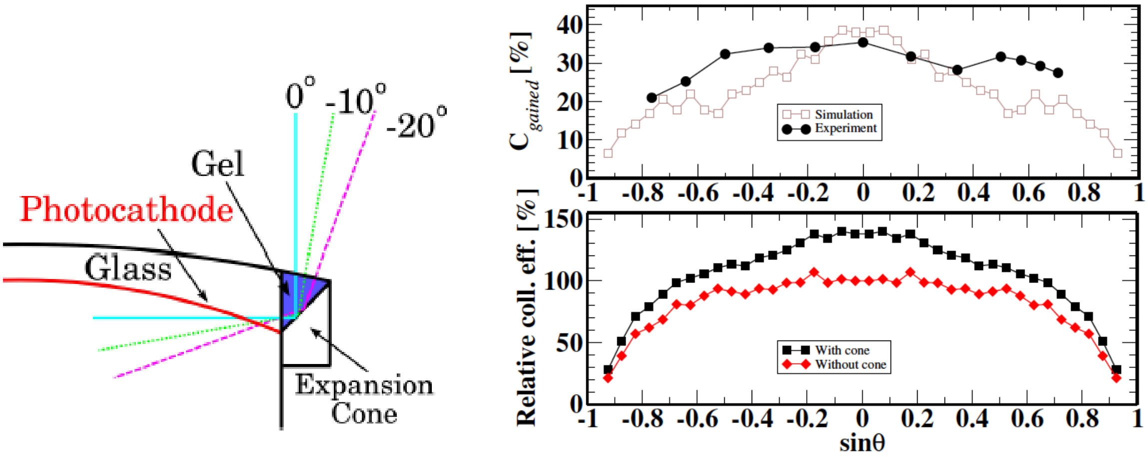

Figure 3.2: Left: Depiction of the light collection by an expansion cone. Right upper: gained collection efficiency as a function of the $\sin\theta$, being θ the angle of incidence. Right lower: collection efficiency as a a function of $\sin\theta$ with and without expansion cone. See [156] for details.

settings for each tube. The concept of "All-data-to-shore" is adopted. In particular, for each digitized hit, the threshold crossing time and the time-over-threshold are sent to shore. Each optical module requires about 10 W of electrical power and has 1 Gb/s readout bandwidth.

All DOMs are synchronized to the sub-nanosecond level by means of a clock signal broadcast from shore. The time offsets of the individual PMTs will be calibrated onshore before deployment, and will be continuously monitored in situ by means of a system of light beacons meant to illuminate groups of DOMs at known times; this system comprises laser beacons located on the sea bottom and LED pulsers located inside the DOMs. The instrumentation mounted in each DOM comprises a piezo-sensor for acoustic positioning purposes, a tiltmeter and a compass, as well as sensors of the temperature and humidity inside the DOM for monitoring purposes. The internal structure of the DOM has been carefully designed to efficiently remove heat from the electronics using a mushroom shaped aluminium structure that transfer it to the sea via the glass sphere.

A breakdown structure of the DOM is shown in fig. 3.3.

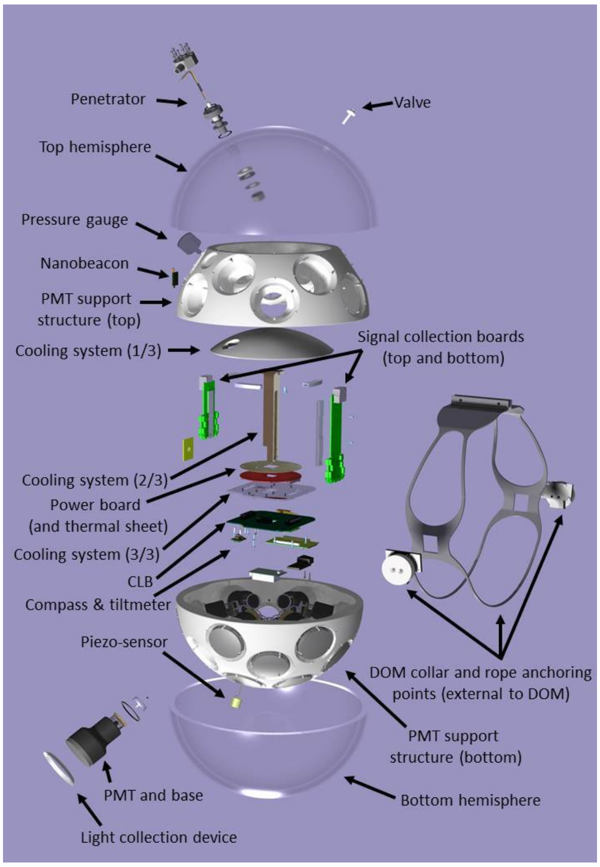

Figure 3.3: Internal structure of the KM3NeT DOM.

A prototype DOM has been mounted on the instrumentation line of ANTARES which has been installed in the ANTARES detector site on April 2013 (see fig. 3.4). The device is still working nominally. The data collected in the first months of data taking [157] show a baseline in the hit rate corresponding to an average rate of about 8 kHz per PMT that is stable. Because the DOM contains many PMTs it is possible to look for coincidences of hits within the single optical module. The sum of hit rates

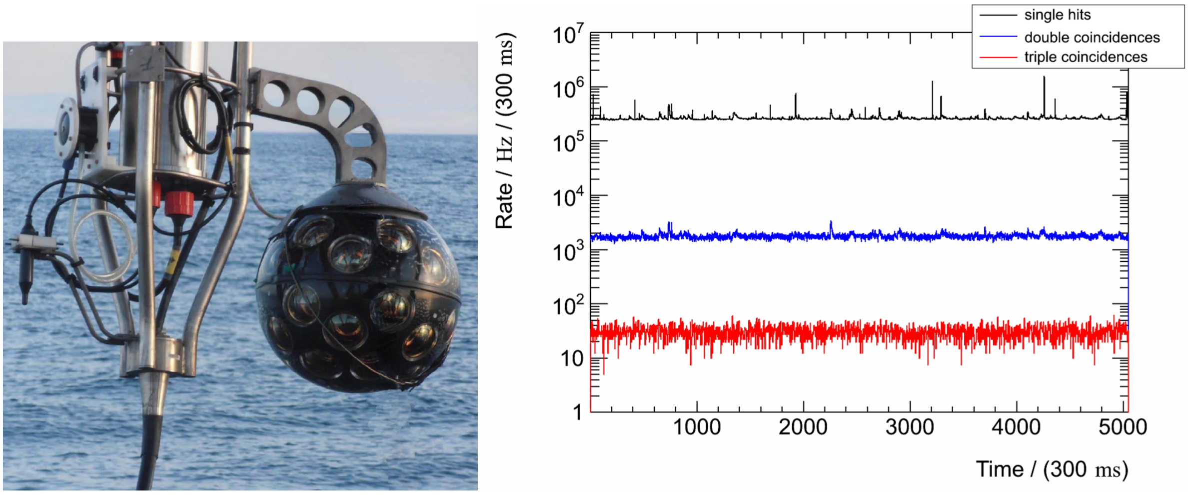

Figure 3.4: Left: Prototype DOM installed on the instrumentation line of ANTARES during deployment. Right: Rates of events as a function of the time measured in 100 ms bins. The top trace is for single hits while the lower traces are for two- and threefold coincidences within a 20 ns window [157].

of all PMTs in the DOM in 100 ms timeframe bins are shown in the right panel of 3.4 together with the rate for twofold and threefold coincidences as a function of time. A two- (three-)fold coincidence is defined by the occurence of a hit in two (three) PMTs within a time window of 20 ns. To provide adequate statistics the rate of threefold coincidences is averaged over 300 ms.

DOM is also capable of detecting multiple photons from a single ^{40}K decay, as demonstrated by fig. 3.5. These plots show the time difference ΔT between hits in separate PMTs for increasing angular separation of the phototubes. The clear Gaussian peak centered at $\Delta T = 0$ indicates the detection of two photons from the same ^{40}K decay. The peak becomes less prominent as the angular separation increases from 33° in fig. 3.5A to 65° in fig. 3.5B to 120° in fig. 3.5C. When the PMTs are back to back as in fig. 3.5D the peak has disappeared leaving only random coincidences.

The analysis of the PMT coincidence rates shows also that a single DOM can, by itself, unambiguously identify atmospheric muons. This conclusion can be drawn from fig. 3.6, where the event rate is shown as a function of the coincidence level. The data are compared with a simulation including both the ^{40}K background and the contribution from flux of downgoing atmospheric muons at the depth of the detector. The rates decrease rapidly as a function of the coincidence level as every level increase leads to an extra factor of $Area_{PMT}/4\pi r^2$ in acceptance and so to a rapidly decreasing volume

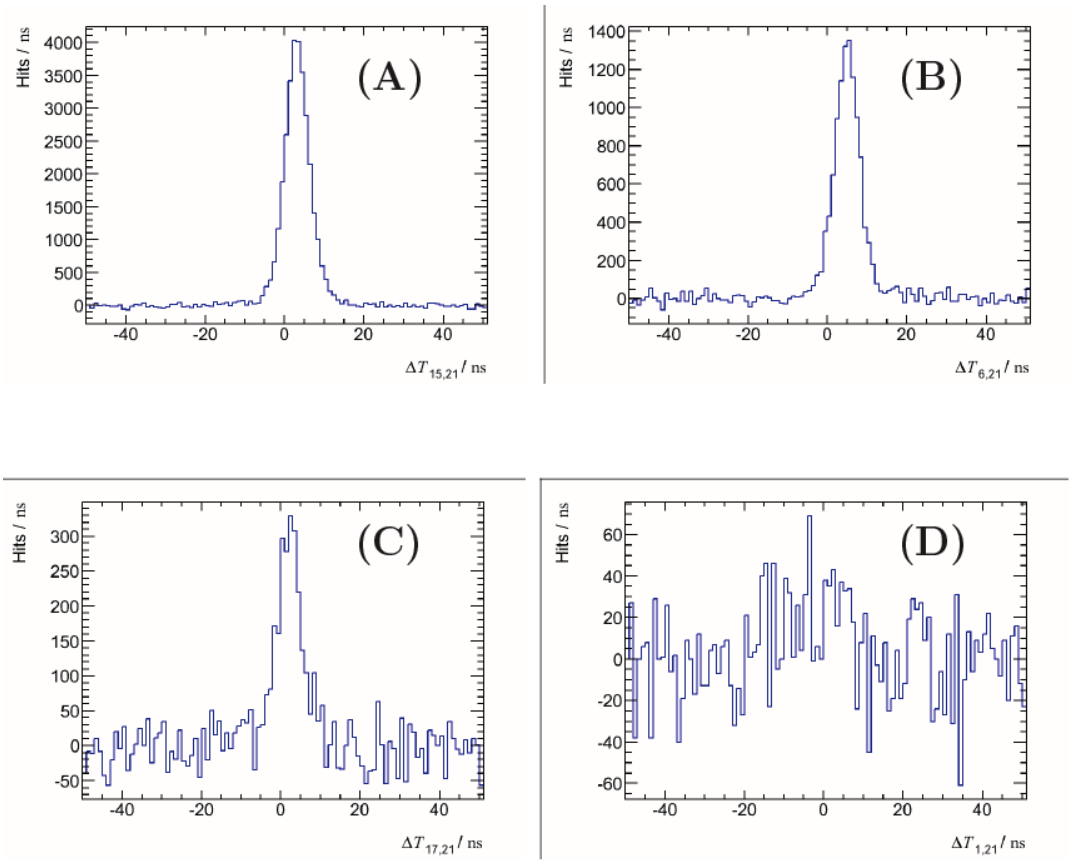

Figure 3.5: Time difference distribution between two PMTs of the DOM, with an angular separation of 33° (A), 65° (B), 120 ° (C) and 165° (D) [157].

of water in which the DOM is sensitive to the ^{40}K decays. Below a coincidence level of 6, the measured event rate is in good agreement with the event rate given by the optical background, except for the single rate, which is very sensitive to the attenuation and scattering length in the water and also has a contribution from bioluminescence is underestimated by the simulation. Above the coincidence level of 6, the signals from atmospheric muon dominate with an excellent agreement between data and the atmospheric muons simulation.

3.2 Detection Units

The optical modules are kept suspended in the sea by vertical structures, which are anchored to the seafloor and kept taught by buoyancy at their top. These structures together with their optical modules are referred as Detection Units (DU) or strings.

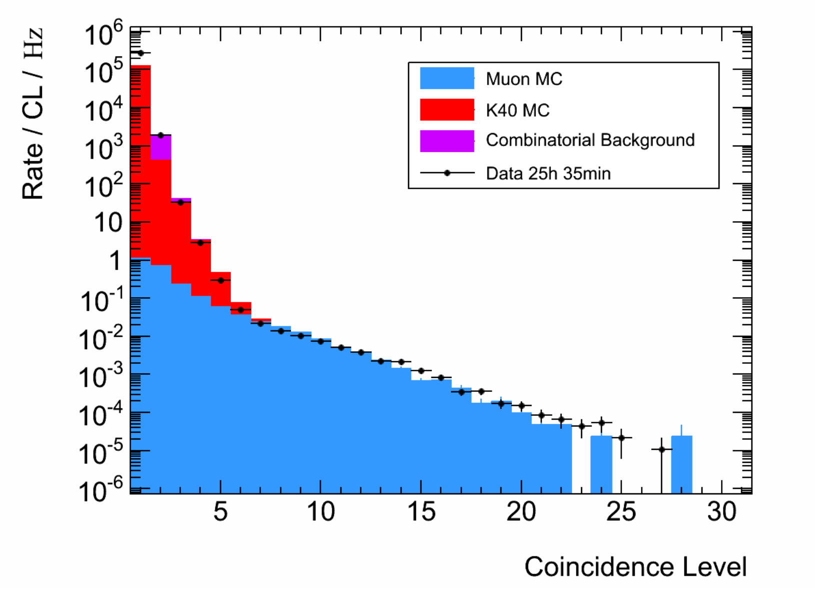

Figure 3.6: The rate of events as a function of the coincidence level (number of PMT with signal in a 20 ns time window). Black dots correspond to data while coloured histograms represent simulations (muons in blue, ^{40}K in red and accidental coincidences in purple). [157].

The DU is kept together by two dyneema ropes, while an electro-optical backbone provides connections for each DOM on two conductors for power and two optical fibers for communications with shore.

A new technique has been developed to deploy strings. Each string is first wound on a launcher vehicle, which has the shape of a sphere with 2 m diameter (see fig. 3.7). The launcher vehicle is lowered to the seabed from a surface vessel. Once the launcher vehicle has reached the seabed, the buoy is released, the string unfurls and rises to its full height, as sketched in fig. 3.7. The launcher vehicle is then recovered for subsequent deployments. This is a convenient approach for simplifying the operations at sea.

The KM3NeT Collaboration is pursuing an extensive qualification campaign for validating all technical choices for DU constructions. The next steps of the qualification project [158] are the construction and installation at the Capo Passero site of a pre-production model of DU, consisting of a reduced-size DU equipped with 3 DOMs and the deployment of a mechanical model of a full-size DU.

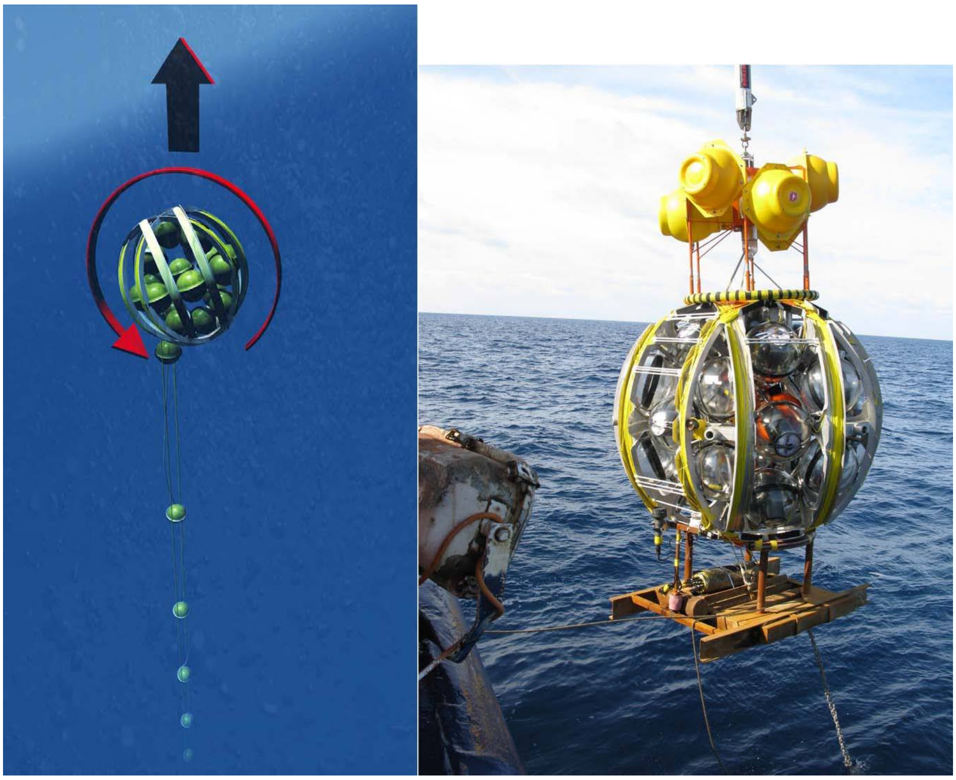

Figure 3.7: Left: unfurling of a KM3NeT DU. Right: Mechanical model of a DU, arranged on the launcher vehicle, being deployed during a test campaign offshore Spain in spring 2013.

3.3 Concept of building blocks

The detector can be considered as a three dimensional array of optical modules. In general, the configuration of such an array is defined by the number of strings, the number of optical modules on each string, the horizontal spacing between strings and the vertical spacing between the optical modules along a string. A study has been made of the detection efficiency as a function of these four parameters for various absorption lengths [159]. In this, the absorption length is varied by simply scaling the default values with one of the following fixed values: 0.9, 1.0, 1.1 or 1.2. The assumed signal corresponds to a flux of neutrinos from the SNR RXJ1713.7-3943. The neutrino energy spectrum expected from this source will be discussed in Chapter 6. Here, the detection efficiency is defined as the number of events with at least 5 L1 hits. An L1 hit is a coincidence of two (or more) hits in the same optical module within a time window of 10 ns. This definition corresponds to the typical configuration of the real-time data filter. The number of signal events as a function of the number of strings and the number of optical models per string is shown in figs. 3.8(a) and 3.8(b), with the total number of optical modules fixed to 12320. The detection efficiency for a fixed total number of optical modules gradually improves with the number of strings and the number of optical modules per string up to a certain point where it flattens out. Beyond 120 strings per detector and 18 optical modules per string, the normalised detection efficiency no longer improves. This result is primarily due to the assumed energy spectrum which is rather hard and has a well defined end-point. Such a spectrum is, however, characteristic for that of any known candidate source in our Galaxy, such as Super Nova Remnants. Hence this result generally applies to the most promising neutrino sources.

The number of signal events as a function of the horizontal spacing between strings and the vertical spacing between optical modules is shown in figs. 3.8(c) and 3.8(d). In this, the number of strings was fixed to 120 and the number of optical modules per string was fixed to 18. There is a maximum of the normalised detection efficiency around 90 m horizontal spacing between strings and 36 m vertical spacing between optical modules. In the vicinity of the optimum, the dependence of the detection efficiency on the configuration is very small.

The aim of this study is defining the smallest size detector with an optimal efficiency, that is called “building block”. The full KM3NeT detector will be constitute by several building blocks to reach the required instrumented volume of few cubic kilometres.

3.4 The installation sites

The Mediterranean Sea offers optimal conditions, on a worldwide scale, to host an underwater neutrino telescope. Careful studies of candidate sites have been carried out identifying several sites that are suitable for an undersea neutrino telescope. The most relevant criteria that lead to the choice of these sites are:

- Closeness to the coast to ease deployment and reduce the expense of the power and signal cable connections to shore;
- A sufficient depth to reduce background from atmospheric muons, and to suppress their misreconstruction as upgoing;
- Good optical properties of the water, i.e. absorption and scattering lengths close

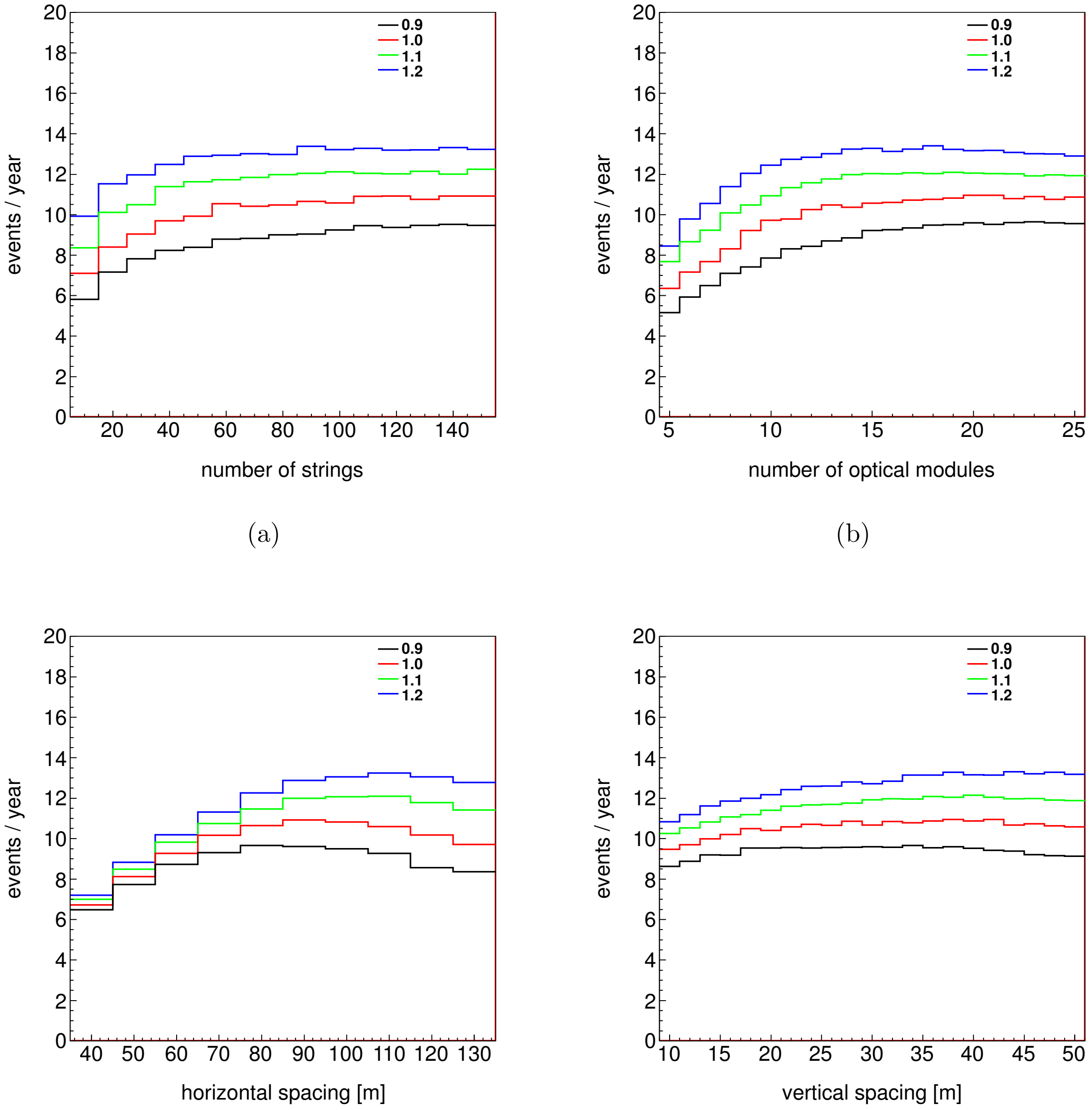

(a) (b)

(c) (d)

Figure 3.8: The expected number of events from an assumed flux of neutrinos from RXJ1713.7-3946 as a function of the number of strings (top-left); the number of optical modules per string (top-right); the horizontal spacing between strings (bottom-left) and the vertical spacing between optical modules (bottom-right). The default configuration corresponds to 120 strings, 20 optical modules per string, horizontal spacing between strings of 100 m and vertical spacing between optical modules of 40 m. The colour coding refers to the scaling factor applied to the absorption length (see text).

to the ones of optically pure sea water for light in the wavelength range of 350 nm to 550 nm;

- Low level of bioluminescence;
- Low rates of biofouling (bacterial film deposition and marine life accretion) on optical surfaces;
- Low rates of sedimentation;
- Stable low sea current velocities.

The locations of the three installation sites proposed by the ANTARES, NEMO and NESTOR collaborations is shown in fig. 3.9. The sites are: the Toulon site located in the Ligurian Sea at a depth of 2475 m, the Capo Passero site located in the West Ionian

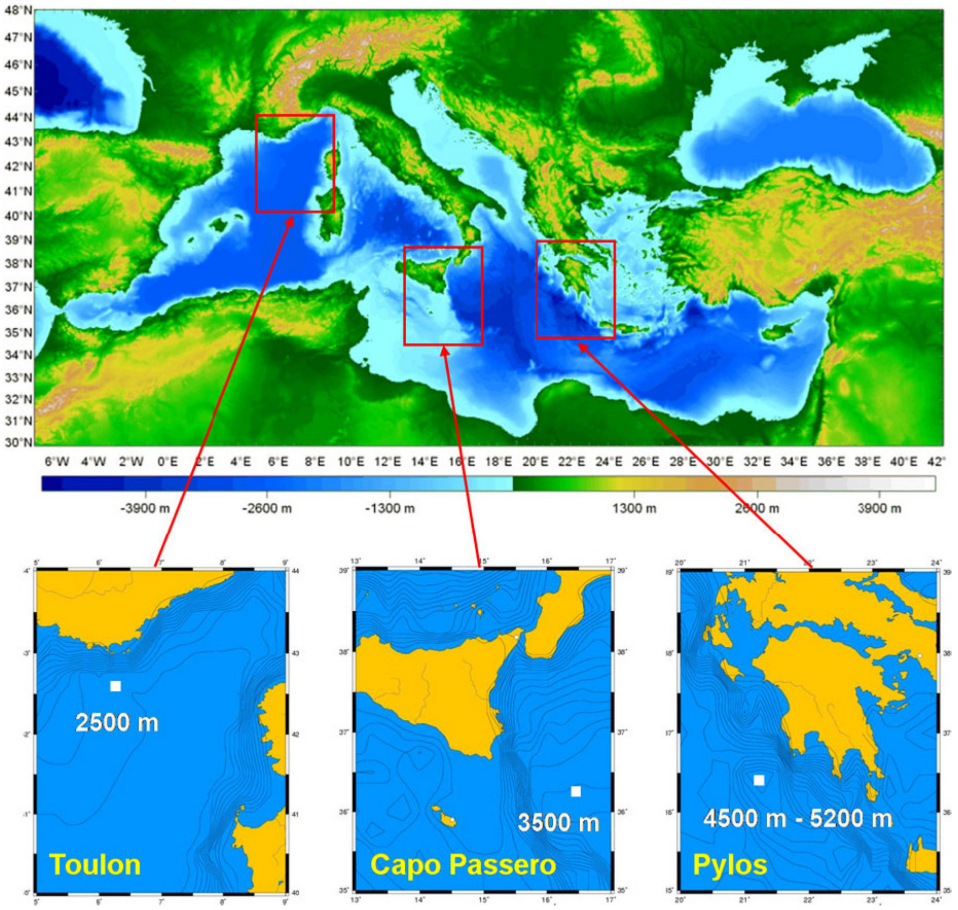

Figure 3.9: The locations of the three installation sites of the KM3NeT neutrino telescope in the Mediterranean Sea.

Sea at a depth of 3500 m, the Pylos site in the East Ionian Sea in three possible location at depths of 5200 m, 4500 m and 3750 m.

A long term characterization of the sites has been performed by studying a large number of oceanographical properties, like deep-sea water optical properties (absorption and diffusion), water environmental properties (temperature, salinity), biological activity (see section 2.1.5), optical background, water currents, sedimentation and seabed nature.

For instance, the light transmission at the Capo Passero site has been investigated [160] using a setup including a commercial instrument (the AC9 by WETLABS) capable of measuring, in a collimated geometry, the absorption and the attenuation coefficients for nine wavelengths ranging from 410 nm to 715 nm. The values of the absorption and attenuation lengths have been determined for each measurement by averaging the data for depths greater than 2850 m [161]. The results of four sets of measurements taken in different seasons are shown in figure 3.10. For comparison, light absorption and attenuation data for optically pure sea water are also shown in figure 3.10. At all wavelengths, deep waters at that location have an absorption length compatible with that of pure sea water. There is no evidence of a seasonal dependence of the optical parameters. The transmission length for Cherenkov photons measured at Capo Passero site is about 70 m.

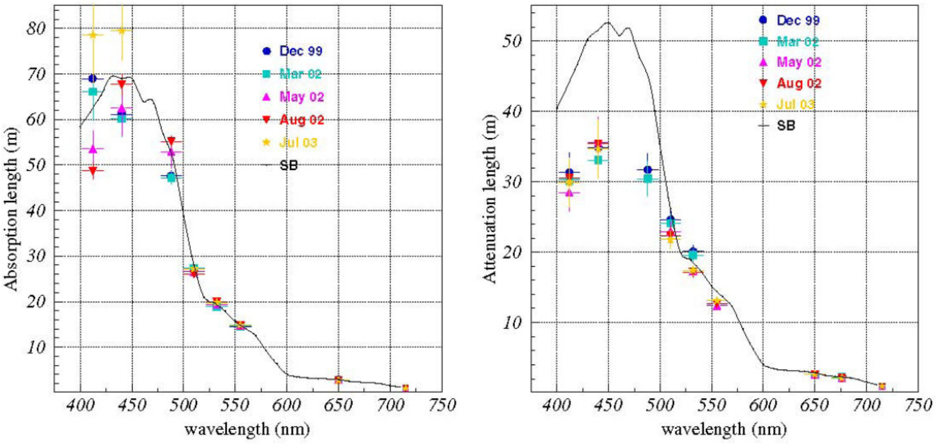

Figure 3.10: Absorption length (left panel) and attenuation length (right panel) measured at the Capo Passero site at four seasons. Also indicated are the the values for optically clean salt water (black lines). Figure taken from [160].

As mentioned elsewhere, the construction concept of KM3NeT will be a facility distributed over several sites. The construction of facilities needed to host the detector has started at the CapoPassero and Toulon site. In particular, the control station is ready at Capo Passero in Italy and already connected to a 100 km electro-optical cable which reaches the depth of 3500 m. A prototype structure of KM3NeT, built with the so-called tower architecture, has been deployed on March 2013 and is providing high quality real-time data useful for prototype qualification and site characterisation. As a first step toward the construction of KM3NeT, a group of 8 more towers, for a total of 670 optical modules, are under construction for deployment at Capo Passero. The deployment of additional 24 strings is then foreseen. The layout of this first group of DUs is shown in fig. 3.11. Here the green dots numbered 1-8 and the red dots numbered 9-32 correspond to the position of the 8 towers and 24 strings respectively while the JB1-JB3 correspond to the secondary junction boxes which route the DUs signals to the main electro-optical cable.

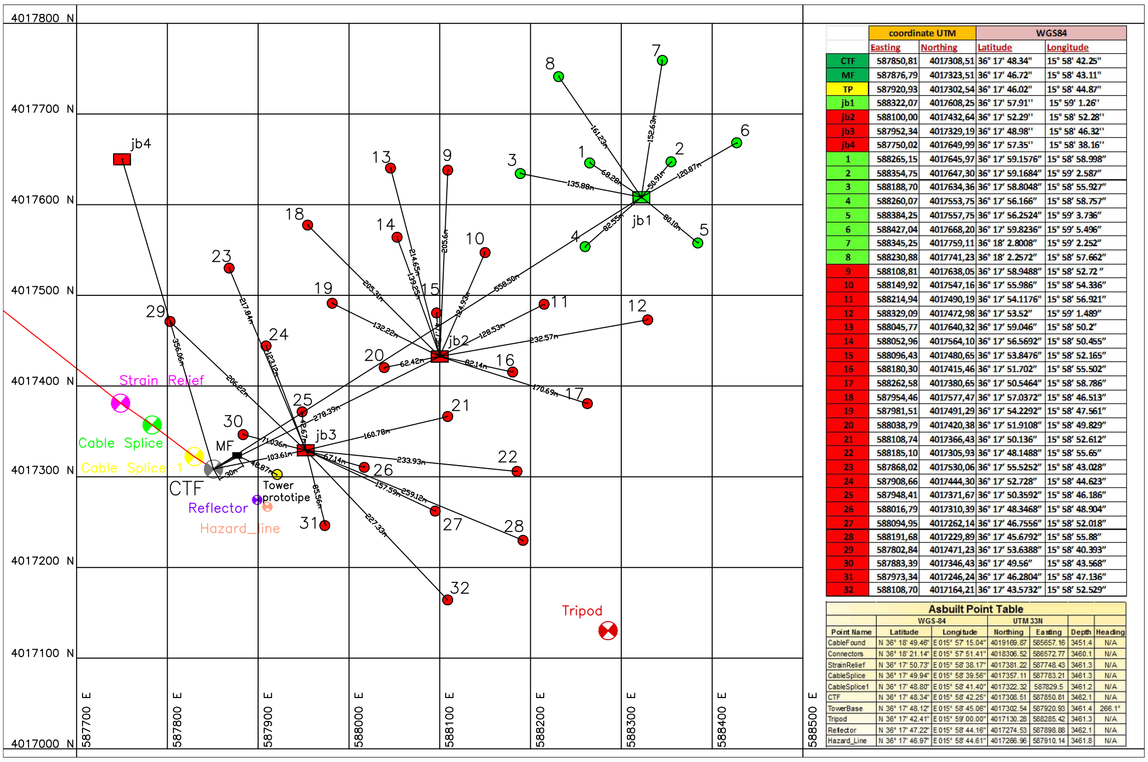

	coordinate UTM		WGS84	
	Easting	Northing	Latitude	Longitude
CTF	587850,81	4017308,51	36° 17' 48.34"	15° 58' 42.25"
MF	587876,79	4017323,51	36° 17' 46.72"	15° 58' 43.11"
TP	587920,93	4017302,54	36° 17' 46.02"	15° 58' 44.87"
jb1	588322,07	4017608,25	36° 17' 57.91''	15° 59' 1.26''
jb2	588100,00	4017432,64	36° 17' 52.29''	15° 58' 52.28''
jb3	587952,34	4017329,19	36° 17' 48.98''	15° 58' 46.32''
jb4	587750,02	4017649,99	36° 17' 57.35''	15° 58' 38.16''
1	588265,15	4017645,97	36° 17’ 59.1576”	15° 58’ 58.998”
2	588354,75	4017647,30	36° 17’ 59.1684”	15° 59’ 2.587”
3	588188,70	4017634,36	36° 17’ 58.8048”	15° 58’ 55.927”
4	588260,07	4017553,75	36° 17’ 56.166”	15° 58’ 58.757”
5	588384,25	4017557,75	36° 17’ 56.2524”	15° 59’ 3.736”
6	588427,04	4017668,20	36° 17’ 59.8236”	15° 59’ 5.496”
7	588345,25	4017759,11	36° 18’ 2.8008”	15° 59’ 2.252”
8	588230,88	4017741,23	36° 18’ 2.2572”	15° 58’ 57.662”
9	588108,81	4017638,05	36° 17’ 58.9488”	15° 58’ 52.72 ”
10	588149,92	4017547,16	36° 17’ 55.986”	15° 58’ 54.336”
11	588214,94	4017490,19	36° 17’ 54.1176"	15° 58’ 56.921”
12	588329,09	4017472,98	36° 17’ 53.52”	15° 59’ 1.489”
13	588045,77	4017640,32	36° 17’ 59.046”	15° 58’ 50.2”
14	588052,96	4017564,10	36° 17’ 56.5692”	15° 58’ 50.455”
15	588096,43	4017480,65	36° 17’ 53.8476”	15° 58’ 52.165”
16	588180,30	4017415,46	36° 17’ 51.702”	15° 58’ 55.502”
17	588262,58	4017380,65	36° 17’ 50.5464”	15° 58’ 58.786”
18	587954,46	4017577,47	36° 17’ 57.0372”	15° 58’ 46.513”
19	587981,51	4017491,29	36° 17’ 54.2292”	15° 58’ 47.561”
20	588038,79	4017420,38	36° 17’ 51.9108”	15° 58’ 49.829”
21	588108,74	4017366,43	36° 17’ 50.136”	15° 58’ 52.612”
22	588185,10	4017305,93	36° 17’ 48.1488”	15° 58’ 55.65”
23	587868,02	4017530,06	36° 17’ 55.5252”	15° 58’ 43.028”
24	587908,66	4017444,30	36° 17’ 52.728”	15° 58’ 44.623”
25	587948,41	4017371,67	36° 17’ 50.3592”	15° 58’ 46.186”
26	588016,79	4017310,39	36° 17’ 48.3468”	15° 58’ 48.904”
27	588094,95	4017262,14	36° 17’ 46.7556”	15° 58’ 52.018”
28	588191,68	4017229,89	36° 17’ 45.6792”	15° 58’ 55.88”
29	587802,84	4017471,23	36° 17’ 53.6388”	15° 58’ 40.393”
30	587883,39	4017346,43	36° 17’ 49.56”	15° 58’ 43.568”
31	587973,34	4017246,24	36° 17’ 46.2804”	15° 58’ 47.136”
32	588108,70	4017164,21	36° 17’ 43.5732”	15° 58’ 52.529”

Asbuilt Point Table

	WGS-84		UTM 33N			
Point Name	Latitude	Longitude	Northing	Easting	Depth	Heading
CableFound	N 36° 18' 49.46"	E 015° 57' 15.04"	4019169.87	585657.16	3451.4	N/A
Connectors	N 36° 18' 21.14"	E 015° 57' 51.41"	4018306.52	586572.77	3460.1	N/A
StrainRelief	N 36° 17' 50.73"	E 015° 58' 38.17"	4017381.22	587748.43	3461.3	N/A
CableSplice	N 36° 17' 49.94"	E 015° 58' 39.56"	4017357.11	587783.21	3461.3	N/A
CableSplice1	N 36° 17' 48.80"	E 015° 58' 41.40"	4017322.32	587829.5	3461.2	N/A
CTF	N 36° 17' 48.34"	E 015° 58' 42.25"	4017308.51	587850.81	3462.1	N/A
TowerBase	N 36° 17' 48.12"	E 015° 58' 45.06"	4017302.54	587920.93	3461.4	266.1°
Tripod	N 36° 17' 42.41"	E 015° 59' 00.00"	4017130.28	588285.42	3461.3	N/A
Reflector	N 36° 17' 47.22"	E 015° 58' 44.16"	4017274.53	587898.88	3462.1	N/A
Hazard_Line	N 36° 17' 46.97"	E 015° 58' 44.61"	4017266.96	587910.14	3461.8	N/A

Figure 3.11: Layout of the first detection units in the Capo Passero site. Green and red dots correspond to towers and strings respectively.

The KM3NeT detection lines production and installation in the Italian and French site is foreseen between the end of 2014 and the beginning of 2015.

Depending on the site, the KM3NeT building blocks will be situated at a latitude λ between 36° and 43° North, allowing in any case to observe upgoing neutrinos from most of the sky. In fact, thanks to the rotation of the Earth, declinations below $-90° + \lambda$ are always visible, while those above $+90° - \lambda$ are never visible. Declinations between these two values are visible for part of the sidereal day. The KM3NeT sky coverage is depicted in fig. 3.12. Most of the Galactic plane, including the Galactic centre, is visible most of the sidereal day. This is a great advantage for the detector since many source of interest for the neutrino astronomy are located in the Galactic plane. KM3NeT will thus ideally complement the field of view of Icecube, which is already taking data at the South Pole.

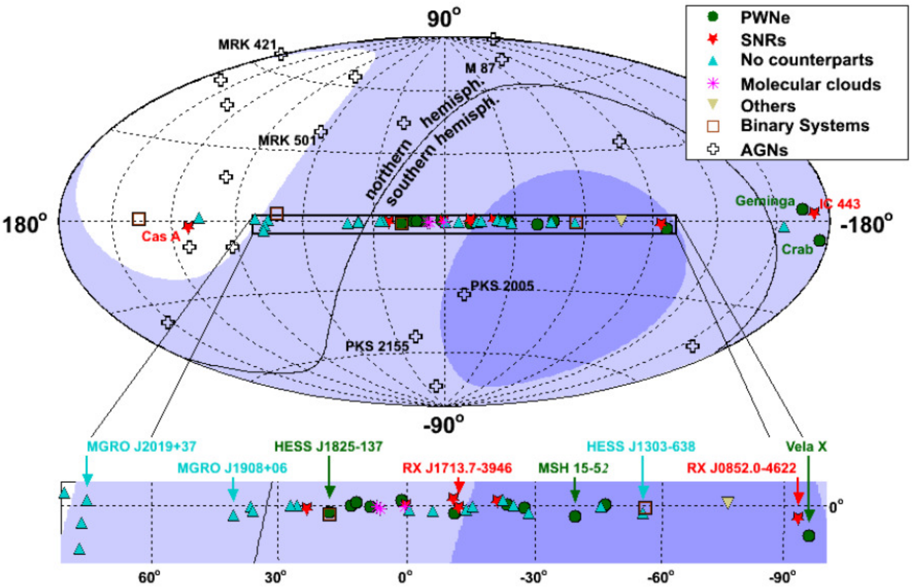

Figure 3.12: Sky coverage in Galactic coordinates for a detector located in the Mediterranean Sea and at the South Pole. The shading indicates the visibility for a detector in the Mediterranean with 2π downward coverage; dark (light) areas are visible at least 75% (25%) of the time. The locations of recently observed sources of high energy gamma-rays are also indicated.

CHAPTER 4

SOFTWARE SIMULATION TOOLS

In general, Monte Carlo simulation tools are necessary for understanding the effect of detector systematics and for being able to interpret the data recorded by a detector. Especially during the design phase of KM3NeT, where no real working detector does exist, Monte Carlo simulations are the only way to properly compare different possible design options and to evaluate their physics potential.

The software used in this thesis has been developed by the ANTARES Collaboration [162] and adapted to km^3-scale detectors. The code provides a complete simulation of the incident muon neutrinos, including their interaction in the medium and the propagation of the resulting secondary particles, the light generation and propagation in water and the detector response. The depth and the optical water properties measured at the Sicilian Capo Passero site have been used [160]. Background light due to the presence of ^{40}K in salt water and bioluminescence has been simulated adding an uncorrelated hit rate of 5 kHz per PMT and a time-correlated hit rate of 500 Hz per DOM (two coincident hits in different PMTs inside the same DOM) due to the genuine coincidences from Potassium decays.

The codes are written in `C++` and `fortran` languages. The output of each code is an ASCII-based text file that will be the input of the next code in the chain. A scheme of the simulation chain is shown in fig. 4.1. The code `GENDET` is used for the generation of the detector geometry. Then, atmospheric or signal muon neutrinos are generated trough `GENHEN` while atmospheric muons are generated with `MUPAGE`. The muon propagation through the detector and the generation of the hits due to Čerenkov

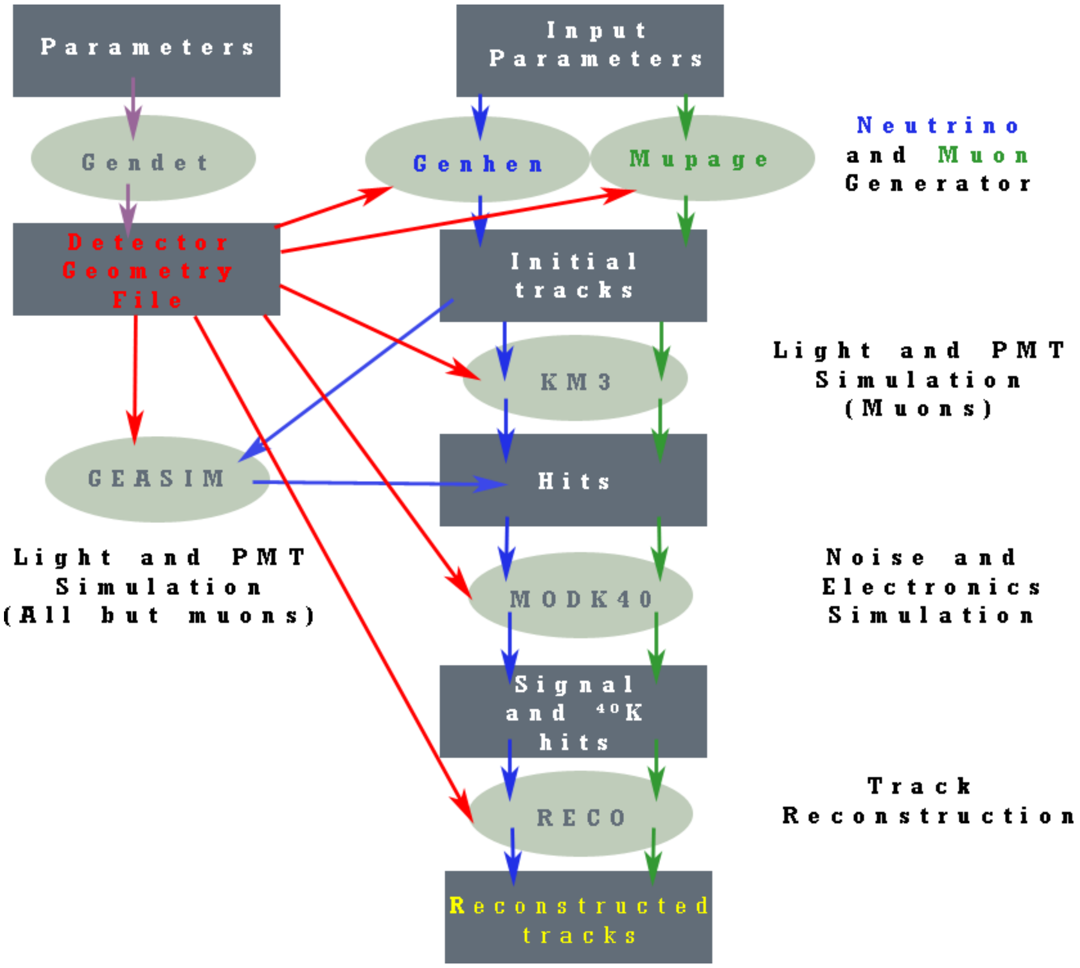

Figure 4.1: Scheme of the codes used to simulate the events in ANTARES and KM3NeT.

photon is provided by `KM3`. The other secondary particles generated at the interaction vertex and the consequent generation of hits due to Čerenkov photons is performed through `GEASIM`. The noise hits due to ^{40}K uncorrelated background are added using `MODK40`. Finally, the track is reconstructed.

In the following the single steps for a complete MC simulation will be described, while the reconstruction code will be discussed in detail in Chapter 5.

4.1 The detector geometry

The code `GENDET` [163], that is the first step of the simulation, generates an ASCII file with a complete information of the detector geometry. User can specify the kind of footprint of the detector (square, hexagonal or custom defined), its geographic coordinates, the spatial coordinates of PMTs and the list of all constitutive components (buoy, tubes, OM, etc) with their main characteristics. A footprint on sea-bed of one of the detector layouts simulated in this thesis is shown in figure 4.2. All the simulations presented in this thesis use the geographic coordinates (36° 16′ N 06° 10′ E) and the depth (3500 m) of the Capo Passero site.

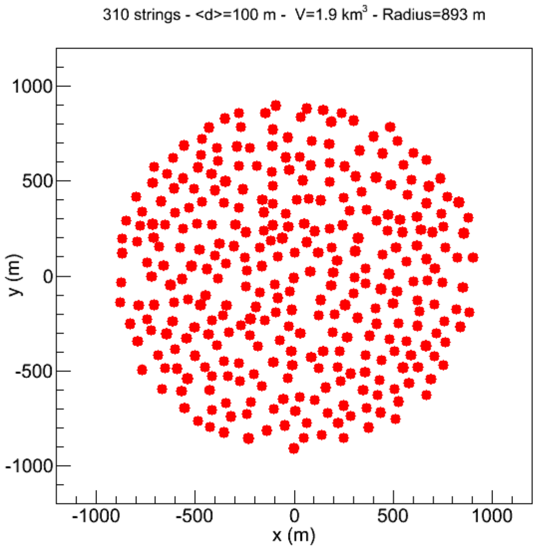

Figure 4.2: Footprint of the detector geometry with 310 DU having an average distance of 100 m.

4.2 Neutrino event generation: GENHEN

The `GENHEN` code is used to generate the neutrino-induced muon flux at the detector. This program includes a complete simulation of incident neutrinos, their interactions in the medium and of the resulting secondary particles up to neutrino energies of 10^8 GeV. Produced muons are propagated to the detector and their energy loss is calculated in the process.

Since the cross-section of the CC interaction is very small, simulating all the neutrino events would be disadvantageous in terms in cpu-time. Therefore, the code generates only neutrinos that interact inside or near the detector and are able to produce detectable muons. A cylindrical volume containing the instrumented volume of the detector, extended by three times the light absorption length in water is defined as the so-called *can* (see fig. 4.3). In the generation presented here the absorption length measured at the Capo Passero site $\lambda_{abs} = 70$ m is assumed. The *can* represents the Čerenkov-sensitive volume, such that photons produced beyond it have neglectable probability to reach a PMT and produce signals.

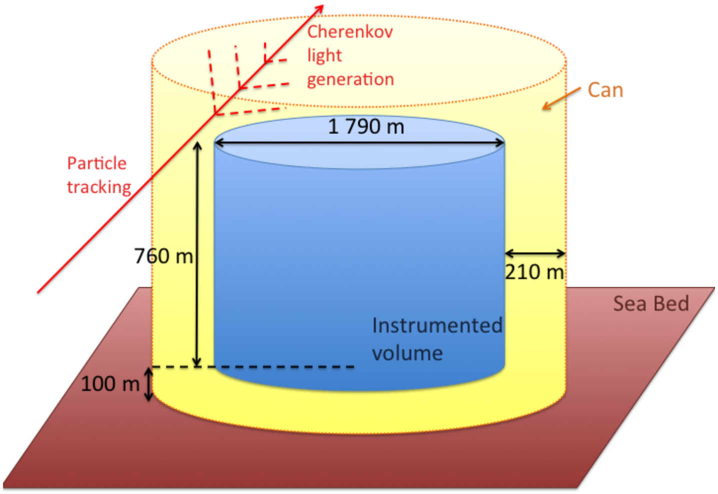

Figure 4.3: Overview of the detector geometry for the event simulation used in `GENHEN`. Neutrino interactions are generated in a large volume (tens of kilometres). The resulting muons are propagated to the can (yellow); only inside it the Cherenkov light and the detector response are simulated.

Analogously, the generation volume (V_{gen}) is defined as the volume beyond which a muon has neglectable probability to reach the *can*. The size of V_{gen} strongly depends on the maximum energy of the generated spectrum (E_{max}), on the corresponding maximum muon range in water R_w and in rock R_r and on the angular range of the simulation. For a 360° simulation, the generation volume will be a cylinder surpassing the can by R_r in height for up-going events or $R_w \cos\theta_{max}$ for down-going events, and having R_w as radius.

Neutrinos with energies according to a user defined power law spectrum are generated within this volume and their interactions are simulated, taking into account the different media, rock and water, around the detector. The neutrino direction is sampled isotropically in a user defined zenith angle range, or can be produced according to a point source with a given declination. The neutrino interactions are then simulated using LEPTO [164] (for deep inelastic scattering) and RSQ [165] (for resonant and quasi-elastic events). If interaction vertex is outside the can, the shortest distance from the neutrino vertex position to the can is calculated. If this distance is greater than the maximum muon range at that neutrino energy, no muon produced by this neutrino will ever reach the can and the event is rejected with no further processing. For the remaining events with the interaction vertex inside the can, all the particles produced in the interaction are recorded (position, direction, energy, etc.) for further processing. On the other hand, if the vertex is outside the can, only the muon is kept and it is transported to the can using one of the muon propagation codes MUSIC [166], MUM [167] or PropMu [168].

4.2.1 Neutrino fluxes and event weights

The procedure described can generate events starting from a specific energy spectrum $E^{-\gamma}$. Anyway is possible to reweight the flux with another spectrum. In order to obtain the rate of event corresponding to a differential flux of a specific model

$$\Phi^{mod}(E_\nu, \theta_\nu) = \frac{d\phi_\nu^{mod}}{dE_\nu d\Omega dS dt}, \tag{4.1}$$

the events generated with E_ν and θ_ν in a given interval $dE_\nu d\theta_\nu$ have to be reweighted with the ratio between the model flux and the generated flux:

$$W_{event} = \frac{\Phi^{mod}(E_\nu, \theta_\nu)}{\Phi^{gen}(E_\nu, \theta_\nu)} \tag{4.2}$$

The flux of simulated interacting neutrinos arriving at the Earth is:

$$\Phi^{gen}(E_\nu, \theta_\nu) = \frac{d\phi_\nu^{gen}}{dE_\nu d\Omega dS dt} = \frac{N_{tot}}{V_{gen} I_\theta I_E E^X \sigma(E_\nu) \rho N_A t_{gen} P(E_\nu, \theta_\nu)} \tag{4.3}$$

where the following parameters are used:

- V_{gen} $[m^3]$: is the total generation volume.
- $I_\theta[sr]$ the angular phase space factor $2\pi \cdot [cos(\theta_{max}) - cos(\theta_{min})]$ where θ_{max} and θ_{min} are the maximum and minimum angles of generation.
- I_E the energy space factor, equal to $(E_{max}^{1-\gamma} - E_{min}^{1-\gamma})/(1-\gamma)$ (where E_{max} and E_{min} are the maximum and minimum energies of generation) and to $ln(E_{max}/E_{min})$ for $\gamma = 1$.

- $\sigma(E)$ $[m^2]$ the total neutrino cross-section for energy E.
- $\rho \cdot N_A$ the number of target nucleon per m^3 (N_A is the Avogadro's constant $N_A = 6.022 \times 10^{23} mol^{-1}$). The code works in unity "water equivalent" , fixing to one the density of all material and dividing the physical distances for the effective density.
- P_{Earth} is the probability for the neutrino to penetrate the Earth and vary from 0 to 1. It is defined as $P_{Earth}(E_\nu, \theta_\nu) = e^{-N_A \sigma(E_\nu) \rho_\theta}$, where ρ_θ is the amount of matter that the neutrino encounters.
- t_{gen} is the generation time (arbitrary).
- N_{tot} is the total number of generated events.

From eq. 4.2 and eq. 4.3 it follows that:

$$W_{event} = \frac{\Phi^{mod}(E_\nu, \theta_\nu)}{\Phi^{gen}(E_\nu, \theta_\nu)} = \frac{V_{gen} I_\theta I_E E^X \sigma(E_\nu) \rho N_A P(E_\nu, \theta_\nu)}{N_{tot}} \times \Phi^{mod}(E_\nu, \theta_\nu) \tag{4.4}$$

The quantity

$$W_{gen} = \frac{V_{gen} I_\theta I_E E^X \sigma(E_\nu) \rho N_A P(E_\nu, \theta_\nu)}{N_{tot}} \text{ [GeV m}^2\text{ sr sec]} \tag{4.5}$$

is independent from the particular flux choice and can be calculated in the generation phase. Then, to obtain a distribution of events corresponding to Φ^{mod}, the user has just to multiply the weight of each event to Φ^{mod}.

4.3 Generation of atmospheric muons

The generation of atmospheric muons can be performed using programs like `CORSIKA` [169] that allows a detailed simulation of extensive air showers initiated by high energy cosmic ray particles. Anyway, in order to save computing time, a fast MC generator is essential especially when the simulation is for a very large detector. The software used in this thesis is the `MUPAGE` [170] package that reduce at minimum the time of calculations. The program is developed from parametric formulas derived in [170], that describe the flux, the angular distribution and the energy spectrum of underwater muon bundles with maximum depth from 1.5 to 5 km w.e. and with zenith angles less than 85°. The parametrization of the interaction of cosmic rays and the propagation in the atmosphere up to the sea leve is based on HEMAS [171] code, while the propagation of muons until 5 km under the level of the sea was performed by MUSIC [166]. MUPAGE generates muons directly on a cylindrical surface with an high, radius and position defined by users (but usually it is used the same surface of the can in `GENHEN`). It's assumed that all the muon bundles are parallel to the axis of the shower and that they arrive at the same time into a plane perpendicular at the axis. For every N simulated events a "livetime" is estimated. The livetime is the interval of time in which the flux correspondent to N muons is produced in nature.

4.4 Propagation of particles and light production

Once that particles are generated they must be propagated through the volume. In order to take into account the light produced in water, we have three types of particles inside the can:

- Muons that are characterized by long, approximately straight tracks continuously losing energy and emitting Cherenkov photons. They also suffer stochastic losses which produce independent electromagnetic (EM) showers.
- EM showers that are either produced by bremsstrahlung photons from muons or by electrons at the neutrino interaction vertex. All their energy is deposited in a short distance (on the scale of the detector) and can generally be considered point-like. They contain a large number of electrons and hence, statistically, showers of a similar energy all have similar properties.
- Hadrons at the neutrino interaction vertex, that have complex decay chains and the amount of light they produce depends on the primary particle and its particular set of decays. In addition, they may produce muons in the final state which may travel a significant distance. Hence, they are not amenable to parametrization in the same way electrons and muons are.

The codes that propagate and simulate light are `KM3` and `GEASIM`.

4.4.1 KM3

`KM3` [172] is used to generate the light produce by the muon. The code takes into account all the muon interaction mechanisms with matter (multiple scattering, ionization, bremsstrahlung, couple production, anelastic scattering,...), its energy loss and Čerenkov photons emission, with all the related absorption and diffusion procesesses in the sea water. The produced photons are then propagated to the OMs. Simulating each single photon would take huge CPU time. This is avoided by generating absorption and diffusion photon tables with different photon energies and then using interpolations on these premade tables. These tables also contain the OM properties and have to be re-calculated for each type of OM that is considered.

The `KM3` package is divided into three subpackages:

1. `GEN`: Generates "photon fields" at various radii from a muon track segment or an electromagnetic shower;
2. `HIT`: Transform the photon fields from GEN into "hit probability distributions" in a photomultiplier tube;
3. `KM3MC`: A detector simulation program which uses the hit probability distributions generated in `HIT` along with a geometrical description of the detector to simulate events in it.

GEN

GEN simulates the generation of Cherenkov light by a particle in a given medium (in this case water), including light from any secondary particles. A complete GEANT3.21 [173] simulation is used at this step. GEN tracks the Cherenkov photons through space with wavelength-dependent absorption and scattering taken into account (see fig. 3.10), recording the position, direction and arrival time of photons at spherical shells of various radii. Its output consist of:

- A table containing all the photons recorded in each spherical shell.
- An ASCII file containing the information relevant to the simulation (particle type, energy, number of processed events, track length, medium type, number of events stored in each shell, water model used, etc.)

HIT

Using the photon fields created by GEN, HIT creates the Optical Module hit distributions for muon track segments and EM showers.
The hit position, direction, energy and time are read shell by shell and stored. Since a large number of hits is recorded for each shell, these shells are divided in bin of $\cos(\theta)$ (see fig. 4.4). For each bin in $\cos(\theta)$ the flux of photons is weighted by the PMT effective area and orientation. The PMT effective area is given by:

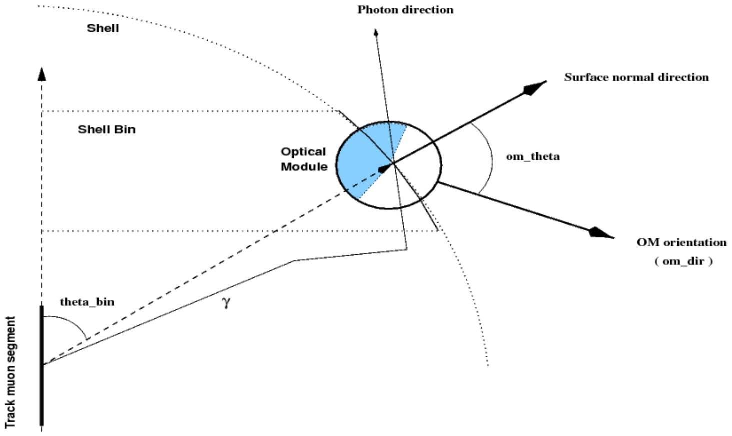

Figure 4.4: A schematic diagram of the geometry used to generate the photon tables.

$$A_{eff}^{OM} = A_{geom}(\theta_{OM}) \times QE(\lambda) \times CE \times P_{trans}^{glass}(\lambda, \theta_{OM}) \times P_{trans}^{gel}(\lambda, \theta_{OM}) \tag{4.6}$$

where λ is the photon wavelength, $QE(\lambda)$ is the quantum efficiency (the probability that a photon generates a photoelectron inside the PMT), CE is the collection efficiency (the probability that an electron into the PMT be accelerated until the first photocathod) and finally P_{trans}^{glass} and P_{trans}^{gel} are the transmissions probability for the glass and the gel that constitutes the OM.

KM3MC

Finally `KM3MC` first reads the users inputs and the output of `HIT`. Muons are than propagated through the can volume with the `MUSIC` package, generating segment of track (of the same dimension of those used by `GEN`) until the muon stops or leave the detector. If the energy loss is greater than a threshold value, an EM shower is generated in a random position of the segment track.

From tracks parameter and showers (initial and final position, direction, time of occurrence) and from photon tables are obtained the signal "hits". Every hit is characterized by the identification of PMT involved, by the number of deposited photoelectrons (p.e.) and by the photon arrival time.

4.4.2 GEASIM

`GEASIM` [174] is a `GEANT3.21` based full simulation propagator and deals with all the products of the neutrino interaction. In this full simulation work `KM3` is used as muon propagator and `GEASIM` has been set to take into account the hadronic showers produced at the interaction vertex. Each shower is treated up to its final products, but no light scattering is included. This detailed particle tracking greatly increases the cpu-time and it actually has an important role only in the "low" energy range (less then 1 TeV), therefore it is used only for the low energy study discussed in Chapter 7.

4.5 Generation of optical background: `MODK40`

Once the muon-induced photon hits are stored, `MODK40` is used to add spurious hits due to the submarine optical background discussed in section 2.1.5. `MODK40` permits to generate random hit with a frequency defined by users in an interval of time $\Delta t = (t_f - t_l) + 2t_O$, where t_f and t_l are the arrival times of the first and the last hit of the event respectively and t_O the delay to add before and after the simulated event (in the simulations presented in this thesis $t_O = 1000$ ns). `MODK40` can also simulate the digitalization of the detector. It can transform the light simulated Cherenkov photons with optical background into a electronic signal with the appropriate gain factors and electronic noise.

A random background rate of 5 kHz is assumed for each PMT, including dark current, ^{40}K decays, and bioluminescence. In addition to random coincidences, an L1(two coincident hits in different PMTs inside the same DOM) rate of 500 Hz is assumed, due to genuine coincidences from potassium decays. The probabilities for each pair of PMTs inside a multiPMT to produce such a coincidence is shown in figure 4.5.

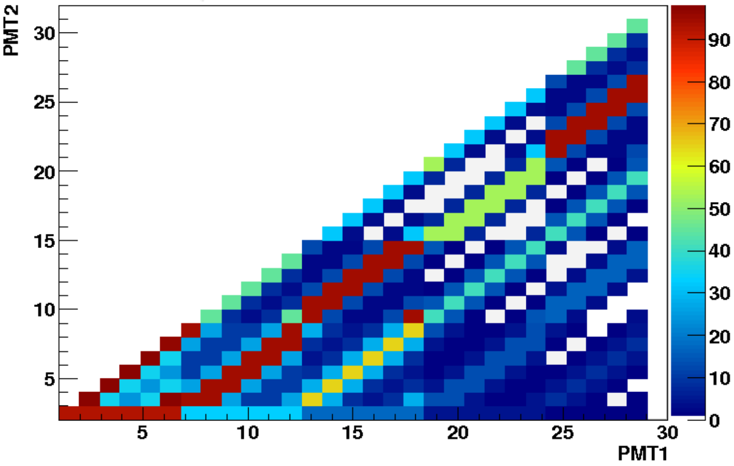

Figure 4.5: Probabilities (unit 10^{-4}) of a genuine coincidences due to potassium decays as a function of the PMT number in a multiPMT optical module.

CHAPTER 5

MUON TRACK RECONSTRUCTION

The track reconstruction algorithm permits to estimate muon (and consequently neutrino) directions using the combined information of the PMT spatial positions and the Cherenkov photon arrival times. The reconstruction code used in this work is based on the strategy described in [175] but it has been radically modified to exploit the multi-PMT peculiarities. The original code was written for a detector using large area PMTs (8-10 inch). The DOM developed by the KM3NeT collaboration has instead 31 small (3 inch) PMTs localised in a 17″ sphere (see sec. 3), and thus it requires to substitute the charge information with the multiplicity of hits on the same DOM, studying a specific hit selection and taking into account the PMT directional sensitivity.

After an initial hit selection, requiring space-time coincidences between hits, the reconstruction proceeds through four consecutive fitting procedures, each using the result of the previous one as starting point. The first step, called prefit, is a linear fit and therefore does not require an input track. Each fitting stage helps in getting close to the true track. In fact, the last fit produces the most accurate result, but it works well only if it receives as input an estimate of the muon track parameters that is not too far from the true track parameters. Moreover, the efficiency of the algorithm is improved with a scanning of all sky in steps of 3° starting from the prefit track, thus generating 7200 tracks. For each direction the fitting procedures are performed and the solution with the highest likelihood per degree of freedom is chosen as the best one. A scheme is shown in fig. 5.1.

All the plots presented in this chapter refer to a detector made of 310 strings, each

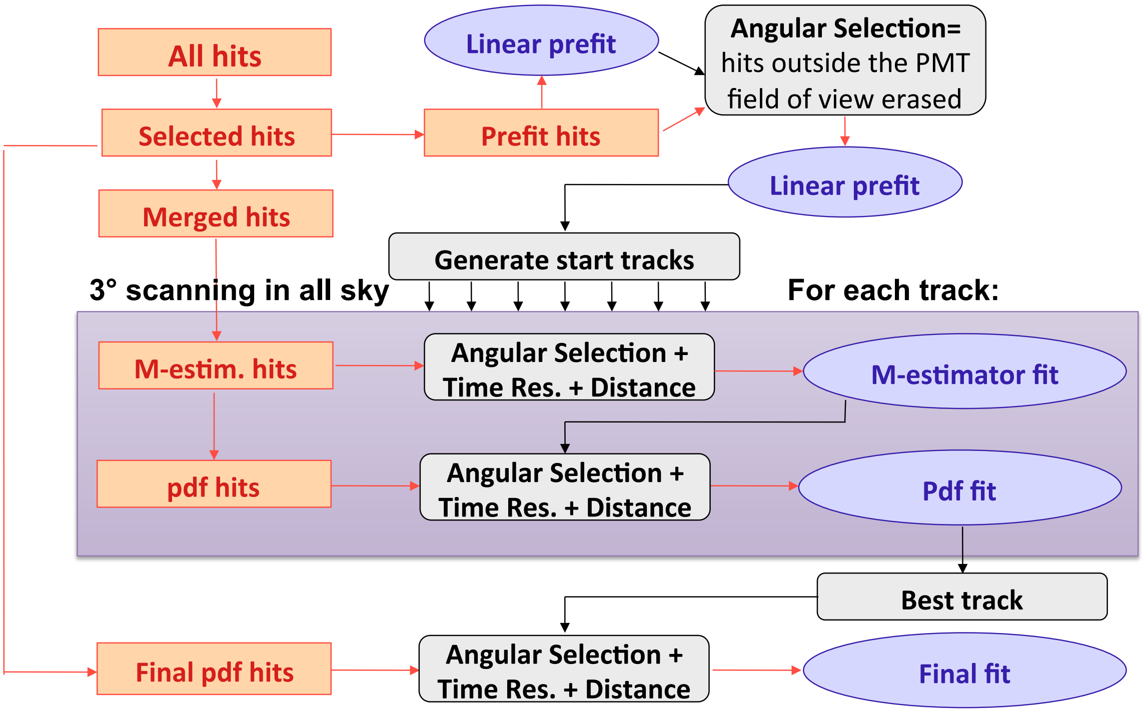

Figure 5.1: Schematic depiction of the reconstruction algorithm.

one equipped with 20 DOM vertically aligned at a distance of 40 m between each other. The distribution of the strings on the seabed is roughly circular with an average distance between strings of 100 m (see fig. 4.2). In these simulations muon neutrinos are generated with an energy ranging from 100 GeV to 100 PeV. The optical background due to the presence of ^{40}K in salt water has been simulated adding an uncorrelated hit rate of 5 kHz per PMT and a time-correlated hit rate of 500 Hz per DOM (two coincident hits in different PMTs inside the same DOM).

5.1 Track description

The algorithm described here is designed for the reconstruction of muon tracks with energies above about 100 GeV. A version of the code optimised for the low energy regime is discussed in Chapter 7.

Muons with $E_\mu \gtrsim 100$ GeV can traverse the whole detector. Both angular deviation of the muon track from a straight line (due to multiple scattering) and the deviation of the muon velocity from the velocity of light in the vacuum c (due to finite energy) are very small and therefore will be neglected. Muon tracks can be characterised by the position $\mathbf{P} \equiv (p_x, p_y, p_z)$ of the muon at a fixed time t_0 and its normalised direction $\vec{d} \equiv (d_x, d_y, d_z)$, that can be parameterised in terms of the azimuthal and zenithal angles ϕ and θ: $\vec{d} \equiv (sin\theta cos\phi, sin\theta sin\phi, cos\theta)$. The task of a reconstruction algorithm is to provide an estimate of the five parameters $p_x, p_y, p_z, \theta, \phi$ and a track fit quality parameter that can be used to reject badly reconstructed events. There is not a dedicated algorithm to calculate the muon energy but, for the analysis on point like source, the number of selected hits is adopted as an energy estimator.

One of the most important quantities used in the reconstruction is the so called "time residual", defined as the difference between the expected time of arrival t^{th} of the photon on the PMT and the recorded hit time t_i. The time residual is calculated under the assumptions that the event starts at a time t_0, the muon travels on a straight line with speed c and the Cherenkov light is emitted at a Cherenkov angle $\theta_C \sim 42°$ with respect to the muon direction with a speed c/n, where n is the refractive index in the medium ($n \sim 1.35$). Fig. 5.2 shows a sketch of the track description employed in the reconstruction. Defining $\vec{v} = \mathbf{Q}_i - \mathbf{P}$ as the vector that goes from the point $\mathbf{P}$ to the hit position $\mathbf{Q}_i$, the expected arrival time of the photon on the PMT can be written as a function of the components of $\vec{v}$ parallel and perpendicular to the muon direction, that are respectively $l = \vec{v} \cdot \vec{d}$ and $k = \sqrt{|\vec{v}|^2 - l^2}$. In fact, the distance from $\mathbf{P}$ to the point $\mathbf{P}_i$ where the light is emitted, is

$$\overrightarrow{\mathbf{PP}_i} = l - (k/\tan\theta_C),$$

while the path travelled by the photon to reach the PMT is

$$b = k/\sin\theta_C.$$

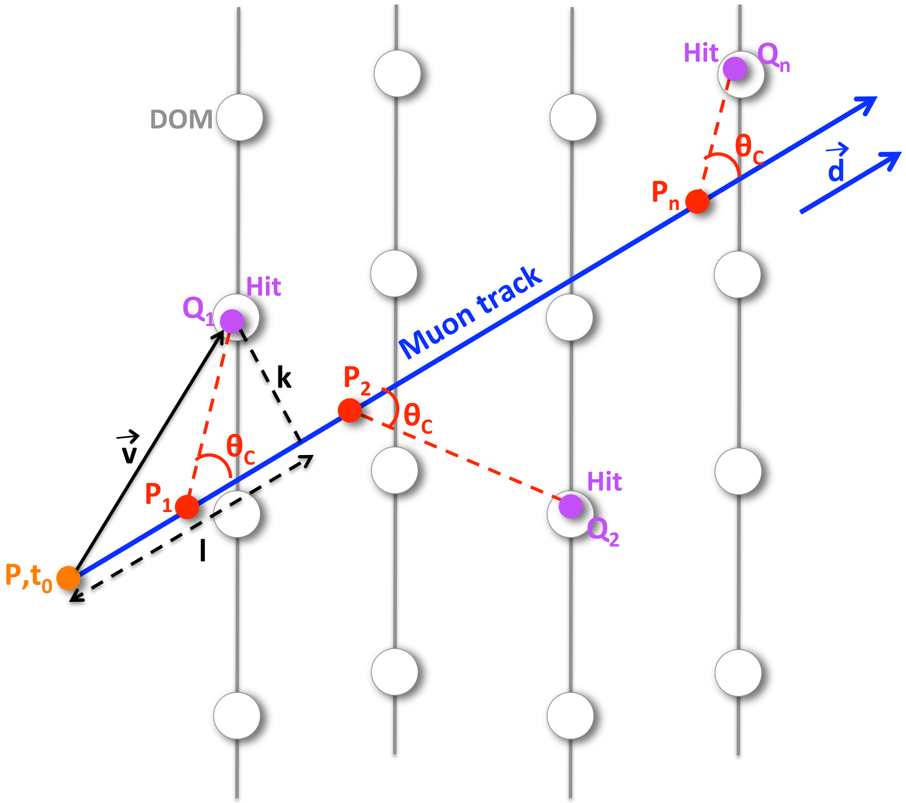

Figure 5.2: Description of the geometry for the detection of the Čerenkov light emitted by a muon (blue line) that goes trough the point $\mathbf{P}$ (orange point) in direction $\vec{d}$. The Čerenkov light (red dashed lines) reaches the PMTs located in points $\mathbf{Q}_i$ (lilac points).

Therefore, the arrival time of the light in $\mathbf{Q}_i$ is given by

$$t^{th} = t_0 + \frac{1}{c}\left(l - \frac{k}{\tan\theta_C}\right) + \frac{1}{c/n}\left(\frac{k}{\sin\theta_C}\right). \tag{5.1}$$

Note that, knowing the time t_i and the position of each hit $\mathbf{Q}_i$, the time residual $r_i = t_i - t_i^{th}$ depends only on the parameters $\mathbf{P}$ and $\vec{d}$.

Another quantity that characterises the Cherenkov light emission is the expected angle of incidence θ_i of the photon on the PMT, i.e. the angle between the direction of the photon and the pointing direction of the PMT (see fig. 5.3). Assuming the emission at the Cherenkov angle θ_C, $a = \cos\theta_i$ can be calculated as

$$a = \left[\vec{v} - \vec{d}\left(l - \frac{k}{\tan\theta_C}\right)\right] \cdot \vec{w} \tag{5.2}$$

where $\vec{w}$ is the normalised direction of the PMT axis. For a head-on collision of a photon with the photocathode $a = -1$, whereas $a = 1$ means that the photon hits the insensitive rear of the PMT.

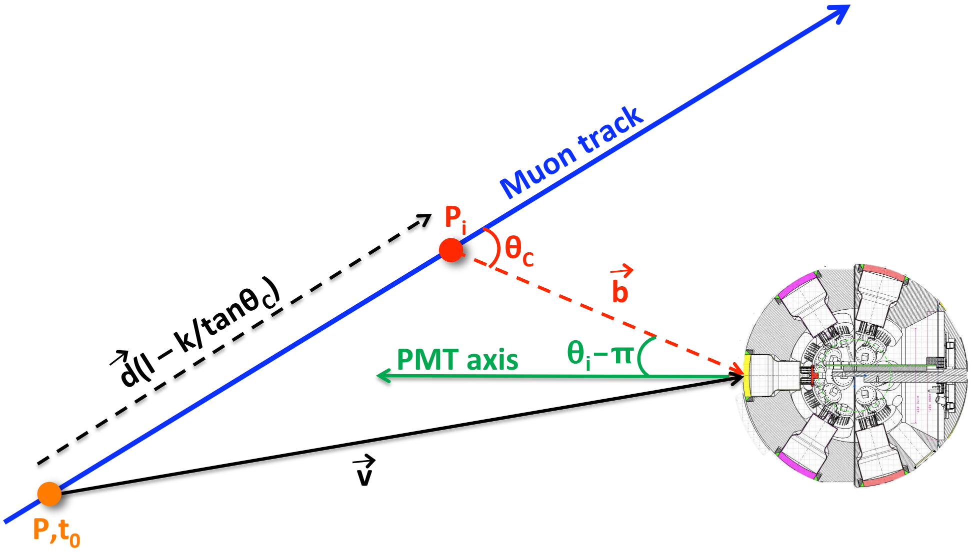

Figure 5.3: Scheme showing how the expected angle of incidence θ_i of the photon on the PMT can be calculated (see text).

5.2 Hit selection

Hits from ^{40}K added to the signal hits make the track reconstruction more complex, therefore a hit selection is required before the actual reconstruction starts. The requirement of space-time coincidences between the hits can be a simple and efficient way to perform this task, since hits due to optical background are uncorrelated. In particular, the code examine all hits to look for the following patterns:

L1 simple coincidence between 2 PMTs on the same OM in a time window Δt $=$ 10 ns;

T0 coincidence between a hit part of an L1 coincidence, and a simple hit on adjacent or next-to-adjacent OMs on the same string in a time window Δt $=$ 10 ns $+2t_d$, where t_d is the time required by the light to travel the distance d between the two hits;

N1 coincidence between 2 hits part of 2 L1 coincidences on OMs on nearby strings, in a time window Δt $=$ 10 ns $+2t_d$;

T1 the same condition of T0 but between 2 L1 hits;

L2 simple coincidence between 3 PMTs on the same OM in a time window Δt $=$ 10 ns;

L3 simple coincidence between 4 or more PMTs on the same OM in a time window Δt = 10 ns;

Each coincidence pattern gives a "score" to the corresponding hit. The hierarchy of the coincidence patterns is chosen on the basis of the probability that the considered pattern can be randomly generated by the background hits (L1 < T0 < N1 < T1 < L2 < L3). In fact, this probability can be calculated analytically or from the simulations, resulting to be about 67% for L1, 35% for T0, 2.6% for N1, 2% for T1, 0.7% for L2 and 0.08% for L3 in the case of an optical background given by an uncorrelated hit rate of 5 kHz per PMT and an L1 hit rate of 500 Hz per OM. The score is stores as 6 bit pattern with L1 $\Rightarrow 2^0$, T0 $\Rightarrow 2^1$, N1 $\Rightarrow 2^2$, T1 $\Rightarrow 2^3$, L2 $\Rightarrow 2^4$, L3 $\Rightarrow 2^5$. As an example, a hit having a coincidence L1 but also T1, will gain a score $2^0 + 2^3 = 9$. Converting the final score in a binary number the original patterns can be easily recalled.

The event is processed only if there are at least 3 OMs with L1 hits or if there is a T1 or N1 or L2 coincidence. For the accepted events, the hit with the highest score is chosen as the "reference hit", h_{ref}. In 99.6% of the events the h_{ref} turns out to be a signal hit. All the other hits have to be in a causality relation with the reference hit, therefore a "Causality Filter" can be applied to reject background hits. If Δt e Δr are the time delay and space distance between each hit and the reference hit, the Causality Filter requires that

$$|\Delta t| - \frac{\Delta r}{v} < 20ns \quad \cap \quad \left| |\Delta t| - \frac{\Delta r}{c} \right| < 500ns \tag{5.3}$$

where v is the group velocity of light in water.

The first equation of 5.3 requires that the hit time delay $|\Delta t|$ is compatible (within a time window of $20ns$) with the time taken by the Čerenkov wave front, which is moving with velocity v, to cover the distance Δr (see Fig. 5.4a). The second condition takes into account that, in case of large distances, light absorption doesn't allow the Čerenkov photon to move far from the initial muon track (see Fig. 5.4b). In this case, Δt is compared with the time taken by the muon, which moves with velocity c, to cover the distance Δr.

Hits that fulfil the condition 5.3 are called *Selected hits*, while all the other hits are discarded. Fig. 5.5 shows the effect of this selection in terms of efficiency and purity. If $Nhit_{sig}$ is the total number of signal hits in the event, $Nhit_{sig}^{sel}$ is the number of signal hits

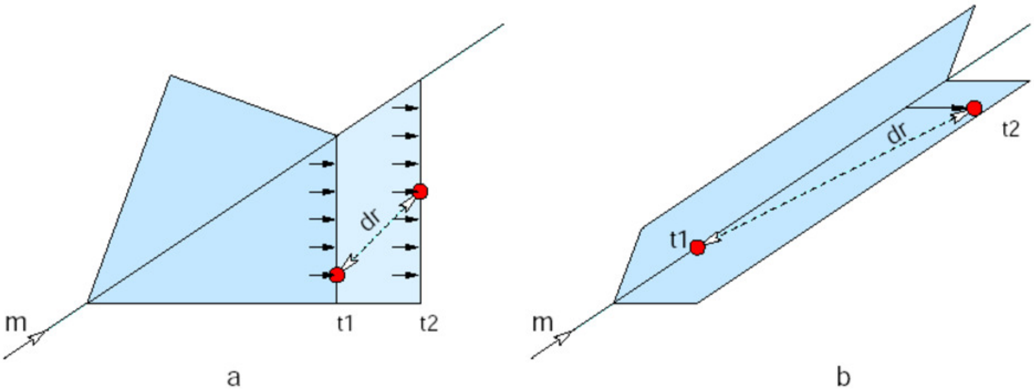

Figure 5.4: Scheme of Čerenkov light propagation to explain reco causality filter. In the case *a*, *hits* are close and belong to the same wave front. On the contrary, in the case *b*, distant *hits* can be correlated to the muon track.

in the set of selected hits and $Nhit^{sel}$ is the total number of selected hits, the efficiency and purity can be defined as:

$$efficiency = \frac{Nhit^{sel}_{sig}}{Nhit_{sig}} \quad , \quad purity = \frac{Nhit^{sel}_{sig}}{Nhit^{sel}} \tag{5.4}$$

In fig. 5.5 the purity of the initial hit set is also reported as reference. This result shows that the causality filter allows to keep 90% of the signal hit with a purity increasing with energy from 6% to 30%. Even if the contamination of background hits is still high, with this first selection the purity is enhanced by one order of magnitude with respect to the initial hit set at low energies and it is tripled at higher energies.

The following step is the merging of the *Selected hits* on the same PMT that are separated by less then 20 ns, obtaining as result the list of the *Merged hits*.

5.3 Prefit - Step 1

The first step in the track reconstruction procedure is the “linear prefit”. This is a linear fit through the positions of the hits. Although not very accurate, it has the advantage that it requires no starting point.

In order to obtain a linear relation between the hit positions and the track parameters, it is assumed that the hits occur on points that are located along the muon track. This is expected to be a reasonable approximation if the length of the muon track in the detector is much larger than the attenuation length of the light. If $\mathbf{Q}_i \equiv (x_i, y_i, z_i)$

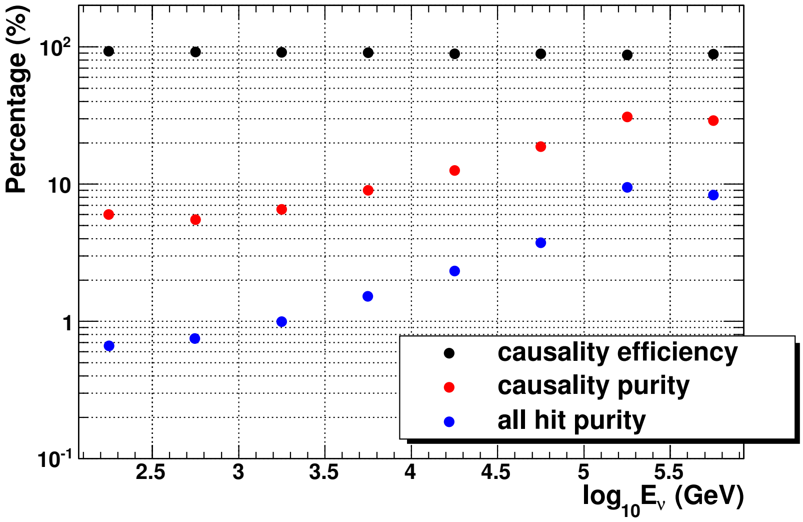

Figure 5.5: Efficiency and purity of the causality filter as a function of the neutrino energy (see text). The purity of the initial hit set is shown for reference.

is the position of a given hit occurring at a time t_i and the track is parametrised as a point on the track $\mathbf{P} \equiv (p_x, p_y, p_z)$ and a set of director cosines $\vec{d} \equiv (d_x, d_y, d_z)$, the linear relation between the hit positions and the track parameters is:

$$\begin{cases} x_i = p_x + d_x c t_i \\ y_i = p_y + d_y c t_i \\ z_i = p_z + d_z c t_i \end{cases} \tag{5.5}$$

that can also be written as $\mathbf{Q}_i = f(t_i; \mathbf{P}, \vec{d}) = \mathbf{P} + \vec{d} c t_i$. Applying the least squares method, the track parameters $\mathbf{P}$ and $\vec{d}$ can be estimated as those that minimise the quantity

$$\chi^2 = \sum_{i=1}^{N} \frac{(\mathbf{Q}_i - f(t_i; \mathbf{P}, \vec{d}))^2}{\sigma_i^2}. \tag{5.6}$$

where σ_i are the errors on the hit positions. The σ_i are estimated from the Monte Carlo simulations calculating the average distance between the muon track and the PMTs as a function of the hit amplitude. It is assumed that the errors on the x, y and z components of the position of a given hit are equal.

The minimum of χ^2 is calculated setting its derivatives with respect to the parameters $\mathbf{P}$ and $\vec{d}$ equal to zero. Defining $w_i \equiv 1/\sigma_i$, the final value of the parameters are:

$$\mathbf{P} = \frac{\sum_i w_i \mathbf{Q}_i \sum_i w_i t_i^2 - \sum_i w_i t_i \sum_i w_i \mathbf{Q}_i t_i}{\Delta} \tag{5.7}$$

$$c\vec{d} = \frac{\sum_i w_i \mathbf{Q}_i t_i \sum_i w_i - \sum_i w_i t_i \sum_i w_i \mathbf{Q}_i}{\Delta} \tag{5.8}$$

where $\Delta = \sum_i w_i t_i^2 - (\sum_i w_i t_i)^2$.

The hits used to perform the "prefit", called *Prefit hits*, are a subset of the *Merged hits* having a score $> 2^0$ therefore coincidences more complex then L1. Once a first estimate of the parameters $\mathbf{P}$ and $\vec{d}$ is obtained, the evaluation for each hit of the expected angle of incidence θ_i of the photon on the PMT is possible using eq. 5.2. An "angular selection" is applied discarding all the hits with $\cos\theta_i > -0.5$. The prefit is then repeated with the new hit set. In any case, at least 3 hits are required to perform the fit, otherwise the event is descarded.

The angular selection allows to exploit the PMT directionality. As a reference, the angular acceptance of the PMTs is reported in tab. 5.1. For directions with $\cos\theta_i > -0.5$ it is less than 50%.

Table 5.1: Angular acceptance of the PMT, ϵ, including the effect of the expansion cone, for different values of the angle of incidence θ_i of the photon on the PMT.

$\cos\theta_i$	ϵ
-1.0	1.565
-0.95	1.453
-0.9	1.295
-0.85	1.149
-0.8	1.013
-0.75	0.903
-0.7	0.812
-0.65	0.738
-0.6	0.670
-0.55	0.615
-0.5	0.562
-0.45	0.506
-0.4	0.456
-0.35	0.404
-0.3	0.354
-0.25	0.309
-0.2	0.263
-0.15	0.220
-0.1	0.178
-0.05	0.138
0.0	0.101
0.05	0.069
0.1	0.041
0.15	0.019
0.2	0.004
0.25	0.000

The set of *Prefit hits* has a purity greater then 90%, as it can be seen in fig. 5.6, while the efficiency of the selection ranges from 52% to 76%.

5.4 Maximum Likelihood

The next fit procedures are based on the method of "maximum likelihood". Consider a random variable x distributed according to a probability density function (PDF)

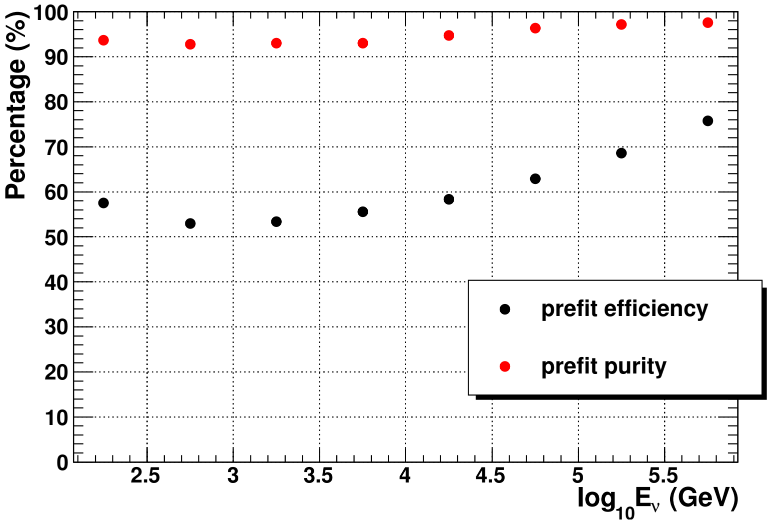

Figure 5.6: Efficiency and purity of the hit set used during the prefit phase.

$f(x|\theta)$, being $\theta = (\theta_1, \theta_2, ...\theta_m)$ a list of parameters. This means that performing an experiment to measure x, the probability of observing x in the interval $[x', x' + dx]$ is $f(x'|\theta)dx$. If the parameters θ are unknown and a set of n measurement $(x_1, x_2, \ldots, x_n)$ of x is available, the values of the parameters can be determined as those which maximise the probability of observing the measured data. Under the assumption that the measurements are independent, this probability is given by

$$L(x_1, x_2, \ldots, x_n|\theta) = \prod_i f(x_i|\theta) \tag{5.9}$$

and it is called "likelihood function".

In the case of the muon track reconstruction, we have to determine the track parameters $\mathbf{P}$ and $\vec{d}$ knowing the hits positions $\mathbf{Q}_i$ and their time t_i. The likelihood function is often written in terms of the time residuals $r_i = t_i - t_i^{th}$ (see sec. 5.1), therefore equation 5.9 can be re-written as :

$$L(event|track) \equiv L(hit|\mathbf{P}, \vec{d}) = \prod_i f(t_i, \mathbf{Q}_i|t_i^{th}) = \prod_i f(r_i). \tag{5.10}$$

Equivalently the parameters can be found by minimising the sum

$$-\,logL = -\sum_i log(f(r_i)) = -\sum_i g(r_i). \tag{5.11}$$

5.5 M-estimator Fit - Step 2

The functions $f(r_i)$ or $g(r_i)$ can be calculated fitting the time residual distributions extracted by the light production step of the Monte-Carlo procedure (sec. 4.4.1). However, a likelihood fit that uses the correct PDF has the disadvantage that finding the global maximum of the likelihood is often difficult. In fact, for large values of the residuals r, the PDF is a relatively flat function and therefore local maxima in the likelihood function can appear. This implies that it is crucial to start the maximisation procedure as close as possible to the true track parameters. On the other hand, the $f(r_i)$ can be chosen in such a way that the hypothesis which maximise L does not change too much when a small number of data points is not well described by $f(r_i)$. This quality is called robustness. The "M-estimators" are a well known class of robust estimators that include different forms of $f(r_i)$. A typical M-estimator is $g(r_i) = r^2$ that gives the least square method.

In particular, as intermediate step between the prefit and a maximum likelihood fit with a realistic PDF, a maximum likelihood fit based on a function $f(r_i)$ that describes the data for small residuals has been chosen. The behaviour of this $f(r_i)$ for large residual is a trade-off between a reproduction of the data and the ease of finding the global maximum. The likelihood function to be minimised in this step is

$$- logL = -\sum_i (-2\sqrt{1 + r_i^2/2} + 2) \qquad (5.12)$$

The function $g(r_i) = -2\sqrt{1 + r_i^2/2} + 2$ is shown in the left panel of fig. 5.7 labelled as "M-estimator", together with $-r^2$ and the realistic PDF used in the next fit step, referred as "logL". The three functions coincide for small values of r but behave very differently for large values. The performance of these different estimators is illustrated in the right panel of fig. 5.7 in terms of the angle $\Delta\Omega_{\mu,mest}$ between the generated muon track and the one fitted with the three estimators. In all the three fits the prefit track is used as starting point. The function chosen as M-estimator permits to gain 40% of events with $\Delta\Omega_{\mu,mest} < 1^\circ$ with respect to $-r^2$ and 30% with respect to $logL$.

The hits used for this fit, called (*M-estimator hits*), are selected among the *Merged hits* on the basis of the result of the prefit. In order to be selected, a hit must have a time residual between -150 and 150 ns and a distance from the prefit track less than 100 m or it has to be labelled as L3 hit. Moreover, the same angular selection described

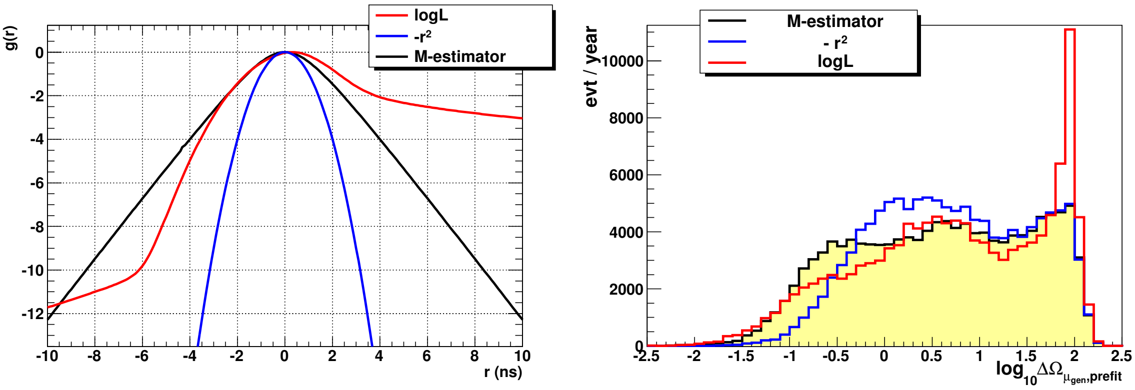

Figure 5.7: Left panel: Function used as M-estimator compared to $-r^2$ and to the function used in the next fit step. Right panel: logarithm of the angular distance, in degrees, between the generated muon track and the track fitted with the three functions shown in the left panel. Events are weighted with the atmospheric neutrino flux.

before is applied to the *M-estimator hits*, using the prefit track as reference track. If the set of *M-estimator hits* does not contain at least 6 hits, the fit cannot be performed.

5.6 Pdf Fit - Step 3

The third and fourth fitting procedures estimate the parameters of the track maximising likelihood functions, that have been parameterised by fitting a set of histograms obtained from Monte Carlo simulations of muons traversing the detector. The PDF of the third fit has been calculated not including background hits, while the one used in the fourth fit considers them. These likelihood functions remain the same as the original strategy [175], except for the amplitude dependence which has been neglected. Some attempts to adapt the PDF to the KM3NeT detector has been performed without positive results.

The likelihood function used in the third fitting procedure is shown if fig. 5.8. It has 3 different functional forms depending on the time residual value.

$$g(r) = \begin{cases} 0.5(\log(1 + r^2/\sigma^2)) + c - \log(a_2) - l_2 r & \text{, if } r < -10 \text{ ns} \\ \log(G + S \cdot F) + c & \text{, if } -10 \text{ ns } \leq r \leq 10 \text{ ns} \\ 0.5(\log(1 + r^2/\sigma^2)) + c - \log(a_1) + l_1 r & \text{, if } r > 10 \text{ ns} \end{cases} \quad (5.13)$$

where σ, c, a_2, l_2, a_1 and l_1 are constant extracted from the fit of time residual distributions obtained after the light production step of the Monte Carlo procedure. G, S and F are the following functions:

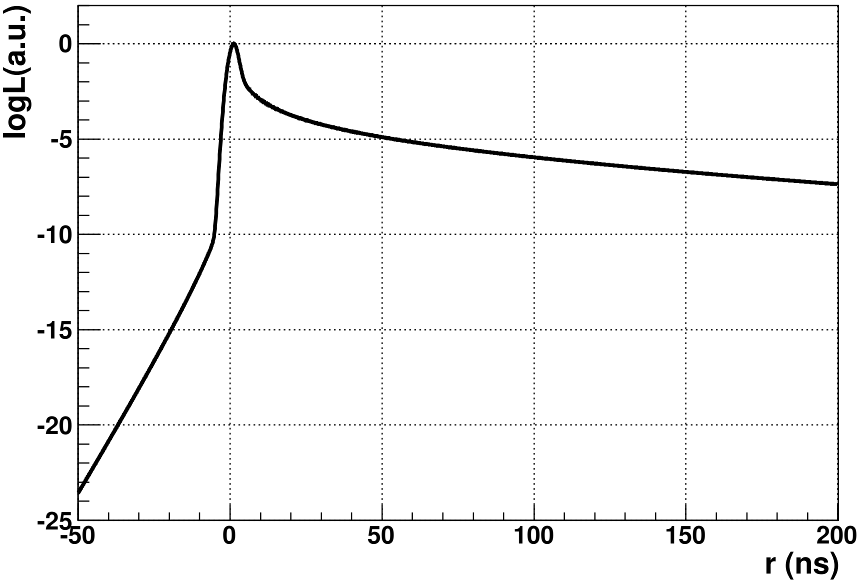

Figure 5.8: The likelihood function used in the third step of the fitting algorithm.

$$
\begin{aligned}
G &= \exp(-0.5 \cdot r^2/\sigma^2) && (5.14)\\
S &= 1/\sqrt{1+r^2/\sigma^2} && (5.15)\\
F &= \frac{a_1 \cdot \exp((2-l_2)\cdot r) + a_2 \cdot \exp(-l_2 \cdot |r|)}{\exp(2r)+1} && (5.16)
\end{aligned}
$$

The fit is performed with hits that are a subset of the *M-estimator hits* and are called *Pdf hits*. This time, to select the hits, their time residuals r are calculated with respect to the track resulting from the M-estimator. If R_{RMS} is the root mean square of the *M-estimator hits* residuals distribution, a hit is accepted if $-0.5 \times R_{RMS} < r < R_{RMS}$ and if its distance from the M-estimator track is less than 300 m. As in the previous case, all the L3 hit are added and the angular selection is applied to the hit set. Moreover, the fit works better if it uses only one hit per DOM, choosing the hits on the basis of their score. Also this fit requires a minimum number of 6 hits to be performed.

5.7 Scan procedure

To improve the efficiency of the algorithm, a scanning of the whole sky is performed by repeating step 2 and 3 using as input a large number of starting tracks that differ from the prefit. If the prefit track is identified by a point $\mathbf{P}_{pre}$ and a direction $\vec{d}_{pre}$, the additional starting points are obtained by rotating the prefit track by step of 3° around the point $\mathbf{P}_{pre}$. The resulting 7200 starting track pass all trough the point $\mathbf{P}_{pre}$, so the evaluation of this point is quite relevant.

As described in the previous sections, the hit set used in each fit procedure is accurately selected on the basis of the time-space correlation with the starting track Using time residuals, therefore, some of this tracks are discarded because the number of hits remaining after the hit selection is not sufficient to proceed. The M-estimator and the Pdf fit are performed for all the remaining tracks and the best one is kept for further processing. The parameter utilised to choose the best track is the likelihood per degree of freedom

$$\Lambda = -\frac{logL}{N_{dof}} = -\frac{logL}{N_{hit} - 5} \tag{5.17}$$

where $logL$ is the value of the likelihood function, N_{hit} is the number of hits used to perform the Pdf fit and N_{dof} is the number of degree of freedom. In this case $N_{dof} = N_{hit} - 5$ since we have 5 free parameters (3 coordinates of the point $\mathbf{P}$ on the track and the angles ϕ and θ). Since one hit per DOM is used, the number of hits N_{hit} coincides with the number of DOMs involved in the selection. It is also possible to classify the tracks using a linear combination of Λ and N_{hit}

$$Q = N_{hit} - w \cdot \Lambda \tag{5.18}$$

This quality parameter favours solutions with a large number of hits correlated to the track. The value of the weight w that permit a better identification of the best track, is $w = 1$. In fact, if the track is chosen according to the best Q, the number of events that have $\Delta\Omega_{\mu,fit} < 1°$ increases of 4% with respect to the case when Λ is the criterion to select the best track, therefore Q is used in the code as track quality classifier. Fig. 5.9 shows the angular error for the track chosen after the “Pdf fit”, the corresponding “M-estimator” track and the initial prefit track. The improvement in each step of the reconstruction is evident.

5.8 Final Fit - Step 4

Once the best track has been chosen, a further adjustment of the track direction is achieved with the last fit, using the best track as starting point.

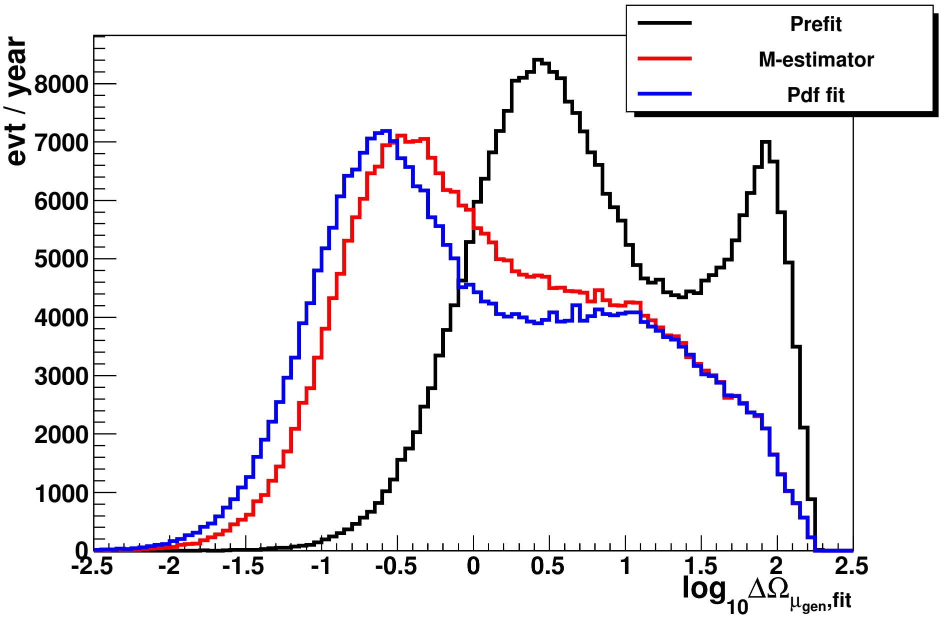

Figure 5.9: Logarithm of the angular distance, in degrees, between the generated muon track and the chosen track of the "Pdf fit", the corresponding "M-estimator" track and the initial prefit track. Events are weighted with the atmospheric neutrino flux.

The hits employed in this fit, called *final pdf hits*, are selected among the *Selected hits* if they have residuals between -250 and 250 ns and a distance from the best track less than 100 m. Then, even in this case, L3 hit are added, the angular selection is applied using the best track as reference track and one hit per DOM is selected according to its score.

The PDF used in this step is described in detail in [175]. The basic idea is to take into account the contributions from both the background hits and the signal hits. It is assumed that an event consists of hits all with residuals between $-T/2$ and $T/2$. The time window, $T = 500$ ns, is assumed to be large enough to contain all signal hits while background hits are uniformly distributed in time. The PDF is a function of the time residuals, but also of the parameters a and b (see sec. 5.1) and of the hit amplitude A:

$$f(r_i|a_i, b_i, A_i) = \frac{P^{sig}(r_i|A_i)N^{sig}(a_i, b_i, A_i) + R^{bkg}}{N^T(a_i, b_i, A_i)} \tag{5.19}$$

where $P^{sig}(r_i|A_i)$ is the signal PDF, $N^{sig}(a_i, b_i, A_i)$ is the expected number of signal hits, R^{bkg} is the background rate and $N^T(a_i, b_i, A_i)$ is the total number of expected hits

$$N^T(a_i, b_i, A_i) = N^{sig}(a_i, b_i, A_i) + R^{bkg}T$$

The factor $1/N^T(a_i, b_i, A_i)$ in eq. 5.19 ensures that the function $f(r)$ is normalised in the interval $(-T/2, T/2)$.

The function $P^{sig}(r_i|A_i)$ was parameterised separately for hits in 5 amplitude bins ($A < 1.5$ p.e., 1.5 p.e. $< A < 2.5$ p.e., 2.5 p.e $< A < 5$ p.e., 5 p.e. $< A < 10$ p.e., $A >$ 10 p.e.) using the following functional form:

$$\frac{dP^{sig}}{dr} = \begin{cases} \mathcal{A} \exp\left(\frac{-(r-\tau)^2}{2\sigma^2}\right) & \text{, if } r < c_1 \text{ ns} \\ \mathcal{B}(\alpha r^3 + \beta r^2 + \gamma r + 1) & \text{, if } c_1 \text{ ns } \leq r \leq c_2 \text{ ns} \\ \mathcal{C}\frac{e^{r/\eta}}{r+\rho} & \text{, if } r > c_2 \text{ ns} \end{cases} \tag{5.20}$$

The peak of the distribution is fitted with a Gaussian, while the tail has been approximated by an exponential. These two functions are joined together by a 3rd degree polynomial function.

The expected number of signal hits N^{sig} for a given amplitude bin is factorised as

$$N^{sig}(a_i, b_i) = N^{sig}(b_i) \times f(a_i) \tag{5.21}$$

The expected number of signal hits as a function of b and the angular acceptance function are obtained by fitting the simulated events.

The percentage of events reconstructed within 0.1°, 0.3°, 1°, 3° and 10° from the muon track is shown in the Table 5.2 for the prefit track, the chosen Pdf fit track, the corresponding M-estimator track and the final track. The events are weighted with the atmospheric neutrino flux.

Table 5.2: Percentage of events reconstructed within and angle $\Delta\Omega$ with respect to the true muon track by the different fitting algorithm that constitute the four step of the reconstruction. The spectrum of the atmospheric neutrinos is assumed.

$\Delta\Omega$	0.1°	0.3°	1°	3°	10°
Prefit	0.2	2.2	12.7	37.4	60.4
M-estimator	6.7	25.4	47.0	63.4	78.0
Pdf fit	11.3	32.8	51.3	64.8	78.2
Final fit	12.7	34.2	51.6	64.0	76.1

The final result of the algorithm is evaluated calculating for each neutrino energy bin the median of three different angles (see fig. 5.10):

- $\Delta\Omega_{\nu,fit}$, the angular distance of the generated neutrino from the reconstructed track, that gives the detector angular resolution;

- $\Delta\Omega_{\mu,fit}$, the angle between the muon obtained from the generated neutrino interaction and the reconstructed track, which permit to check the performance of the reconstruction algorithm;

- $\Delta\Omega_{\nu,\mu}$, called "intrinsic angle", the angular distance between the generated neutrino and the corresponding muon, that represents the physics limit to the detector pointing accuracy.

The three angles are all decreasing with the energy. Above 200 GeV, $\Delta\Omega_{\mu,fit}$ is less then 1 degree and above 10 TeV is less then 0.2°. The detector resolution is about 0.2° at 15 TeV and reaches 0.1° at 160 TeV.

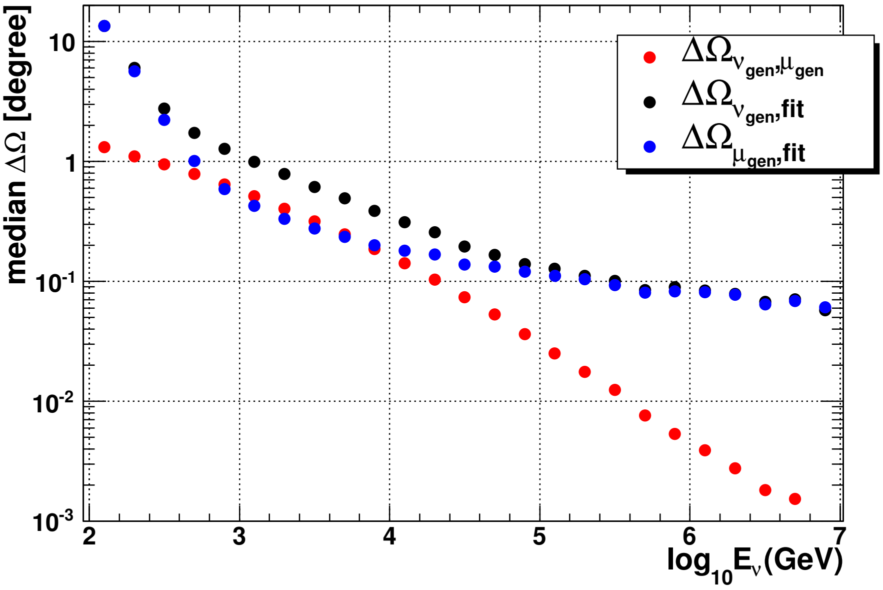

Figure 5.10: For each energy bin, the median of the angle between the generated muon neutrino and the outgoing muon (red dots), between the generated neutrino and the reconstructed track (black dots) and between the muon and the reconstructed track (blue dots) are evaluated.

5.9 Estimators of the reconstruction quality

The philosophy adopted in the reconstruction algorithm is to reconstruct as many events as possible without trying to reduce the number of badly reconstructed events by intermediate selection criteria. Rather, selection criteria can be applied afterwards, depending on the demands of the specific physics analysis. In this section, two variables are introduced which can be used to reject badly reconstructed events.

An obvious way to discriminate good and bad events is a cut on the value of the parameter Λ, defined in eq. 5.17. The correlation between Λ and the detector resolution is shown in the left panel of fig. 5.11 while the right panel shows the distribution of Λ for events with $\Delta\Omega_{\nu,fit}$ greater and less than 1°. The condition $\Lambda > -7$ permits to reject 90% of events with $\Delta\Omega_{\nu,fit} > 1^\circ$ preserving 62% of the events with $\Delta\Omega_{\nu,fit} < 1^\circ$

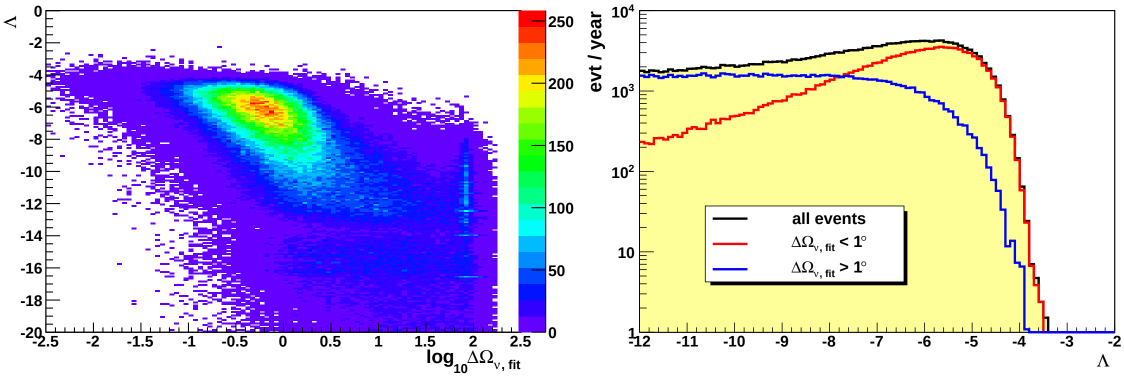

Figure 5.11: Left panel: Λ versus the logarithm of the angular distance $\Delta\Omega_{\nu,fit}$ between the generated neutrino and the fitted track. Right panel: Λ distribution for events with $\Delta\Omega_{\nu,fit} > 1^\circ$ and $\Delta\Omega_{\nu,fit} < 1^\circ$.

The other variable that allows for an evaluation of the reconstruction quality is the uncertainty on the direction of the reconstructed track β, calculated from the errors on θ and ϕ, $\Delta\theta$ and $\Delta\phi$. Considering confidence intervals of 1σ in each of the two dimensions θ and ϕ, a confidence ellipse is obtained. It consists of the part of the parameter space where the value of the negative logarithmic likelihood $-logL$ has changed by 1/2 with respect to the best value resulting from the fit $-logL_{best}$. If the shape of the $-logL$ around its minimum is assumed to be Gaussian, the error covariance matrix $\mathbf{V}$ can be obtained from the second derivatives of the likelihood function at the fitted minimum with respect to the parameters vector $\mathbf{x} \equiv (p_x, p_y, p_z, \theta, \phi)$:

$$[\mathbf{V}^{-1}]_{ij} = -\frac{\partial^2 logL}{\partial x_i \partial x_j} \tag{5.22}$$

If $\mathbf{V}^{-1}$ is invertible, the errors $\Delta\theta$ and $\Delta\phi$ are estimated inverting the matrix $\mathbf{V}^{-1}$. The corresponding uncertainty on the direction of the reconstructed track is

$$\beta = \sqrt{\sin\theta\Delta\phi^2 + \Delta\theta^2} \tag{5.23}$$

The left panel of fig. 5.12 shows how the parameter β is correlated to the detector resolution. The values of β for events with $\Delta\Omega_{\nu,fit} > 1°$ and $\Delta\Omega_{\nu,fit} < 1°$ are illustrated in the right panel. It's evident that a cut on β can help to separate badly reconstructed events from the well reconstructed. As an example, a cut $\beta < 0.2°$ rejects 82% of the events with $\Delta\Omega_{\nu,fit} > 1°$ keeping 67% of the events with $\Delta\Omega_{\nu,fit} < 1°$.

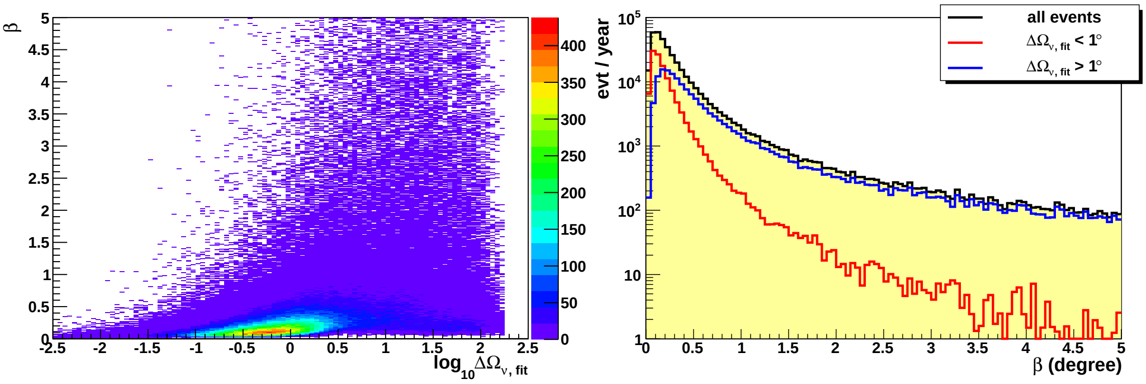

Figure 5.12: Left panel: β versus the logarithm of the angular distance $\Delta\Omega_{\nu,fit}$ between the generated neutrino and the fitted track. Right panel: β distribution for events with $\Delta\Omega_{\nu,fit} > 1°$ and $\Delta\Omega_{\nu,fit} < 1°$.

The two parameters Λ and β are not completely uncorrelated, as demonstrated by fig. 5.13, but the simultaneous use of the two cuts is advantageous. In fact, requiring the two conditions $\Lambda > -7$ and $\beta < 0.2°$, 94% of the events with $\Delta\Omega_{\nu,fit} > 1°$ are rejected and 53% of the events with $\Delta\Omega_{\nu,fit} < 1°$ are kept. In the right panel of fig. 5.13 the distribution of $\Delta\Omega_{\nu,fit}$ is shown for all the reconstructed events and for the events selected with the cuts $\Lambda > -7$ and $\beta < 0.2°$. The percentages of reconstructed events with $\Delta\Omega_{\nu,fit} < 1°$, $\Delta\Omega_{\nu,fit} > 1°$ and $\Delta\Omega_{\nu,fit} > 10°$ that survive to different cuts on Λ and β are indicated in the Table 5.3.

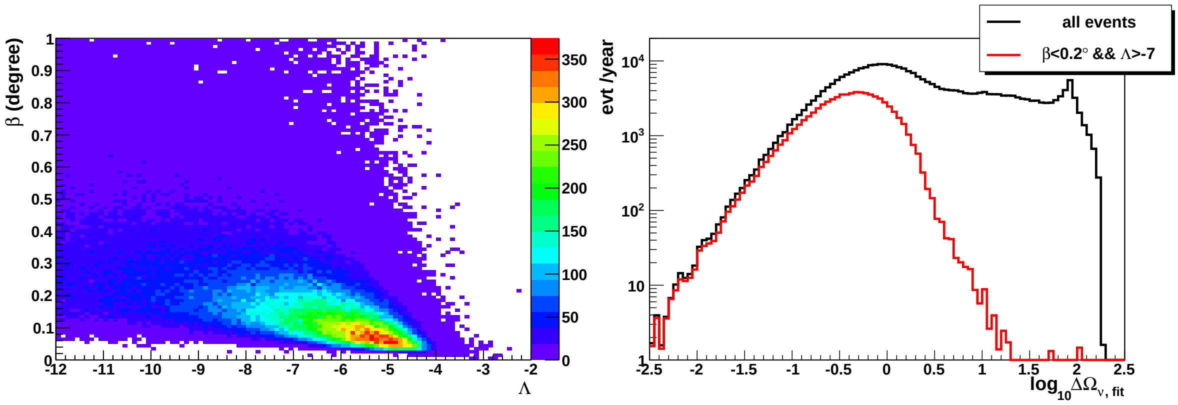

Figure 5.13: Left panel: β versus Λ. Right panel: logarithm of $\Delta\Omega_{\nu,fit}$ for all the reconstructed events and for those with $\Lambda > -7 \& \beta < 0.2°$.

Table 5.3: Percentage of the total number of reconstructed events that fulfil different conditions on β and Λ and have $\Delta\Omega_{\nu,fit}$ in the intervals specified in the first column.

	$\Lambda > -8$	$\Lambda > 7$	$\beta < 0.3°$	$\beta < 0.2°$	$\Lambda > -8 \& \beta < 0.3°$	$\Lambda > -7 \& \beta < 0.2°$
$\Delta\Omega_{\nu,fit} < 1°$	77	62	83	67	71	53
$\Delta\Omega_{\nu,fit} > 1°$	18	10	33	18	13	6
$\Delta\Omega_{\nu,fit} > 10°$	1.2	0.2	19	10	0.5	0.03

The plots presented in this section are weighted with the atmospheric neutrino flux, just to show how the reconstruction and the cuts work, but during the event analysis the cuts are tuned to maximise the signal to noise ratio.

5.10 Number of hits as energy estimator

The track reconstruction code doesn't contain an energy estimator. However, the number of hits used in the last fit step N_{hit} can play this role. Fig. 5.14 shows the correlation between N_{hit} and the neutrino energy. For each neutrino energy bin, the median of the N_{hit} distribution is reported. The error bars represent 16% and 84% quantiles, that are equivalent to 1σ error in the case of a Gaussian distribution. Even if N_{hit} is not an exact energy estimator, it is possible to select events with energy greater then a given value using a cut on N_{hit}. As an example, a cut on $N_{hit} > 30$ permits to select events with energy greater then 1 TeV as it is shown in the left in fig. 5.14. In fact, only 3% of the events with $E < 1$ TeV has $N_{hit} > 30$. The energy distributions of all the reconstructed events and the events with $N_{hit} > 30$ and $N_{hit} < 30$ are shown in the right panel of fig. 5.14.

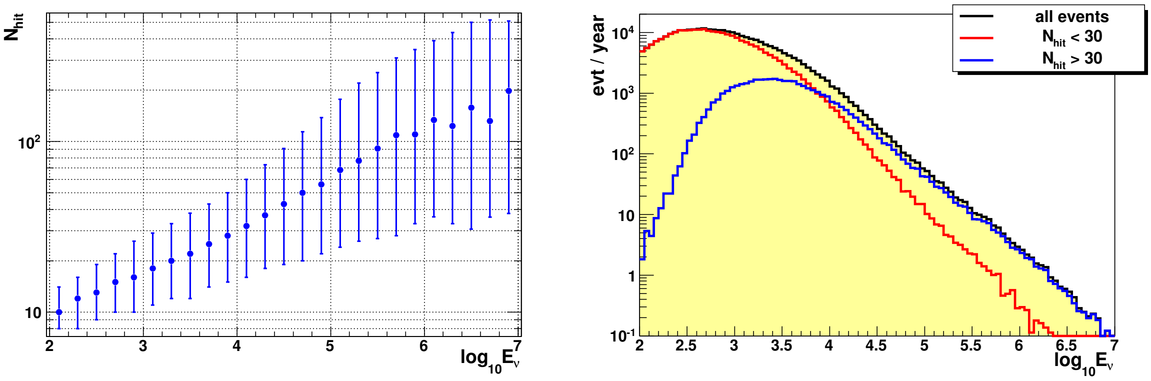

Figure 5.14: Left panel: median number of N_{hit} as a function of the generated neutrino energy. The error bars represent 16% and 84% quantiles. Right panel: logarithm of generated neutrino energy for all the reconstructed events and for those with $N_{hit} > 30$ and $N_{hit} < 30$.

CHAPTER 6

POINT-LIKE SOURCE SEARCH: METHODS AND RESULTS

Point source searches look for a statistical excess originating in narrow sky regions where the sources are located. The weak neutrino signal from a cosmic source stems on the large background of atmospheric muons and neutrinos, both produced by the interaction of primary cosmic rays with the atmosphere. In this chapter the two main statistical methods applied to the search of cosmic neutrino sources will be presented together with the obtained results in the analysis of two specific sources, the SNR RXJ 1713.7-3946 and the PWN Vela X.

Except when otherwise specified, all the plots presented in this chapter refer to a detector made of 2 blocks of 310 strings, each one equipped with 20 DOMs vertically aligned at a distance of 40 m between each other. The strings are distributed on the seabed with random positions within a roughly circular area and with an average distance of 100 m (see fig. 4.2). The described detector layout will be considered as the "reference detector".

The effect of the distance between strings is also investigated in the analysis. In fact, the study of the SNR RXJ 1713.7-3946 is performed for the reference detector but also for three other layouts with 90, 115 and 130 m distance between detection units.

6.1 Effective area and angular resolution

For a given neutrino flux $d\Phi_\nu/dE_\nu d\Omega_\nu$ the expected event rate dN_ν/dt at the neutrino telescope is the convolution of this flux with a quantity called neutrino effective area $A^\nu_{eff}(E_\nu,\theta_\nu)$:

$$\frac{dN_\nu}{dt} = \iint A^\nu_{eff}(E_\nu,\theta_\nu)\frac{d\Phi_\nu}{dE_\nu d\Omega_\nu}\, dE_\nu\, d\Omega_\nu. \tag{6.1}$$

Therefore, A^ν_{eff} is an important parameter of the detector. The effective area represents the area of a 100% efficient surface for detecting throughgoing neutrinos. In other words, it permits to display the detection efficiency, i.e. the fraction of incident neutrinos the detector can reconstruct. The A^ν_{eff} is calculated as:

$$A^\nu_{eff}(E_\nu,\theta_\nu) = V_{eff}(E_\nu,\theta_\nu) \times \sigma(E_\nu) \times (\rho N_A) \times P(E_\nu,\theta_\nu). \tag{6.2}$$

Here ρN_A is the target nucleon density (being ρ the density of the target material and N_A the number of particles per gram), $\sigma(E_\nu)$ is the neutrino-nucleon cross section, $P(E_\nu,\theta_\nu)$ is the probability for neutrino absorption in the Earth and $V_{eff}(E_\nu,\theta_\nu)$ is the effective volume. The latter is obtained scaling the generation volume V_{gen} defined in the generation phase (see section 4.2), with the ratio of the reconstructed events N_{rec} (or selected according to a given criterion) and the generated events N_{gen}:

$$V_{eff}(E_\nu,\theta_\nu) = \frac{N_{rec}(E_\nu,\theta_\nu)}{N_{gen}(E_\nu,\theta_\nu)}V_{gen} \tag{6.3}$$

The number of generated events N_{gen} in a given energetic and angular interval $[E_1, E_2]$ and $[\cos\theta_1, \cos\theta_2]$ can be calculated from the total number of simulated interactions N_{total}. If the generated spectrum is a power law E$^{-\alpha}$, N_{gen} is given by:

$$N_{gen}(E_\nu,\theta_\nu) = \frac{\cos\theta_2 - \cos\theta_1}{\cos\theta_{max} - \cos\theta_{min}} \times \frac{\int_{E_1}^{E_2} E^{-\alpha}dE}{\int_{E_{min}}^{E_{max}} E^{-\alpha}dE} \times N_{total} \tag{6.4}$$

being E_{min}, E_{max}, $\cos\theta_{min}$ e $\cos\theta_{max}$ the minimum and maximum values of the generated energy and zenith angle.

Fig. 6.1 shows the effective area for all the reconstructed events, for the upgoing events and for the upgoing events selected with quality cuts chosen for the discovery

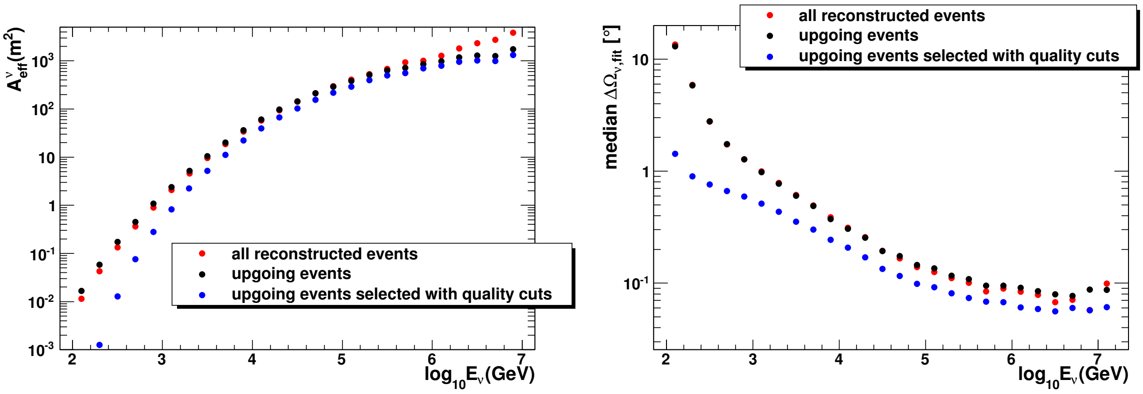

Figure 6.1: Left panel: Neutrino effective area for all the reconstructed events (red points) , for the upgoing events (black points) and for the upgoing events selected with the quality cuts tuned in the discovery potential calculation for the source SNR RXJ 1713.7-3946. Right panel: Angular resolution for the same event classes.

potential calculation, which will be described after. The A^{ν}_{eff} increases with the neutrino energy and above 1 PeV a depletion appears for upgoing events due to the Earth absorption. The quality cuts reduce the neutrino effective area at low energy, especially below 1 TeV.

The figure also shows for the same events the detector angular resolution, that is defined as the median of the angular deviation between the direction of reconstructed muon track and the true neutrino direction obtained form the Monte Carlo. As expected, there is no difference in the angular resolution for all the events and the upgoing events only, but the quality cuts improve it, permitting to reach 0.2° at 10 TeV.

6.2 Statistical methods for the point sources search

The search for point-like sources of neutrinos is one of the most important tasks of a neutrino telescope. The two basic questions are: can a source be seen with a given significance (e.g. 3σ or 5σ) in a given fraction of hypothetical experiments (e.g. 50%)? And, if no source is discovered, what is the source flux that can be excluded at a given confidence level (e.g. 90%)? The answer to the first question yields the detector's discovery potential, whereas the second question leads to the detector's sensitivity.

The two approaches used to calculate these quantities are the "binned" and "unbinned" methods. In general, the data in high energy astronomy consist of a set of events distributed throughout a region of the sky, and can be modelled by two hypotheses: either the data consist solely of background events, i.e. the null hypothesis, or the data additionally contains a signal from an astrophysical source. The signal and background event distributions are governed by probability density functions (PDFs), describing the event angular distribution, energy spectrum, time distribution, etc. Any difference between the signal and background PDFs provides an opportunity to differentiate events produced by an astrophysical source from the background. Binned and unbinned methods use these PDFs in different ways.

Binned methods are based on the idea to split up the sky into a grid and searching in each bin for an excess of signal events over the background. A poissonian distribution of the events is assumed in each bin. In this case, the optimisation of the signal to background ratio is performed considering only events with directions that are near the actual source's direction, i.e. by using a so-called search cone, that for a point source should have a radius of the same order of the detector angular resolution or greater. Additionally, the relative number of signal and background events can be influenced by various track quality cuts. The cuts leading to optimal values for discovery potential and sensitivity will usually be different and have to be found using an optimisation process.

On the other hand, the unbinned method evaluates the probability to have a given number of signal events for the given background and signal models. This method requires a significantly higher computing time than the binned approach but it is more sensitive and powerful. In fact, while the unbinned method takes the maximum profit of the shape of the PDFs, in the binned method all of the event information is reduced to a binary classification: either the event passes the selection and is counted, or it does not. In this way a fraction of potential signal events is always lost. Moreover, information contained within the event distribution that could indicate the relative agreement of each event with signal or background, is lost. For example, events at the edge of a search bin are not as indicative of a point source as events near the centre, but they are counted the same.

6.2.1 Discovery Potential with the binned method

The discovery potential [176] is determined from the number of detected events, n_α, in a given detector live time Δt that has a probability of α or less to originate purely from background in $1 - \beta = 50\%$ of all the hypothetical experiments. If $\alpha = 2.85 \times 10^{-7}$

(area of the one-sided Gaussian tail beyond 5σ), the observation of n_α would correspond to a significance of 5σ and a confidence level (CL) of 50%. If the significance required is 3σ then $\alpha = 1.35 \times 10^{-3}$.

In order to calculate n_α, the average number of background events $\langle n_b \rangle$ in Δt is extracted from the simulation and the minimum (critical) number of events, n_0, that satisfies

$$\sum_{n_{obs} \equiv n_0}^{\infty} P(n_{obs} | \langle n_b \rangle) \leq \alpha \tag{6.5}$$

is determined, where $P(n_{obs} | \langle n_b \rangle)$ is the Poisson probability for observing n_{obs} events given an expected number of background events $\langle n_b \rangle$. The value n_0 is the minimum number of events required to claim a deviation from the background-only hypothesis with a statistical significance defined by the p-value α. If the average number of signal events in Δt is $\langle n_s \rangle$, then $n_0 = \langle n_b \rangle + \langle n_s \rangle$ and the signal strength n_α that lead to an observation with a p-value less than α in a fraction $1 - \beta$ of the experiments is the value that fulfils

$$P_{5\sigma} = \sum_{n_{obs} \equiv n_0}^{\infty} P(n_{obs} | \langle n_b \rangle + n_\alpha) = 1 - \beta. \tag{6.6}$$

The number n_α depends only on $\langle n_b \rangle$. Fig. 6.2 shows n_α as a function of $\langle n_b \rangle$ for different values of α and β.

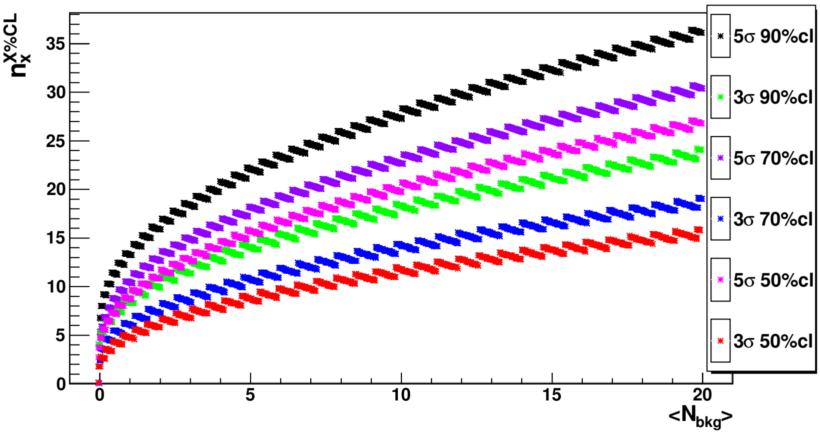

Figure 6.2: The number of events required for the discovery (5σ) or the evidence (3σ) of a source are reported as function of the mean of background events.

Given an arbitrary source spectrum Φ_s predicting $\langle n_s \rangle$ signal events in Δt, the minimum flux Φ_α needed for a discovery (discovery flux) after an observation time of Δt, is

$$\Phi_{\alpha} = \Phi_{s} \times \frac{n_{\alpha}(\langle n_{b} \rangle)}{\langle n_{s} \rangle} \tag{6.7}$$

The ratio $n_{\alpha}(\langle n_{b} \rangle) / \langle n_{s} \rangle$ is usually called “Model Discovery Potential” (MDP).

In the calculation discussed in this thesis, the MDP, and therefore the discovery flux, is minimised selecting the signal and background events by applying cuts on the radius of the search cone around the source position R_{bin}, on the number of hits used during the reconstruction N_{hit}, on the quality fit parameter Λ and on the uncertainty on the direction of the reconstructed track β.

From the discovery flux, the number of years required to claim the discovery of a given source can be calculated. In fact, the observation time Δt can be tuned to reach the condition $\Phi_{\alpha} = \Phi_{s}$ or equivalently $n_{\alpha}(\langle n_{b} \rangle) = \langle n_{s} \rangle$.

6.2.2 Sensitivity with the binned method

Feldman and Cousins have proposed a method to quantify the “sensitivity” of an experiment independently of experimental data by calculating the average upper limit, $\bar{\mu}$, that would be obtained in absence of a signal [177]. It is calculated from the mean number of expected background events in Δt, $\langle n_{b} \rangle$, by averaging over all limits obtained from all possible experimental outcomes. Therefore, if $\mu_{90}(n_{obs}, \langle n_{b} \rangle)$ is the upper limit at confidence level of 90% when n_{obs} is the observed number of events, the average upper limit is:

$$\bar{\mu}_{90}(\langle n_{b} \rangle) = \sum_{n_{obs}=0}^{\infty} \mu_{90}(n_{obs}, \langle n_{b} \rangle) P(n_{obs}, \langle n_{b} \rangle). \tag{6.8}$$

where $P(n_{obs}, \langle n_{b} \rangle)$ is the Poisson probability to observe n_{obs} events given an expected number of background events $\langle n_{b} \rangle$. The $\bar{\mu}_{90}(\langle n_{b} \rangle)$ represents the average maximum limit of background fluctuation at 90% confidence level, observed after hypothetical repetitions of an experiment with an expected background and no true signal. The trend of $\bar{\mu}_{90}$ as a function of $\langle n_{b} \rangle$ is shown in fig. 6.3.

If a source model Φ_{s} predicts a mean number of signal events $\langle n_{s} \rangle$, the average flux limit Φ_{90} is found by scaling the normalisation of the flux model such that the number of expected events equals the average upper limit:

$$\Phi_{90} = \Phi_{s} \times \frac{\bar{\mu}_{90}(\langle n_{b} \rangle)}{\langle n_{s} \rangle} \tag{6.9}$$

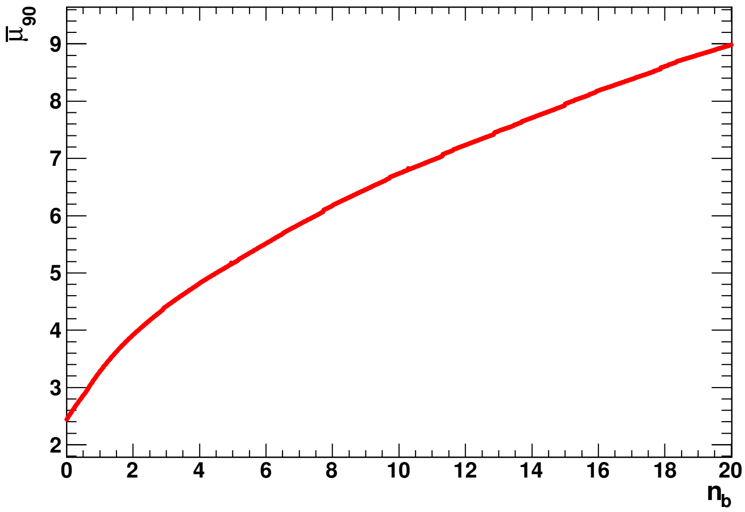

Figure 6.3: $\bar{\mu}_{90}$ (90% of confidence level), as a function of the mean number of background events.

The Φ_{90} is what is called "sensitivity" in this thesis. The ratio $\bar{\mu}_{90}(\langle n_b \rangle)/\langle n_s \rangle$ is called Model Rejection Factor (MRF) and, as the MDP, is minimised selecting the signal and background events with cuts on R_{bin}, N_{hit}, Λ and β. Usually the cuts that minimise the MRF are not the same that minimise the MDP.

6.2.3 Unbinned method

In general, when the compatibility of the data with two different hypothesis H_0 and H_1 has to be tested, a test statistic λ is calculated. The test statistic can be in principle any function of the data but is chosen such that, if H_0 is true, it is expected to have a different value with respect to the case when H_1 is true. Thus, the value of λ indicates whether the data is more compatible with H_0 or with H_1. Usually, for each hypothesis, the probability density functions of the test statistic, $P(data|H_0)$ and $P(data|H_1)$, can be calculated, as illustrated in fig. 6.4. It is possible to define a "rejection region" ω, that is a set of values of λ for which H_1 is likely true. In other words, if the value of λ calculated from the data lies within the rejection region, the hypothesis H_0 is rejected in favour of H_1. However, since the two distributions corresponding to the two hypothesis are not completely separated, it is possible that λ is contained in the rejection region, even though H_0 is true and in this case H_0 will be wrongly rejected.

For a given value λ_α, the probability of rejecting H_0 when H_0 is true, is evaluated at

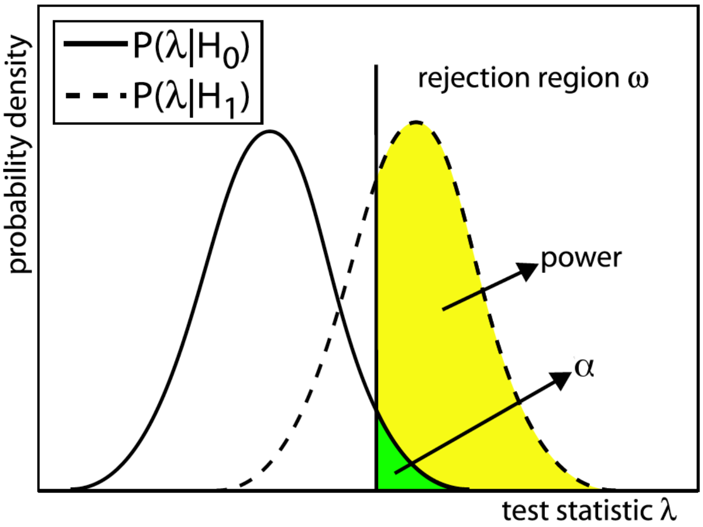

Figure 6.4: Illustration of hypothesis testing. The probability density functions of the test statistic for H_0 and H_1 are shown. The rejection region ω is the region to right of the vertical line. The filled regions are related to the confidence level and the significance of the test.

a given significance α corresponding to the integral of $P(data|H_0)$ for $\lambda \geq \lambda_\alpha$ and it is indicated in green in fig. 6.4. On the other side, the integral of $P(data|H_1)$ for $\lambda \geq \lambda_\alpha$ indicates the probability to chose H_1 if H_1 is true and represents the "power" of the test (yellow area if fig. 6.4) [178].

In the search for neutrino point sources the hypothesis $H_0 = H_{bkg}$ is the condition that the data set consist only of background events and the hypothesis $H_1 = H_{bkg+sig}$ is the case occurring when events from a cosmic source are present in addition to the background. The test statistic can be chosen in many different way but, in the method presented here, it is defined as the ratio of the probabilities that the data can be interpreted under the assumption that $H_{bkg+sig}$ is the correct model over the hypothesis H_{bkg}:

$$\lambda = \log \left[\frac{P(data|H_{bkg+sig})}{P(data|H_{bkg})} \right] \tag{6.10}$$

The corresponding test is called the Neyman-Pearson test, or likelihood ratio test [179–181]. In this case, the test statistic λ is usually indicated with LR.

After the reconstruction and selection procedures, the data collected in a given period of time consists of a number n of uncorrelated events, so LR can be written as:

$$LR = log \frac{\prod_{i=1}^{n} P(x_i|H_{sig+bkg})}{\prod_{i=1}^{n} P(x_i|H_{sig})} = \sum_{i=1}^{n} log \frac{P(x_i|H_{sig+bkg})}{P(x_i|H_{sig})} \tag{6.11}$$

Each event x_i has a declination δ_i and a right ascension RA_i. Assuming to know the coordinates (δ, RA) of the candidate neutrino source, for each event the angular distance α_i from the source is calculated and the probabilities $P(x_i|H_{sig+bkg})$ and $P(x_i|H_{bkg})$ are:

$$\begin{aligned} &P(x_i|H_{sig+bkg}) = \frac{n_{sig}}{n} \times P_{sig}(\alpha_i) + \left(1 - \frac{n_{sig}}{n}\right) \times P_{bkg}(\alpha_i) \\ &P(x_i|H_{bkg}) = P_{bkg}(\alpha_i) \end{aligned} \tag{6.12}$$

where:

- n_{sig} is the number of signal events in the sample of n events, therefore n_{sig}/n and $1 - (n_{sig}/n)$ are the fractions of signal and background events respectively. This parameter is unknown and is estimated maximising LR.
- $P_{sig}(\alpha_i)$ and $P_{bkg}(\alpha_i)$ are respectively the probability density function for the signal and for the background, that are extracted from the Monte-Carlo simulations as the one dimensional normalised distributions of α for the generated background and signal events.

Replacing expressions 6.12 in equation 6.11 yields:

$$LR = \sum_{i=1}^{n} log \frac{\frac{n_{sig}}{n} \times P_{sig}(\alpha_i) + \left(1 - \frac{n_{sig}}{n}\right) \times P_{bkg}(\alpha_i)}{P_{bkg}(\alpha_i)} \tag{6.13}$$

The output of the algorithm is the maximised LR value and the corresponding fitted n_{sig} value.

This procedure is first applied to many samples of background only events obtained by Monte-Carlo simulations of atmospheric neutrinos. For each sample, the maximum value of LR, LR^{max}_{bkg}, is recorded. The distribution of LR^{max}_{bkg} is equivalent to P($\lambda|H_0$) in fig. 6.4 so fixing the required significance, e.g. 5σ, the critical value $LR_{5\sigma}$ is calculated such that:

$$\int_{LR_{5\sigma}}^{+\infty} LR^{max}_{bkg} = 2.85 \times 10^{-7} \tag{6.14}$$

Then, the procedure is repeated adding a number N_{signal} of simulated signal events to the sample of background events. In this case case the values of LR^{max} give the P($\lambda|H_1$) of fig. 6.4. For each N_{signal} the corresponding power is calculated as:

$$\int_{LR_{5\sigma}}^{+\infty} LR_{signal}^{max} = power. \tag{6.15}$$

If $n_{5\sigma}$ is the value of N_{signal} such that the power reaches 50%, then $n_{5\sigma}$ represents the number of events that lead to an observation with a p-value less than 5σ with a 50% confidence level.

If the analysis has been performed with a model for the source that predicts a flux Φ_s and a mean number of signal events $\langle n_s \rangle$, the discovery flux will be:

$$\Phi_\alpha = \Phi_s \times \frac{n_\alpha}{\langle n_s \rangle} \tag{6.16}$$

The unbinned method described here and used in this work is based on the "fixed-sky search". Another possible procedure is the so-called "full-sky search", which doesn't use any assumption on the source position but looks for any possible neutrino source in the observable sky.

6.3 SNR RXJ 1713.7-3946

The young shell-type supernova remnant (SNR) RX J1713.7-3946 is at present the SNR with one of the widest coverages along the electromagnetic spectrum. Its high energy gamma-ray emission has been observed by HESS in several campaigns [182] and extends up to about 100 TeV suggesting that the CR protons responsible may have energies close to the knee, 10^{15} eV, if the γ-rays production is hadronic. A γ-ray map of RX J1713.7-3946 is shown in the left panel of fig. 6.5. A thick, almost circular shell structure with the brightest regions is visible in the north-west. The X-ray contours detected by the ASCA satellite [183] are overlaid to the HESS image to demonstrate the similarity of the gamma-ray and X-ray morphology. The relatively large size and the complex morphology of RX J1713.7-3946 are accompanied by a large intensity spectrum which is shown in the right panel of fig. 6.5. The HESS collaboration fitted the spectrum with different functional forms indicated in table 6.1. A pure power-law is clearly ruled out, while the alternative spectral models provide significantly better description of the data (the χ^2 is smaller). In fig. 6.5 the data are fitted with a power law function with exponential cutoff of the form $dN/dE = I_0 E^{-\Gamma} exp(-(E/E_c)^\beta)$ where $I_0 = 34.1 \times 10^{-12}$ cm^{-2} s^{-1} TeV^{-1}, $\beta = 0.5$, $\Gamma = 1.8$ and $E_c = 3.7$ TeV.

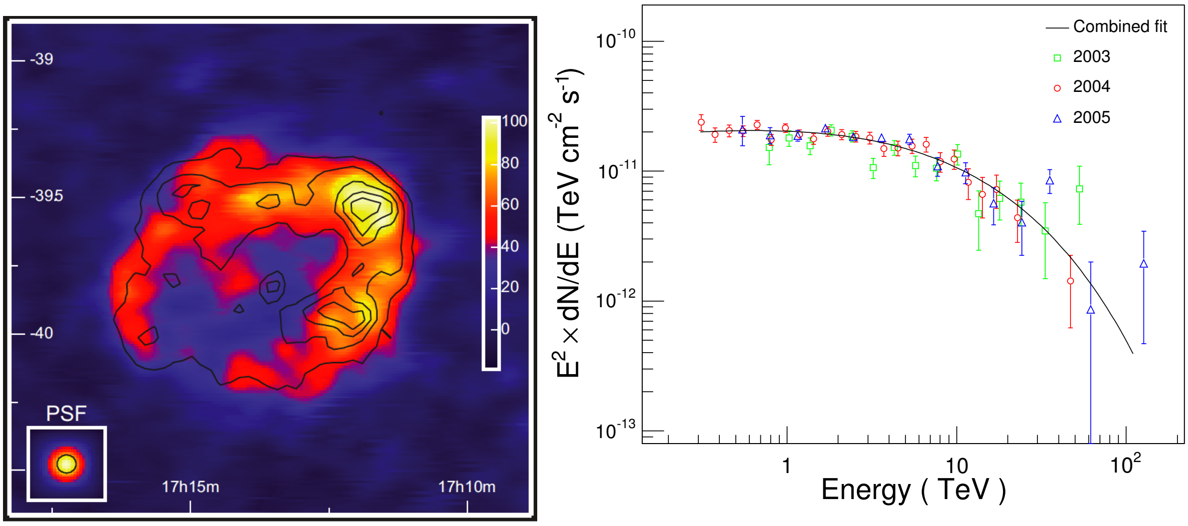

Figure 6.5: Left panel: combined HESS image of the SNR RX J1713.7-3946 from the 2004 and 2005 data [182]. A simulated point source (*PSF*) as it would appear in this data set is also shown. The linear colour scale is in units of excess counts. ASCA contours are drawn as black lines for comparison.
Right panel: HESS gamma-ray spectrum generated from data of 2003, 2004 and 2005. The black solid line denote the best fit result and for comparison, the best fit of a power law with exponential cutoff, obtained solely from the 2004 data, is shown as dashed red line.

The origin of the TeV gamma-ray emission from the RX J1713.7-3946 has been a matter of active debate. A detailed discussion on the interpretation of the HESS data in an hadronic or leptonic scenario can be found in [184]. To identify the mechanism responsible for the generation of the gamma rays, the wide-band electromagnetic spectra from radio to multi-TeV gamma rays must be compared to model calculations. The spatial correlation between the ASCA X-ray and the HESS gamma-ray data supports the idea that both are produced by the same population, namely electrons. On the other hand, the observation of molecular clouds associated with the SNR and the shape of the gamma-ray spectrum suggest a possible hadronic scenario. Recently the Fermi-LAT observed the RX J1713.7-3946 emission in the GeV energy range [185], but even adding this important piece of information, the large uncertainties on crucial parameters like the magnetic field strength and the effective ambient density, which are not directly accessible to measurements, hamper decisive conclusions on the possible production scenario.

Assuming a γ transparent source and a 100% hadronic origin of the observed gamma-ray flux, the measured gamma-ray spectrum can be used to derive the expected neutrino

Table 6.1: Fit results of the RX J1713.7-3946 γ-ray emission detected by HESS for different spectral models [182]. The fit range is chosen form 0.3 to 113 TeV. The differential flux normalisation I_0 is given in units of $10^{-12} cm^{-2} s^{-1} sr^{-1} TeV$.

Fit formula	Fit Parameters			χ^2
$I_0 E^{-\Gamma}$	$I_0 = 20.5 \pm 0.4$	$\Gamma = 2.32 \pm 0.01$		145.6
$I_0 E^{-\Gamma} e^{-(E/E_c)^\beta}$	$I_0 = 21.3 \pm 0.5$	$\Gamma = 2.04 \pm 0.04$	$\beta = 1.0$, $E_c = 17.9 \pm 3.3$	39.5
	$I_0 = 34.1 \pm 2.5$	$\Gamma = 1.79 \pm 0.06$	$\beta = 0.5$, $E_c = 3.7 \pm 1.0$	34.3
	$I_0 = 40.5 \pm 1.5$	$\Gamma = 1.74 \pm 0.02$	$\beta = 0.45$, $E_c = 2.3 \pm 0.2$	34.2
$I_0 E^{-\Gamma + \beta log E}$	$I_0 = 20.6 \pm 0.5$	$\Gamma = 2.02 \pm 0.04$	$\beta = -0.29 \pm 0.03$	38.8

emission, or at least an upper limit to the neutrino flux.

The phenomenological approach described by Vissani *et al.* [40, 186, 187] can be to estimate the muon neutrino and anti-neutrino fluxes reaching the Earth from the SNR RX J1713.7-3946. The method takes into account that photons are mainly produced by $\pi^0 \to \gamma\gamma$ and $\eta \to \gamma\gamma$, while muon neutrinos come mainly from the decay chain of charged pions and kaons. Consequently, the first information needed is the relative number of pions, kaons and η produced by cosmic rays at any given energy. Moreover, the effect of neutrino oscillation is added to all the processes that generate ν_μ and $\bar{\nu}_\mu$. Finally, simple analytic expressions for the expected muon neutrino and antineutrino fluxes are obtained:

$$\begin{array}{l} \Phi_{\nu_\mu}[E] = 0.380\,\Phi_\gamma[E/(1-r_\pi)] + 0.0130\,\Phi_\gamma[E/(1-r_K)] + \int_0^1 \frac{dx}{x}\, k_{\nu_\mu}(x)\,\Phi_\gamma(E/x) \\ \Phi_{\bar{\nu}_\mu}[E] = 0.278\,\Phi_\gamma[E/(1-r_\pi)] + 0.0090\,\Phi_\gamma[E/(1-r_K)] + \int_0^1 \frac{dx}{x}\, k_{\bar{\nu}_\mu}(x)\,\Phi_\gamma(E/x) \end{array} \tag{6.17}$$

In both equations the first two terms describe neutrinos produced in pions (first term) and kaons (second) decays and the third term takes into account neutrinos produced by muon decay. The parameters r_π and r_K are the squares of the ratio between the muon mass and the charged pion and kaon mass:

$$r_\pi = (m_\mu/m_\pi)^2 = 0.573 \quad , \quad r_K = (m_\mu/m_K)^2 = 0.0458 \tag{6.18}$$

The kernels $k_{\nu_\mu}(x)$ and $k_{\bar{\nu}_\mu}(x)$ are given by:

$$k_{\nu_\mu}(x) = \begin{cases} x^2(15.34 - 28.93\,x) & \text{if } x \le r_K \\ 0.0165 + 0.1193x + 3.747x^2 - 3.981x^3 & \text{if } r_K < x < r_\pi \\ (1-x)^2\,(-0.6698 + 6.588x) & \text{if } x \ge r_\pi \end{cases} \tag{6.19}$$

$$k_{\overline{\nu}_\mu}(x) = \begin{cases} x^2(18.48 - 25.33\,x) & \text{if } x \leq r_K \\ 0.0251 + 0.0826x + 3.697x^2 - 3.548x^3 & \text{if } r_K < x < r_\pi \\ (1-x)^2\,(0.0351 + 5.864x) & \text{if } x \geq r_\pi \end{cases} \tag{6.20}$$

A different approach for the estimate of neutrino spectra has been reported by Kelner *et al.* [38]. In this case the parameterization of the neutrino spectra is based on simulation of proton-proton interactions using the SIBYLL [188] code.

The expected total flux $\Phi_{\nu_\mu}(E) + \Phi_{\overline{\nu}_\mu}(E)$ from the SNR RX J1713.7-3946 calculated with the Vissani *et al.* method, assuming as Φ_γ the flux reported by HESS, is shown with a blue line in fig. 6.6. The black dashed line corresponds to the parametrisation of the neutrino flux obtained following the Kelner *et al.* prescription that is:

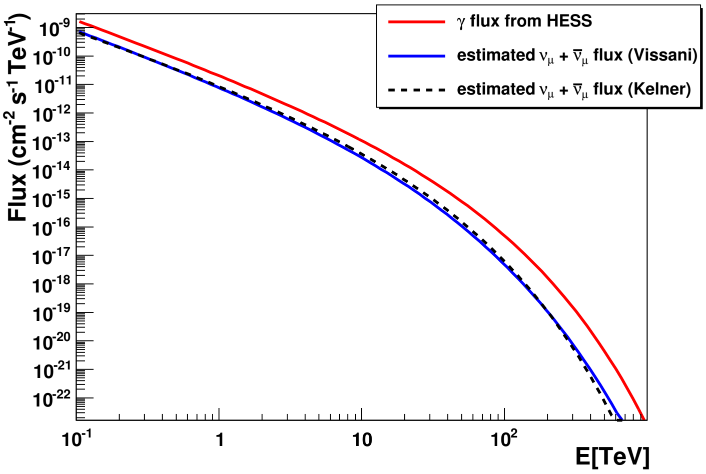

Figure 6.6: High energy γ-ray flux from SNR RXJ 1713.7-3946 measured by HESS (red line) with the corresponding total muon neutrino and antineutrino flux (blue line) obtained with the Vissani prescription and the Kelner parametrisation used in this analysis (black dashed line).

$$\Phi(E) = 16.8 \times 10^{-15} \left[\frac{E}{\text{TeV}}\right]^{-1.72} e^{-\sqrt{E/2.1\text{TeV}}}\text{GeV}^{-1}\text{s}^{-1}\text{cm}^{-2} \tag{6.21}$$

The two approaches give compatible results. In this work eq. 6.21 is used to calculate the neutrino flux from the SNR RX J1713.7-3946.

6.3.1 Event generation

The SNR RXJ 1713.7-3946 has been simulated as a neutrino emitting homogeneous disk with an extension of 0.6° centred at the declination of $\delta = -40°$ and a right ascension of $RA = 258.4°$. Muon neutrinos are generated homogeneously within this region with energies between 10^2 and 10^8 GeV. The source is visible for a detector located in the Mediterranean Sea 79.7% of the time. The assumed neutrino spectrum is described by eq. 6.21.

The background of atmospheric ν_μ and $\overline{\nu}_\mu$ is simulated in the energy range $10^2 - 10^8$ GeV and over the full solid angle. As discussed before, the atmospheric neutrino flux is the result of the interaction of cosmic ray with the atmosphere and is characterised by two main components: the "conventional flux" due to pions and kaons and their subsequent decay chains, and the "prompt" contribution due to the decay of mesons containing heavy quarks. In this work, the events are weighted to reproduce the conventional atmospheric neutrino flux following the Bartol model [119]. A prompt contribution is also taken into account. The models in [123, 124] have been considered and the model with the highest neutrino flux, corresponding to the highest prediction of the Recombination Quark Parton Model (RQPM) [135], has been used in the present analysis. Fig. 6.7 shows the energy distributions of the atmospheric and source neutrinos reconstructed up to 6° above the horizon and within 1° from the source.

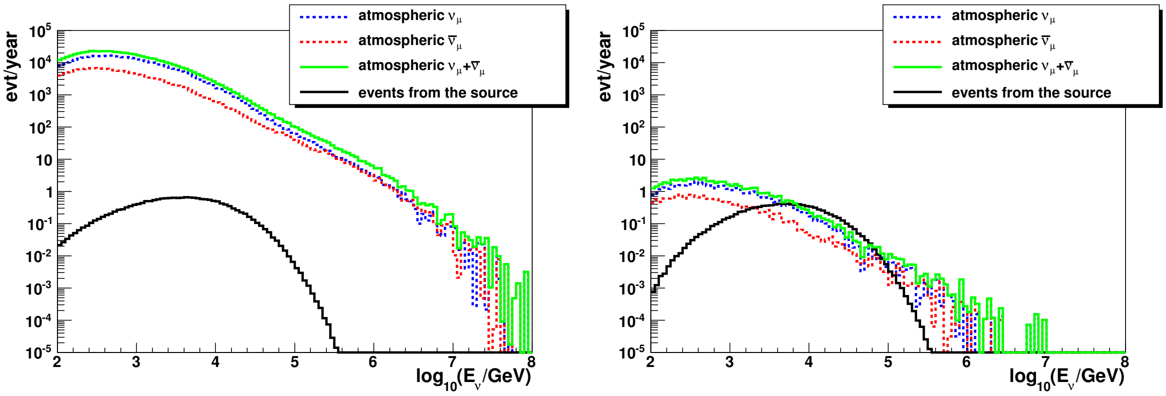

Figure 6.7: Energy of the reconstructed atmospheric ν_μ and $\bar{\nu}_\mu$ events and of the neutrinos coming from the source assuming the energy spectrum of eq. 6.21. In the left panel only events reconstructed up to 6° above the horizon are considered. In the right plot the condition that the reconstructed track is within 1° from the source is added.

The generation of atmospheric muons is a time consuming task, therefore only a small production of atmospheric muons have been simulated only for the reference detector trough the MUPAGE code (see section 4.3). This production consists in a sample with $1\,\mathrm{TeV} \leq E_b < 10\,\mathrm{TeV}$, where E_b is the sum of energies of all single muons in a bundle. This sample is statistically equivalent to a live time of 47 min. To efficiently increase statistics in the high-energy region, an additional sample equivalent to 10 h of live time has been generated with $E_b \geq 10\,\text{TeV}$. The events have been reweighted to obtain the expected number of events in one year of data taking.

Atmospheric muons have not been included in the calculations when the reference detector is compared to other layouts. However, the presence of this background has been taken into account selecting only events up to 6° above the horizon. In fact, a depletion of the muon flux at a depth of 3500 m where the detector will be located (CapoPassero site) is expected, allowing to look few degrees above the horizon. The behaviour of atmospheric muons can be checked trough the generated samples.

Fig. 6.8 shows, on the left, the distribution of the generated and reconstructed zenith angle for atmospheric muons. In the reference system of these simulations, events with $\theta < 90°$ are upgoing while events with $\theta > 90°$ are downgoing.

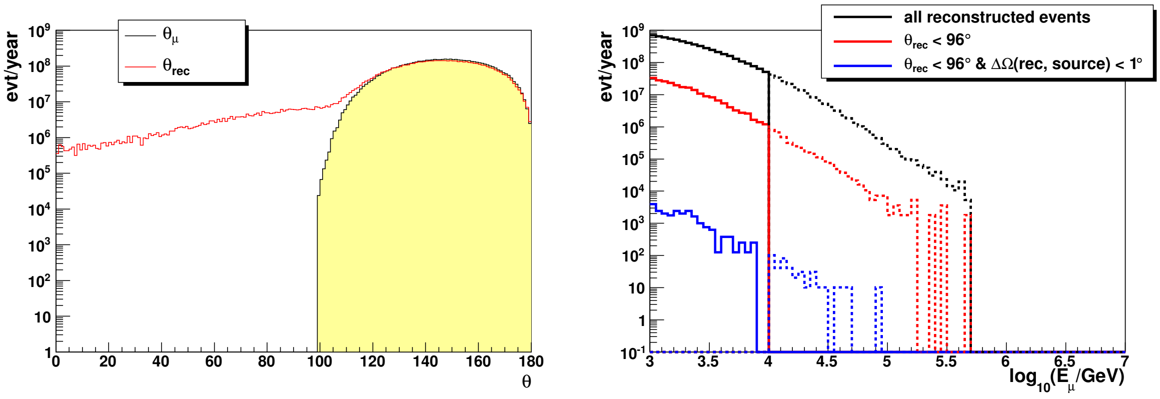

Figure 6.8: Left panel: atmospheric muons zenith angle at generation and reconstruction level. Right panel: atmospheric muon energy spectrum for three different event selections. The solid lines refer to the muons generated with $1\,\text{TeV} \leq E_b < 10\,\text{TeV}$, while the dashed lines refer to muons with $E_b \geq 10\,\text{TeV}$.

The muon energy spectrum for all the reconstructed events is shown in the right panel of fig. 6.8. The atmospheric muon background is strongly reduced considering only events with $\theta < 96°$ and considering only events within 1° from the source.

6.3.2 Event selection

In order to reduce the large amount of misreconstructed downgoing muons and atmospheric neutrinos and to select the best reconstructed events in our data sample, some quality cuts have to be applied to reconstructed events. As discussed in sec. 6.2, the sensitivity and discovery potential calculated with the binned method are optimised with cuts on the radius of the search cone around the source position R_{bin}, on the number of hits used during the reconstruction N_{hit}, on the quality fit parameter Λ and on the uncertainty on the direction of the reconstructed track β. An example of the differences in the distribution of these quantities between atmospheric muons, atmospheric neutrinos and signal neutrinos is given in fig. 6.9 where only events reconstructed up to 6° above the horizon and within 1° from the source centre are considered. The plots show for each value of a given variable x' the numbers of events of different species that have $x > x'$. In this way a cumulative distribution is obtained. The parameter Λ is

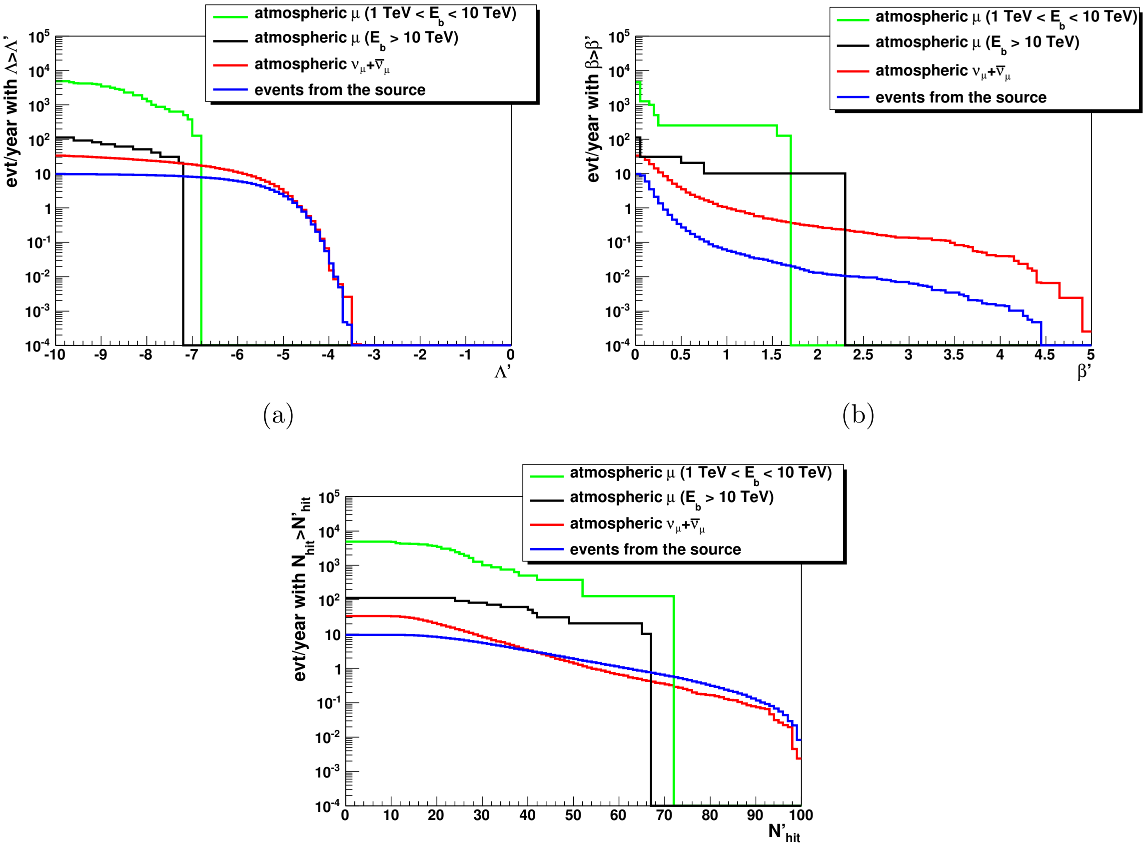

(a)

(b)

(c)

Figure 6.9: Cumulative distributions of the variables Λ, β and N_{hit} for events reconstructed with $\theta_{rec} \leq 96°$ and an angular distance from the centre of the RXJ1713.5-3946 $\Delta\Omega(rec, source) < 1°$. In figs. 6.9(b) and 6.9(c) an additional cut $\Lambda \geq -10$ is applied .

the more efficient to distinguish muon from neutrino events (see fig. 6.9(a)) while an appropriate cut on N_{hit} permit to select a sample of events with a number of signal neutrinos larger than the atmospheric neutrinos (see fig. 6.9(c)).

6.3.3 Results

Sensitivity

In order to optimise the detector geometry with respect to the distance between the DUs, several detector design have been considered. In particular, simulations have been performed for four possible distances between the DUs (90, 100, 115, 130 m). The method used for the sensitivity calculation is described in sec. 6.2.2 and the results are shown in fig. 6.10 as a function of the DU distance. The sensitivity flux Φ_{90} has the same functional dependence on the energy as the source flux, but a different normalisation factor k_{90}. Therefore in this case:

$$\Phi_{90}(E) = k_{90} \times \left[\frac{E}{\text{TeV}}\right]^{-1.72} e^{-\sqrt{E/2.1\text{TeV}}} \tag{6.22}$$

Table 6.2 contains the cuts that minimise the sensitivity for the 4 different layouts as well as the corresponding values of MRF and k_{90}. The sensitivity is calculated for one observation year. In general, for all the calculations presented here, different combinations of the cuts exist that give the same flux or a close value. Only one of the possible combinations is reported in the following tables.

Table 6.2: Model rejection factor (MRF) and normalisation factor of the flux sensitivity (k_{90}) for one observation year, with the cuts that minimise it for the four considered distances between DUs. The corresponding number of atmospheric neutrinos ν_{atm} and signal events ν_s are reported.

DU Distance	β	Λ	N_{hit}	R_{bin}	$k_{90}(\text{GeV}^{-1}\text{s}^{-1}\text{cm}^{-2})$	MRF	ν_{atm}	ν_s
90	1°	-7	26	0.74°	1.65×10^{-14}	0.98	7.0	5.8
100	1°	-7	21	0.74°	1.61×10^{-14}	0.96	7.5	6.0
115	1°	-7	13	0.74°	1.68×10^{-14}	1	7.2	5.9
130	1°	-7	14	0.74°	1.75×10^{-14}	1.04	6.0	5.5

In fig. 6.10 the sensitivity is reported for one observation year in terms of the flux in eq. 6.22 at $E_\nu = 1$ TeV. The minimum is reached for a distance of about 100 m.

Discovery potential (binned method)

As in the case of the sensitivity flux, the discovery flux can be written as:

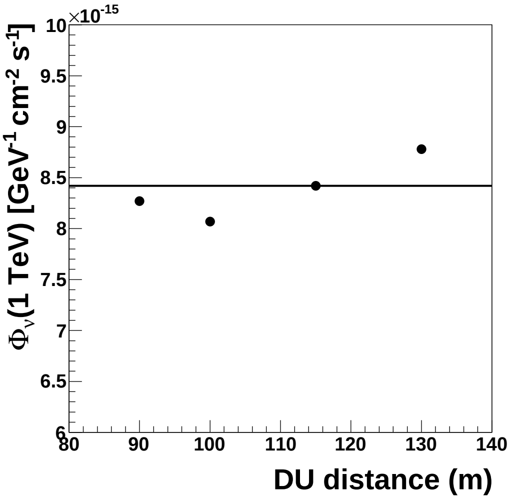

Figure 6.10: Flux sensitivity (90% CL) at 1 TeV of the full KM3NeT detector as a function of string distances for the source RX J1713.7-3946. The continuous line represents the 1 TeV flux value of eq. 6.21.

$$\Phi_{5\sigma}(E) = k_{5\sigma} \times \left[\frac{E}{\text{TeV}}\right]^{-1.72} e^{-\sqrt{E/2.1\text{TeV}}} \tag{6.23}$$

Table 6.3 contains the cuts that minimise the discovery flux calculated with the binned method (see sec. 6.2.1) after one observation year for the four different distances between DUs, fixing the significance at 5σ (3σ in Tab. 6.4) and the confidence level at 50%. The resulting values of the MDP and $k_{5\sigma}$ in tab. 6.3 confirm that among the 4 considered options, the layout with 100 m distance between DU is more suitable for the search of RXJ 1713.7-3946.

Table 6.3: Model dscovery potential (MDP) and normalisation factor of the discovery flux ($k_{5\sigma}$) with the cuts that minimise it for the four considered distances between DUs. The corresponding number of atmospheric neutrinos ν_{atm} and signal events ν_s are reported.

DU Distance	β	Λ	N_{hit}	R_{bin}	$k_{5\sigma}$(GeV^{-1}s^{-1}cm^{-2})	MDP	ν_{atm}	ν_s
90	1°	-7	27	0.70°	4.79×10^{-14}	2.85	5.9	15.6
100	1°	-7	20	0.74°	4.69×10^{-14}	2.79	7.9	17.8
115	1°	-7	21	0.70°	4.89×10^{-14}	2.91	4.9	14.7
130	1°	-7	22	0.70°	5.04×10^{-14}	3.00	3.6	13.1

The effect of the atmospheric muon background has been checked for the reference detector. With the addition of the muon events in the calculation, the same discovery

Table 6.4: Model dscovery potential (MDP) and normalisation factor of the discovery flux ($k_{3\sigma}$) with the cuts that minimise it for the four considered distances between DUs. The corresponding number of atmospheric neutrinos ν_{atm} and signal events ν_s are reported.

DU Distance	β	Λ	N_{hit}	R_{bin}	$k_{3\sigma}(\mathrm{GeV}^{-1}\mathrm{s}^{-1}\mathrm{cm}^{-2})$	MDP	ν_{atm}	ν_s
90	1°	-7	31	0.68°	2.63×10^{-14}	1.56	4.2	7.5
100	1°	-7	25	0.66°	2.57×10^{-14}	1.52	4.8	7.9
115	1°	-7	15	0.70°	2.72×10^{-14}	1.62	6.6	9.1
130	1°	-6.9	23	0.68°	2.73×10^{-14}	1.63	3.1	6.6

flux reported in Tab. 6.3 is obtained but with more stringent cuts ($\beta = 0.5$, $\Lambda = -7$, $N_{hit} = 21$ and $R_{bin} = 0.69°$). The effect of these cuts is shown in fig. 6.11 where the energy distribution of atmospheric ν_μ and $\bar{\nu}_\mu$ and source neutrinos is plotted only for the events having $\beta \leq 0.5$, $\Lambda \geq -7$, $N_{hit} \geq 21$ and $R_{bin} \leq 0.69°$.

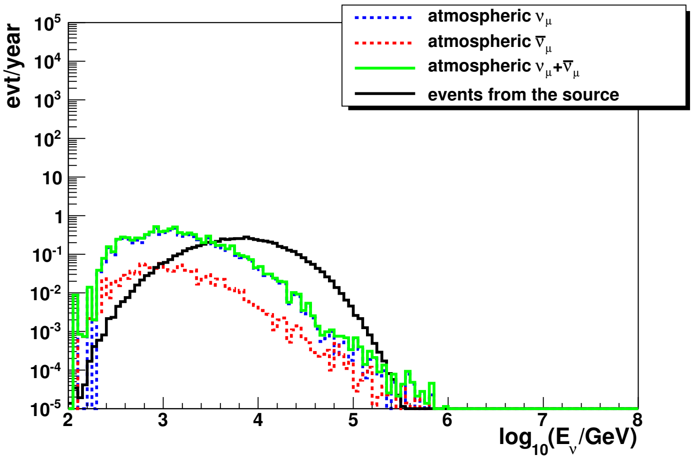

Figure 6.11: Energy of the reconstructed atmospheric ν_μ and $\bar{\nu}_\mu$ events and of the neutrinos coming from the source RXJ 1713.7-3946 applying the cuts optimised in the discovery potential calculation ($\beta \leq 0.5$, $\Lambda \geq -7$, $N_{hit} \geq 21$ and $R_{bin} \leq 0.69°$). Only events reconstructed up to 6° above the horizon are considered.

The trend of the discovery flux as a function of the number of observation years is shown in fig. 6.12. The discovery flux reaches the flux expected from the source after about 6 observation years. The number of years required to claim the discovery at 5σ and 3σ for different DUs distance are reported in tab. 6.5 and 6.6 together with the corresponding quality cuts and is also shown in fig. 6.13.

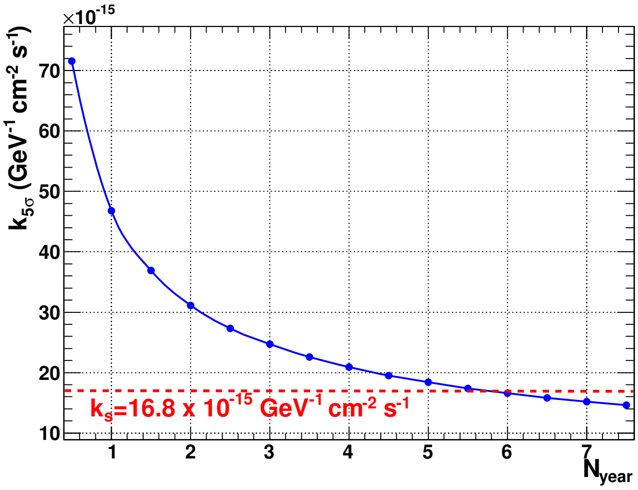

Figure 6.12: Normalisation factor of the discovery flux calculated at a significance of 5σ and a CL of 50% as a function of the number of observation years for the reference detector. The horizontal red dashed line is the normalisation factor of the flux expected from the RXJ 1713.7-3946.

Table 6.5: Number of years $N_{year}^{5\sigma}$ to claim the discovery (5σ, 50% CL) with the cuts that minimise the discovery flux for the four considered distances between DUs. The corresponding number of atmospheric neutrinos ν_{atm} and signal events ν_s are reported.

DU Distance	β	Λ	N_{hit}	R_{bin}	$N_{year}^{5\sigma}$	ν_{atm}	ν_s
90	1°	-6.8	36	0.68°	6.2	17.1	24.6
100	1°	-6.9	30	0.66°	5.9	19.0	25.7
115	1°	-6.7	24	0.62°	6.6	19.5	26.1
130	1°	-6.9	23	0.64°	6.5	17.7	25.0

Discovery potential (unbinned method)

The unbinned method is applied only to the reference detector for the discovery potential calculation. As discussed in sec. 6.2.3, the key ingredients of the method are the probability density functions for the signal and the background as a function of the distance of the reconstructed tracks from the source, $P_{sig}(\alpha)$ and $P_{bkg}(\alpha)$. These quantities are obtained from the Monte Carlo simulations as the normalised distributions of α and are shown in fig. 6.14 in the case of the SNR RXJ 1713.7-3946 source.

The behaviour of the $P_{sig}(\alpha)$ depends on the angular errors of the reconstruction procedure but also on the source extension of 0.6° used in the neutrino generation. $P_{sig}(\alpha)$ is plotted up to $\alpha = 5°$ since its value can be considered null for larger values of

Table 6.6: Number of years $N_{year}^{3\sigma}$ to claim the discovery (3σ, 50% CL) with the cuts that minimise the discovery flux for the four considered distances between DUs. The corresponding number of atmospheric neutrinos ν_{atm} and signal events ν_s are reported.

DU Distance	β	Λ	N_{hit}	R_{bin}	$N_{year}^{3\sigma}$	ν_{atm}	ν_s
90	1°	-7	30	0.70°	2.2	10.5	11.2
100	1°	-7	30	0.68°	2.1	7.2	9.5
115	1°	-7	13	0.70°	2.4	16.1	13.5
130	1°	-7	23	0.68°	2.3	7.2	9.5

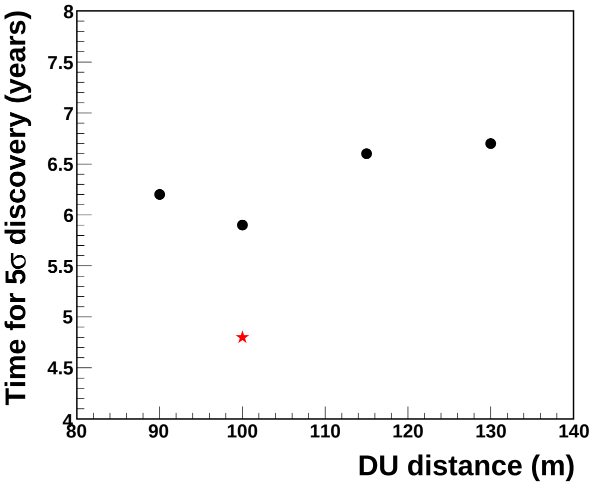

Figure 6.13: Number of years to claim the discovery (5σ, 50% CL) of the full KM3NeT detector as a function of string distances for the source RX J1713.7-3946 calculated with the binned method (black points). The red star shows the result for the unbinned search method at 100 m DU distance (this result will be discussed in the next section).

α.

Another important step in the unbinned procedure is the preparation of the background event samples to be analysed. To obtain an accurate result many samples are needed. In this case 20000 samples are used. Each sample contains a number of events equal to the number of expected atmospheric neutrinos in a given period of time Δt. Previous studies show that the results improve by applying quality cuts to select the events. The best approach should be to optimise the cut that minimise the discovery flux as in the binned method but, since the unbinned strategy is time consuming, the same cuts on Λ, N_{hit} and β that optimise the discovery flux calculated with the binned method have been used. In particular, to speed up the algorithm, the discovery flux has been calculated for $\Delta t = 0.5$ years. In this case the cuts that optimise the binned dis-

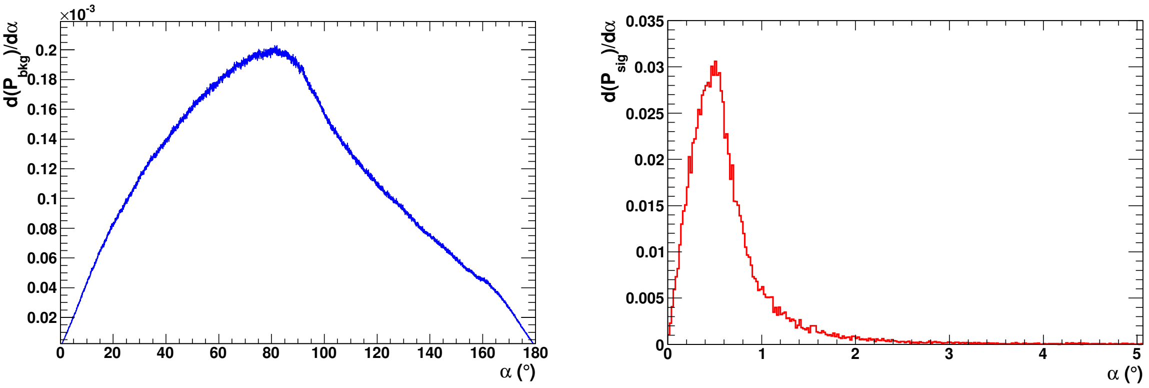

Figure 6.14: Probability density function for the signal (right panel) and for the background (left panel) calculated as the angular distance from the centre of the source SNR RXJ 1713.7-3946.

covery flux are $\Lambda \geq -7$, $N_{hit} \geq 21$, $\beta \leq 0.5°$. The number of expected events obtained applying these cuts on the full sky samples is:

- 4.24 signal events (Kelner flux of eq. 6.21);
- 50224.1 atmospheric neutrinos;
- 18795.6 atmospheric antineutrinos.

Each background sample contains 69020 background events provided as couples of declination δ_i and right ascension RA_i corresponding to the reconstructed tracks, randomising the time of the generated events. After applying the unbinned procedure the maximum value of LR, LR^{max} is stored for each sample and the integral of the cumulative distribution of LR^{max} is shown in fig. 6.15. This plot shows for each value of LR_i^{max} the integral of the normalised LR^{max} distribution for $LR^{max} > LR_i^{max}$. This distribution is fitted to an exponential (red dashed lines) and the values corresponding to 5σ and 3σ significance of the test statistic, $LR_{5\sigma}$ and $LR_{3\sigma}$, are indicated. The value of $LR_{3\sigma}$ can be extracted directly from the histogram while $LR_{5\sigma}$ is extrapolated from the exponential function.

The procedure is then repeated adding to the sample of background events a number N_{signal} of simulated signal events. The distribution of LR^{max} and n_{sig} obtained after maximisation of eq. 6.13 are shown in fig. 6.16 for different values of N_{signal}.
The integrals for $LR^{max} > LR_{3\sigma}$ and for $LR^{max} > LR_{5\sigma}$ give the probabilities, $P_{3\sigma}$ and $P_{5\sigma}$, of making a discovery at the 3σ and 5σ significance level. $P_{3\sigma}$ and $P_{5\sigma}$ are shown

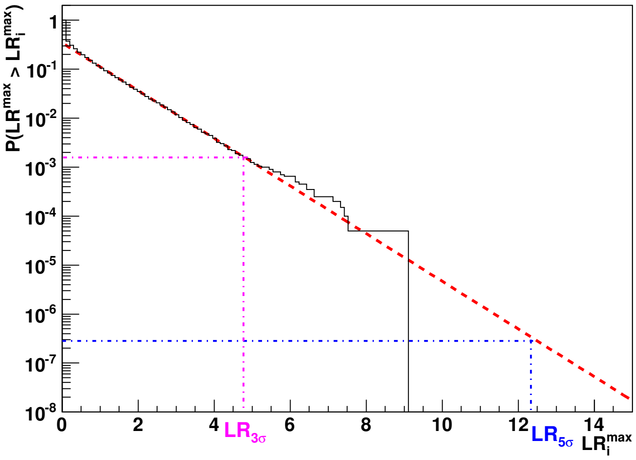

Figure 6.15: Cumulative distribution of the LR^{max} value extracted during the analysis for the source SNR RXJ 1713.7-3946. The red dashed line is the exponential function that fits the histogram. The values corresponding to 5σ and 3σ significance of the test statistic are shown.

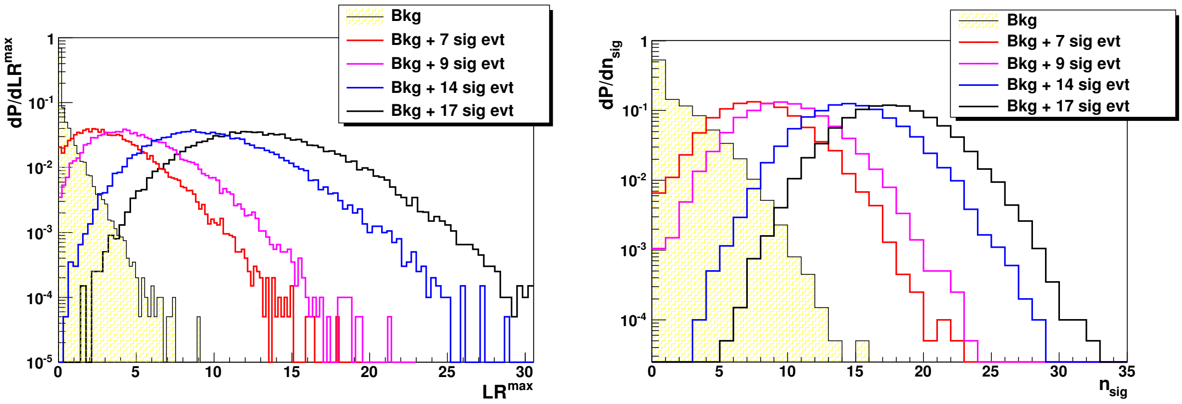

Figure 6.16: LR^{max} distribution (left) and fitted number of signal events (right).

in fig. 6.17 as a function of N_{signal}.

Fixing $P_{3\sigma} = P_{5\sigma} = 50\%$, the corresponding values $n_{3\sigma} = 8.4$ and $n_{5\sigma} = 16.0$ represent the number of events that lead to an observation with a p-value less than 3σ and 5σ, respectively, in 50% of the experiments. The corresponding discovery fluxes are:

$$k_{3\sigma} = 1.68 \times 10^{-14} \frac{8.4}{4.24} = 3.33 \times 10^{-14}\,\mathrm{GeV}^{-1}\,\mathrm{s}^{-1}\,\mathrm{cm}^{-2}$$

$$k_{5\sigma} = 1.68 \times 10^{-14} \frac{16}{4.24} = 6.34 \times 10^{-14}\,\mathrm{GeV}^{-1}\,\mathrm{s}^{-1}\,\mathrm{cm}^{-2}$$

These fluxes are 10% lower then the results obtained with the binned method, as indicated in tab. 6.7. This percentage of improvement has been confirmed repeating the

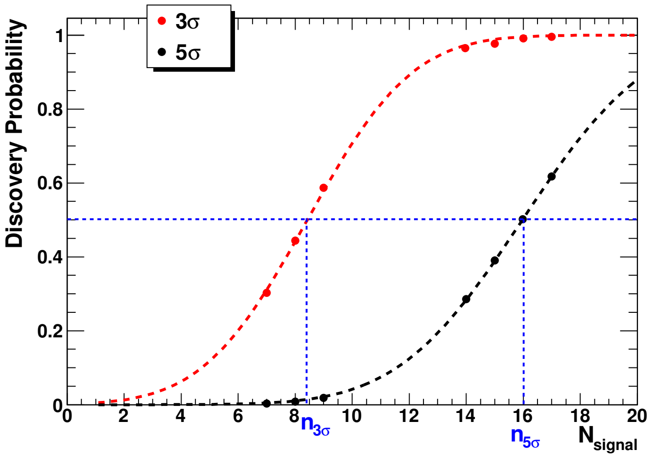

Figure 6.17: Probability for a 3σ (red points) and 5σ (black points) discovery as a function of the number of signal events added to each background sample. The points obtained by the analysis are fitted with a cumulative Gaussian distribution. The horizontal dotted blue line corresponds to the probability to make a discovery in 50% of the pseudo-experiments.

analysis for 1.5 observation years.

Table 6.7: Comparison between the binned and unbinned method in terms of the discovery flux calculated at 0.5 observation years. The normalisation factors of the fluxes are expressed in unit of $\text{GeV}^{-1}\,\text{s}^{-1}\,\text{cm}^{-2}$ and the percentage of improvement gained with the unbinned approach is also indicated.

Significance	k_{binned}	$k_{unbinned}$	Improvement
3σ	3.82×10^{-14}	3.33×10^{-14}	13%
5σ	7.09×10^{-14}	6.34×10^{-14}	11%

In order to calculate the number of year needed for the 3σ and 5σ discovery of the RXJ 1713.7-3946, the curve of fig. 6.12 is scaled reducing all the fluxes by 10%, as shown in fig. 6.18.

The summary of the number of year needed for the RXJ 1713.7-3946 discovery, calculated with the binned and unbinned method is reported in tab. 6.8

6.4 Vela X

Vela X is one of the nearest pulsar wind nebulae and it is associated with the energetic Vela pulsar PSR B0833-45. Even if PWNe are generally treated as leptonic sources, interpretation of TeV γ-ray emission from Vela X in terms of hadronic interaction is

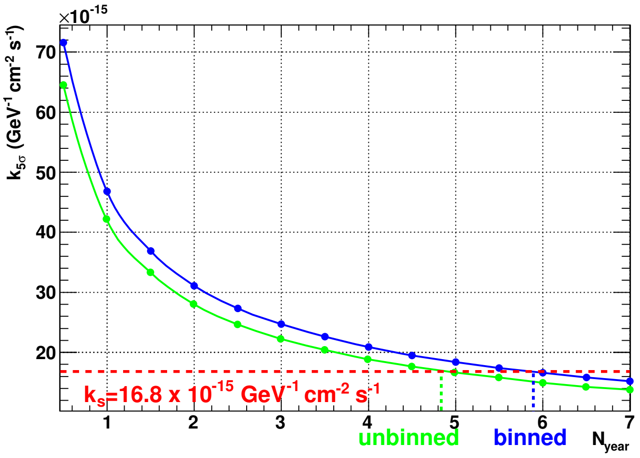

Figure 6.18: Zoom of fig. 6.12. The green line is obtained reducing the discovery flux by the 10%.

Table 6.8: Number of years N_{year} to claim the discovery at 5σ and 3σ with 50% CL.

Significance	N_{year}^{binned}	$N_{year}^{unbinned}$
3σ	2.1	1.8
5σ	5.9	4.8

discussed by some authors (see i.e. [189] [190]). The first VHE γ-ray emission from Vela X was reported by the HESS Collaboration [191] and was found to be coincident with a region of X-ray emission discovered with ROSAT as a filamentary structure extending south-west from the pulsar to the centre of Vela X. The high-energy γ-ray observation has been recently updated [192] with data from the 2005-2007 and 2008-2009 observation campaigns and using a more accurate method for the background subtraction. The new data are characterised by a higher gamma-ray flux and a harder energy spectrum.

For the analysis in [192], events in the Vela X region within a radial distance of 1.2° around the central position α = 08$^{\rm h}$ 35$^{\rm m}$00$^{\rm s}$, δ = -45° 36′00″ (J2000) are considered. A differential energy spectrum extracted from the inner region (within a radius $<$ 0.8°) of Vela X is shown in the left panel of fig. 6.19 in red. The best approximation of the energy spectrum in the ineer region corresponds to an exponentially cut-off power-law function ($\mathrm{d}\Phi(E)/\mathrm{d}E = N_0(E/1\mathrm{TeV})^{-\Gamma}e^{-E/E_{\rm cut}}$) with an index Γ=1.36 $\pm$ 0.06$_{\rm stat}$ $\pm$ 0.12$_{\rm sys}$, a cutoff energy $E_{\rm cut}$=(13.9 $\pm$ 1.6$_{\rm stat}$ $\pm$ 2.6$_{\rm sys}$) TeV and N_0=(11.6 $\pm$ 0.6$_{\rm stat}$ $\pm$ 2.4$_{\rm sys}$) $\times$ $10^{-12}\,\mathrm{cm}^{-2}\,\mathrm{s}^{-1}\,\mathrm{TeV}^{-1}$. An analysis of the outer ring between 0.8° and 1.2° is

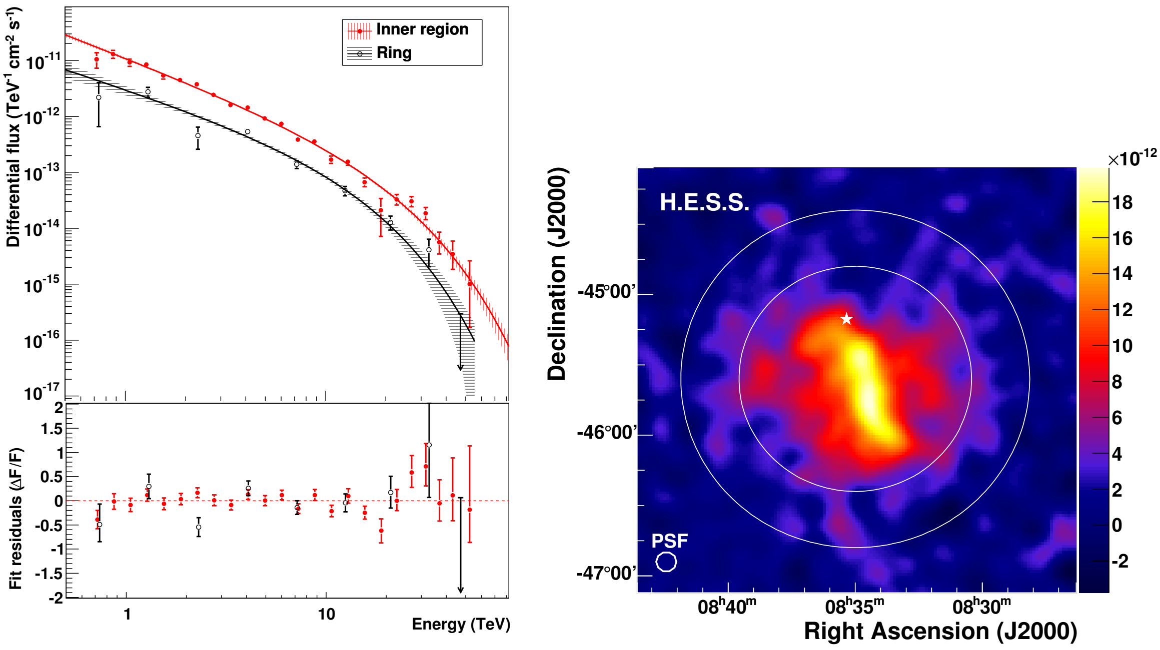

Figure 6.19: Left panel: differential γ-ray spectrum of Vela X in the TeV energy range. Filled red circles: inner integration region $< 0.8°$; open black circles: ring extension (between $0.8°$ and $1.2°$). Both spectra are fitted with a power law with exponential cutoff. The shaded bands correspond to the statistical uncertainty of the fit.
Right panel: HESS VHE γ-ray surface brightness (cm^{-2} s^{-1} deg^{-2}) of Vela X integrated between 0.75 TeV and 70 TeV. The circles are drawn with radii of $0.8°$ and $1.2°$, respectively, around the central position of the VHE γ-ray emission. The white star marks the position of the pulsar PSR B0833-45.

also included in [192] but in this thesis only the inner region has been considered.

The left panel of fig. 6.19 shows the surface brightness map of Vela X and its surroundings, revealing one of the largest objects in the VHE γ-ray domain.

In the hypothesis of a transparent source and 100% hadronic emission, from the γ-ray emission of the inner region the corresponding neutrino emission spectrum is derived using the Vissani prescription (see section 6.3) and is shown in fig. 6.20. The neutrino spectrum is parametrised as an exponentially cut-off power-law function of the form:

$$\Phi(E) = 7.2 \times 10^{-15} \left[\frac{E}{\mathrm{TeV}}\right]^{-1.36} e^{-(E/7\mathrm{TeV})}\,\mathrm{GeV}^{-1}\mathrm{s}^{-1}\mathrm{cm}^{-2} \tag{6.24}$$

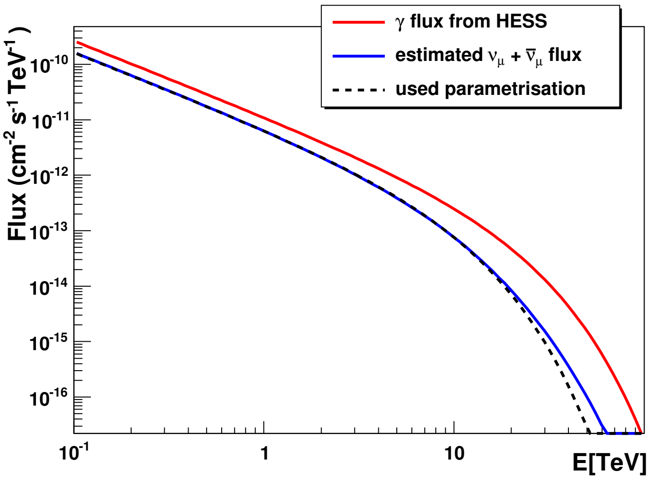

Figure 6.20: High energy γ-ray flux from HESS (red line) with the corresponding total muon neutrino and antineutrino flux (blue line) obtained with the Vissani prescription and the parametrisation using for this analysis (black dashed line) of the PWN Vela X.

6.4.1 Event generation

Neutrinos from the PWN Vela X have been generated with energies between 10^2 and 10^8 GeV and the source extension has been simulated as a flat spatial distribution within a disk with 0.8° radius centred at a declination $\delta = -45.6°$ that corresponds to an average visibility for a detector located in the Mediterranean Sea of 89.2%. The same background generated for the analysis of the SNR RXJ1713.7-3946 has been used also for the Vela X. In this case, only the reference detector (DU distance 100 m) has been considered. The energy distributions of the atmospheric and source neutrinos reconstructed as upgoing and within 1° from the source centre are shown in fig. 6.21.

Comparing the spectra fig. 6.21 with the corresponding spectra for the RXJ1713.7-3946 in fig. 6.7, the differences in the source spectra are visible. The number of events expected from the Vela X is higher then the number of expected atmospheric neutrinos in the energy region between about 4 TeV and 40 TeV, even without quality cuts.

6.4.2 Event selection

The criterions for the event selection are analogous to the ones discussed in sec. 6.3.2in the case of RXJ1713.7-3946. In fig. 6.22 the cumulative distributions of Λ, β and N_{hit} are shown for events reconstructed up to 6° above the horizon and within 1° from the source centre. Being the Vela X more intense and extended than the

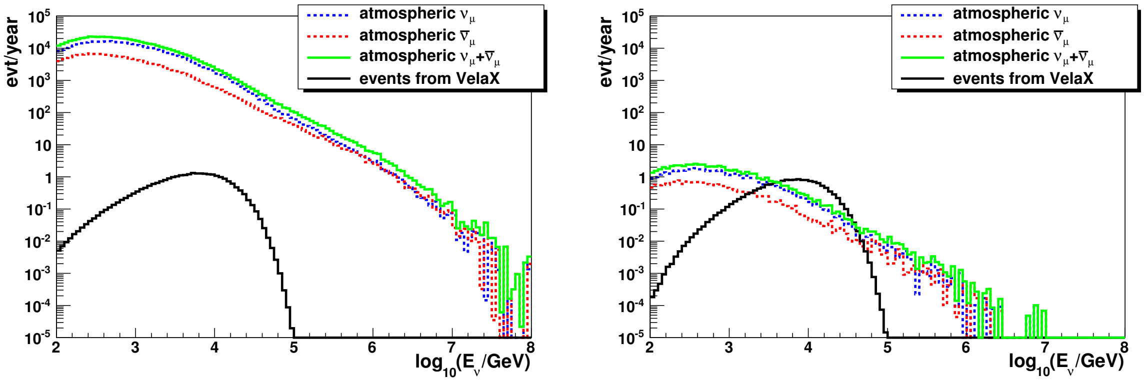

Figure 6.21: Energy of the reconstructed atmospheric ν_μ and $\bar{\nu}_\mu$ events and of the neutrinos coming from the Vela X assuming the energy spectrum of eq. 6.24. In the left panel only events reconstructed up to 6° above the horizon are considered. In the right plot the condition that the reconstructed track is within 1° from the source is added.

RXJ1713.7-3946, looser cut are required.

6.4.3 Results

For the Vela X, only the analysis with the binned method has been performed and the small atmospheric muon production has been included in the calculation. Both the sensitivity, Φ_{90}, and discovery flux, $\Phi_{5\sigma}$ or $\Phi_{3\sigma}$, can be written as:

$$\Phi_{90/5\sigma/3\sigma}(E) = k_{90/5\sigma/3\sigma}\left[\frac{E}{\text{TeV}}\right]^{-1.36} e^{-(E/7\text{TeV})} \tag{6.25}$$

The values of k_{90}, $k_{5\sigma}$ and $k_{3\sigma}$ for one observation year are indicated on tab. 6.9 with the corresponding quality cuts.

Table 6.9: Sensitivity and discovery flux, calculated for one year of observation. The cuts that minimise them, the values of MRF and MDP, and the corresponding number of atmospheric neutrinos ν_{atm} and signal events ν_s are also reported. No atmospheric muons remain after the cuts.

Parameter	β	Λ	N_{hit}	R_{bin}	k (GeV^{-1}s^{-1}cm^{-2})	MRF/MDP	ν_{atm}	ν_s
Sensitivity	1°	-6.9	25	0.91°	$k_{90} = 4.88 \times 10^{-15}$	MRF = 0.68	10.7	6.9
Discovery 3σ	0.5°	-6.8	25	0.89°	$k_{3\sigma} = 7.94 \times 10^{-15}$	MDP = 1.1	9.9	10.8
Discovery 5σ	1°	-6.9	23	0.87°	$k_{5\sigma} = 14.3 \times 10^{-15}$	MDP = 1.99	11.2	20.5

The cuts on the search cone around the source position are in general larger with respect to the analysis of RXJ1713.7-3946 since the source extension is larger. In fig.

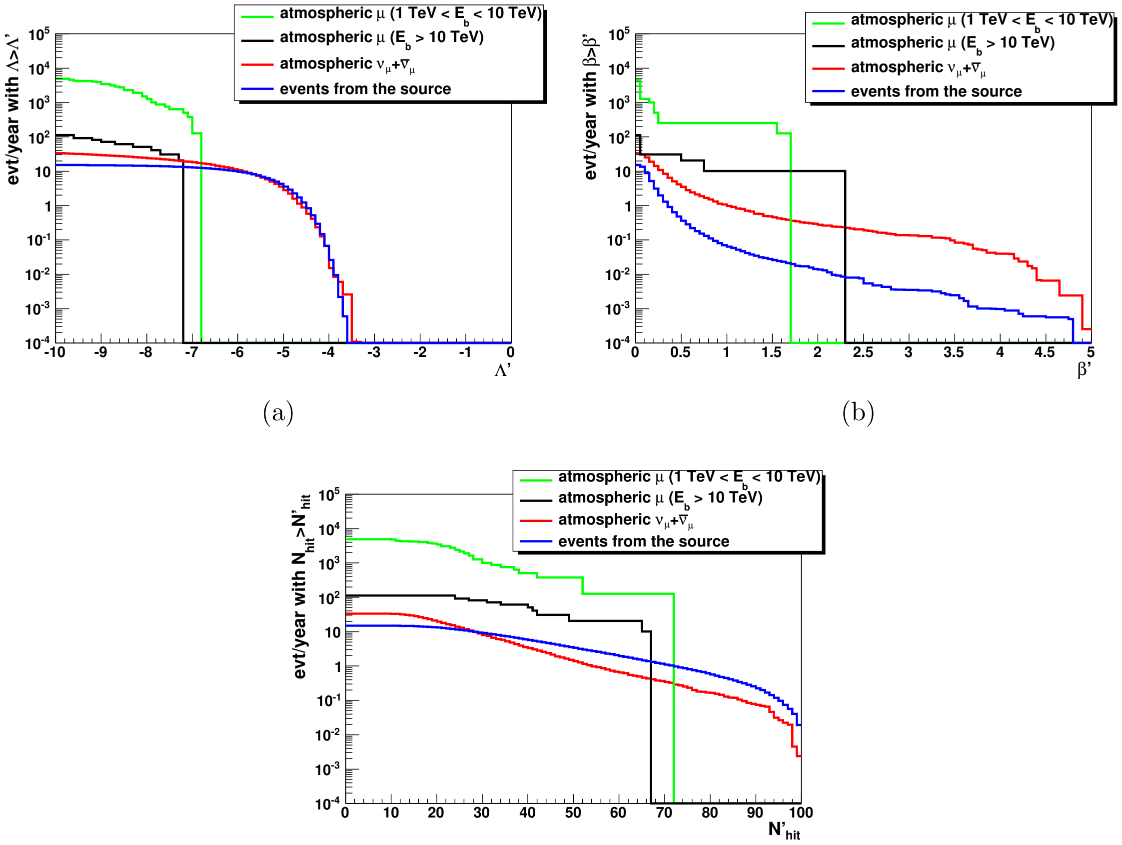

(a)

(b)

(c)

Figure 6.22: Cumulative distributions of the variables Λ, β and N_{hit} for events reconstructed with $\theta_{rec} \leq 96°$ and an angular distance from the source centre $\Delta\Omega(rec, source) < 1°$. In fig. 6.22(b) and 6.22(c) an additional cut $\Lambda \geq -10$ is applied.

6.23 the energy distribution of atmospheric ν_μ and $\bar{\nu}_\mu$ and source neutrinos is plotted for the events selected with the cuts that optimise the 5σ discovery flux.

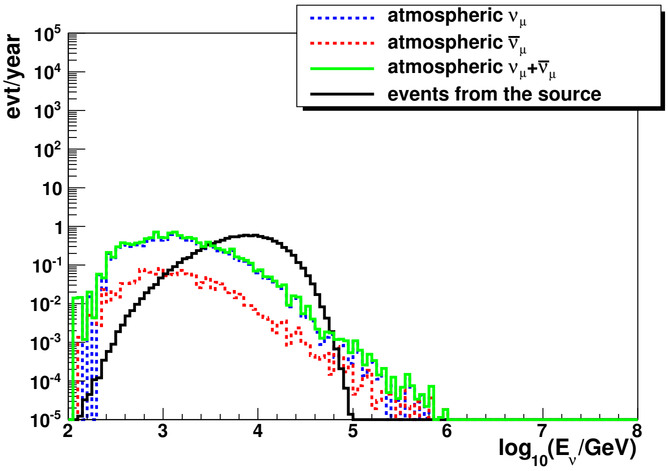

Figure 6.23: Energy of the reconstructed atmospheric ν_μ and $\bar{\nu}_\mu$ events and of the neutrinos coming from the Vela X applying the cuts optimised in the discovery potential calculation ($\beta \leq 1$, $\Lambda \geq -6.9$, $N_{hit} \geq 23$ and $R_{bin} \leq 0.87°$). Only events reconstructed up to 6° above the horizon are considered.

Fig. 6.24 shows the discovery flux as a function of the number of observation years. The discovery of the Vela X is expected after 3.3 years of data taking with requiring a significance of 5σ while, for a significance of 3σ, 1.2 years are needed. Tab. 6.10 contains the quality cuts relative to the discovery calculation.

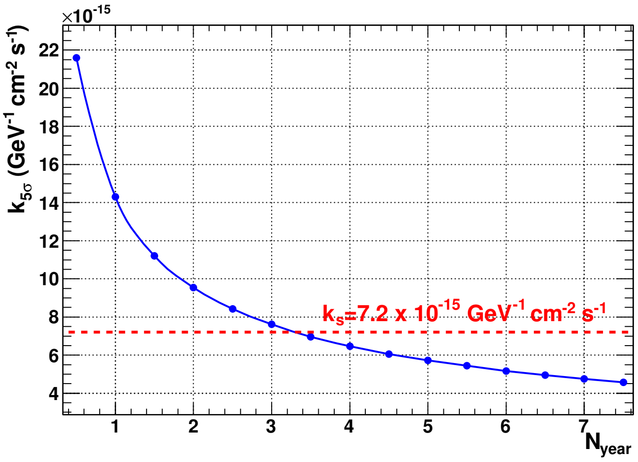

Figure 6.24: Normalisation factor of the discovery flux calculated at a significance of 5σ and a CL of 50% as a function of the number of observation years for the reference detector. The horizontal red dashed line is the normalisation factor of the flux expected from the Vela X.

Table 6.10: Number of years N_{year} to claim the discovery of Vela X at 5σ and 3σ with 50% CL. The corresponding quality cuts are indicated.The corresponding numbers of atmospheric neutrinos ν_{atm} and signal events ν_s collected after N_{year} are reported. No atmospheric muons remain after the cuts.

Parameter	β	Λ	N_{hit}	R_{bin}	N_{year}	ν_{atm}	ν_s
Discovery 3σ	0.5°	-6.8	25	0.84°	1.2	10.5	11.1
Discovery 5σ	0.5°	-6.9	25	0.86°	3.3	30.9	31.8

6.5 Point source with E^{-2} spectrum

In order to easily compare the KM3NeT performance with the existent neutrino telescopes Antares and Icecube, the sensitivity flux Φ_{90} and the 5σ discovery flux $\Phi_{5\sigma}$ have been calculated for a generic point-source with an E^{-2} flux for an observation time of 4 years. These Φ_{90} and $\Phi_{5\sigma}$ fluxes are shown in the left panel of fig. 6.25 as a function of the source declination. For reference the corresponding sensitivity values of Icecube and Antares are shown in the right panel (same figure of section 2.2.1).

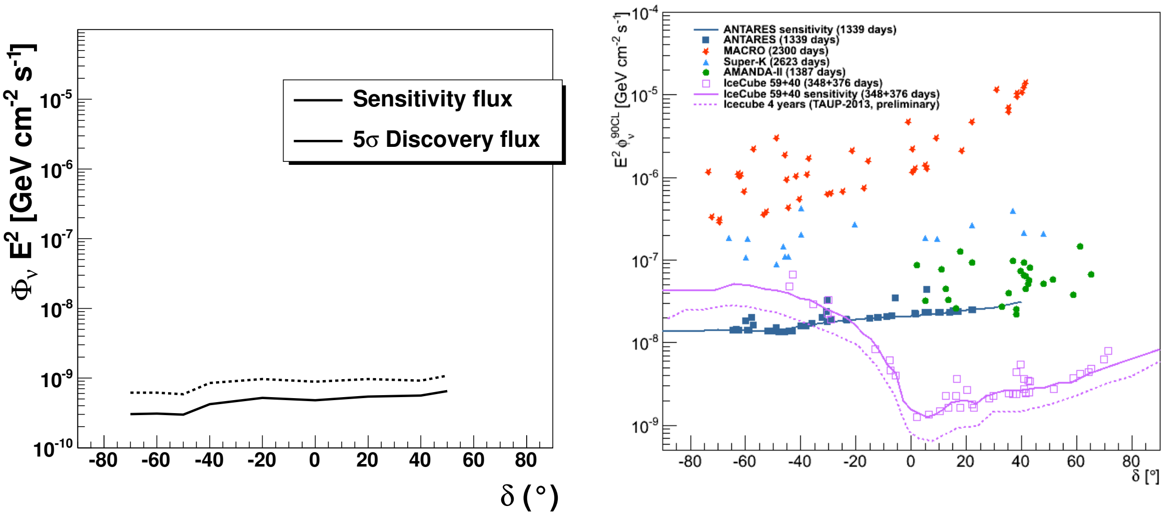

Figure 6.25: Left: 5σ discovery flux and sensitivity flux to a source with an E^{-2} spectrum for 4 observation years as a function of the declination. Right: upper limits and sensitivity flux to sources with an E^{-2} flux for the Antares and IceCube detector [147].

CHAPTER 7

ORCA FEASIBILITY STUDY

After the recent measurement of a non-zero value of the θ_{13} neutrino mixing parameter, the determination of the neutrino mass hierarchy (MH) has become a priority for many future neutrino experiments. The mass hierarchy can be determined using matter effects on oscillations inside the Earth. This, however, requires a long baseline, a very large detector and an intense beam. Cosmic ray interactions in the atmosphere give a natural beam of neutrinos. The IceCube and Antares detectors have already proven that the measure of the atmospheric neutrino oscillations is possible with the Cherenkov neutrino telescopes [193, 194].

The KM3NeT collaboration is undertaking a feasibility study "Oscillation Research with Cosmics in the Abyss" (ORCA), to evaluate the potential of a mass hierarchy measurement with a dedicated detector. In this chapter the motivation and the status of ORCA will be discussed.

7.1 Theoretical considerations

The experiments with solar, atmospheric and reactor neutrinos have provided compelling evidences for the existence of neutrino oscillations, described as transitions in flight between the different flavour neutrinos ν_e, ν_μ and ν_τ (or antineutrinos $\bar{\nu}_e$, $\bar{\nu}_\mu$ and $\bar{\nu}_\tau$), caused by nonzero neutrino masses and neutrino mixing [195]. In the formalism of the local quantum field theory, this means that the flavour neutrino fields $\nu_l(x)$ are linear combinations of the fields of three massive neutrinos $\nu_j(x)$:

$$\nu_l(x) = \sum_j U_{lj}\nu_j(x), \quad l = e, \mu, \tau. \tag{7.1}$$

The neutrino mixing matrix U is a unitary matrix often called Pontecorvo-Maki-Nakagawa-Sakata (PMNS) or Maki-Nakagawa-Sakata (MNS) mixing matrix. In the case of n neutrino flavours and n massive neutrinos, the $n \times n$ unitary neutrino mixing matrix U can be parametrised by $n(n-1)/2$ Euler angles and $n(n+1)/2$ phases. If the massive neutrinos ν_j are Dirac particles (ν_j and $\bar{\nu}_j$ are distinct particles), only $(n-1)(n-2)/2$ phases are physical and can be responsible for CP violation in the leptonic sector. If $n = 3$, U can be written as a function of 3 angles θ_{12}, θ_{13}, θ_{23} and a phase δ:

$$U = \begin{pmatrix} c_{13}c_{12} & c_{13}s_{12} & s_{13}e^{-i\delta} \\ -c_{23}s_{12} - s_{13}s_{23}c_{12}e^{i\delta} & c_{12}c_{23} - s_{13}s_{23}s_{12}e^{i\delta} & c_{13}s_{23} \\ s_{23}s_{12} - s_{13}c_{23}c_{12}e^{i\delta} & -c_{12}s_{23} - s_{13}c_{23}s_{12}e^{i\delta} & c_{13}c_{23} \end{pmatrix} \tag{7.2}$$

where s_{ij} and c_{ij} are the sine and cosine respectively of the mixing angle between state i and j.

The neutrino oscillation probabilities depend, in general, on the neutrino energy, E, on the source-detector distance L, on the elements of U and on $\Delta m^2_{ij} \equiv (m^2_i - m^2_j)$. These probabilities can be expressed as:

$$P(\nu_\alpha \to \nu_\beta) = \delta_{\alpha\beta} - 4\sum_{i>j} Re(U^*_{\alpha i}U_{\beta i}U_{\alpha j}U^*_{\beta j}) \cdot \sin^2\Phi_{ij} \pm 2\sum_{i>j} Im(U^*_{\alpha i}U_{\beta i}U_{\alpha j}U^*_{\beta j}) \cdot \sin^2\Phi_{ij} \tag{7.3}$$

where

$$\Phi_{ij} \equiv 1.27\frac{\Delta m^2_{ij}[\mathrm{eV}^2/\mathrm{c}^4]L[\mathrm{km}]}{E_\nu[\mathrm{GeV}]}$$

In the case of 3 neutrino mixing there are only two independent neutrino mass squared differences, say $\delta m^2 = m_2^2 - m_1^2 \neq 0$ and $\Delta m^2 = m_3^2 - (m_1^2 + m_2^2)/2 \neq 0$. The numbering of massive neutrinos is arbitrary. It proves convenient, to identify $|\delta m^2|$ with the smaller of the two neutrino mass squared differences, which, as it follows from the data, is responsible for the solar ν_e and reactor $\bar{\nu}_e$ oscillations. On the other hand, the larger neutrino mass square difference $|\Delta m^2|$, can be associated with the experimentally observed oscillations of the atmospheric ν_μ and $\bar{\nu}_\mu$ and accelerator ν_μ.

Usually it's assumed $m_1 < m_2$, so that $\delta m^2 > 0$. With these choices made, there are two possibilities: either $m_1 < m_2 < m_3$, or $m_3 < m_1 < m_2$, as depicted in fig 7.1. The first option is called "normal hierarchy" (NH) and gives $\Delta m^2 > 0$, the second one is indicated as "inverted hierarchy" (IH) and corresponds to $\Delta m^2 < 0$.

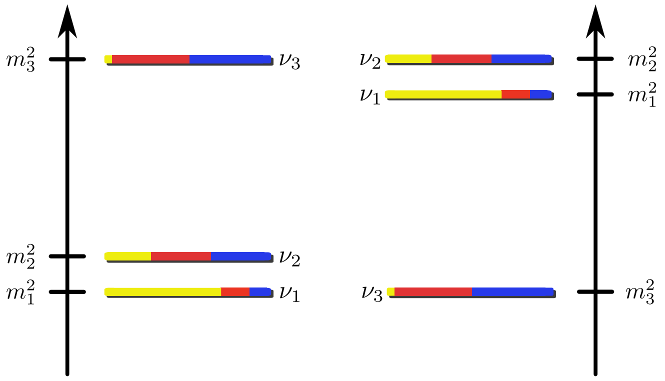

Figure 7.1: Graphical representation of the neutrino mass eigenstates. Yellow refers to ν_e, red stands for ν_μ and blue for ν_τ. Left column is the normal hierarchy while the right columns indicates the inverted hierarchy.

At present, no single oscillation experiment can sensitively probe the full parameter space spanned by (δm^2, $\pm\Delta m^2$, θ_{12}, θ_{13}, θ_{23}, δ). The result of a global analysis for both mass hierarchies, taken from [196], is reported in tab. 7.1.

Except from the phase δ, the oscillation parameters are constrained with significant accuracy but no hint exists about the sign of Δm. However, the recent measurement of θ_{13} [197, 198], whose value results larger than expected, opens up the possibility to determine the mass hierarchy (MH). In fact, matter effects that can allow to distinguish IH from NH depend on θ_{13}.

The presence of matter can change drastically the pattern of neutrino oscillation since neutrinos can interact with particles forming the matter. This induces an additional

Table 7.1: Results of the global 3ν oscillation analysis, in terms of best-fit values and allowed 1, 2 and 3σ ranges for the 3ν mass-mixing parameters [196]. We remind that Δm^2 is defined herein as $m_3^2 - (m_1^2 + m_2^2)/2$, with $+\Delta m^2$ for NH and $-\Delta m^2$ for IH.

Parameter	Best fit	1σ range	3σ range
$\delta m^2/10^{-5}$ eV^2 (NH or IH)	7.54	7.32 – 7.80	6.99 – 8.18
$\sin^2\theta_{12}/10^{-1}$ (NH or IH)	3.07	2.91 – 3.25	2.59 – 3.59
$\Delta m^2/10^{-3}$ eV^2 (NH)	2.43	2.33 – 2.49	2.19 – 2.62
$\Delta m^2/10^{-3}$ eV^2 (IH)	2.42	2.31 – 2.49	2.17 – 2.61
$\sin^2\theta_{13}/10^{-2}$ (NH)	2.41	2.16 – 2.66	1.69 – 3.13
$\sin^2\theta_{13}/10^{-2}$ (IH)	2.44	2.19 – 2.67	1.71 – 3.15
$\sin^2\theta_{23}/10^{-1}$ (NH)	3.86	3.65 – 4.10	3.31 – 6.37
$\sin^2\theta_{23}/10^{-1}$ (IH)	3.92	3.70 – 4.31	3.35 – 6.63
δ/π (NH)	1.08	0.77 – 1.36	—
δ/π (IH)	1.09	0.83 – 1.47	—

phase for ν_e and thus changes the oscillation probability in such a way that

$$P(\nu_\alpha \to \nu_\beta) - P(\bar{\nu}_\alpha \to \bar{\nu}_\beta) \neq 0$$

Mikheyev, Smirnov and Wolfenstein [199, 200] found that matter effect are expected to be important when the resonance condition,

$$\Delta m_{31}^2 \cos(2\theta_{13}) = 2\sqrt{2} G_F N_e E_\nu \tag{7.4}$$

is satisfied. In eq. 7.4, N_e is the electron number density in the medium and G_F is the Fermi constant. Depending on the sign of Δm_{31}^2, the presence of the matter leads to a resonance enhancement of one of the oscillations $\nu_\alpha \to \nu_\beta$ or $\bar{\nu}_\alpha \to \bar{\nu}_\beta$, and suppresses the other one. This disparity between the behavior of neutrinos and antineutrinos is a consequence of the fact that the matter is not charge-symmetric (it contains e$^-$, p and n, but does not contain their antiparticles) and therefore the oscillations in matter are neither CP nor CPT invariant. Making use of the different matter effects for neutrinos and antineutrinos seems therefore the ideal way to distinguish among the two possibilities: normal versus inverted mass hierarchy. In particular, upward going atmospheric neutrinos that traverse the Earth provide an excellent tool to tackle the neutrino mass ordering. For the Earth, the average electron number densities are $\bar{N}_e^{core} = 5.4\, N_A\,\mathrm{cm}^{-3}$ in the core and $\bar{N}_e^{mantle} = 2.2\, N_A\,\mathrm{cm}^{-3}$ in the mantle [201], with Avogadro's number N_A. Hence, from eq. 7.4, tha resonance takes place at energies $E_{res}^{core} \approx 3$ GeV for the core and $E_{res}^{mantle} \approx 7$ GeV for the mantle. The Earth density profile according to the PREM model [201] is shown in fig. 7.2. Given abrupt periodical changes in matter density, the mixing can be enhanced although the matter density is not at the resonance value. This phenomenon is known as "parametric enhancement" and an explanation can be found in [202].

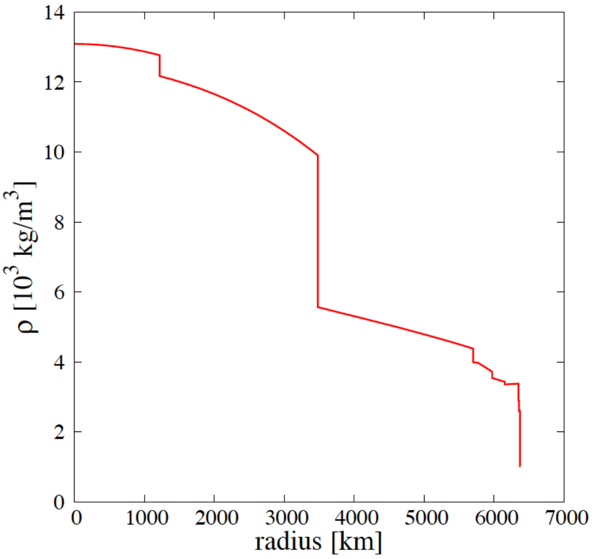

Figure 7.2: Earth density profile according to the PREM model [201].

Using as input the matter distribution of the PREM model and the central values of the neutrino parameters in tab. 7.1, the survival probabilities for muon and antimuon neutrinos have been calculated and are shown in fig. 7.3 as a function of the neutrino energy for several values of the zenith angle [203]. The bands show the uncertainty due to the present uncertainty in the mass squared differences and the mixing angles. From these figures it is clear that the survival probabilities for muon neutrinos with normal hierarchy are the same as those for muon antineutrinos with inverted hierarchy. However, since both atmospheric fluxes and cross sections are higher for neutrinos compared to antineutrinos, the differences survive. The largest effect is seen in a relatively small energy band around 5-10 GeV neutrino energy.

It should be noted that a limited energy and zenith angle resolution could wash out any measurable effect.

Deep sea (or deep ice) neutrino telescopes offer the possibility to make a MH determination using atmospheric neutrinos by taking benefit of the high statistics that can be accumulated and of the possibility to scan different zenith angles. On the other hand,

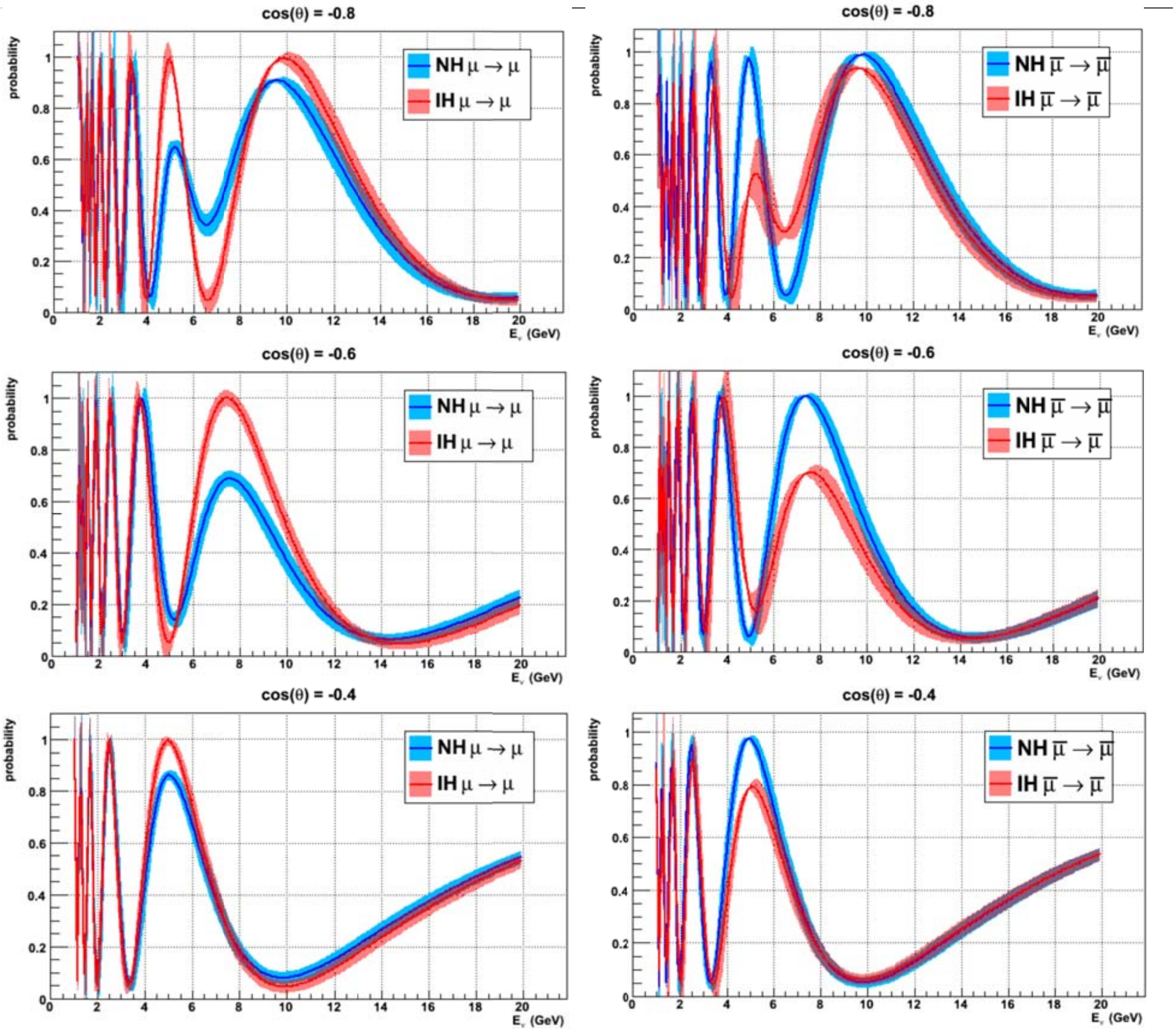

Figure 7.3: Survival probabilities for ν_μ (left) and $\bar{\nu}_\mu$ (right) passing through the Earth, as a function of energy and zenith angle, for normal and inverted hierarchy.

the measurement is affected by shortcomings related to flavour identification of events and to the accuracy on energy and angular reconstruction.

7.2 ORCA detector

The detector should provide sufficient resolution on the muon neutrino energy and its zenith angle as well as sufficient instrumented volume to detect enough events and reduce the statistical uncertainties. Background rejection of downgoing muons from cosmic ray interactions above the telescope is also a crucial issue.

At the energy of interest the muon energy estimation is based on a measurement of the range of the muon produced in the CC interaction of the muon neutrino (see fig.

2.5). Typically half of the neutrino energy is taken by the muon (about two thirds for antineutrinos; see fig. 2.9). On average, a muon of 6 GeV will travel about 25 m. A reasonable energy measurement therefore need Cherenkov light measurements distributed at a spacing of a few meters. The KM3NeT detector with the layout described in the chapters 4 and 5 is not suitable for this purpose. For ORCA, both the vertical and the horizontal spacing need to be reduced. Vertically this can essentially be done at will, while horizontally a limitation is imposed by the bending of the lines due to the sea currents. For a line with 6 m vertical spacing and 20 modules the maximum deviation at the top of the line is about 10 m assuming a sea current of 30 cm/s. In addition, the accuracy with which a string can be placed on the sea bottom is from Antares experience about 5 m [146]. It is assumed that the deployment of strings distant 20 m is feasible. Anything smaller may be possible but would require different deployment techniques. The collaboration therefore decided to start the feasibility study with a detector consisting of 1000 optical modules distributed, with 6 m spacing, over 50 strings placed in a semi-random pattern in a circular footprint (see figure 7.4). The technology adopted is the one described in sec. 3. The mean distance between strings is 20 m. The instrumented volume is about $1.75 \times 10^6\,\mathrm{m}^3$.

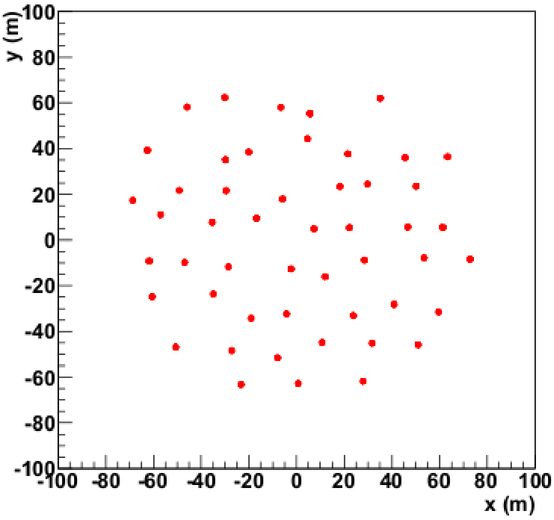

Figure 7.4: Position of the strings on the sea floor for the detector used in the simulations.

7.3 Sensitivity estimate with a toy analysis

A first estimate of the sensitivity to the mass hierarchy has been done for a detector with a volume of 1 Mton [203, 204]. The contamination of other neutrino flavours is not estimated at the moment. Algorithm to distinguish ν_μ and $\bar{\nu}_\mu$ are not available, thus the two species are summed. Additional assumptions are:

- the muon zenith angle is measured perfectly;
- events are selected with the neutrino vertex inside the instrumented volume and at least 15 hits;
- an energy resolution of 25% is considered.

If N_{NH} and N_{IH} are the rate of expected $\nu_\mu + \bar{\nu}_\mu$ events in the case of normal and inverted hierarchy, the relative difference between normal and inverted hierarchy can be written as $(N_{IH} - N_{NH})/N_{NH}$ and it is shown in fig. 7.5.

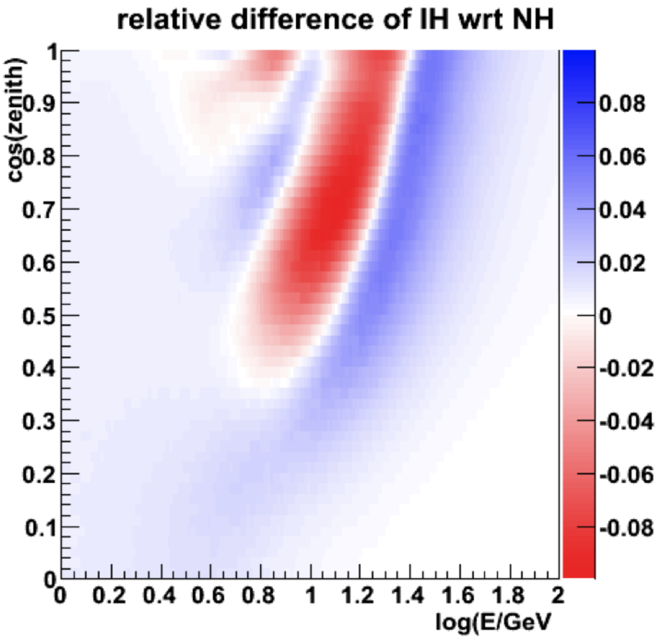

Figure 7.5: Relative difference between normal and inverted hierarchy with the assumption discussed in the text.

Applying the assumed resolutions and acceptance a maximum of about 10% difference remains between IH and NH.

A likelihood ratio test is used to estimate the probability of being able to exclude one hierarchy with a given significance. In fig. 7.6 the significance for a correct MH identification is shown as a function of the exposure expressed in Mton per year.

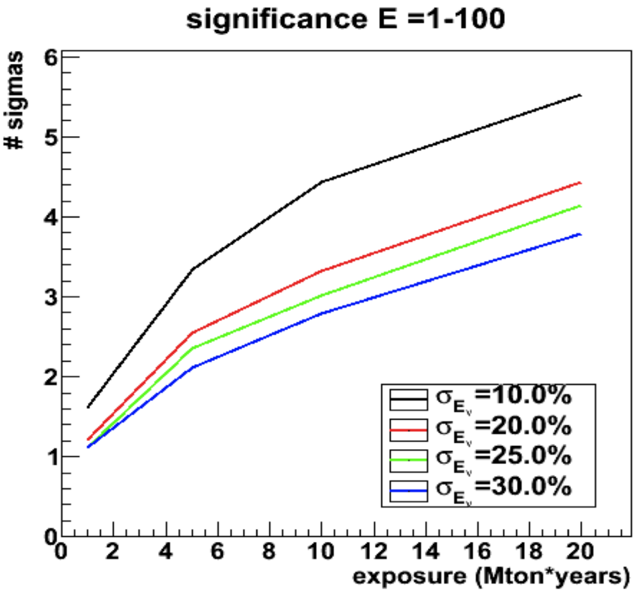

Figure 7.6: Relative difference between normal and inverted hierarchy with the assumption discussed in the text.

For instance a detector with an effective volume of 3 Mton and an observation time of 5 years is required to reach a significance of 3σ (5σ) if the energy resolution is 25% (10%). The energy resolution and the effective volume are therefore key parameters for this measurement.

7.4 Simulation

The codes described in cap. 4 have been used to generate and propagate neutrinos, simulate their charge-current interaction, generate the Cherenkov light due to muons and to the hadronic shower, add the optical background produced by ^{40}K decay in water. In particular, the `GENHEN` code, that was designed for the high energy regime ($E_\nu > 100$ GeV), has been checked for consistency in the low energy range ($E_\nu \approx 10$ GeV), against the more recent and used `GENIE` Monte Carlo code [205]. Only muon neutrino and anti-neutrino CC events are generated with energy between 2 GeV and 1 TeV.

For the high energy simulations ($E_\nu > 100$ GeV) discussed in Chapter 5, the hits produced by the hadronic shower have been neglected since the muon track is long enough ($\sim$ km) such that the interaction vertex is outside the instrumented volume. In the low energy regime ($E_\nu \approx 10$ GeV) considered here, the events are contained inside the instrumented volume and the spatial extension of the hadronic shower is comparable with the muon track length. A full simulation of the light due to the particles produced at the interaction vertex is then performed. For this purpose the code `GEASIM`, has been used (see section 4.4.2).

7.5 Reconstruction of the muon direction

The reconstruction described in Chapter 5 was optimised for high energy muon neutrinos ($E_\nu \gtrsim 100$ GeV) while, for the mass hierarchy determination, the energy of interest is smaller of one or two orders of magnitude. The considered detector is different too. The code has been then slightly modified to be adapted at the new conditions. The main changes concern the hit selection and the Pdf used in one of the fit steps.

7.5.1 Hit selection

The detector layout simulated for ORCA is much denser than the one used in Chapters 4 and 5. The hit selection can be adapted to this detector, taking advantage of the short distance between OMs to distinguish background and signal hit trough space-time coincidences. In fact, the time window used to identify a coincidence between two hits on two PMTs at a certain distance d is chosen as $\Delta t = t_{offset} + 2t_d$ (see sec. 5.2), where t_{offset} is a fixed offset and t_d is the time required by the light to travel the distance d. If d is reduced, Δt decreases. Therefore, the probability that two background hits, randomly generated, have a time difference less than the coincidence window will decrease too, since this probability is proportional to Δt. In other words, a dense detector allows a more efficient hit selection.

With respect to the coincidence patterns described in sec. 5.2, one additional pattern N0 is considered that consists of a coincidence between one L1 hit and one simple hit on OMs on nearby strings, in a time window $\Delta t = 10\,\mathrm{ns} + 2t_d$.

The “Causality filter” is also performed and only the hit with coincidence patterns more complex than L1 are used, while the others are discarded.

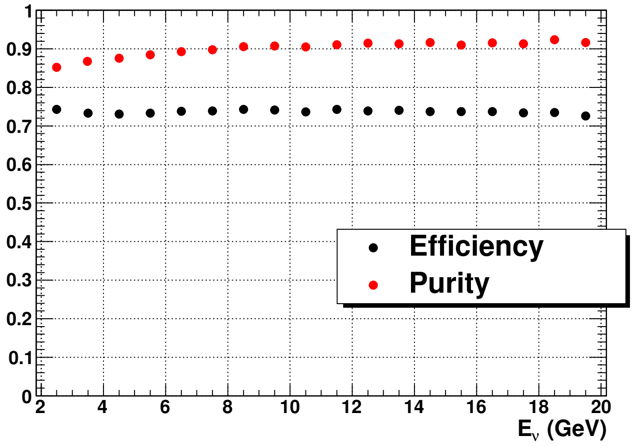

Figure 7.7: Efficiency and purity of the initial hit selection as a function of the neutrino energy (see text).

The performance of the hit selection is illustrated in fig. 7.7 in terms of the efficiency and purity, defined in section 5.2. The selection contains about 75% of the total number of signal hits. Among the total number of selected hits, 90% are true signal hits. For this calculation, all hits that are not due to the optical background are considered signal hits. In other words, both hits produced by the muon and the hadronic shower are identified as signal hits.

7.5.2 Fit steps

The steps of the algorithm described in Chapter 5 are the same for the version of the code discussed here. Only, the Pdf used in the step 3 (see sec. 5.6) has been adapted to the low energy regime keeping the same functional form. The likelihood function appears in this case as in fig. 7.8.

7.6 Muon vertex and track length estimate

A dedicated algorithm for the muon energy estimate is needed for the ORCA study. In this case, the selection of the events imply containment conditions. In fact, since the muon energy is estimated from the muon track length, the track has to be at least partially contained in the instrumented volume. For this reason an estimate of the position of the interaction vertex has been also studied. In addition, a vetoing system would be useful but it has not been implemented at the moment.

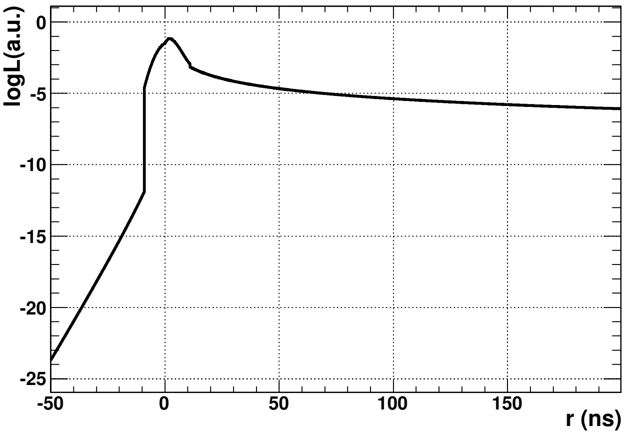

Figure 7.8: The likelihood function used in the third step of the fitting algorithm.

The estimate of the track length and of the vertex position proceeds trough different phases:

1. The detected photons are projected back to the track according to the Cherenkov angle. The first track length estimate, l'_μ is then defined as the distance between the position of the first and last projected photon on the track. The first projected photon is the first vertex estimate $\mathbf{V}'$. If the muon is generated inside or near the instrumented volume $\mathbf{V}'$ is an estimate of the interaction vertex, otherwise it indicates the first photon seen by the detector. For these reason in the following the vertex estimate will be called “pseudo-vertex” estimate.
2. Some specific features of the hits from the hadronic shower are identified and used to select a set of hit around the first pseudo-vertex estimate.
3. The selected hits are fitted with the hypothesis of originating from a single point. This fit gives a second pseudo-vertex estimate $\mathbf{V}''$ and a second track length estimate l''_μ.
4. The final pseudo-vertex estimate $\mathbf{V}$ is chosen between the first and the second according the likelihood value of the fit. The corresponding l_μ is kept.

In the following each stage will be described in detail.

7.6.1 Phase 1 - First estimates

The procedure to estimate $\mathbf{V}'$ and l'_μ is sketched in fig. 7.9. It is assumed that the track direction have already been reconstructed and a subset of hits correlated to the track, called *track-hits*, have been selected. From the position Q_i and the time t_{Qi} of each hit, the corresponding photon emission point P_i and the emission time t_i can be easily calculated. The emission points P_i are ordered on the basis of their occurrence time t_i, and the first point P_0 is the first pseudo-vertex estimate $\mathbf{V}'$. If P_n is the last emission point identified, $|P_n - P_0|$ corresponds to the first track length estimate l'_μ.

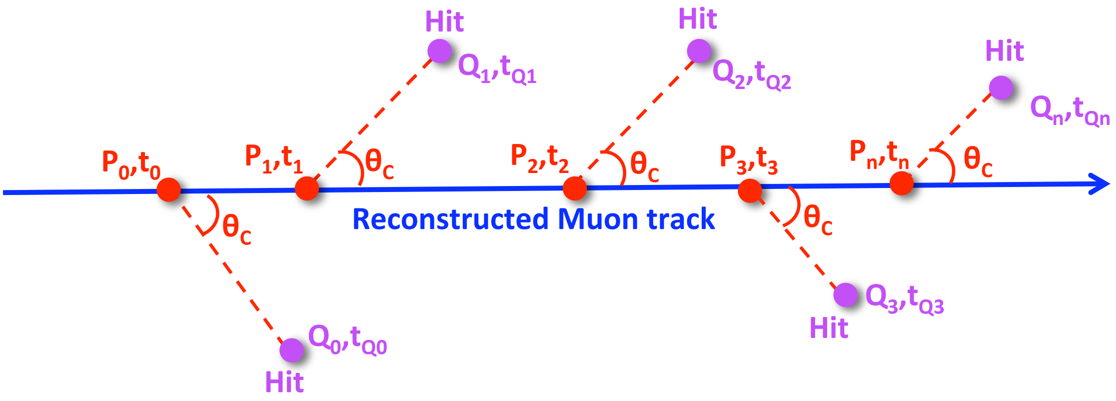

Figure 7.9: Scheme to explain how the track length is estimated.

Due to the contamination of the optical background and hadronic shower photons, a strict selection is needed to identify the *track-hits*. Some conditions are applied to perform this hit selection:

- A maximum orthogonal distance from the reconstructed track of 50 m;
- A time residual with respect to the reconstructed track in the interval (-10,10) ns;
- $\cos\theta_i < 0$, where θ_i is the expected angle of incidence of the photon on the PMT;
- a minimum density of one point P_i for each 2 meters along the track segment $\overrightarrow{P_0 P_n}$. For reference this density has been estimated projecting the true hits produced by the muon on the true muon track and it is about 3 points per meter.

The purity and efficiency of the selected set of hits, as defined in section 5.2, are shown in fig. 7.10. For each event, the efficiency indicates the fraction of the total number of hits from track that are identified trough the selection; the purity refers to the fraction of the total number of selected hits that are true hits from track. In the left panel of fig. 7.10, the mean efficiency and purity are calculated for bins of inelasticity, $y = (E_\nu - E_\mu)/E_\nu$, of width 0.1. The percentage of background hits contained in the set of *track-hits* is also indicated and its value is below 2%. For low values of y, the largest of the neutrino energy is transferred to the muon and almost all the selected hits are true hits produced by the muon (purity ≈ 1). In fact, the contamination due the shower hits will be very low in this case and only the optical background hits have to be discarded. When $y \approx 1$ the hadronic shower takes quite all the neutrino energy and most of the detected hits are due to the shower. Consequently, the purity of the selection decreases. On the contrary, the efficiency is quite constant with y having values between 0.6 and 0.7. The right panel of fig. 7.10, shows the efficiency and purity as a function of the muon energy. The points are the mean values in bins of 1 GeV. Above 2 GeV the purity of the selection is about 80%. For $E_\mu < 2$ GeV the muon track length is less then about 8 m and it is difficult to identify. In this case, the set of selected hit results more contaminated with the hits from the hadronic shower. As in the left plot, the efficiency is about 60-70%.

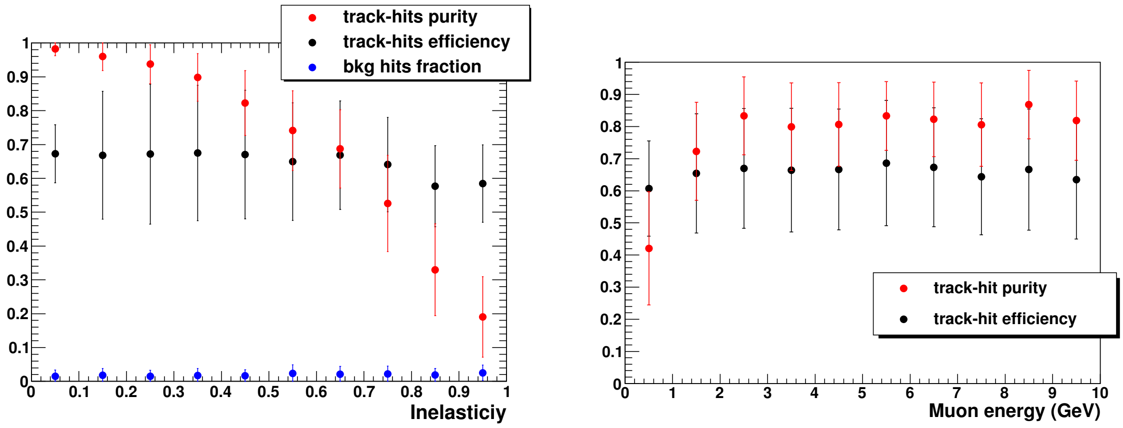

Figure 7.10: Purity and efficiency of the hit selection used for the track length estimate as a function of the inelasticity for events with $E_\nu < 20$ GeV (left) and of the muon energy (right). The points are the mean values and the errors are the root mean squares of the distributions. In the left plot the blue points indicates the fraction of hits due to the optical background in the set of *track-hits* is also indicated.

This plots demonstrates that even if in general the *track-hits* are quite well identified, the contamination of hits from shower can be high, e.g. when y is high or E_μ is low. As a consequence the track length is overestimated and the vertex position results distant some meters from the real interaction vertex. In fact the particles produced at the vertex may travel backwards with respect to the muon direction. For instance, fig.

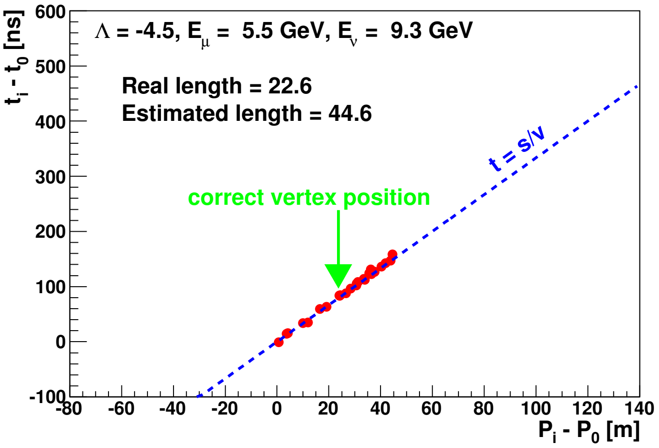

Figure 7.11: Position of the emission points and corresponding time for one specific event characterised by a good reconstruction of the track direction but with the track length largely overestimated. The green arrow indicates the position of the real vertex on the track.

7.11 shows the position of the emission points for a specific event whose track length is overestimated for the presence of hits from the hadronic shower wrongly identified as hits from the muon track.

7.6.2 Phase 2 - Selection of hits from the hadronic shower

A study of the distribution in time and space of hits produced at the interaction vertex has been performed. The goal is the determination of specific features that in the reconstruction phase can be used to distinguish hadronic shower hits among hits due to the optical background and to the muon. In fig. 7.12 some useful time-space behaviours of the hadronic shower extracted from Monte-Carlo are summarised. Only events generated with $E_\nu < 20$ GeV are studied. Since the simulated hits are analysed, the interaction vertex position and the muon direction are known and the radial distance d of each hit from the vertex can be calculated, as sketched in 7.12(a). The distribution of d in fig. 7.12(b) shows that the most of shower hits are produced near the vertex. The projection of d along the muon track l is always positive for hits produced by the muon but can be negative for the shower hits (see fig. 7.12(c)) because they can travel backwards w.r.t. the muon direction. The component of d orthogonal with respect to

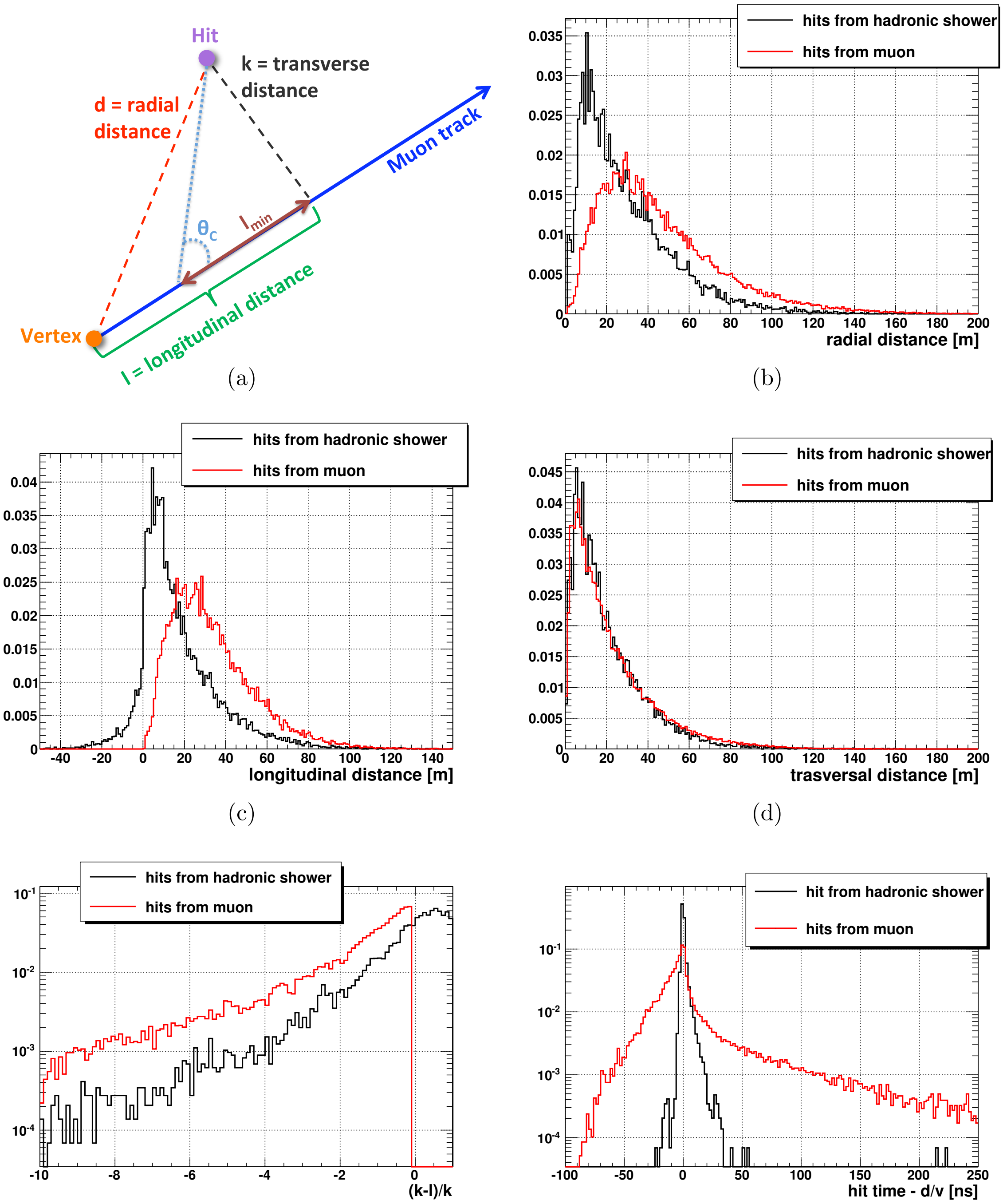

(a) (b)

(c) (d)

(e) (f)

Figure 7.12: Using the geometrical description depicted in 7.12(a), the plots show the distribution of the distance, d, from the vertex (7.12(b)), the projection of this distance on the muon track, l, (7.12(c)) and the orthogonal projection w.r.t. the muon track, k, (7.12(d)). The panel 7.12(e) is discussed in the text. The plot 7.12(f) refers to the time residual calculated as all light is originated from the vertex. Only events with $E_\nu < 20$ GeV are considered.

the muon direction is indicated with k and the distribution of k is quite similar for shower and muon hits.

The hits produced by the muon are emitted at a Cherenkov angle $\theta_C \approx 42°$ from the muon track. This restriction can be exploited. In fact, the minimum value of l for a hit produced by the muon is given by

$$l_{min} = k \cdot \cot \theta_C \approx 1.1k. \tag{7.5}$$

This condition is verified when the photon emission point is close to the vertex. It proves useful rewrite eq. 7.5 as $(k - l_{min})/k = -0.1$. The distribution of $(k - l)/k$ is shown if fig. 7.12(f). As expected, the maximum value of $(k - l)/k$ for hits produced by the muon is -0.1.

The time evolution of the shower hits can also be studied. Under the simple assumption that all the hits are emitted from the vertex at a time t_V, a hit distant d from the vertex should occur at a time $t_V + d/v$, if v is the speed of light in the medium. A "time residual" can be thus defined as $\Delta t = t_i - (t_V + d/v)$, where t_i is the time of the hit. For hits due to the shower and to the muon track, Δt is shown in fig. 7.12(f). The distribution of Δt for hits due to the muon track has a peak at zero corresponding to the photons emitted in the first meters of the muon track, but in general it can assume higher values.

Taking profit from this study, the conditions applied to select hits from the shower are: $l < 120$ m, $k < 100$ m, $|\Delta t| < 50$ ns, $(k - l)/k > -2$. The first two conditions are intended to reject the optical background hits and identify a region where the shower is likely to be. The other two are used to distinguish the shower hits from the hits due to the muon track. The used cuts are chosen in order to distinguish as much as possible shower hits from muon and background hits but on the other hand trying to keep the few hits that are produced at low energy. The input hit set is the one obtained from the initial selection discussed in the section 7.5.1. Obviously the real vertex is unknown, so the first pseudo-vertex estimated $\mathbf{V}'$ is used to calculate k, l and Δt. The set of hits selected in this phase is called *shower-hits*.

Finally, the performance of the selection is shown in fig. 7.13 in terms of its efficiency and purity. As discussed in the previous section, when the inelasticity y is close to zero, quite all the neutrino energy is transferred to the muon and the selected hits will contain few hits due to the shower. Increasing the inelasticity y, the fraction of energy taken

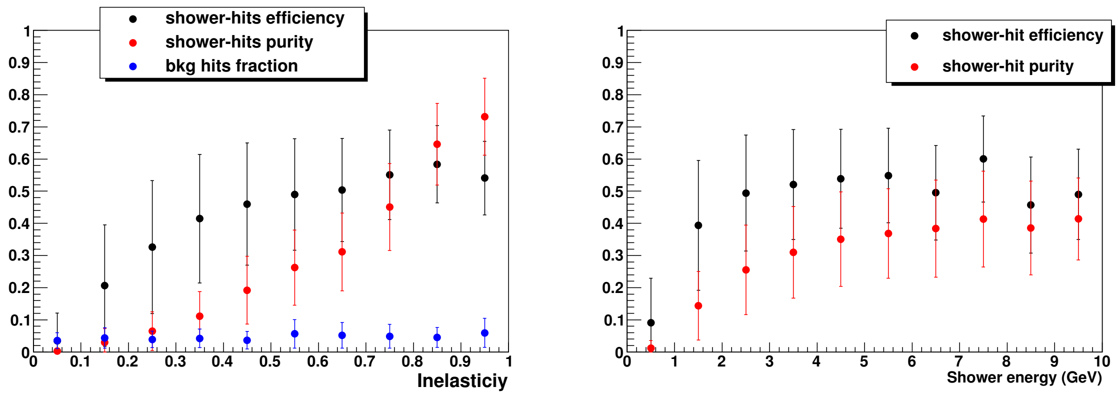

Figure 7.13: Purity and efficiency of the hit selection used for the vertex position estimate as a function of the inelasticity for events with $E_\nu < 20$ GeV (left) and of the shower energy (right). The points are the mean values and the errors are the root mean squares of the distributions. In the left plot the fraction of hits due to the optical background in the set of selected hits is also indicated.

by the shower enhances and the selection works better. From the left plot of fig. 7.13, it can be seen that the efficiency of the selection reaches about 50% and the maximum purity is 70%. The contamination due to the background hits is around 2-3%.

The right plot of 7.13 shows the purity and efficiency as a function of the shower energy. Both the quantities tend to increase with the shower energy.

7.6.3 Phase 3 - Bright point fit

To find the vertex position a maximum likelihood fit applied to the selected *shower-hits*. A function obtained from the Δt distribution for the simulated shower hits is used as PDF. In fig. 7.14 the PDF is superimposed to the Δt distribution. Four functions are used to fit the time residual distribution in different intervals. The red curves refer to two gaussians, the green curve is an exponential function and the blue one is a polynomial. The fit is mono-dimensional since the condition that the vertex belongs to the track is imposed.

7.6.4 Phase 4 - Final result

The final estimate of vertex position is chosen among the first emission point and the result of the fit. The criterion for the choice is the likelihood of the fit $logL$ divided by the number of degrees of freedom N_{dof}. Here $N_{dof} = N_{hit} - 1$, where N_{hit} is the number of hits used to perform the fit and 1 is the number of free parameters. If

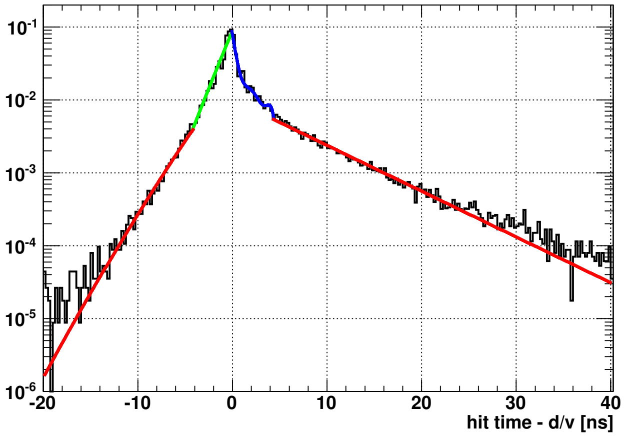

Figure 7.14: Time residual calculated as all light is originated from the vertex (black line). The coloured curves are the fitting functions in different intervals of Δt.

$logL/(N_{hit}-1) > -7.5$ the second vertex estimate is chosen otherwise the first estimate is kept. The last condition is verified only in 6% of the events with neutrino energy less then 20 GeV. The distance between the final estimated vertex and the real vertex is shown in the left plot of fig. 7.15, together with the result of the first and second estimate.

Once the vertex has been identified, the track length in scaled according to the distance from the estimated vertex and the last back projected photon on the track. The muon energy is estimated as $E_R = 0.24\, l_{\mu}^{rec}$ GeV, if the estimated track length l_{μ}^{rec} is expressed in meters. The ratio of the simulated muon energy E_{μ} and the corresponding muon track length l_{μ} is shown in the right plot of fig. 7.15. The quantity E_{μ}/l_{μ} is slightly increasing with E_{μ} but the reference value of 0.24 seems reasonable in the energy range of interest.

7.7 Performance of the reconstruction algorithm

As mentioned before, a selection of the events based on some containment conditions is needed for this analysis. Such conditions are based only on the results of the reconstruction since an external veto has not been studied at the moment. One possible containment criterion is the selection of events with the muon reconstructed vertex inside the instrumented volume. Such events are called here semi-conatined events. Clearly, the vertex estimate is the key element for this event selection. The performance of the

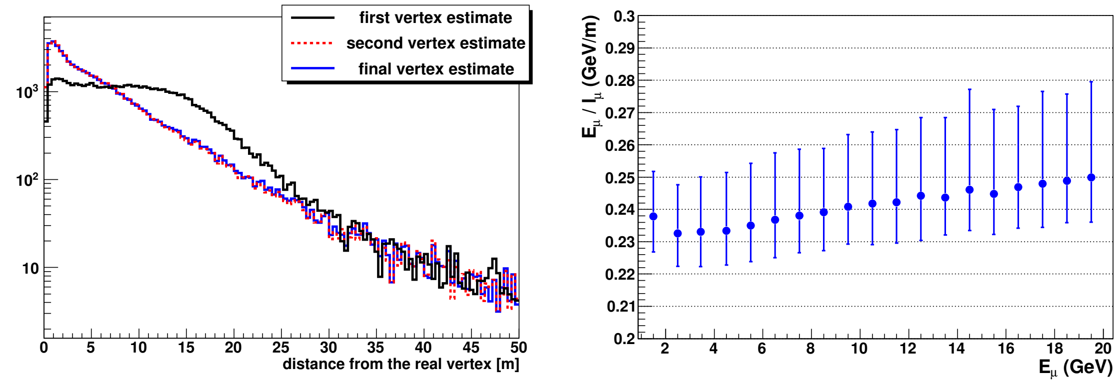

Figure 7.15: Left: distance between the real and the estimated vertex for the different phases of the reconstruction. Right: Ratio of the true muon energy and the corresponding track length as a function of E_μ. For each energy bin the median of the distribution is indicated with dots. The error bars refers to the 16% and 84% quantiles of the distribution.

vertex estimate algorithm is shown in the left panel of fig. 7.16. For semi-contained events reconstructed as upgoing, the plot shows the median distance between the true and estimated vertex position, $distance(P^{true}_{vertex}, P^{reco}_{vertex})$, as a function of the neutrino energy. The markers indicate the median of the distributions for energy bins of 2 GeV. The value of $distance(P^{true}_{vertex}, P^{reco}_{vertex})$ is of the order of a few meters both for all reconstructed events and for the events selected with an additional quality cut $\Lambda > -6.5$.

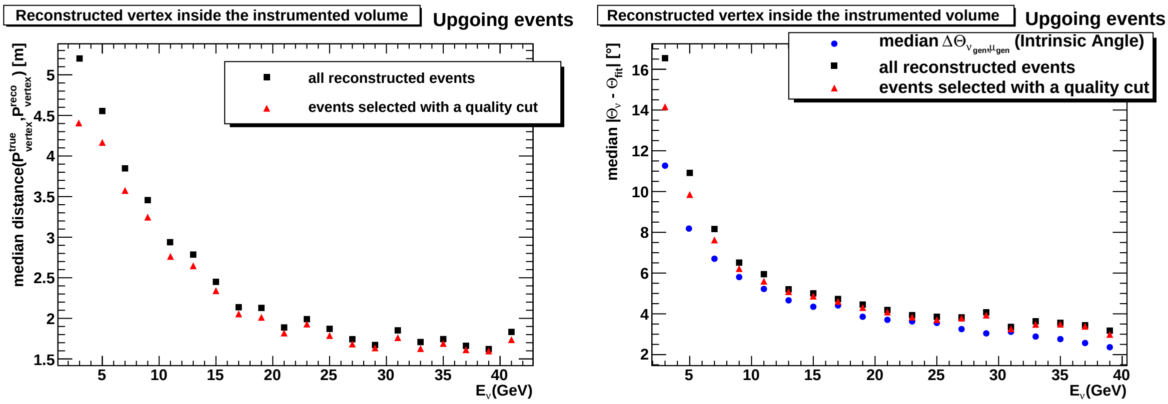

Figure 7.16: Left: Distance between the true and estimated vertex position for events reconstructed as upgoing and with the reconstructed vertex inside the instrumented volume. For each energy bin the plot shows the median of the distribution. Right: Angular distance between the reconstructed and true neutrino zenith angle. The events are selected as discussed for the left plot. For reference the “intrinsic angle” is shown.

The quality cut is chosen to select events that have the error on the zenith angle $|\theta_\nu - \theta_{fit}|$ close to the “intrinsic angle”, that is the difference between the true neutrino and muon zenith angles. The effect of the quality cut can be seen in the right panel of fig. 7.16, where the median of $|\theta_\nu - \theta_{fit}|$ is plotted for semi-contained events reconstructed as upgoing distinguishing the median value for all reconstructed events and for events having $\Lambda > -6.5$.

As discussed in section 7.3, the significance relative to the mass hierarchy identification is calculated as a function of the exposure, which is the product of the detector effective volume and the number of observation years. The effective volume V_{eff} can be defined as the volume of a 100% efficient detector for observing neutrinos that interact within that volume (see equation 6.3). Assuming a seawater density of 1.025 g/cm^3, the effective volume is converted in effective mass M_{eff}. The M_{eff} calculated for semi-contained events reconstructed as upgoing is plotted in fig. 7.17 as a function of the neutrino energy taking into account also the quality cuts $\Lambda > -6.5$. The effective mass increases with the neutrino energy until 10 GeV and then it is more or less constant.

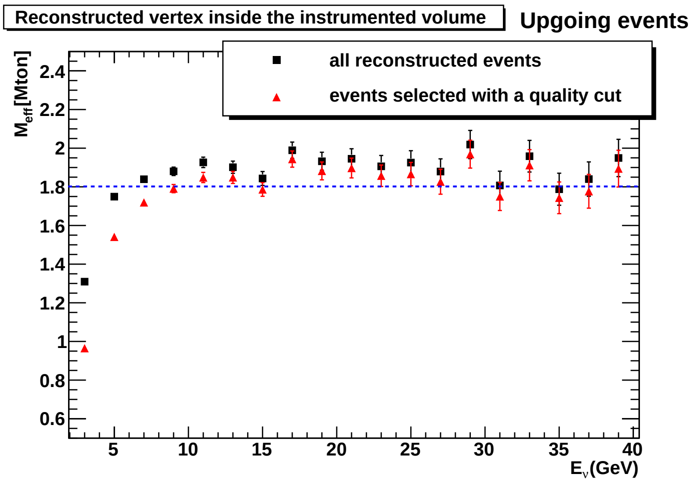

Figure 7.17: Effective mass as a function of the neutrino energy for semi-contained events reconstructed as upgoing. The M_{eff} is calculated for all reconstructed events (red tringles) and events having $\Lambda > -6.5$ (black squares).

The last parameter to evaluate is the neutrino reconstructed energy. The code described in the previous section estimates only the muon energy. The left plot of fig. 7.18 shows with a solid line the reconstructed muon energy E_R as a function of the true muon energy E_μ for the semi-contained events. The median of E_R and the quantiles at 16% and 84% (equivalent 1σ for a gaussian distribution) are indicated. Clearly, without any kind of external veto, it is not possible to understand if the track really ends or if the light deposit stops only because the track goes outside the instrumented volume.

Therefore the muon track length and consequently the muon energy is underestimated. Another containment condition has been then studied defining the "contained events" as the events that have the estimated ending point closer to the detector centre than the estimated vertex. This condition is very strict. In fact a large part of the events really contained in the instrumented volume is lost. However, this selection results the best among the other possibilities that have been considered at the moment. Further studies are ongoing to develop more complex containment conditions.

In the left plot of fig. 7.18 the median of E_R for contained events is shown with a dashed line. The reconstructed energy is more correlated to the true muon energy in this case. For reference, the trend of E_R as a function of E_μ is shown in the right plot of fig. 7.18 for events with the true muon track contained in the instrumented volume. As in the previous case the correlation between E_R and E_μ is good demonstrating that the muon energy reconstruction works well for the true contained events.

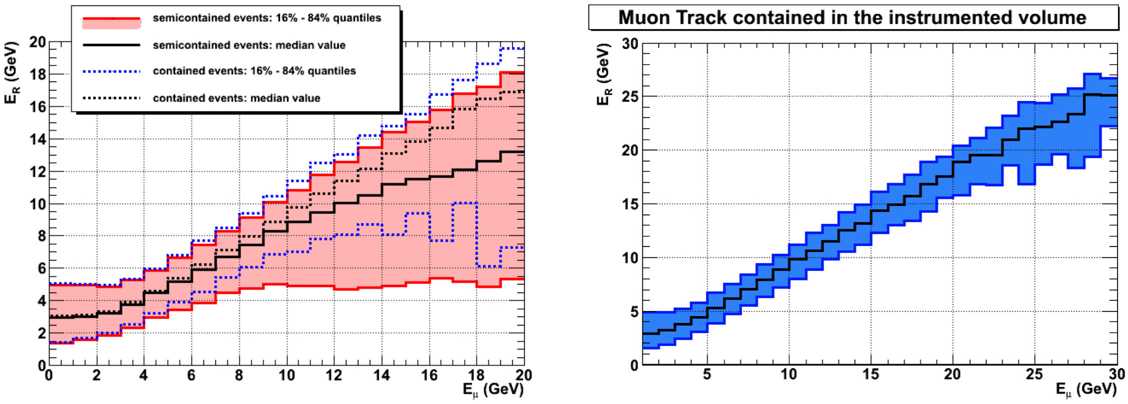

Figure 7.18: Left: reconstructed muon energy E_R as a function of the true muon energy E_μ for the semi-contained events (solid lines) and contained events (dashed lines) reconstructed as upgoing. The black lines refer to the median of E_R distribution in each bin of 1 GeV in E_μ. The blue lines are 16% and 84% quantiles of the distributions of E_R in each bin. Right: E_R as a function of E_μ for the events with the true muon track contained in the instrumented volume. The black line is the median and the blue lines are 16% and 84% quantiles.

In fig. 7.19 the difference $|E_\nu - E_R|$, where E_ν is the neutrino energy, is shown as a function of E_ν for contained and semi-contained events. In this case no visible difference is present between contained and semi-contained events. In fact, since the neutrino energy fraction that is carried out from the muon is about 50% in the GeV energy range, to infer the neutrino energy an estimate of the energy deposited in the hadronic shower is also necessary. At the moment further studies are on-going to evaluate the energy of the hadronic shower in order to obtain the complete estimate of the neutrino energy.

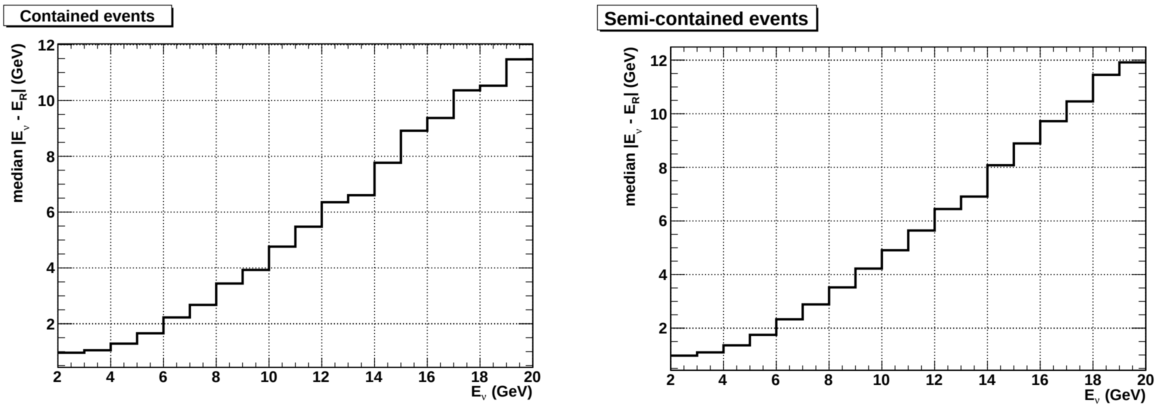

Figure 7.19: Absolute value of the difference between the reconstructed energy E_R and the neutrino energy E_ν as a function of the neutrino energy E_ν for contained (left) and semi-contained events (right). For each bin of E_ν the median of $|E_\nu - E_R|$ is shown.

To improve the neutrino energy estimate the following procedure has been used. The median value neutrino energy E_ν calculated for bin of E_R of 1 GeV has been plotted as a function of E_R, as shown in the left plot of figs. 7.20 and 7.21. The function $f(E_R)$ that fits the median values distribution is then used as estimator of E_ν, as shown in the right panel of figs. 7.20 and 7.21. In this way an energy resolution of about 35% is reached at 10 GeV.

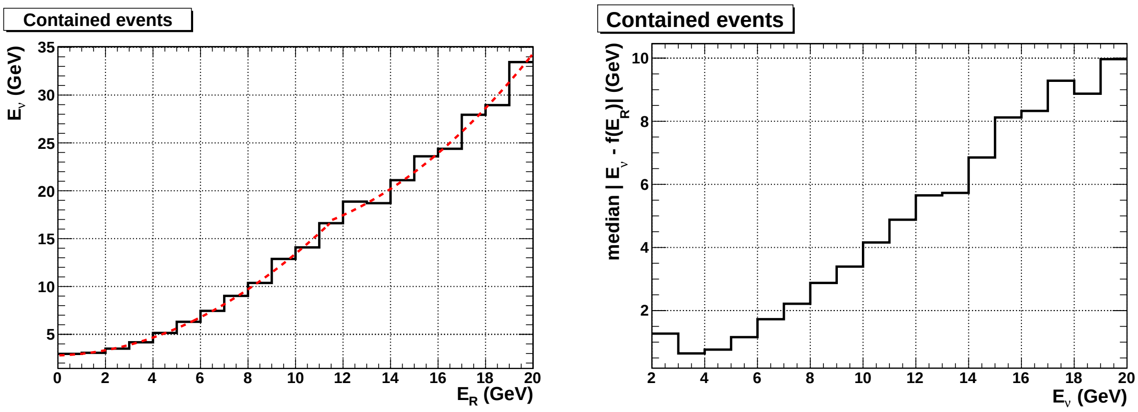

Figure 7.20: Left: median of neutrino energy E_ν as a function of the reconstructed energy E_R for contained events reconstructed us upgoing (black line). The red dashed line is the fitting function f(E_R). Right: absolute value of the difference between f(E_R) and the neutrino energy E_ν as a function of the neutrino energy E_ν for contained events reconstructed as upgoing.

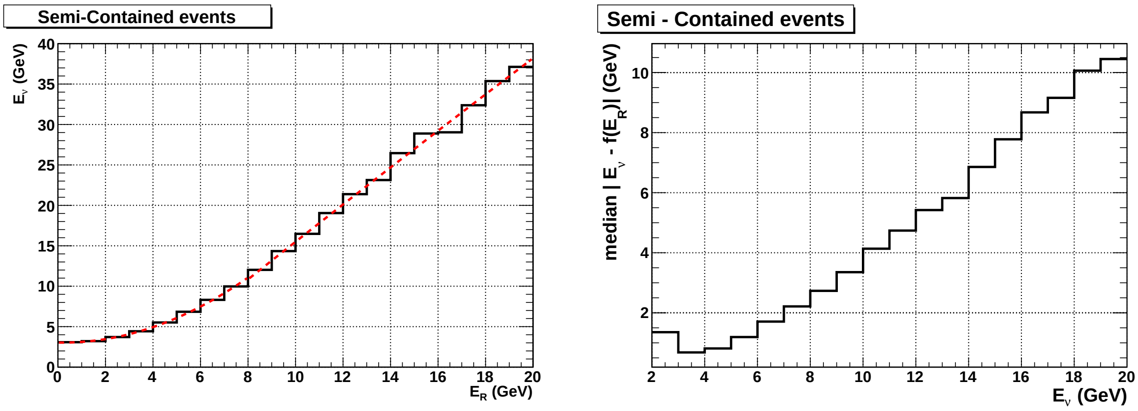

Figure 7.21: Left: median of neutrino energy E_ν as a function of the reconstructed energy E_R for semicontained events reconstructed us upgoing (black line). The red dashed line is the fitting function f(E_R). Right: absolute value of the difference between f(E_R) and the neutrino energy E_ν as a function of the neutrino energy E_ν for semicontained events reconstructed as upgoing.

7.8 Muon background rejection

As mentioned before, the measurement of the mass hierarchy is based on the detection of upgoing atmospheric neutrinos, but the background due to atmospheric muons wrongly reconstructed as upgoing can contaminate the sample of atmospheric neutrinos. A first study to evaluate the possibility to reject atmospheric muons has been performed [206] using the reconstruction described here. It has been observed that the distribution of the reconstructed pseudo-vertex is quite different for upgoing atmospheric neutrinos and muons as shown in figs. 7.22 and 7.23 where only atmospheric neutrinos with energy less then 20 GeV are considered. In fig. 7.22, r is the distance from the central axis of the detector, that is $r = \sqrt{x^2 + y^2}$.

Since wrongly reconstructed atmospheric muons have their pseudo-vertexes outside the instrumented volume, while neutrino events have theirs closer or inside the detector, it seems reasonable to use this simple quantity to perform the rejection of atmospheric muons. As an example, requiring a cut on $r < 70$ m, with additional cuts on $\Lambda < -4.9$ and $\beta < 2°$ the muon contamination is reduced to 10%.

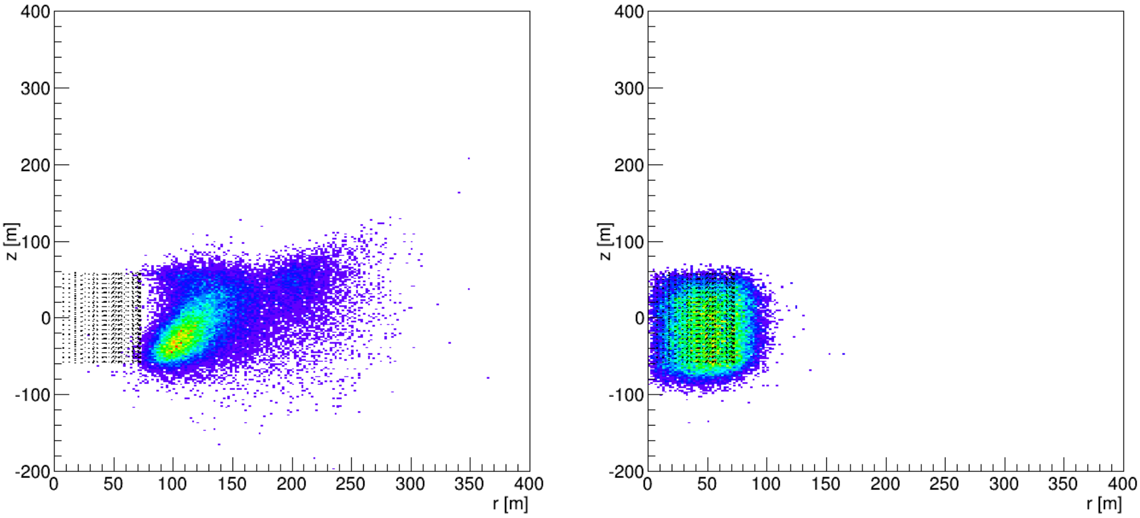

Figure 7.22: r-z distribution of the reconstructed track pseudo-vertex for upward going atmospheric muons (left) and neutrinos (right). Also shown the positions of the ORCA OMs, representing the instrumented volume. A selection cut $\beta < 2^\circ$ and $\Lambda > -5$ is applied here.

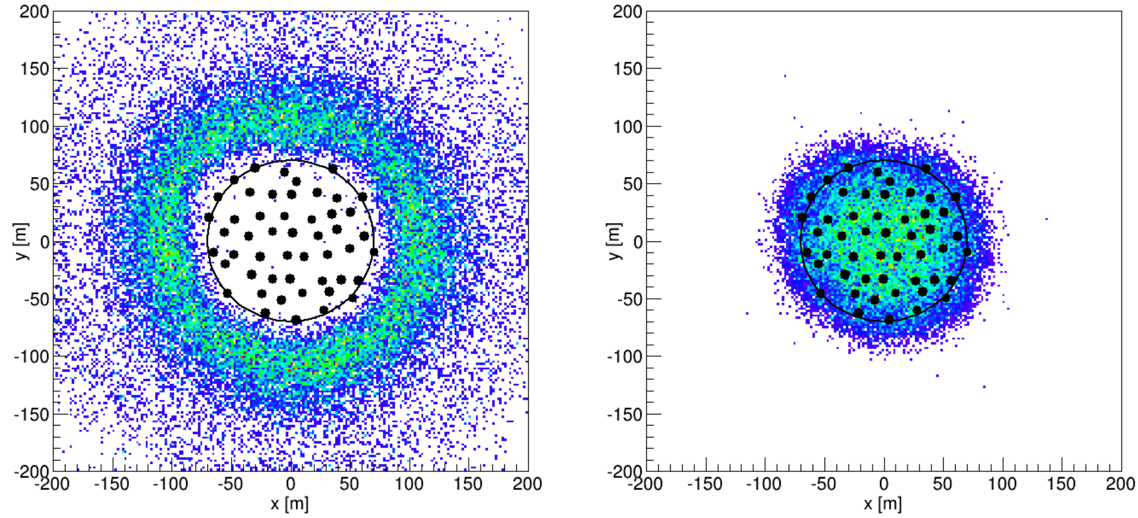

Figure 7.23: x-y distribution of the reconstructed track pseudo-vertex for upward going atmospheric muons (left) and neutrinos (right). Also shown the positions of the ORCA OMs, representing the instrumented volume. A selection cut $\beta < 2^\circ$ and $\Lambda > -5$ is applied here.

CONCLUSIONS

KM3NeT will be the next-generation km^3-scale neutrino telescope to be installed in the depths of the Mediterranean Sea. At present the most sensitive neutrino telescope in the world is the IceCube detector at the South Pole, which has instrumented about a km^3 of polar ice. Recently the IceCube collaboration has reported evidence of a flux of cosmic high energy neutrinos exceeding the expected flux of atmospheric neutrinos by a statistically significant factor, de facto opening a new era of neutrino astronomy.

With several cubic kilometers of sea water instrumented with thousand of optical sensors, KM3NeT will be the most sensitive high energy neutrino telescope, with a sensitivity exceeding that of IceCube by a substantial factor. The construction of KM3NeT is based on a novel type of optical sensor, the Digital Optical Module, realised by arranging many small photomultipliers inside a pressure resistant glass sphere. This concept allows better performances with respect to the standard single large-area photomultiplier used in Antares and IceCube, since photon counting and directionality are possible due to photocatode segmentation. The aim of this work was to develop a new muon track reconstruction procedure appropriate for such a detector and evaluate the performances of the telescope through a complete Monte-Carlo simulation.

Using this algorithm, the detector sensitivity (flux that can be excluded at 90% CL) and discovery potential (flux that can be detected at 5σ or 3σ above the background noise) for two galactic sources that appear to be the best candidates neutrino sources, the Supernova Remnants RXJ1713.7-3946 and Pulsar Wind Nebula Vela X, have been evaluated. The observation time required for the discovery of these sources at 5σ is about

5 year (2 years at 3σ) for the RXJ1713.7-3946 and about 3 years (1 year at 3σ) for the Vela X. This analysis leads to the conclusion that at least the more intense galactic sources are at reach for KM3NeT. The sensitivity to point sources for an E^{-2} spectrum has also been evaluated and the results shows that KM3NeT will overtake by 50 times the performance of Antares, the detector operating at present in the Mediterranean Sea and exceeds the IceCube sensitivity in the whole sky.

Recently it has been also proposed to exploit underwater Cherenkov neutrino telescopes to investigate the neutrino mass hierarchy by studying atmospheric neutrino oscillations at low energies ($E \sim 10$ GeV). To perform such studies an as much as possible accurate determination of the neutrino energy and of the zenith angle are crucial. This requires a much denser array of photosensors with adequate containment conditions. First simulations show that with an effective volume of 3 Mton and an observation time of 5 years a significance of 3σ (5σ) can be achieved if the energy resolution is 25% (10%), assuming only contained events and a perfect knowledge of the muon zenith angle.

To approach these assumptions an ad hoc reconstruction algorithm has been developed and is presented in this thesis. This algorithm allows to identify with an error of a few meters the interaction vertex that is used for the containment conditions. The error on the reconstructed zenith angle is less than 1° above about 8 GeV. The muon energy is reconstructed through the muon track length allowing to achieve a neutrino energy resolution of about 35% at 10 GeV. Further improvements are expected by including also the reconstruction of the hadronic shower, which will require a dedicated algorithm that has not yet been developed. The contamination due to electron and tau neutrino still needs to be considered.

APPENDIX A

COSMIC RAY ACCELERATION

The idea of stochastic acceleration was first developed by E. Fermi in 1949 [207]. He observed that when a charged particle collides against moving magnetic fields, for example magnetised interstellar clouds moving in random direction with a velocity v, it gains an average fractional energy per collision of the order of v^2. In fact, although the particle gains energy moving towards the "magnetic mirror" and looses when moving away from it, on average the probability for approaching the mirror is higher than the one for receding from the mirror. This mechanism, called "second-order Fermi acceleration", reproduces a power law energy spectrum but its spectral index depends on the clouds velocity and the acceleration is not enough to reproduce the observed spectrum. However, if the "magnetic mirror" is regularly shaped, for example, as a plain wave as in the case of a magnetised shock front, the fractional energy gain per reflection turns out to be proportional to the first order of the velocity v of the moving mirror, which strongly increase the acceleration efficiency for non-relativistic motion. This mechanism, discussed below and known as "first-order Fermi acceleration", was suggested in the late 1970s [208–210] and is under continuous development [211–213].

Figure A.1 depicts the situation in the 'lab' frame, where the plane shock wave front propagates through the stationary interstellar medium (ISM) with velocity $-\vec{u}_1$. The shocked gas flows away from the shock with a velocity $\vec{u}_2$ relative to the shock front, and $\mid \vec{u}_2 \mid < \mid \vec{u}_1 \mid$. Thus, in the laboratory frame the gas behind the shock moves to the left with velocity $\vec{V} = -\vec{u}_1 + \vec{u}_2$, that can be interpreted as the velocity of the shocked gas ("downstream") relative to the unshocked gas ("upstream"). The cosmic

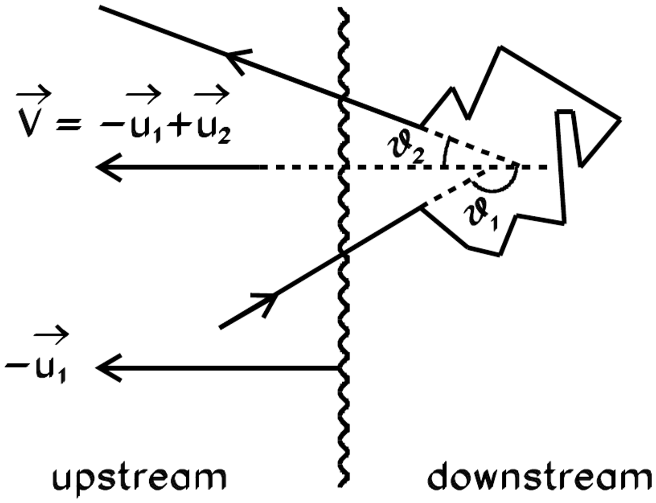

Figure A.1: Acceleration at a plane shock front.

ray gas contained in the interstellar medium in the upstream region is isotropic. As the shock approaches some of the gas particles cross the shock and move downstream. The downstream particles are also isotropized. Some of them can scatter back and cross the shock again in the upstream direction. The particles always gain energy by crossing the shock because the elastic collisions are head-on in the corresponding frames. If the particle enters the shocked region with energy E_1, assumed already sufficiently relativistic, in the rest frame of the moving gas it has total energy:

$$E'_1 = \Gamma E_1 (1 - \beta \cos \theta_1) \tag{A.1}$$

where Γ and $\beta \equiv V/c$ are the Lorentz factor and velocity of the downstream relative to the upstream. Since all the "scatterings" are elastic, the energy of the particle in the moving frame just before it escapes is $E'_2 = E'_1$. If we transform this energy back to the laboratory frame, we have the energy of the particle after its encounter with cloud:

$$E_2 = \Gamma E'_2 (1 - \beta \cos \theta'_1). \tag{A.2}$$

For simplicity, (A.1) and (A.2) are written for a particle that is already sufficiently relativistic so that $E \approx pc$. Substituting (A.1) into (A.2), now gives the energy change for the particular encounter characterised by θ_1 and θ_2,

$$\frac{\Delta E}{E_1} = \frac{1 - \beta \cos \theta_1 + \beta \cos \theta'_2 - \beta^2 \cos \theta_1 \cos \theta'_2}{1 - \beta^2} - 1. \tag{A.3}$$

Averaging over all the possible angles θ_1 and θ_2, we obtain the average fractional energy gain per encounter:

$$\xi \sim \frac{4}{3}\beta = \frac{4}{3}\frac{u_1 - u_2}{c}. \tag{A.4}$$

This means that the energy of the particle is increased by a constant factor every time it goes back and forth over the shock front, so after n crossing the particle energy will be

$$E_n = E_0(1+\xi)^n \tag{A.5}$$

where E_0 is the energy at injection into the accelerator. The number of encounters needed to reach the energy E_n is therefore

$$n = \frac{ln(E_n/E_0)}{ln(1+\xi)}. \tag{A.6}$$

At any encounter the particle can escape from the region that is occupied by the magnetic clouds with some probability P_{esc}. If the particle escapes, its energy does not increase any more so the probability that the particle reach the energy E_n can be calculated as the probability that the particle remains in the acceleration region long enough to encounter n times the magnetic clouds that is $(1-P_{esc})^n$. Thus, the number of particles accelerated to energies higher than E_n is proportional to the number of particles that remain in the acceleration region for more than n cloud encounters and can be expressed as

$$N(\geq E) \; \propto \; \frac{1}{P_{esc}}\left(\frac{E_n}{E_0}\right)^{-\gamma}. \tag{A.7}$$

In conclusion, the Fermi mechanism leads to the desired power law spectrum of energies with integral spectral index:

$$\gamma = ln\left(\frac{1}{1-P_{esc}}\right)/ln(1+\xi) \approx \frac{P_{esc}}{\xi} \tag{A.8}$$

To calculate P_{esc}, it can been observed that for a large plane shock the rate of shock encounters is the projection of the isotropic cosmic ray flux of density ρ_{CR} onto the plane front of the shock, which is $\rho_{CR}/4$. The rate of escaping the shock through convention downstream away (which is the only way of leaving a plane shock of infinite length) is the product of the same cosmic ray density times the convention velocity u_2. The escape probability is the ratio of the escape rate to the encounter rate

$$P_{esc} = \frac{\rho_{CR} u_2}{\rho_{CR}/4} = \frac{4u_2}{c} \tag{A.9}$$

and therefore from the (A.8), the integral spectral index is:

$$\gamma = \frac{P_{esc}}{\xi} = \frac{3}{u_1/u_2 - 1}. \tag{A.10}$$

A shock can form when $u_1 > c_1$, (c_1 is the sound speed in the gas). The continuity of mass flow across the shock ($\rho_1 u_1 = \rho_2 u_2$), together with the kinetic theory of gases, gives:

$$\frac{u_1}{u_2} = \frac{\rho_2}{\rho_1} = \frac{(c_p/c_v + 1)M^2}{(c_p/c_v - 1)M^2 + 2} \tag{A.11}$$

where $M = u_1/c_1$ is the Mach number of the flow. For monoatomic gas the ratio of specific heats is $c_p/c_v = \frac{5}{3}$, so:

$$\gamma \approx 1 + \frac{4}{M^2}. \tag{A.12}$$

For a strong shock, with $M \gg 1$, $\gamma \sim 1$, which is the result expected to describe the observed cosmic ray spectrum (we remind that for an integral spectral index close to 1, the differential spectral index is about 2).

The subject of particle acceleration is much more complicated than the very simplified analysis given here, see books like [2] or [1] for a most accurate discussion on this topic.

BIBLIOGRAPHY

[1] T. Stanev, *High Energy Cosmic Ray*, Springer, 2004.

[2] T. K. Gaisser, *Cosmic Rays and Particle Physics*, Cambrige University Press, Cambrige, 1990.

[3] M. Nagano and A. A. Watson, *Rev. Mod. Phys. 72* (2000), 689.

[4] V. F. Hess, *Phys. Zeits. 14* (1912), 1153.

[5] Web-site `http://www.physics.utah.edu/~whanlon/spectrum.html`.

[6] Web-site `http://www.cosmic-ray.org/index.html`.

[7] Web-site `http://eas.ysn.ru/`.

[8] Web-site `http://www-akeno.icrr.u-tokyo.ac.jp/AGASA/`.

[9] Web-site `http://www.auger.org/`.

[10] Web-site `http://www.telescopearray.org/`.

[11] C. J. Cesarsky, *Ann. Rev. Astron. Astroph. 18* (1980), 289.

[12] P. O. Lagage and C. J. Cesarsky, *J. Astron. Astroph. 125* (1983), 249.

[13] J. R. Hoerandel, *Astropart. Phys. 21* (2004), 241.

[14] K.-H. Kampert and M. Unger, *Astroparticle Physics 35* (2012), 660.

[15] The Pierre Auger collaboration, *JCAP 02* (2013), 026.

[16] R. U. Abbasi et al., The High Resolution Flys Eye Collaboration, *Phys. Rev. Lett. 104* (2010), 161101.

[17] W. F. Hanlon for the Telescope Array Collaboration, *Proceedings of ICRC2013, to be published* (2013).

[18] D. Leonid et al., The Yakutsk Collaboration, *Proceedings of ICRC2013, to be published* (2013).

[19] H. Tokuno et al., Telescope Array collaboration, *Proceedings of ICRC2013, to be published* (2013).

[20] R.U. Abbasi et al., The High Resolution Flys Eye Collaboration, *Astropart. Phys. 30* (2008), 175.

[21] J. Abraham et al., Pierre Auger collaboration, *Science 318* (2007), 938.

[22] ——, *Astropart. Phys. 29* (2008), 188.

[23] P. Abreu et al., Pierre Auger collaboration, *Astropart. Phys. 34* (2010), 314.

[24] K. Greisen, *Phys. Rev. Lett. 16* (1966), 748.

[25] G. T. Zatsepin and V. A. Kuzmin, *Sov. Phys. JETP Lett. 4* (1966), 78.

[26] M. Takeda et al., *Phys. Rev. Lett. 81* (1998), 1163.

[27] R.U. Abbasi et al. (HiRes Collaboration), *Phys. Rev. Lett. 92* (2004), 151101.

[28] ——, *Astropart. Phys. 32* (2009), 53.

[29] J. Abraham et al., (The Pierre Auger Collaboration), *Phys. Lett. B 685* (2010), 239.

[30] T. Abu-Zayyad et al., (The Telescope Array collaboration), *Astrophys. J. Lett. 768* (2013), L1.

[31] D. De Marco, P. Blasi, A. V. Olinto, *Astropart. Phys. 20* (2003), 53.

[32] M. Takeda et al., *Astropart. Phys. 19* (2003), 447.

[33] T.K. Gaisser, T. Stanev and S. Tilav, *Frontiers of Physics* (2013), 1.

[34] G. D. B. et al., *Astropart. Phys. 34* (2010), 274.

[35] A. M. Hillas, *Ann. Rev. Astron. Astrophys. 22* (1984), 425.

[36] K. Ptitsyna and S. Troitsky, *Physics - Uspekhi 53* (2010), 691. `arXiv:0808.0367 [astro-ph]`.

[37] G. Sigl, *Proceedings of the SIF - ISAPP School "Neutrino Physics and Astrophysics" 182* (2011), 145. `arXiv:1202.0466 [astro-ph]`.

[38] S. R. Kelner, F. A. Aharonian and V. V. Bugayov, *Phys. Rev. D 74* (2006), 063007.

[39] A. Kappes, J. Hinton, C. Stegmann and F. Aharonian, *The Astroph. J. 656* (2007), 870.

[40] F. Vissani, *Astropart. Phys. 26* (2006), 310.

[41] W. A. et al., *The Astroph. J. 697* (2009), 1071.

[42] N. et al., *The Astroph. J. Supll. Series 199* (2012), 31.

[43] J. Ballet and T.H. Burnett for the Fermi-LAT Collaboration, *Proceedings of ICRC2013, to be published* (2013).

[44] Web-site `http://www.lanl.gov/milagro`.

[45] Web-site `http://argo.na.infn.it`.

[46] Web-site `http://www.hawc-observatory.org`.

[47] Web-site `http://english.ihep.cas.cn/ic/ip/LHAASO`.

[48] Web-site `http://www.mpi-hd.mpg.de/hfm/HESS/`.

[49] Web-site `https://magic.mpp.mpg.de/`.

[50] Web-site `http://veritas.sao.arizona.edu/`.

[51] Web-site`http://tevcat.uchicago.edu/`.

[52] A. A. A. et al., *The Astroph. J. 708* (2010), 1254.

[53] P. Sapienza and G. Riccobene, *La Rivista Del Nuovo Cimento 32* (2009), 591.

[54] J. K. Becker, *Phys. Rep. 458* (2008), 173.

[55] A. M. Hillas, *J. Phys. G: Nucl. Phys. 31* (2005), R95.

[56] W. Blaade and F. Zwicky, *Phys. Rev. 46* (1934), 76.

[57] M. Ackermann et al., *Science 339* (2013), 807.

[58] A. Bamba et al., *The Astroph. J. 589* (2003), 827.

[59] J. Vink and J. M. Laming, *The Astroph. J. 584* (2003), 758.

[60] H. J. Völk et al., *Astron. Astroph. 433* (2005), 229.

[61] Y. Uchiyama et al., *Nature 449* (2007), 576.

[62] Y. Uchiyama and F. A. Aharonian, *The Astroph. J. Lett. 677* (2008), L105.

[63] S. Gabici, F. A. Aharonian, and S. Casanova, *Mon. Not. R. Astron. Soc. 396* (2009), 629.

[64] F. Aharonian et al., *The Astroph. J. 661* (2007), 236.

[65] M. Paz Arribas et al., *Proceedings of ICRC2011 7* (2011), 141.

[66] B. M. Gaensler and P.O. Slane, *ARA&A 44* (2006), 17.

[67] I. F. Mirabel and L. F. Rodriguez, *Nature 392* (1998), 673.

[68] I. F. Mirabel, *Science 312* (2006), 1759.

[69] F. AHARONIAN ET AL., (H.E.S.S. COLL.), *Astron. Astrophys. 460* (2006), 743.

[70] ——, *Astron. Astrophys. 442* (2005), 1.

[71] J. ALBERT, ET AL., (MAGIC COLL.), *Science 312* (2006), 1771.

[72] A. LEVINSON AND E. WAXMAN, *Phys. Rev. Lett. 87* (2001), 171101.

[73] C. DISTEFANO ET AL., *Astrophys. J. 575* (2002), 378.

[74] W. BEDNAREK, *Astrophys. J. 631* (2005), 466.

[75] F AHARONIAN ET AL., *J. Phys. Conf. Series 39* (2006), 408.

[76] H. R. CHRISTIANSEN, M. ORELLANA AND E. G. ROMERO, *Phys. Rev. D 73* (2006), 063012.

[77] E. G. ROMERO AND M. ORELLANA, *Astron. Astrophys. 439* (2005), 237.

[78] M. G. AARTSEN ET AL., THE ICECUBE COLLABORATION, *submitted to The Astrophysical Journal* (2013). `arXiv:1307.6669`.

[79] S. ADRÍAN-MARTÍNEZ ET AL., THE ANTARES COLLABORATION, *Astrophys. J. 760* (2012), 53.

[80] M. SU AT AL., *Astrophys. J. 724* (2010), 1044.

[81] A. FRANCKOWIAK AND D. MALYSHEV ON BEHALF OF THE FERMI-LAT COLLABORATION, *Proceedings of ICRC2013, to be published* (2013).

[82] G. DOBLER, *Astrophys. J. 750* (2012), 17.

[83] D. PIETROBON ET AL., *Astrophys. J. 755* (2012), 69.

[84] P. A. R. ADE ET AL. (PLANCK COLLABORATION), *`arXiv:1208.5483`* (2012).

[85] E. CARRETTI ET AL., *Nature 493* (2013), 66.

[86] R. CROCKER AND F. AHARONIAN, *Phys. Rev. Lett. 106* (2011), 101102.

[87] B. C. LACKI, *`arXiv:1304.6137`* (2013).

[88] S. Thoudam, `arXiv:1304.6972` (2013).

[89] D. O. Chernyshov et al., *ICRC2011 proceedings,* `ArXiv:1109.2619` (2011).

[90] P. Mertsch and S. Sarkar, *Phys. Rev. Lett. 107* (2011), 091101.

[91] S. Adrían-Martínez et al.,The Antares Collaboration, `arXiv:1308.5260v1` (2013).

[92] S. Adrian-Martinez et al.,The KM3NeT Collaboration, *Astropart. Phys. 42* (2013), 7.

[93] R. J. Gould and G.Schreder, *Phys. Rev. Lett. 16* (1966), 252.

[94] E. Waxman and J. Bahcall, *Phys. Rev. D 59* (1998), 023002.

[95] K. Mannheim, R. J. Protheroe and J. P. Rachen, *Phys. Rev. D 63* (2000), 023003.

[96] M. Ambrosio, et al., *Astropart. Phys. 19* (2003), 1.

[97] A.V. Avrorin, et al., *Astron. Lett. 35* (2009), 651.

[98] G.W. Sullivan for the IceCube Collaboration, *Nucl. Phys. B (Proc. Suppl.) 235* (2013), 346.

[99] S. Biagi on behalf of the ANTARES Collaboration, *2013 Rencontres de Moriond proceedings,*`arXiv:1308.5260` (2013).

[100] R. V. E. Lovelace, *Nature 262* (1976), 649.

[101] K. Mannheim, *Astropart. Phys. 3* (1995), 295.

[102] F. Halzen and E. Zas, *Astrophys. J. 488* (1997), 669.

[103] R. J. Protheroe, *ASP Conf. Ser. 121* (1997), 585.

[104] A. Achterberg et al. (IceCube Coll.), *Phys. Rev. D 76* (2007), 042008.

[105] J. K. Becker, P. L. Biermann and W. Rhode, *Astropart. Phys. 23* (2005), 355.

[106] F. Halzen and A. OMurchadha, `arXiv:0802.0887` (2008).

[107] B. Fanaroff, L. Bernard and J. M. Riley, *Mon. Not. R. Astron. Soc. 167* (1974), 31.

[108] J. P. Conner, W. D. Evans and R. D. Bellan, *Astrophys. J. 157* (1969), L157.

[109] W. S. Paciesas et al., *Astrophys. J. Suppl. Series 122* (1999), 465.

[110] R. Wijers, M.J. Rees and P. Mészáros, *Mon. Not. R. Astron. Soc. 288* (1997), L51.

[111] T. J. Galama et al., *Nature 395* (1998), 670.

[112] J. Hjorth et al., *Nature 423* (2003), 847.

[113] T. Piran, *Phys. Rep. 314* (1999), 575.

[114] R. Abbasi at al., The IceCube collaboration, *Nature 484* (2012), 351.

[115] R. J. Protheroe and P. A. Johnson, *Astropart. Phys. 4* (1996), 253.

[116] O. E. Kalashev et al., *Phys. Rev. D 66* (2002), 063004.

[117] A. M. Taylor and F. Aharonian, *Phys. Rev. D 76* (2009), 083010.

[118] A. T. D. Hooper and S. Sarkar, *Astropart. Phys. 23* (2005), 11.

[119] V. Agrawal et al., *Phys. Rev. D 53* (1996), 1314.

[120] G.D. Barr et al., *Phys. Rev. D 70* (2004), 023006.

[121] M. Honda et al., *Phys. Rev. D 75* (2007), 043006.

[122] G. Battistoni et al., *Astropart. Phys. 12* (2000), 315.

[123] C.G.S. Costa, *Astropart. Phys. 16* (2001), 193.

[124] R. Enberg, M.H. Reno and I. Sarcevic, *Phys. Rev. D 78* (2008), 043005.

[125] A. Martin et al., *Acta Phys. Pol. B 34* (2003), 3273.

[126] S. Adrían-Martínez et al., the Antares Collaboration, *Eur. Phys. J. C 73* (2013), 2606.

[127] R. Abbasi et al., *Astropart. Phys. 34* (2010), 48.

[128] ——, *Phys. Rev. D 83* (2011), 012001.

[129] ——, *Phys. Rev. D 84* (2011), 082001.

[130] ——, *Phys. Rev. D 79* (2009), 102005.

[131] M. A. Markov and I. M. Zheleznykh, *Nucl. Phys. 27* (1961), 385.

[132] A. Roberts et al., *Rev. of Mod. Phys. 64* (1992), 259.

[133] V. Aynutdinov et al., The Baikal Collaboration, *Nucl. Instrum. Methods A 567* (2006), 433.

[134] Andres E. et al., *Astropart. Phys. 13* (2000), 1.

[135] E.V. Bugaev et al., *Phys. Rev. D 58* (1998), 054001.

[136] The IceCube Collaboration, *Science 342* (2013), 1242856.

[137] F. Bernard, PhD thesis, University of Marseille, 2000.

[138] J. A. Formaggio and G. P. Zeller, *Rev. Mod. Phys. 84* (2012), 1307.

[139] R. Gandhi et al., *Astropart. Phys. 5* (1996), 81.

[140] C. Carlogeanu, *Muon interactions at high energies*, *ANTARES-Physics/1998-003* (1998).

[141] M. Ackermann et al., *J. Geophys. Res. 111* (2006), D13203.

[142] C. D. Mobley, *Light and Water: radiative transfer in natural waters*, Academic Press, San Diego, 1994.

[143] M. A. et al. (NEMO collaboration). http://nemoweb.lns.infn.it/sites/SiteReport/NEMO-Site-Report.pdf.

[144] V. Agrawal et al., *Phys. Rev. D 53* (1996), 1314.

[145] A. Okada, *Astropart. Phys. 2* (1994), 393.

[146] M. Ageron et al., The Antares Collaboration, *Nucl. Instrum. Methods A 656* (2011), 11.

[147] M. Spurio for the Antares Collaboration, *Proceedings of TAUP2013, to be published* (2013).

[148] A. Achterberg et al., The IceCube Collaboration, *Astropart. Phys. 26* (2006), 155.

[149] M. G. Aartsen et al., The IceCube Collaboration, *Nucl. Instrum. Methods A 711* (2013), 73.

[150] ——, *Phys. Rev. Lett. 111* (2013), 021103.

[151] Web-site `http://www.km3net.org/home.php`.

[152] G. Aggouras et al., *Nucl. Phys. B (Proc. Suppl.) 151* (2006), 279.

[153] E. Migneco et al., *Nucl. Instr. Meth. A 588* (2008), 111.

[154] KM3NeT Technical Design Report, available on `http://www.km3net.org/home.php`.

[155] M. Circella et al. for the KM3NeT Collaboration, *Proceedings of ICRC2013, to be published* (2013).

[156] The KM3NeT collaboration, *JINST 8* (2013), T03006.

[157] ——, *article in preparation.*

[158] M. Circella et al. for the KM3NeT Collaboration, *Proceedings of ICRC2013, to be published* (2013).

[159] M. De Jong for the KM3NeT Collaboration, *Proceedings of ICRC2013, to be published* (2013).

[160] G. Riccobene et al., *Astropart. Phys. 27* (2007), 1.

[161] A. Capone et al., *Nucl. Instr. Meth. A 487* (2002), 423.

[162] D. Bailey, PhD thesis, Wolfson College, Oxford, 2002. available on `http://antares.in2p3.fr/Publications/index.html`.

[163] F. C. Brunner, *ANTARES-Software/2000-008* (2000).

[164] G. Ingelmann, A. Edin and J. Rathsman, *Comput. Phys. Commun. 101* (1997), 108.

[165] G. Barr, PhD thesis, University of Oxford, 1987.

[166] P. Antonioli et al., *Astropart. Phys. 7* (1997), 357.

[167] I. A. Sokalski et al., *Phys. Rev. D 64* (2001), 074015.

[168] P. Lipari and T. Stanev, *Phys. Rev. D 44* (1991), 3543.

[169] Web-site `http://www-ik.fzk.de/corsika/`.

[170] Y. Becherini et al., *Astropart. Phys. 25* (2006), 1.

[171] A. Margiotta, *ANTARES Internal note, ANTARES-Soft/2004-002* (2004).

[172] L. T. S.Navas, *ANTARES Internal note,ANTARES-Software/1999-011* (1999).

[173] Web-site `http://wwwasd.web.cern.ch/wwwasd/geant/`.

[174] J. Brunner "Geasim: User manual" available at `http://antares.in2p3.fr/internal/software/geasim.html`.

[175] A. J. Heijboer, PhD thesis, Universiteit van Amsterdam, 2004.

[176] G. C. Hill, J. Hodges, B. Hughey, A. Karle and M. Stamatikos, *Proceedings of PHYSTAT05* (2006), 108.

[177] G. J. Feldman and R. Cousins, *Phys. Rev. D 57* (1998), 3873.

[178] G. Cowan, *Statistical data analysis*, Oxford University Press, 1998.

[179] W. J. Metzger, *Statistical methods in data analysis*, 2001. `http://www.pg.infn.it/l3/biasini/dott/metzeger.ps`.

[180] M. G. Kendal and A. Stuart, *The advanced theory of statistics, Vol. 2*, Griffin, 1973.

[181] J. Neyman and E. Pearson, *Phil. Trans. R. Soc. A 231* (1933), 289.

[182] F. Aharonian et al., *Astron. Astroph. 464* (2007), 235.

[183] Y. Uchiyama, T. Takahashi, and F. A. Aharonian, *Publ. Astron. Soc. Japan 54* (2002), L73.

[184] F. Aharonian et al., *Astron. Astroph. 449* (2006), 223.

[185] A. A. Abdo et al., *The Astroph. J. 734* (2011), 28.

[186] F. L. Villante and F. Vissani, *Phys. Rev. D 78* (2008), 103007.

[187] F. Vissani and F. Villante, *Nucl. Instrum. Methods A 588* (2008), 123.

[188] R. S. Fletcher et al., *Phys. Rev. D 50* (1994), 5710.

[189] D. Horns at al., *Astron. Astrophys. 451* (2006), L51.

[190] L. Zhang and X. C. Yang, *The Astroph. J. 699* (2009), L153.

[191] F. Aharonian et al., *Astron. Astrophys. 448* (2006), L43.

[192] ——, *Astron. Astrophys. 548* (2012), A38.

[193] S. Adrían-Martínez et al., the Antares Collaboration, *Phys. Lett. B 714* (2012), 224.

[194] I. C. M. G. Aartsen et al.

[195] J. Beringer et al.(PDG), *Phys. Rev. D 86* (2012), 010001.

[196] G.L. Fogli et al., *Phys. Rev. D 86* (2012), 013012.

[197] F. P. An et al. (Daya-Bay Collaboration), *Phys. Rev. Lett. 108* (2012), 171803.

[198] J.K. Ahn et al. (RENO Collaboration), *Phys. Rev. Lett. 108* (2012), 191802.

[199] L. Wolfenstein, *Phys. Rev. D 17* (1978), 2369.

[200] S. Mikheev and A. Y. Smirnov, *Sov. J. Nucl. Phys. 42* (1985), 913.

[201] A. M. Dziewonski and D. L. Anderson, *Phys. Earth Planet. Interiors 25* (1981), 297.

[202] E. K. Akhmedov, *Pramana - J. Phys. 54* (2000), 47. `arXiv:9907435 [hep-ph]`.

[203] P. Kooijman for the KM3NeT Collaboration, *Proceedings of ICRC2013, to be published* (2013).

[204] A. J. Heijboer. private communication.

[205] Web-site`http://www.genie-mc.org/`.

[206] L. Fusco. private communication.

[207] E. Fermi, *Phys. Rev. 75* (1949), 1169.

[208] W. I. Axford, E. Lear and G. Skadron, *Proc. 15th ICRC 11* (1977), 132.

[209] A. R. Bell, *Mon. Not. R. Astr. Soc. 182* (1978), 443.

[210] G. F. Krymsky, *Dokl. Akad. Nauk. SSSR 243* (1977), 1306.

[211] L. O. Drury, *Rept. Prog. Phys. 46* (1983), 973.

[212] J. R. Jokipii, *Astrophys. J. 313* (1987), 842.

[213] F. C. Jones and D. C. Ellison, *Space SCi. Rev. 58* (1991), 259.